9-9-2016

Integration of Biomolecular Recognition Elements with Solid-State Devices

Kan Fu
University of Connecticut - Storrs, kan.fu@uconn.edu

Integration of Biomolecular Recognition Elements with Solid-State Devices

Kan Fu, PhD

University of Connecticut, 2016

Continued advances in stand-alone chemical sensors requires the introduction of new materials and transducers, and the seamless integration of the two. Electronic sensors represent one of the most efficient and versatile sensing transducers that offer advantages of high sensitivity, compatibility with multiple types of materials, network connectivity, and capability of miniaturization. With respect to materials to be used on this platform, many classes and subclasses of materials, including polymers, oxides, semiconductors, and composites have been investigated for various sensing environments. Despite numerous commercial products, major challenges remain. These include enhancing materials for selectivity/specificity, and low cost integration/ miniaturization of devices. Breakthroughs in either area would signify a transformative innovation.

In this thesis, a combined materials and devices approach has been explored to address the above challenges. Biomolecular recognition elements, exemplified by aptamers, are the most recent addition to the library of tunable materials for specific detection of analytes. At the same time, nanoscale electrical devices based on tunnel junctions offer the potential for simple design, large scale integration, field deployment, network connectivity, and importantly, miniaturization to the molecular scale. To first establish a framework for studying sorption properties of solid oligonucleotides, custom designed aptamers sequences were studied to determine equilibrium partition coefficients. Linear-solvation-energy-relationship (LSER) analysis provides

quantifications of non-covalent bonding properties and reveals the dominance of hydrogen bonding basicity in oligonucleotides. We find that DNA-analyte interactions have selective sorption properties similar to synthetic polymers. LSER analysis provides a chemical basis for material-analyte interactions. Oligonucleotide sequences were integrated with gold nanoparticle chemiresistors to transfer the selective sorption properties to microfabricated electrical devices. Responses generated by oligonucleotides under dry conditions were similar to standard organic mediums used as capping agents and suggests that DNA-based chemiresistor sensors operate with a similar mechanism based on sorption induced swelling. The equilibrium mass-sorption behavior of bulk DNA films could be translated to the chemiresistor sensitivity profiles. Our work establishes oligonucleotides, including aptamers, as a class of sorptive materials that can be systematically studied, engineered, and integrated with nanoscale electronic sensor devices. Experiments to investigate secondary structure effects were inconclusive and we conclude that further work should investigate DNA aptamers in buffered, aqueous environments to unequivocally establish the ability of chemiresitors to signal molecular recognition.

Concurrent with the above studies, device integration and miniaturization was investigated to combine many sensing materials into a single, compact design. Arrays of nanoscale chemiresistors with critical features on the order of 10 – 100 nm were developed, using dielectrophoretic assembly of gold nanoparticles to control placement of the sensing material with nanometer accuracy. The nanoscale chemiresistors achieved the smallest known gold nanoparticle chemiresistors relying on just 2 – 3 layers of nanoparticles within 50 nm gaps, and were found to be more robust and less dependent on film thickness than previously published designs. Due to

shorter diffusion paths, the sensors are also faster in response and recovery. A proof-of-concept, integrated single-chip sensor array was created and it showed similar response patterns as non-integrated sensor arrays. Dielectrophoresis is established as a key enabler for nanoscale, integrated devices.

Based on the major findings of the thesis work, additional investigations were initiated to investigate the potential for nanoscale chemiresitor sensors to operate in buffered, aqueous (liquid) flow cells. Preliminary experiments show that chemiresistor sensing is transferable to liquid environments where analyte molecules are observed to partition from the bulk liquid to the sensing materials, leading to a detectable change of the device electrical properties. Comparing micron- and nano-scale devices fabricated using aqueous oligonucleotide-functionalized gold nanoparticles, it was found that nanoscale chemiresistors are more resistant to solvent damage than 5 μm chemiresistors. We conclude that future experiments to investigate aptamer sensing in aqueous solutions is a promising direction.

Overall, this thesis is a significant contribution to materials development and device design to attain improved sensor selectivity and higher levels of device integration. First, it offers a scheme for design, selection, and validation of materials that confer analyte-specific interactions. Second, it paves the way for large scale sensor integration and parallel operation on a single chip. Lastly, it offers an approach to combine biomolecular recognition elements with electronic devices into robust, nanoscale detection systems.

Based on the major findings of the thesis work, additional investigations were initiated to investigate the potential for nanoscale chemiresitor sensors to operate in buffered, aqueous (liquid) flow cells. Preliminary experiments show that chemiresistor sensing is transferable to liquid environments where analyte molecules are observed to partition from the bulk liquid to the sensing materials, leading to a detectable change of the device electrical properties. Comparing micron- and nano-scale devices fabricated using aqueous oligonucleotide-functionalized gold nanoparticles, it was found that nanoscale chemiresistors are more resistant to solvent damage than 5 μm chemiresistors. We conclude that future experiments to investigate aptamer sensing in aqueous solutions is a promising direction.

Overall, this thesis is a significant contribution to materials development and device design to attain improved sensor selectivity and higher levels of device integration. First, it offers a scheme for design, selection, and validation of materials that confer analyte-specific interactions. Second, it paves the way for large scale sensor integration and parallel operation on a single chip. Lastly, it offers an approach to combine biomolecular recognition elements with electronic devices into robust, nanoscale detection systems.

Integration of Biomolecular Recognition Elements with Solid-State Devices

Kan Fu

B. Eng., National University of Singapore, 2011

M.S., University of Connecticut, 2014

A Dissertation

Submitted in Partial Fulfillment of the

Requirements for the Degree of

Doctor of Philosophy

at the

University of Connecticut

2016

APPROVAL PAGE

Doctor of Philosophy Dissertation

Integration of Biomolecular Recognition Elements with Solid State Devices

Presented by

Kan Fu, B.Eng., M.S.

Major Advisor _____
Brian G. Willis

Associate Advisor _____
Bryan D. Huey

Associate Advisor _____
Yu Lei

University of Connecticut
2016

Acknowledgments

First of all, I thank my advisor, Dr. Brian G. Willis, for his constant guidance, support, motivation, and understanding throughout my graduate student career. I am grateful to have this opportunity to work on a project that encompasses the frontiers of materials science and nanotechnology. I admire him for his scientific insights, passion for innovations, strong work ethics, and unwavering support for my endeavors, all of which will continue to influence me in years to come. His patience and enthusiasm helped me build confidence, improve my research skills, and overcome many challenges. Through my studies with him, I have not only become a better scientist, but also a better person.

My special thanks to my associate advisors Dr. Bryan Huey, Dr. Yu Lei, Dr. Fotios Papadimitrakopoulos, and Dr. Gregory A. Sotzing for providing valuable inputs and expertise to this work. In addition to their wise words, I am also grateful for the laboratory and instrumentation support I have had from every single one of them. Next, I am proud and fortunate to have been surrounded by a group of excellent lab mates. I sincerely thank my past and present lab mates Dr. Han Wang, Dr. Xiaoqiang Jiang, and Jie Qi for their day-to-day help in my research efforts, joyous company, and inspirations. My gratitude for the hardworking undergraduate students who assisted me in my lab – Nathanael Chan, Natalie Von Achen, Andrew LaMarche, Wyatt Pedrick, John Scovill, and Nicholas Oliveira.

This work would not have been possible without the help of my collaborators. I thank Dr. Shihui Li, Dr. Yong Wang, Dr. Shutang Chen, and Dr. Jing Zhao for their kind assistance in materials preparation. I thank Dr. Leslie M. Shor, Mitchell Cyr, Dr. Anson W. Ma, and Yang Guo for their assistance in printing technologies. I am also thankful to various forms of technical support I received from Adam Wentworth, Dr. Lichun Zhang, Dr. Roger Ristau, Dr. Yasemin Kutes, Gary Lavigne, Dr. Laura Pinatti, Dr. Jack Gromek, Dr. Eric Donkor, Jian Ren, Dr. Yumin Zhu, Dr. Xiangcheng Sun, Wei Wu, Curtis Guild, Dr. Yixin Liu, Hui-Jan Lin, Dr. Yongku Cho. I thank Mark Drobney, Joseph Csiki, John Fikiet, Amadeusz Nasuta, and Peter Glaude from the machine and electronic shops for assistance in fabricating my experimental setups. The kind help from administrative staff at University of Connecticut – Lorri Lafontaine, Susan Soucy, Leah Winterberger, and Cathy McCrackan are greatly appreciated. I acknowledge Office of Naval Research and National Science Foundation for funding my research.

Outside of the thesis work, I thank my friends and roommates at University of Connecticut, who made my life as a graduate student exciting and memorable. I thank my friends around the world for immense intellectual and emotional support, especially in times of hardship.

Finally, I dedicate this thesis to my family. The love, support, and faith from my parents made me who I am. I thank my grandparents and extended family for always been helping and inspiring me to overcome challenges and better myself.

Table of Contents

List of Tables

List of Figures

Chapter 1

INTRODUCTION

1.1 Chemical sensors

Chemical sensors are devices which convert a chemical state into an electrical signal.[1] For example, the chemical state can refer to concentration species, partial pressures, activities of atoms, molecules, or biologically relevant compounds to be detected in gas, liquid, or solid phase. Sensing of small molecules is of utmost importance, primarily due to many types of small molecules, either in gaseous or liquid phase, that could either be indicative of environment wellness, bodily health, or be toxic or hazardous species that warrant corrective measures. While types of small molecules of interest are many, the types of transducing mechanisms and sensing materials are also abundant. Signals that can be collected are typically conductivities, electrical potentials, capacitances, oscillating frequencies of a mass, position displacements, optical constants, photon emission, etc. For users to understand these changes in signals, sensors are usually packaged and integrated with computer systems, this way signals can be recorded and displayed in user-friendly fashions.

Essential to all of the sensors is the interaction of the sensing interface with the analytes. The absorption or adsorption of analyte species onto the sensing element materials within the

chemical sensors are the first of a cascade of events that generates the eventual signals (Figure 1.1). The interactions between the sensing material and the analyte, whether adsorption, absorption, or ligand-receptor binding, and their effect on one or more measurable properties of the material, generate the signal. The sensing process could occur in the gas phase, where the interaction is between gaseous molecules and the solid sensing material, or it could be in the liquid phase, where the species interacting with the sensing materials are dissolved analyte molecules.

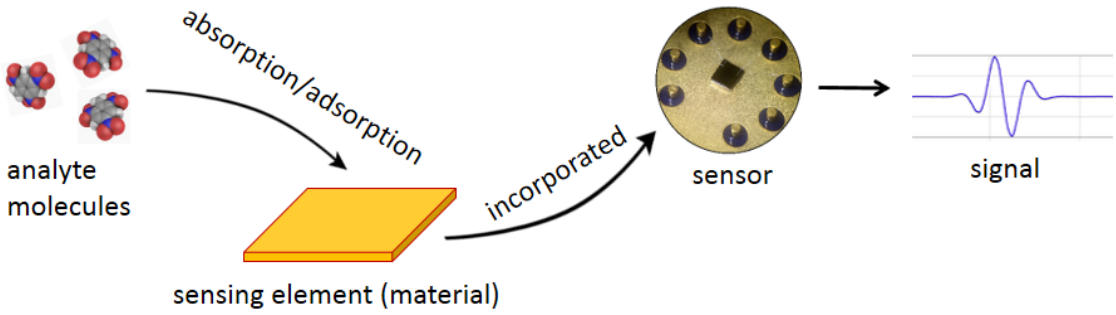

Figure 1.1 Principle of chemical sensors

The ability of the material to interact with the analytes therefore plays a dominant role in the performance of the sensors. However, it needs to be recognized that the chemical sensor as a system relies not only on the active sensing material, but also on recent innovations in manufacturing technology, microelectronics, and micromachining which play important roles in a complex system.[2] Chemical sensors is an interdisciplinary field that compounds materials chemistry and physics, materials processing technology, power system, and signal processing.

1.1.1 Electronic chemical sensors

In the contemporary world, chemical sensors for small molecules are ubiquitous. Electronic sensors are one of the most attractive and versatile classes of sensors. This class of sensors offers simple circuitry, easy integration with electronic circuits, and potential for miniaturization. Metal oxide semiconductors, metal oxide semiconductor field effect transistors, conducting polymers, piezoelectric crystals, etc. are some of the examples of commercially available electronic sensors.[3] Common to all of the listed examples is the detection of changes in electrical current upon exposure to the analyte. Figure 1.2 illustrates the effects of analyte partitioning into the sensor materials. As molecules are absorbed by the film in between electrodes, they induce structural or charge transport condition changes in the film, which are reflected as changes in measured resistance of the material.

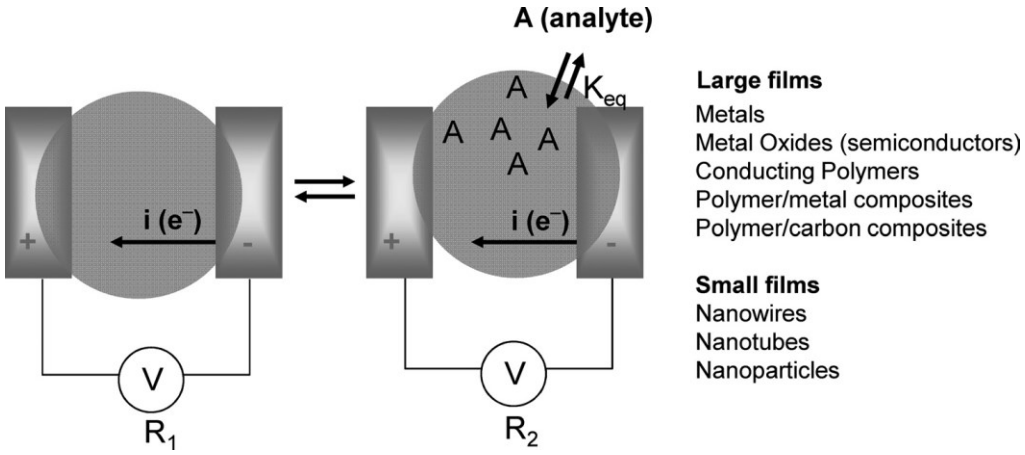

Figure 1.2 Generic representation of chemiresistor film placed between two metal electrodes. Upon absorption of analyte (A), the measured resistance changes from R1 to R2 under a constant electrical potential V.[4]

Sensor development is driven by application. For example, carbon monoxide gas poses a serious health and safety concern in households.[5] Carbon monoxide detectors based on electrochemical fuel cell technologies were developed as a common household appliance to alert residents of potential dangerous carbon monoxide levels. To analyze complex mixtures of gaseous compounds, electronic noses (e-noses) were developed to employ an array of independently semi-selective and reversible sensors combined with pattern recognition algorithms.[6] Sensor arrays are developed for tasks that require differentiation of analyte mixtures, for example, food and beverage quality control, environmental monitoring, disease diagnosis, workplace hazard warning, and leakage monitoring.[3, 7]

1.1.2 Benchmarks in chemical sensor research

1.1.2.1 Selectivity

In analytical chemistry, selectivity describes the ability of discriminating methods to quantify analytes of interest with less interference from other components. It is a quantifiable measurement of the performance of analytical instrument. Specificity is an extreme case of selectivity, representing the case that no component in a mixture other than the analyte contributes to the result.[8] While this ideal case can be hardly achieved, achieving a more selective sensor or any other analytical instrument than the past is a technological goal and, as will be discussed in Section 1.1.3, a performance enhancement factor of sensors and sensor arrays.

1.1.2.2 Sensitivity and limit of detection (LOD)

Sensitivity is expressed as the slope of sensor response against analyte concentration at any given analyte concentration rage. Limit of detection (LOD) is universally taken as three times the

baseline noise divided by sensitivity. Therefore, the unit in which analyte concentration is important in both the sensitivity and LOD calculations. The absolute concentration is typically used for gases. For vapor analytes, absolute concentrations are still a valid way of comparison sensor-to-sensor performance. However, for comparison between different vapors on the same sensing material, especially between vapors of very different saturation vapor pressures, the ratio of vapor pressure versus saturation vapor pressure (p/p_0) becomes a more useful way of comparison. The use of p/p_0 as the standard unit of vapor concentration corrects for the tendency of more volatile molecules to stay as gas molecules and the propensity of less volatile molecules to condense on the sensors.

1.1.2.3 Response speed

Sensors are designed to respond to a dynamic analyte exposure, and to recover after the analyte is removed. Response speed characterizes the time it takes for sensors to reach equilibrium with the surroundings. This parameter depends on the sensor volume and diffusion speed of molecular species. Similarly, when analyte is removed from the surroundings, the time it takes for a sensor to recover to its initial status by desorbing the analyte molecules is a benchmark of the sensor recovery speed. In real-time sensing tasks, the environment is dynamic, and only an instantaneous equilibrating sensor would reflect the true analyte concentrations. A faster-responding chemical sensor would give a more accurate reading in changing environments, which is the case when multiple data points need to be taken within a short period of time.

1.1.3 Trends and challenges in chemical sensor research

1.1.3.1 Selectivity enhancement

Compared to generic laboratory analytical instruments dedicated to chemical identification and analysis based on gas chromatography (GC), sensors offer simplicity, portability, low cost, and suitability for field applications. However, cross-interference is a major issue with commercial sensors, as shown in Table 1.1 for a particular series of commercial gas sensors.

Table 1.1 Cross interference of common commercial gas sensors[9]

		sensor											
		CO	H_2S	SO_2	NO_2	Cl_2	ClO_2	HCN	HCl	PH_3	NO	H_2	NH_3
gas	CO	100	2	1	0	0	0	0	0	0	0	20	0
	H_2S	10	100	1	-8	-3	-25	200	60	3	10	20	10
	SO_2	0	10	100	0	0	0	-	40	-	0	0	-40
	NO_2	-20	-20	-100	100	12	-	-70	-	-	30	0	0
	Cl_2	-10	-20	-25	90	100	20	-20	6	-10	0	0	0
	ClO_2	-	-	-	-	-	20	100	-	-	-	-	-
	HCN	15	10	50	1	0	0	100	35	1	0	30	5
	HCl	3	0	0	0	2	0	0	100	0	15	0	0
	PH_3		-	-	-	-	-	0	300	100	-	-	-
	NO	10	1	1	0	-	-	-5	45	-	100	30	50
	H_2	60	0.05	0.5	0	0	0	0	0	0	0	100	0
	NH_3	0	0	0	0	0	0	0	0	0	0	0	100

When two or more gases are present, the additive or subtractive responses will give false information about the target gas. Similar cross sensitivities issues have also been reported with organic vapor sensors used for atmospheric monitoring.[10] In addition, commercial gas sensors are usually affected by environmental humidity, which limits their accuracy in less controlled field applications.[11] Cross reactivity effects in the gas sensors are also pervasive in organic vapor sensors that operate with various materials – conducting polymers,[12], graphitic materials,[13] and gold nanoparticle nanocomposites.[4]

To overcome the issue of cross sensitivity, one solution is the use of multiple sensors in a sensor array or electronic noses.[14] Electronic noses mimic the mammalian olfaction system, which utilizes a large array of olfactory receptor cells, none of which being highly selective to odor molecules.[15] Olfactory receptor family is one of the largest known mammalian gene families, with approximately 400 functional genes coding for olfactory receptors.[16] Each odorant can elicit responses from a number of receptors, probably with different response amplitudes. These responses are transmitted as signals in neurons to the olfactory bulb in the frontal lobe or limbic system of the brain as shown in **Figure 1.3**(a).

The neural network in human olfactory system, is highly convergent. For every 10,000 – 20, 000 primary receptor neurons, each secondary or mitral cell neuron receives a single signal. Through recognition of the spatial and temporal patterns of the signals by the neural network, the odor is identified at the perceptual level. The natural neural networks play an important part in the information processing pathway,[17] but it is complex. Designing artificial neural networks (ANN) represents an effort to mimick the mammalian olfaction system most closely, and it offers the benefits of greater flexibility and parallel computational capability that speeds up analysis.[15]

Using the multi-layer perceptron (MLP) architecture, ANN imitates the similar principles in data processing in a human olfactory system, and has been realized using small sensor arrays in classification of organic vapors.[18-21]

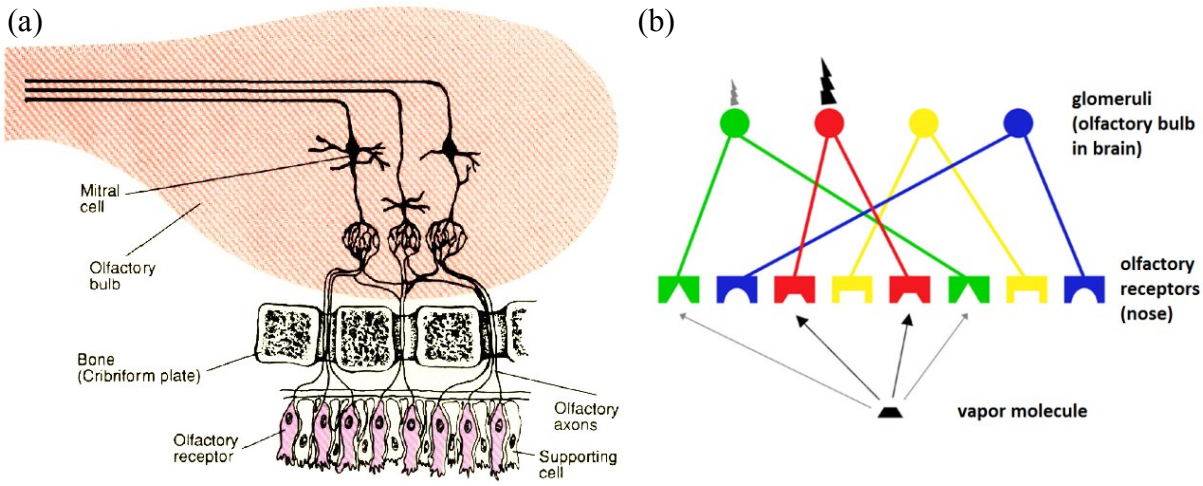

Figure 1.3 (a) Human olfactory cells in the nose and nerve connections into the brain;[22] (b) Simplified diagram of neural network in mammalian olfactory system.[23]

In addition to ANN, two types of analytical methods are also commonly used. Multivariate analysis is a method that reduces high dimensionality in partly correlated data to smaller, less correlated data dimensions. For example, principal component analysis (PCA), linear discriminant analysis (LDA), cluster analysis (CA), partial least squares (PLS).[24] Graphical analysis, using bar charts, profile polar plots, radar plots, is the third way of representing relatively simple data sets. In general, the effectiveness of a sensor array to differentiate analytes is dependent on the number of sensors of different selectivity used.[7, 25] These two types are simpler and more straightforward than neural networks, but are less sophisticated and universal.[26] Table 1.2 lists some examples of

commercial electronic noses. A common limitation across all of the listed commercial examples is their limited vapor identification and quantification capabilities. These commercial electronic noses are adequate in differentiating one mixture from the other, but the information they give is qualitative, and further information on identification of chemical analyte is not accessible.[27]

Table 1.2 Examples of commercial electronic noses[27]

Manufacturer	Sensor type	Array size	Application	Feature
Airsense Analytics	MOS	10	Quality control and environmental safety	Portable
Alpha MOS	MOS	6 – 18	Quality control and product development	Headspace autosampler
Cantion	Piezo-resistive cantilever	8	Food and water safety, medical diagnostics, and life science research	Gas and liquid phase samples
Dr. Födisch AG	MOS	10, 12	Environmental monitoring and industrial process control	
GSG Mess- und Analysengeräte GmbH	MOS, QCM	4 – 16	Food quality control, environmental monitoring, industrial process control	Hand-held and research-grade devices
MSA Safety	SAW	2	Mine safety, chemical warfare agent detection	
Sacmi	MOS	6	Quality control and environmental safety	Continuous outdoor monitoring
RST Rostock System-Technik GmbH	MOS	6	Indoor Environmental safety	
Sysca AG	MOS	16	Industrial process control and environmental safety	Hand-held option
Technobiochip	QCM	8	Food quality control, medical diagnostics, environmental monitoring, and industrial process control	

The reason for this limitation on current chemical sensor technology is the inability to obtain a selective response to a target analyte, given the millions of known molecular species, the

variations in environmental conditions, and the variations in analyte amount or concentration.[2] Sensor arrays are subject to background interference,[28] and members of the sensor array lack the selectivity displayed by mammalian olfactory receptors.[7, 29] Increasing the different types of currently available chemical sensors does not expand the limits to the useful dimensions of the sensor array.[7] While limited new information is obtained by adding members to the sensor array, the consequential amplification in noise also occurs. As reflected by Table 1.2, the practical commercial electronic noses usually consist of a few to more than 10 sensors in an array, but never above 20. Therefore, despite laboratory-scale success in differentiating odors of different samples from the same class and rapid development of computational technologies in data processing, information-rich, quantitative sensor arrays are still in the developmental stage.

A fundamental problem that awaits solutions is the improvement in sensor selectivity, whether it works as discrete detector, or functions in a sensor array. This is particularly the case when one or two analytes in a mixture is of particular interest. As a result of lack of sufficient selectivity, the electronic noses would not be able to pick up its quantity accurately. Even for a particular mixture, the overwhelming part of an odor may be attributable to only one compound present at only trace levels.[15] Current cross-reactive sensor arrays with limited selectivity would be an ineffective solution for this purpose, especially with respect to analyte quantification. In fact, the human olfactory system is powerful in that increase in odor concentration produces different perceptions, an indication of the recruitment of new receptor types. For example, 1-heptanol smells like cucumber at just above odor threshold level but has a citrus smell at 729 ppm above odor threshold level,[30] indole has a flowery smell at low concentrations but fecal smell at high concentrations.[31] The human nose can also tell the distinctive odor differences between (R)-(+)-limonene and (S)-(-)-limonene, which are enantiomers that differ only in chirality.[32] These

differences show that the olfactory sensors not only have greater varieties of sensors, but also have highly selective elements that pick up minute differences between molecules. Therefore, sensors and sensor arrays using conventional materials may be useful for some applications, but accurate field determination of analytes of interest would require (1) more selective sensors, and (2) more varieties of sensors in the array. These advancements coupled with more mature computational technologies would produce smarter, quantitative, and more informative sensor systems.

Many approaches have been explored to address the issues of selectivity. Cavitands were investigated for possible shape-selective binding of small molecules. However, careful analysis has shown that the dispersion forces of the sensing material dominates over selective host/guess interactions.[33] Molecularly imprinted polymers (MIPs) is one approach that uses the target molecule to create cavities, with typical enhancement in selectivity.[34] However, manufacturing MIPs is not practical due to necessary template removal which is costly and ineffective.[35] Most importantly, the non-specific interactions present in MIPs make the specificity of this method unable to match that of receptor-analyte systems in biological systems.

1.1.3.2 Miniaturization

In recent years, miniaturization, portability, power efficiency, response speed, and network connectivity are common trends in sensor development.[36] Chemical sensors find important application in internet of things (IoT) that enable network connectivity and optimized sensor networks. The information reflected by individual sensors can be combined and processed to generate unprecedented spatial and temporal knowledge, for example in the field of environmental monitoring, wearable health monitoring systems, agricultural production monitoring, mine safety, and habitat monitoring.[37-40] Sophisticated sensor networks require individual sensors to be tiny,

power saving, inexpensive, and easily replaced.[38] To probe the limitation of microfabrication technology, the *Smart Dust* project was started to package autonomous sensing, computing, and communication system within a cubic-millimeter "mote" to form the basis of integrated massively distributed sensor networks (Figure 1.4(a)),[41] with integrated sensor mote as small as 16 mm^3 fabricated as of now.[42] These tiny, highly integrated sensor nodes are projected to be the pinnacle innovation of the IoT in the technological community.[43] Chemical sensors would make an important contribution to sensor networks in IoT architecture, as chemical information presented with positional information would be enrich human awareness of its environment and help with decision making and corrective actions. For example, a sensor network with chemical sensors installed on the global scale would track air pollution and help humans make counteractive plans. Sensor networks can also be deployed in water bodies, workplaces, and public areas, and on streets to provide three-dimensional monitoring of hazardous chemicals. To be IoT ready, chemical sensors need to be reduced in size and power consumption but retain their reliability.

Recently, sensors that are integrated with handheld devices (e.g. smartphones) are widely available to average persons, and combined with data processing applications and cloud computing platforms, these sensors provide multidimensional streams of information which reflect can be processed to reflect, for example, health information of the user. Furthermore, the data could be processed by big data analytics software to provide customized services or gather user-related service enhancement recommendations. Current installed sensors on personal phones are microelectronic and some employ microelectromechanical systems (MEMS). For example, MEMS gyroscopes and accelerometers. These sensors are manufactured using standard microelectronic packaging, and are compactly encased, along with all other electronic components, within the handheld devices. (Figure 1.4(b)). A very useful addition to the array of microscopic

sensors already in smartphones would be chemical sensors that will help with user health monitoring and environmental hazard warning. Early development of smartphone sensors has demonstrated the creation of chemiresistor sensor arrays[44] and SPR-based diagnostic devices[45] that can be connected directly to iPhones, but the size of these sensors are considerably large and they need to be carried as accessories to the phones. Reducing the sizes of these chemical sensors to make them truly part of the hand-held devices is a very meaningful technological progress.

(a)

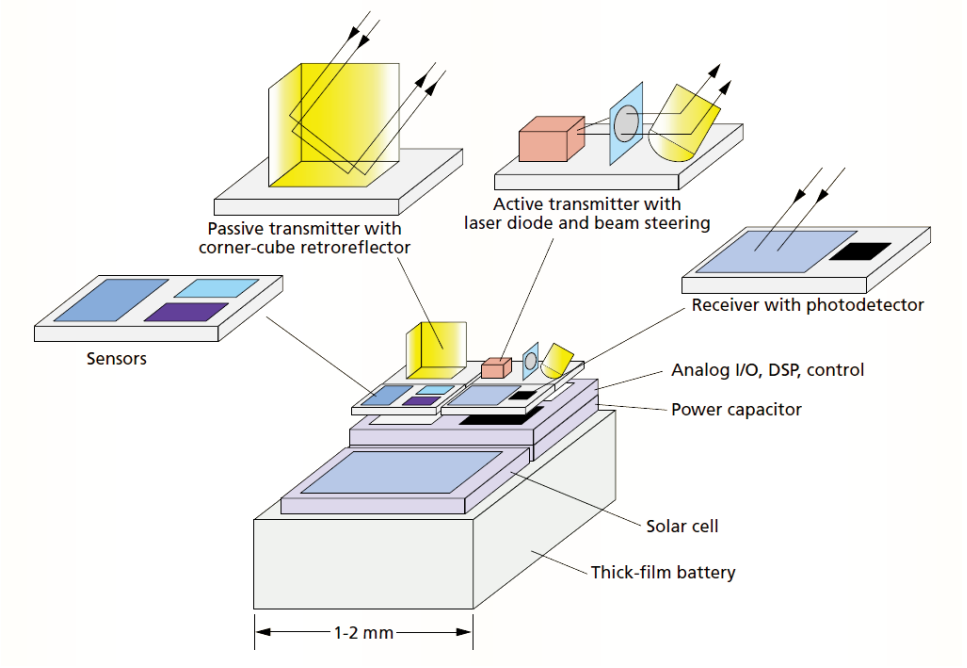

(b)

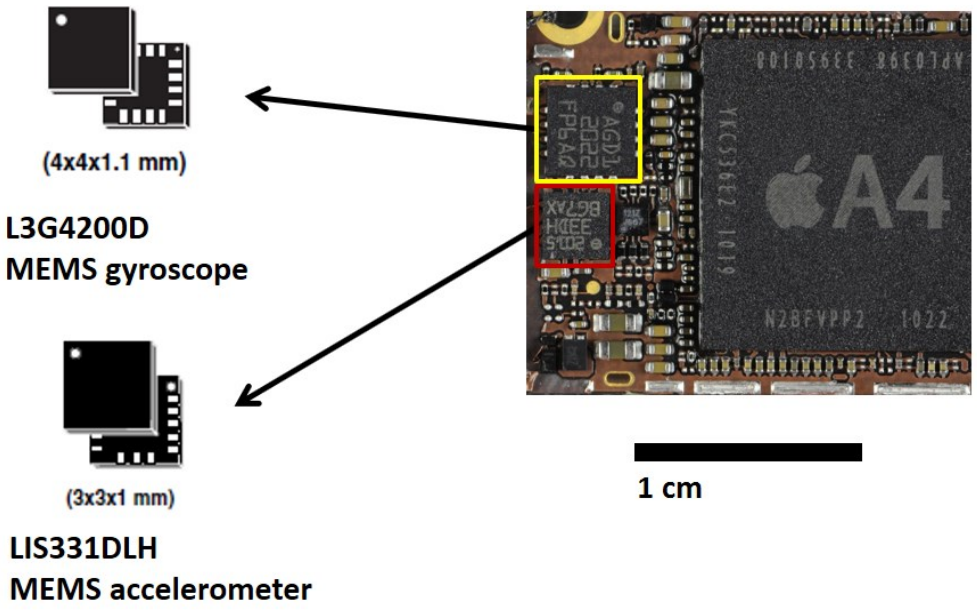

Figure 1.4 (a) Conceptual diagram showing a *Smart Dust* mote's major components: a power system, sensors and integrated circuit.[41] (b) Two MEMS sensors on an Apple iPhone 4, showing the dimensions of packaged sensors.[46-48]

1.2 Molecular electronics and tunneling devices

1.2.1 Single nanogap deivces

As mentioned previously in Section 1.1.1, electronic devices are one of the simplest but most versatile platforms of sensors. One of the simplest types of electronic devices are the nanogap electrodes.[49] Its key element is composed of a pair of conducting electrodes separated by an insulating gap, typically of the range 1 – 5 nm. Nanogap electrodes have potentially a multitude of applications because of the different media that can be inserted in the electrode gap. By inserting different molecular species, specific electronic functions performed by the gap molecules, including electrical rectification, switching, thermoelectricity,[50] and transistor function[51] can be achieved. In all of these examples, nanogap electrodes take advantage of the small, countable number of molecules that are sandwiched in between the electrodes to allow microscopic properties of molecules to be exhibited and amplified. For example, in the molecular rectifier example, the unique asymmetrical arrangement of the donor and acceptor molecules within the nanogap junction results in unidirectional flow of charges.[52] This effect would not be possible with macroscopic isotropic materials.

With respect to chemical sensors, the nanogap is a very practical configuration. The current through a fixed nanogap is dependent on the gap size and the relative permittivity of the nanogap space. The calculation of the tunneling current can be express in Equation 1.1:

$$\boldsymbol{I} = \boldsymbol{J} \cdot \boldsymbol{A} \tag{1.1}$$

where A is the tunneling area and J is the tunneling current density. J can be expressed in the following equation when the applied bias is in the $V < \varphi_0/e$ region,[53]

$$J = (6.2\times10^{10} / \Delta s^2)\{\varphi_I \exp(-1.025\Delta s\varphi_I^{1/2}) - (\varphi_I + V)\exp[-1.025\Delta s(\varphi_I + V)^{1/2}]\} \qquad (1.2)$$

with:

$$\varphi_I = \varphi_0 - (V/2s)(s_1 + s_2) - [5.75/K(s_1 - s_2)]\ln[s_2(s - s_1)/s_1(s - s_2)]$$
$$s_1 = 6/K\varphi_0$$
$$s_2 = s[1 - 46/(3\varphi_0 Ks + 20 - 2VKs)] + 6/K\varphi_0$$

where s is the gap distance, s_1 and s_2 are limits of the barrier height at the Fermi level, $\Delta s = s_2 - s_1$, and φ_0 and K are the barrier height and dielectric constant of the insulator layer. V is the applied voltage between electrodes. From Equation 1.2 it is obvious that the tunneling current depends on the distance between electrodes, barrier height, and the dielectric constant of medium within the gap.

Based on this principle, simple nanogap sensors were developed. Nanogaps on a cracked AuPd film can be used to detect atmospheric hydrogen, which operates on physical expansion of the metallic electrodes and closing of the gap upon hydrogen absorption.[54] The LOD is at 100 ppm, comparable to other types of commercial sensors.[55] On the other hand, reversible adsorption of acetic acid molecules in a tunnel junction dramatically increases the electrical current through the nanogap based on modulating of tunneling current by insertion of permitted molecular orbital energy levels in between the nanogap.[56, 57] The nanogap configuration has found a wide range of sensing applications,[58] demonstrating a practical way of meeting the requirements of miniaturization of sensor devices.

Due to the small size of the nanogap, the fabrication of the single nanogap electrode devices requires a combination of top-down and bottom-up approaches. First, patterned electrodes are defined by a combination of photolithography and electron-beam lithography. Afterwards special techniques such as atomic layer deposition,[59, 60] mechanically controlled break junctions (MCBJs),[61] and electromigration break junction (EBJs)[62] are used to produce the physical nanogap. Despite various techniques that have been explored, reproducible and predictable fabrication of nanogaps is not easy, primarily due to the stochastic processes occurring at the nanoscale. As shown in Figure 1.5, an array of identical tips produces variations in tip structures after modification by ALD technique, with variations in gap distance in the range 2 – 10 nm across the 9 nanogaps included in the SEM images.

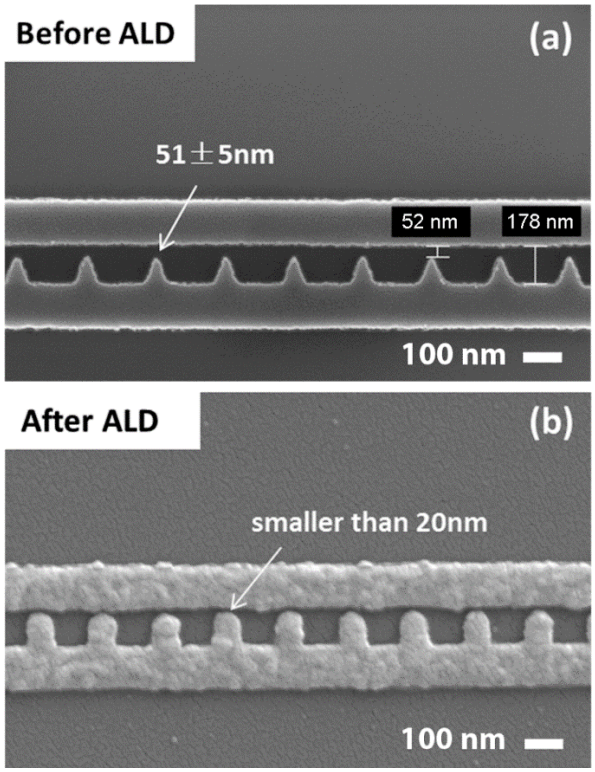

Figure 1.5 (a) An array of e-beam fabricated nanogap with spacing 50 nm; (b) The same type of nanogap modified by ALD growth of copper film, showing variations across tips.[63]

1.2.2 Multiple nanogap deivces

The gold nanoparticle chemiresistor is a new, more complex design of nanogap devices that were designed primarily for sensing of volatile organic compounds.[4] These chemiresistors comprise of multiple layers of organic functionalized gold nanoparticles deposited on interdigitated electrodes (Figure 1.6(a)). These layers of gold nanoparticles form a composite material consisting of alternating highly conductive metallic phase and insulating organic ligand phase. As a result of this mix, the resistance of gold nanoparticle chemiresistor film is in the semiconductor range. Electronic conduction is through an electron hopping mechanism through a chain of conducting gold nanoparticles which form a path (Figure 1.6(b)). Electron-transport mechanism between the electrode and gold nanoparticle cores is the same as that between gold nanoparticle cores. Therefore contact resistance, which would have been a complicating issue in traditional chemiresistors, would be essentially avoided.[64] This fact lends help to the possibility of device miniaturization, because contact contribution to the electron transport would be small even if only a few gold nanoparticles were present. Gold nanoparticle chemiresistor sensors are similar to traditional metal oxide and conducting polymer chemiresistor sensors, differing only in the active sensing materials. To illustrate, the gold nanoparticle film is an array of nanogaps, and its response arises from the collective functioning of a multitude of nanogap sensors.

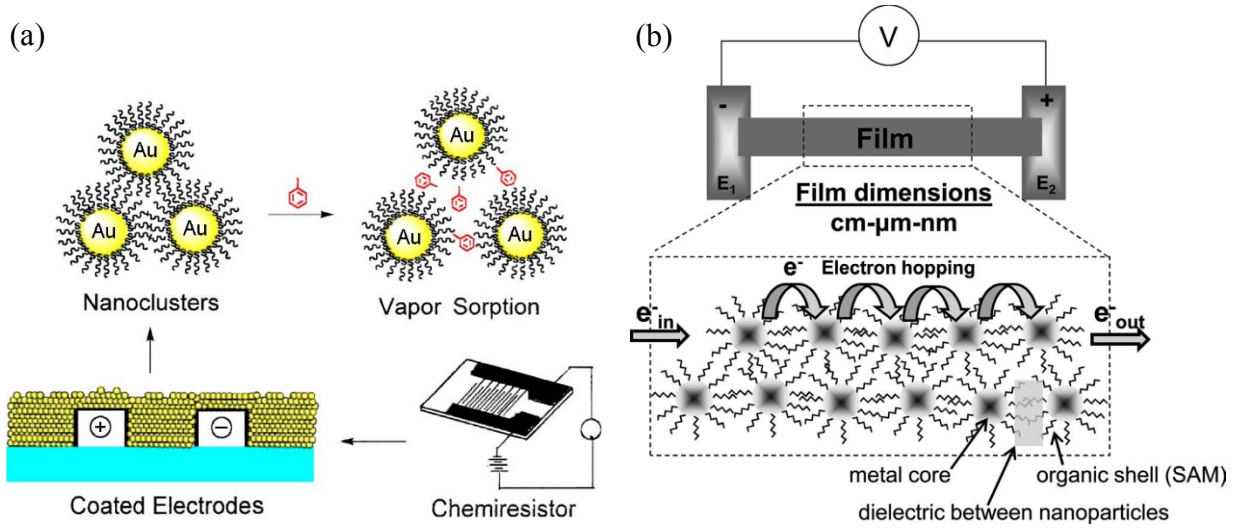

Figure 1.6 (a) Schematics of sensing mechanism of gold nanoparticle chemiresistor sensor;[64] (b) Electron hopping conduction pathway through the gold nanoparticle film.[4]

As vapor phase molecules reversibly adsorb and dissolve into the gold nanoparticle films, swelling of the films occurs, and film resistance changes following the relationship[65]

$$R = \exp(\beta l)\exp\left(-\frac{E_c}{k_B T}\right) \tag{1.3}$$

where β is a decay constant related to the probability of interparticle electron tunneling, l is the interparticle distance, E_c is the activation energy, and k_B is the Boltzmann constant. Further, the activation energy is given by

$$E_c = \frac{1}{4\pi\varepsilon_0\varepsilon_r}\frac{e^2}{r} \tag{1.4}$$

where e is the fundamental charge, ε_0 is the vacuum permittivity, ε_r is the dielectric constant of the organic capping layer separating nanoparticles, and r is the radius of the gold nanoparticle. Comparing Equations 1.1 and 1.3, it is obvious that descriptive parameters are richer for the single nanogap as compared to the nanoparticle films. Due to randomness in packing of gold nanoparticles and ligands, the nanoparticle film is less directional, and the factors that determine the resistance of nanoparticle films are more general. It has already been established that both the interparticle distance and the dielectric constant of organic capping layer affect sensor response strongly,[66, 67] and these two factors are ultimately determined by the intrinsic polarity [66, 68] and molecular size [69, 70] of capping layer molecules. While the quantitative contribution percentages of the effects of distance change and dielectric constant change to the resistivity change of the nanocomposite film have not been well-established, more evidence is available for the dominance of inter-particle distance change effects.[25]

Gold nanoparticles are one of the most attractive materials of the contemporary period, largely due to its stability and ease of surface functionalization with various types of ligands,[71] therefore many sub-classes of gold nanoparticles have been used to build chemiresistor sensors, using identical chemiresistor sensor setup and simple electrical circuitry. Functionalized gold nanoparticles are usually synthesized by reducing a gold ion precursor in the presence of organic ligands. Depending on the desired final product, the as-synthesized gold nanoparticles are then further subject to ligand exchange process to produce a variety of surface functionalities. Well-studied ligands are unfunctionalized alkanethiols, with chain length from six carbons to twelve carbons,[72] as well as amino-,[73] phenyl-,[74] carboxyl-, and hydroxyl-[68] functionalized alkanethiols. To fabricate the sensor devices, a solution of functionalized gold nanoparticle solutions is typically drop-casted,[75] airbrushed,[72] ink-jetted,[76] dip-coated,[77] or electrosprayed[78] onto a microfabricated

interdigitated electrode on a substrate. The solution drop is then dried to form the nanoparticle composite film. Selectivity originates from differences in non-covalent chemical interactions between analyte vapors and the organic phase in the nanocomposite films.[79]

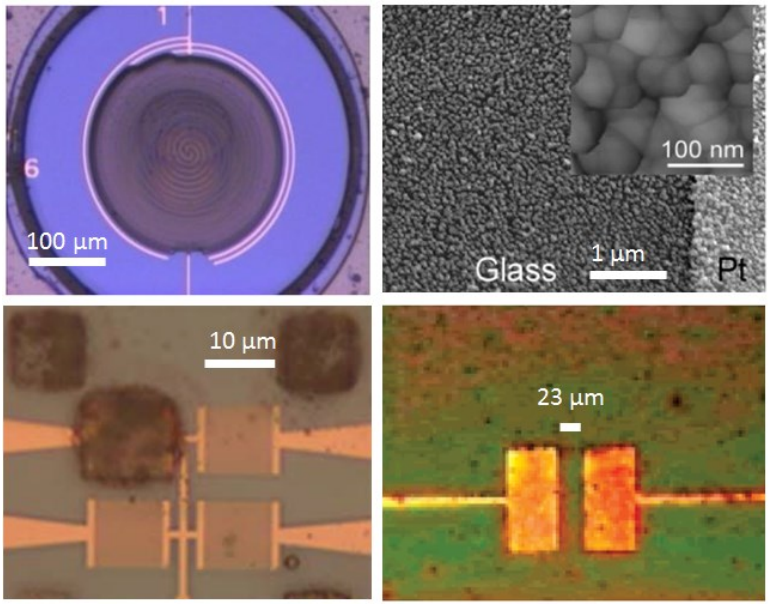

Figure 1.7 Multiple designs and film morphologies of gold nanoparticle chemiresistve sensors[77, 80-82]

Compared to single-nanogap devices, chemiresistors are different in several ways. As the films consist of at least thousands of nanoparticles in an ensemble, the sensor response from each nanogap is inherently averaged. The sensor is considered as a more macroscopic device instead of being dependent on a single nanoscale device. This averaging and combinatorial effect eliminates device-to-device variance, and improves repeatability of devices. Typical response standard deviation of gold nanoparticle chemiresistor vapor sensors is in the range of 5% to 20%.[25,

[66, 67, 83] In the study by Joseph et al., it has been shown that increasing film thickness results in lower device-to-device variations,[67] an observation that lends direct support to averaging effects in error reduction.

Because of the orders of magnitude scale difference between the 2 types of devices, the mechanisms effecting the sensor response are also different. For gold nanoparticle films, the ligands around nanoparticles are stationary and relatively persistent, not counting the ligand degradation effects, while the metallic cores are relatively mobile. The changes to the insulating media in between neighboring nanoparticles caused by absorption of analyte molecules is limited. Therefore, changes in the film resistance is primarily determined by changes in interparticle distance. By contrast, nanogap devices have fixed electrodes defined by fabrication process, but highly variable inter-electrode media. The insertion of molecules of interest dramatically changes the internal environment within the nanogap, creating an on/off effect.

Compared to other types of chemical sensors, the nanogap design offers several advantages. Carbon nanotube and graphene sensors are two types of electronic sensors capable of miniaturization to nanoscale and giving similar conductance signals as nanogap sensors.[84, 85] These graphite-based sensors operate by a combination of electrostatic gating and Shottky barrier effects,[86] giving excellent sensitivity. However, these 2 types of sensors are limited by the type of molecules that can be bound to the carbon nanotube and graphene surface without creating defects. As a result, molecular attachment is usually through π-π stacking forces,[87, 88] which is relatively weak. On the other hand, modification of metallic surfaces by organic molcules is a simpler and more versatile procedure, with a range of functional groups of different bonding strengths to

choose from, such as thiol-Au bonds[75] and amine-Au bonds.[82] In general, these linkages occupy smaller volumes and are more stable than stacking forces.

Optical sensors derive their accuracy from the predictable light-analyte interaction. While in some cases the measurement needs the help of a solid material that interacts with analyte, such as a fluorescent material or a colorimetric material, in other cases the sensors can be even more accurate by not needing a solid material at all.[89] While typically used to monitor gas concentrations, optical instruments were also used to monitor dissolved molecules and volatile organic molecules. In one example, the use of UV-differential optical absorption spectroscopy (UV-DOAS) were used to monitor atmospheric benzene and toluene vapors with similar accuracy as GC systems and detection limit about one-tenth of GC systems.[90] Despite the accuracy and stability advantages of optical systems, the instruments are usually bulky, fragile, power-consuming, and inconvenient for field applications.

Several distinctive benefits are also reported for nanoparticle chemiresistors. Research has also shown that the addition of gate in making it a 3-electrode transistor configuration will enhance the sensitivity of devices.[91] The devices can be dimensionally downscaled while retaining sensitivity.[64, 92] For single nanogap devices, it is possible to use inelastic electron tunneling spectroscopy (IETS) for molecular identification,[56] and single molecule detection.[93] With device resistance at least in the tens of kΩ range, the power consumption is low, which makes it compatible with self-powered sensor networks.

The simplicity of chemiresistor designs provides practical benefits compared to other devices that use more complex transduction mechanisms such as chemitransistors,[94, 95]

fluorescence-based detectors,[96] surface acoustic wave (SAW) sensors,[97] fiber-optic vapor sensors,[98] and surface-enhanced Raman scattering (SERS) sensors.[99]

1.3 Biomolecular recognition elements

1.3.1 Sensing with biomolecules

Nature has bestowed us with a multitude of elegant designs, that inspired a multitude of engineering applications that employ biological materials or biologically inspired materials and designs as keys to their functions. Examples include cellulose-based paper and fabrics, airplanes, structural coloration, Velcro tapes, and mussel-inspired adhesives. For the detection and diagnostic applications in particular, biological and bioinspired molecules have been widely explored for target-specific analysis. Hemeprotein-modified electrodes on electrochemical cells use strong binding between heme groups and carbon monoxide to perform carbon monoxide sensing.[100] More recently, blood glucose meters are based on thin layers of glucose oxidase (GOx) enzyme on electrodes, which reacts with glucose to produce a specific response.[101] Immobilized urease was reported to show irreversible response to urea.[102] The success in using biological materials lies in the availability of target-specific molecules. However, the types of target-specific molecules are limited to molecules that are of physiological importance. For many useful targets, such as hazardous, toxic vapors, explosive compounds, and disease-related metabolites, and substances of forensic importance, artificially designed molecular receptors would be necessary for their detection.

In the second case of human olfactory system, as discussed earlier in Section 1.1.3.1, the number of targets that can be detected are huge and the detection depends on non-specific

interaction between gaseous analyte and olfactory proteins. But to enable this level of non-specific but selective detection, the number of sufficiently selective detectors of the human nose is huge. This challenge calls for a greater variety of molecules that are capable of forming more efficient, more diverse sensor arrays.

1.3.2 Aptamers

Aptamers are oligonucleotide or peptide molecules that bind to specific target molecules. The name "aptamer" was derived from Latin word "aptus" (to fit) and the Greek word "meros" (part), and was first reported in 1990 by Ellington and Szostak of RNA molecules that bind to organic dyes.[103] The interaction between aptamers and their targets are due to complementary three-dimensional conformation between aptamer-target pairs, similar to native protein-protein, protein-DNA, or protein-DNA bindings in organisms. While the building blocks of aptamers – nucleic acids and amino acids – are biological components, the monomer sequences are artificially designed and selected. Aptamers are artificial combinatorial peptides or nucleic acids, but their biomolecular interaction behaviors with target molecules are intrinsically biomimetic. The analogous system in natural systems are ligand-receptor systems, found in cellular signaling, drug actions, and antigen-antibody interactions.

Both peptide and nucleic acid aptamers are generated and selected through an evolutionary approach. Combinatorial strategies were used to generate a pool of diverse candidate molecules which make up a peptide or nucleic acid library.[104] For peptide aptamers, selection would require a molecular biology process. The candidates that have higher affinity will be selected through binding experiments, and the selected high affinity peptides are isolated. The peptide candidates are amplified by repeated binding experiments with target and isolation. Peptides are synthesized

through gene translation *in vivo* or *in vitro*, and the translated peptides integrated with scaffold proteins are then tested against the target molecules under well-controlled conditions. In many cases, the selection process would require the use of *in vivo* systems that use phages, yeast, or bacteria as display systems.[105] In comparison, the selection of nucleic acids aptamers is typically carried out through systematic evolution of ligands by exponential enrichment (SELEX).[104] A vast library containing $10^{13} – 10^{18}$ random oligonucleotide sequences is created. In the next step, the target and the library are brought together under favorable binding conditions to allow nucleic acids with highest affinity to the target to bind to the target. This step is usually carried out by attaching the aptamers to a solid-phase support, or allowing the nucleic acids and target to bind freely in solution. Separation is performed afterwards to obtain the highest-affinity nucleic acids, which are amplified by PCR (for DNA aptamers) or reverse-transcription PCR (RT-PCR for RNA aptamers) to create a new nucleic acid library enriched with higher-affinity aptamer candidates. The entire selection process is then repeated 8 – 15 times to yield several individual sequences that become the choice aptamers for the target. Clearly, nucleic acid aptamers have the advantage of not needing a living system for the synthesis and selection process, fast, and less costly, and therefore are the majority of aptamers studied.[104]

1.3.3 Nucleic acid aptamer sensors

Aptamers have high affinity to their targets. The following equations are typically used to describe biomolecular binding equilibria. For an associative process involving an analyte (A) and the receptor molecule (R), the binding event to form an analyte-receptor complex (C) is simply

$$A + R \leftrightarrow C \tag{1.5}$$

And the association and dissociation constants representing the forward and reverse reactions are respectively

$$K_a = \frac{[\mathrm{C}]}{[\mathrm{A}][\mathrm{R}]} \tag{1.6}$$

$$K_d = \frac{[\mathrm{A}][\mathrm{R}]}{[\mathrm{C}]} \tag{1.7}$$

It is common practice to characterize the strength of a binding reaction in terms of the solution-phase dissociation constant, K_d. For aptamer-target binding, the K_d range is typically in the range of a few nM to tens of μM.[106] This strength is comparable to target binding of cellular signaling proteins and sequence-specific recognition of DNA by transcription factors, both of which are conformation-dependent non-covalent molecular interactions.[107] Table 1.3 lists several examples of targets, aptamers, and K_d values, highlighting three-dimensional conformations of aptamers obtained through experiments or simulations.

Table 1.3 Examples of small molecule targets, their respective aptamers, aptamer structure and sequences, as well as K_d values[108]

	adenosine	estradiol	riboflavin	cholic acid
target structure	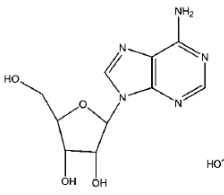	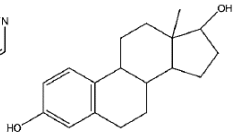	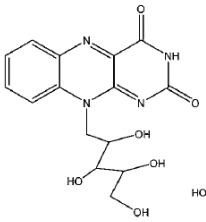	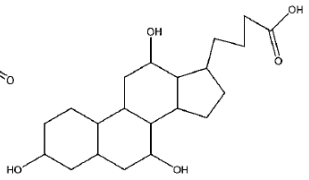
aptamer				
aptamer sequence (5' to 3')	ACCTGGGGGA GTATTGCGGA GGAAGGT	GCTTCCAGCT AATTGAATTA CACGCAGAGG GTAGCGGCTC TGCGCATTCA ATTGCTGCGC GCTGAAGCGC GGAAGC	TTTTTTTTTT GGAACGACGG TGGTGGAGGA GATCGTTCC	GCAGGGTCAA TGGAATTAAT GATCAATTGA CAGACGCAAG TCTCCTGC
K_d	1-10 μM	130 nM	10-100 μM	5 μM

In solution-phase binding studies, aptamers are highlight specific. For example, the anti-theophylline RNA aptamer displayed high-resolution molecular discrimination with K_d of 0.1 μM, which is 10,000-fold greater than its affinity to caffeine that differs from theophylline only by a methyl group at nitrogen atom N-7.[109] Enantioselective L-arginine aptamer selects for its target with 12,000-fold higher affinity than for D-arginine.[110] The targets for aptamers have expanded beyond molecules of biological interest, for example aptamers that bind to trinitrotoluene (TNT),[111] organophosphorous pesticides,[112] and ethanolamine.[113]

Sensors have been developed to successfully exploit this selectivity. For example, an electrochemical biosensor for detection of theophylline was developed, that shows no interference from caffeine and theobromine.[114] On the other hand, cross-reactivity does appear to challenge some aptamer-based sensors, as demonstrated by the extensive cross-selectivity among the 4 small-molecule targets and 4 aptamers studied in the gold nanoparticle plasmonic sensor arrays developed by Chávez et al.[108] Therefore, nucleic acid aptamer sensors can either be designed to give highly specific response to target molecules, or can be integrated into selective, diverse sensor arrays, both of which could be revolutionary advancement in chemical sensing. Over the years, many different transducing platforms have been explored for aptamer-based sensors, including electrochemical sensors, field-effect transistors, piezoelectric crystals, cantilevers, surface plasmon resonance (SPR), fluorescence, and colorimetric systems.[115, 116] Sensors that employ nucleic acid aptamers would be very promising new technologies for next generation chemical detection of small molecules.

1.4 Objectives and scope of dissertation

As demonstrated in Section 1.1, small, highly selective chemical sensors are important technologies in development. Its success relies on both fabrication technology and development more capable materials. In the discussion of device fabrication in Section 1.2, methods derived from semiconductor industries are good foundation, while new technologies for fabrication of nanogaps would be a further step towards nanoscale sensor devices. With respect to the materials, Section 1.3 demonstrated that molecules of biological origins but artificially designed to be more specific to analyte targets is a biomimetic approach that provides more customizable, adaptable,

and efficient sensors. In this dissertation, the synergistic combination of next generation devices and materials is explored.

Small organic molecules were chosen as the model analytes in this study. Chapter 2 describes the experimental methods employed for this systematic study. Single-strand DNA aptamers were chosen as the model sensing material due to their higher stability and lower cost. Chapter 3 describes the fundamental properties of DNA as a sorptive material for vapor phase organic molecules. In Chapter 4, the integration of DNA with gold nanoparticle chemiresistors was investigated. Chapter 5 describes the fabrication of nanoscale gold nanoparticle chemiresistors. Chapter 6 illustrates the operation of nanoscale chemiresistor devices in aqueous environment. Overall, the objective of this dissertation is to provide insights into next generation small-molecule chemical sensors, as well as reveal technical issues faced. The study seeks to pave the way for smaller, more selective electronic sensors that will eventually form the building blocks of information-driven, information-rich sensor networks.

1.5 References

1. Göpel, W.; Jones, T. A.; Kleitz, M.; Lundström, I.; Seiyama, T. *Sensors, Chemical and Biochemical Sensors*. Wiley: **2008**.

2. *Expanding the Vision of Sensor Materials*. National Academies Press: **1995**.

3. Schaller, E.; Bosset, J. O.; Escher, F. 'Electronic Noses' and Their Application to Food. *LWT - Food Science and Technology* **1998**, 31, 305-316.

4. Ibañez, F. J.; Zamborini, F. P. Chemiresistive Sensing with Chemically Modified Metal and Alloy Nanoparticles. *Small* **2012**, 8, 174-202.

5. Carbon Monoxide Questions and Answers https://www.cpsc.gov/en/Safety-Education/Safety-Education-Centers/Carbon-Monoxide-Information-Center/Carbon-Monoxide-Questions-and-Answers-/ (accessed March 15, 2016).

6. Sekhar, P. K.; Brosha, E. L.; Mukundan, R.; Garzon, F. H. Chemical Sensors for Environmental Monitoring and Homeland Security. *The Electrochemical Society Interface* **2010**, 19, 35-40.

7. Röck, F.; Barsan, N.; Weimar, U. Electronic Nose: Current Status and Future Trends. *Chemical Reviews* **2008**, 108, 705-725.

8. Vessman, J.; Stefan, R. I.; Staden, J. F. V.; Danzer, K.; Lindner, W.; Burns, D. T.; Fajgelj, A.; Müller, H. Selectivity in Analytical Chemistry: Recommendations for its Use. IUPAC, Ed. **2001**.

9. Kuiawa, D. Safety in Confined Spaces: Some Things You Need to Know. *EHS Today* 2012, pp 51-52.

10. Austin, C. C.; Roberge, B.; Goyer, N. Cross-sensitivities of electrochemical detectors used to monitor worker exposures to airborne contaminants: False positive responses in the absence of target analytes. *Journal of Environmental Monitoring* **2006**, 8, 161-166.

11. Wang, C.; Yin, L.; Zhang, L.; Xiang, D.; Gao, R. Metal Oxide Gas Sensors: Sensitivity and Influencing Factors. *Sensors (Basel, Switzerland)* **2010**, 10, 2088-2106.

12. Janata, J.; Josowicz, M. Conducting polymers in electronic chemical sensors. *Nat Mater* **2003**, 2, 19-24.

13. Dua, V.; Surwade, S. P.; Ammu, S.; Agnihotra, S. R.; Jain, S.; Roberts, K. E.; Park, S.; Ruoff, R. S.; Manohar, S. K. All-Organic Vapor Sensor Using Inkjet-Printed Reduced Graphene Oxide. *Angewandte Chemie International Edition* **2010**, 49, 2154-2157.

14. Kress-Rogers, E. *Handbook of Biosensors and Electronic Noses: Medicine, Food, and the Environment*. Taylor & Francis: **1996**.

15. Newman, A. R. Electronic Noses. *Analytical Chemistry* **1991**, 63, 585A-588A.

16. Gilad, Y.; Lancet, D. Population Differences in the Human Functional Olfactory Repertoire. *Molecular Biology and Evolution* **2003**, 20, 307-314.

17. Kauer, J. S. Contributions of topography and parallel processing to odor coding in the vertebrate olfactory pathway. *Trends in Neurosciences* **1991**, 14, 79-85.

18. Penza, M.; Cassano, G. Chemometric characterization of Italian wines by thin-film multisensors array and artificial neural networks. *Food Chemistry* **2004**, 86, 283-296.

19. Barkó, G.; Hlavay, J. Application of an artificial neural network (ANN) and piezoelectric chemical sensor array for identification of volatile organic compounds1. *Talanta* **1997**, 44, 2237-2245.

20. Silva, S. F.; Anjos, C. A. R.; Cavalcanti, R. N.; Celeghini, R. M. d. S. Evaluation of extra virgin olive oil stability by artificial neural network. *Food Chemistry* **2015**, 179, 35-43.

21. Sutter, J. M.; Jurs, P. C. Neural Network Classification and Quantification of Organic Vapors Based on Fluorescence Data from a Fiber-Optic Sensor Array. *Analytical Chemistry* **1997**, 69, 856-862.

22. Berne, R. M.; Levy, M. N. *Physiology*. C.V. Mosby Company: **1988**.

23. Young, J. M.; Trask, B. J. The sense of smell: genomics of vertebrate odorant receptors. *Human Molecular Genetics* **2002**, 11, 1153-1160.

24. Berna, A. Metal Oxide Sensors for Electronic Noses and Their Application to Food Analysis. *Sensors (Basel, Switzerland)* **2010**, 10, 3882-3910.

25. García-Berríos, E.; Gao, T.; Theriot, J. C.; Woodka, M. D.; Brunschwig, B. S.; Lewis, N. S. Response and Discrimination Performance of Arrays of Organothiol-Capped Au Nanoparticle Chemiresistive Vapor Sensors. *The Journal of Physical Chemistry C* **2011**, 115, 6208-6217.

26. Gardner, J. W.; Bartlett, P. N. *Electronic Noses: Principles and Applications*. Oxford University Press: **1999**.

27. Stitzel, S. E.; Aernecke, M. J.; Walt, D. R. Artificial Noses. *Annual Review of Biomedical Engineering* **2011**, 13, 1-25.

28. Ramgir, N. S. Electronic Nose Based on Nanomaterials: Issues, Challenges, and Prospects. *ISRN Nanomaterials* **2013**, 2013, 21.

29. Berna, A. Z.; Anderson, A. R.; Trowell, S. C. Bio-Benchmarking of Electronic Nose Sensors. *PLoS ONE* **2009**, 4, e6406.

30. Laing, D. G.; Legha, P. K.; Jinks, A. L.; Hutchinson, I. Relationship between Molecular Structure, Concentration and Odor Qualities of Oxygenated Aliphatic Molecules. *Chemical Senses* **2003**, 28, 57-69.

31. Leffingwell, J. C. Olfaction - A Review. http://www.leffingwell.com/olfact5.htm (accessed March 18, 2016).

32. Friedman, L.; Miller, J. G. Odor Incongruity and Chirality. *Science* **1971**, 172, 1044-1046.

33. Grate, J. W.; Patrash, S. J.; Abraham, M. H.; Du, C. M. Selective Vapor Sorption by Polymers and Cavitands on Acoustic Wave Sensors: Is This Molecular Recognition? *Analytical Chemistry* **1996**, 68, 913-917.

34. Matsui, J.; Akamatsu, K.; Nishiguchi, S.; Miyoshi, D.; Nawafune, H.; Tamaki, K.; Sugimoto, N. Composite of Au Nanoparticles and Molecularly Imprinted Polymer as a Sensing Material. *Analytical Chemistry* **2004**, 76, 1310-1315.

35. Ellwanger, A.; Berggren, C.; Bayoudh, S.; Crecenzi, C.; Karlsson, L.; Owens, P. K.; Ensing, K.; Cormack, P.; Sherrington, D.; Sellergren, B. Evaluation of methods aimed at complete removal of template from molecularly imprinted polymers. *Analyst* **2001**, 126, 784-792.

36. Jones, R.; Meixner, H. *Sensors, Micro- and Nanosensor Technology: Trends in Sensor Markets*. Wiley: **2008**.

37. Dunfan, Y.; Daoli, G.; Wei, W. In *Application of wireless sensor networks in environmental monitoring*, Power Electronics and Intelligent Transportation System (PEITS), 2009 2nd International Conference on, 19-20 Dec. 2009; **2009**; pp 205-208.

38. Burrell, J.; Brooke, T.; Beckwith, R. Vineyard computing: sensor networks in agricultural production. *IEEE Pervasive Computing* **2004**, 3, 38-45.

39. Mainwaring, A.; Culler, D.; Polastre, J.; Szewczyk, R.; Anderson, J. Wireless sensor networks for habitat monitoring. In *Proceedings of the 1st ACM international workshop on Wireless sensor networks and applications*, ACM: Atlanta, Georgia, USA, **2002**; pp 88-97.

40. Niu, X.; Huang, X.; Zhao, Z.; Zhang, Y.; Huang, C.; Cui, L. In *The Design and Evaluation of a Wireless Sensor Network for Mine Safety Monitoring*, Global Telecommunications Conference, 2007. GLOBECOM '07. IEEE, 26-30 Nov. 2007; **2007**; pp 1291-1295.

41. Warneke, B.; Last, M.; Liebowitz, B.; Pister, K. S. J. Smart Dust: communicating with a cubic-millimeter computer. *Computer* **2001**, 34, 44-51.

42. Warneke, B. A.; Scott, M. D.; Leibowitz, B. S.; Lixia, Z.; Bellew, C. L.; Chediak, J. A.; Kahn, J. M.; Boser, B. E.; Pister, K. S. J. In *An autonomous 16 mm³ solar-powered node for distributed wireless sensor networks*, Sensors, 2002. Proceedings of IEEE, 2002; **2002**; pp 1510-1515 vol.2.

43. Rowinski, D. Smart Dust May Become The Pinnacle Innovation Of The Internet Of Things. http://arc.applause.com/2015/08/19/what-is-smart-dust/ (accessed March 19, 2016).

44. NASA Ames Scientist Develops Cell Phone Chemical Sensor. http://www.nasa.gov/centers/ames/news/features/2009/cell_phone_sensors.html (accessed March 19, 2016).

45. Preechaburana, P.; Gonzalez, M. C.; Suska, A.; Filippini, D. Surface Plasmon Resonance Chemical Sensing on Cell Phones. *Angewandte Chemie International Edition* **2012**, 51, 11585-11588.

46. Dixon-Warren, S. J. Motion Sensing in the iPhone 4: MEMS Accelerometer. http://www.memsjournal.com/2010/12/motion-sensing-in-the-iphone-4-mems-accelerometer.html (accessed March 19, 2016).

47. Steinecker, W. H.; Rowe, M. P.; Zellers, E. T. Model of Vapor-Induced Resistivity Changes in Gold−Thiolate Monolayer-Protected Nanoparticle Sensor Films. *Analytical Chemistry* **2007**, 79, 4977-4986.

48. Guo, J. L.; Pang, P. F.; Cai, Q. Y. Effect of trace residual ionic impurities on the response of chemiresistor sensors with dithiol-linked monolayer-protected gold (nano)clusters as sensing interfaces. *Sensor Actuat B-Chem* **2007**, 120, 521-528.

49. Li, T.; Hu, W.; Zhu, D. Nanogap Electrodes. *Advanced Materials* **2010**, 22, 286-300.

50. Sun, L.; Diaz-Fernandez, Y. A.; Gschneidtner, T. A.; Westerlund, F.; Lara-Avila, S.; Moth-Poulsen, K. Single-molecule electronics: from chemical design to functional devices. *Chemical Society Reviews* **2014**, 43, 7378-7411.

51. Martinez-Blanco, J.; Nacci, C.; Erwin, S. C.; Kanisawa, K.; Locane, E.; Thomas, M.; von Oppen, F.; Brouwer, P. W.; Folsch, S. Gating a single-molecule transistor with individual atoms. *Nat Phys* **2015**, advance online publication.

52. Aviram, A.; Ratner, M. A. Molecular rectifiers. *Chemical Physics Letters* **1974**, 29, 277-283.

53. Simmons, J. G. Generalized formula for the electric tunnel effect between similar electrodes separated by a thin insulating film. *Journal of applied physics* **1963**, 34, 1793-1803.

54. Menumerov, E.; Marks, B. A.; Dikin, D. A.; Lee, F. X.; Winslow, R. D.; Guru, S.; Sil, D.; Borguet, E.; Hutapea, P.; Hughes, R. A.; Neretina, S. Sensing Hydrogen Gas from Atmospheric Pressure to a Hundred Parts per Million with Nanogaps Fabricated Using a Single-Step Bending Deformation. *ACS Sensors* **2016**, 1, 73-80.

55. Hübert, T.; Boon-Brett, L.; Black, G.; Banach, U. Hydrogen sensors – A review. *Sensors and Actuators B: Chemical* **2011**, 157, 329-352.

56. Gupta, R.; Appelbaum, I.; Willis, B. G. Reversible Molecular Adsorption and Detection Using Inelastic Electron Tunneling Spectroscopy in Monolithic Nanoscopic Tunnel Junctions. *The Journal of Physical Chemistry C* **2009**, 113, 3874-3880.

57. Hipps, K. W.; Mazur, U. Inelastic electron tunneling: an alternative molecular spectroscopy. *The Journal of Physical Chemistry* **1993**, 97, 7803-7814.

58. Chen, X.; Guo, Z.; Yang, G.-M.; Li, J.; Li, M.-Q.; Liu, J.-H.; Huang, X.-J. Electrical nanogap devices for biosensing. *Materials Today* **2010**, 13, 28-41.

59. Willis, B. G.; Gupta, R. Method of fabricating monolithic nanoscale probes. Google Patents: **2011**.

60. Gupta, R.; Willis, B. G. Nanometer spaced electrodes using selective area atomic layer deposition. *Applied Physics Letters* **2007**, 90, 253102.

61. Perrin, M. L.; Verzijl, C. J. O.; Martin, C. A.; Shaikh, A. J.; Eelkema, R.; van EschJan, H.; van Ruitenbeek, J. M.; Thijssen, J. M.; van der Zant, H. S. J.; Dulic, D. Large tunable image-charge effects in single-molecule junctions. *Nat Nano* **2013**, 8, 282-287.

62. Park, H.; Lim, A. K. L.; Alivisatos, A. P.; Park, J.; McEuen, P. L. Fabrication of metallic electrodes with nanometer separation by electromigration. *Applied Physics Letters* **1999**, 75, 301-303.

63. Jiang, X. Fabrication of Nanogap Electrodes by Selective-area Copper Atomic Layer Deposition. University of Connecticut, 2014.

64. Ancona, M. G.; Snow, A. W.; Foos, E. E.; Kruppa, W.; Bass, R. Scaling Properties of Gold Nanocluster Chemiresistor Sensors. *IEEE Sensors Journal* **2006**, 6, 1403-1414.

65. Terrill, R. H.; Postlethwaite, T. A.; Chen, C.-h.; Poon, C.-D.; Terzis, A.; Chen, A.; Hutchison, J. E.; Clark, M. R.; Wignall, G. Monolayers in Three Dimensions: NMR, SAXS, Thermal, and Electron Hopping Studies of Alkanethiol Stabilized Gold Clusters. *Journal of the American Chemical Society* **1995**, 117, 12537-12548.

66. Ibañez, F. J.; Zamborini, F. P. Chemiresistive Sensing of Volatile Organic Compounds with Films of Surfactant-Stabilized Gold and Gold−Silver Alloy Nanoparticles. *ACS Nano* **2008**, 2, 1543-1552.

67. Joseph, Y.; Guse, B.; Vossmeyer, T.; Yasuda, A. Gold Nanoparticle/Organic Networks as Chemiresistor Coatings: The Effect of Film Morphology on Vapor Sensitivity. *The Journal of Physical Chemistry C* **2008**, 112, 12507-12514.

68. Evans, S. D.; Johnson, S. R.; Cheng, Y. L.; Shen, T. Vapour sensing using hybrid organic-inorganic nanostructured materials. *Journal of Materials Chemistry* **2000**, 10, 183-188.

69. Snow, A. W.; Ancona, M. G.; Park, D. Nanodimensionally Driven Analyte Response Reversal in Gold Nanocluster Chemiresistor Sensing. *Langmuir* **2012**, 28, 15438-15443.

70. Joseph, Y.; Besnard, I.; Rosenberger, M.; Guse, B.; Nothofer, H.-G.; Wessels, J. M.; Wild, U.; Knop-Gericke, A.; Su, D.; Schlögl, R.; Yasuda, A.; Vossmeyer, T. Self-Assembled Gold Nanoparticle/Alkanedithiol Films: Preparation, Electron Microscopy, XPS-Analysis, Charge Transport, and Vapor-Sensing Properties†. *The Journal of Physical Chemistry B* **2003**, 107, 7406-7413.

71. Daniel, M.-C.; Astruc, D. Gold Nanoparticles: Assembly, Supramolecular Chemistry, Quantum-Size-Related Properties, and Applications toward Biology, Catalysis, and Nanotechnology. *Chemical Reviews* **2004**, 104, 293-346.

72. Wohltjen, H.; Snow, A. W. Colloidal Metal−Insulator−Metal Ensemble Chemiresistor Sensor. *Analytical Chemistry* **1998**, 70, 2856-2859.

73. Krasteva, N.; Besnard, I.; Guse, B.; Bauer, R. E.; Müllen, K.; Yasuda, A.; Vossmeyer, T. Self-Assembled Gold Nanoparticle/Dendrimer Composite Films for Vapor Sensing Applications. *Nano Letters* **2002**, 2, 551-555.

74. Kim, Y. J.; Pyo, H.-B.; Park, S.-H. In *Response Properties of the Gold Nanoparticle Sensors toward Benzene and Toluene Vapors*, Sensors, 2006. 5th IEEE Conference on, 22-25 Oct. 2006; **2006**; pp 1078-1080.

75. Peng, G.; Tisch, U.; Adams, O.; Hakim, M.; Shehada, N.; Broza, Y. Y.; Billan, S.; Abdah-Bortnyak, R.; Kuten, A.; Haick, H. Diagnosing lung cancer in exhaled breath using gold nanoparticles. *Nat Nano* **2009**, 4, 669-673.

76. Cooper, J. S.; Raguse, B.; Chow, E.; Hubble, L.; Müller, K.-H.; Wieczorek, L. Gold Nanoparticle Chemiresistor Sensor Array that Differentiates between Hydrocarbon Fuels Dissolved in Artificial Seawater. *Analytical Chemistry* **2010**, 82, 3788-3795.

77. Tokonami, S.; Shiigi, H.; Nagaoka, T. Preparation of Nanogapped Gold Nanoparticle Array for DNA Detection. *Electroanalysis* **2008**, 20, 355-360.

78. Tasaltin, C.; Basarir, F. Preparation of flexible VOC sensor based on carbon nanotubes and gold nanoparticles. *Sensors and Actuators B: Chemical* **2014**, 194, 173-179.

79. Hierlemann, A.; Zellers, E. T.; Ricco, A. J. Use of Linear Solvation Energy Relationships for Modeling Responses from Polymer-Coated Acoustic-Wave Vapor Sensors. *Anal. Chem.* **2001**, 73, 3458-3466.

80. Niti, G.; Ashok, M.; Nathan, L.; Lawrence, S.; Tony, R. R.; Suresh, S.; Lee, W.; Jay, L. S.; Gary, K. F.; Rongchao, J. Robust gold nanoparticles stabilized by trithiol for application in chemiresistive sensors. *Nanotechnology* **2010**, 21, 405501.

81. Covington, E.; Bohrer, F. I.; Xu, C.; Zellers, E. T.; Kurdak, C. Densely integrated array of chemiresistor vapor sensors with electron-beam patterned monolayer-protected gold nanoparticle interface films. *Lab on a Chip* **2010**, 10, 3058-3060.

82. Ibañez, F. J.; Zamborini, F. P. Reactivity of Hydrogen with Solid-State Films of Alkylamine- and Tetraoctylammonium Bromide-Stabilized Pd, PdAg, and PdAu Nanoparticles for Sensing and Catalysis Applications. *Journal of the American Chemical Society* **2007**, 130, 622-633.

83. Wang, L.; Shi, X.; Kariuki, N. N.; Schadt, M.; Wang, G. R.; Rendeng, Q.; Choi, J.; Luo, J.; Lu, S.; Zhong, C.-J. Array of Molecularly Mediated Thin Film Assemblies of Nanoparticles: Correlation of Vapor Sensing with Interparticle Spatial Properties. *Journal of the American Chemical Society* **2007**, 129, 2161-2170.

84. Fowler, J. D.; Allen, M. J.; Tung, V. C.; Yang, Y.; Kaner, R. B.; Weiller, B. H. Practical Chemical Sensors from Chemically Derived Graphene. *ACS Nano* **2009**, 3, 301-306.

85. Nam, K.; Eom, K.; Yang, J.; Park, J.; Lee, G.; Jang, K.; Lee, H.; Lee, S. W.; Yoon, D. S.; Lee, C. Y.; Kwon, T. Aptamer-functionalized nano-pattern based on carbon nanotube for sensitive, selective protein detection. *Journal of Materials Chemistry* **2012**, 22, 23348-23356.

86. Heller, I.; Janssens, A. M.; Männik, J.; Minot, E. D.; Lemay, S. G.; Dekker, C. Identifying the Mechanism of Biosensing with Carbon Nanotube Transistors. *Nano Letters* **2008**, 8, 591-595.

87. So, H.-M.; Won, K.; Kim, Y. H.; Kim, B.-K.; Ryu, B. H.; Na, P. S.; Kim, H.; Lee, J.-O. Single-Walled Carbon Nanotube Biosensors Using Aptamers as Molecular Recognition Elements. *Journal of the American Chemical Society* **2005**, 127, 11906-11907.

88. Lu, Y.; Goldsmith, B. R.; Kybert, N. J.; Johnson, A. T. C. DNA-decorated graphene chemical sensors. *Applied Physics Letters* **2010**, 97, 083107.

89. McDonagh, C.; Burke, C. S.; MacCraith, B. D. Optical Chemical Sensors. *Chemical Reviews* **2008**, 108, 400-422.

90. Lin, T.-Y.; Sree, U.; Tseng, S.-H.; Chiu, K. H.; Wu, C.-H.; Lo, J.-G. Volatile organic compound concentrations in ambient air of Kaohsiung petroleum refinery in Taiwan. *Atmospheric Environment* **2004**, 38, 4111-4122.

91. Chow, E.; Raguse, B.; Müller, K.-H.; Wieczorek, L.; Cooper, J. S.; Hubble, L. J.; Webster, M. S. Transistor-Like Modulation of Gold Nanoparticle Film Conductivity Using Hydrophobic Ions. *Advanced Materials Interfaces* **2014**, 1, 1400062.

92. Cai, Q.-Y.; Zellers, E. T. Dual-Chemiresistor GC Detector Employing Monolayer-Protected Metal Nanocluster Interfaces. *Analytical Chemistry* **2002**, 74, 3533-3539.

93. Kang, S.; Nieuwenhuis, A. F.; Mathwig, K.; Mampallil, D.; Lemay, S. G. Electrochemical Single-Molecule Detection in Aqueous Solution Using Self-Aligned Nanogap Transducers. *ACS Nano* **2013**, 7, 10931-10937.

94. Fan, Z.; Wang, D.; Chang, P.-C.; Tseng, W.-Y.; Lu, J. G. ZnO nanowire field-effect transistor and oxygen sensing property. *Applied Physics Letters* **2004**, 85, 5923-5925.

95. Kauffman, D. R.; Star, A. Carbon Nanotube Gas and Vapor Sensors. *Angewandte Chemie International Edition* **2008**, 47, 6550-6570.

96. He, C.; Zhu, D.; He, Q.; Shi, L.; Fu, Y.; Wen, D.; Cao, H.; Cheng, J. A highly efficient fluorescent sensor of explosive peroxide vapor via ZnO nanorod array catalyzed deboronation of pyrenyl borate. *Chemical Communications* **2012**, 48, 5739-5741.

97. Wohltjen, H. Mechanism of operation and design considerations for surface acoustic wave device vapour sensors. *Sensors and Actuators* **1984**, 5, 307-325.

98. Barnard, S. M.; Walt, D. R. Fiber-optic organic vapor sensor. *Environmental Science & Technology* **1991**, 25, 1301-1304.

99. Tamane, S.; Topal, C. O.; Kalkan, A. K. In *Vapor phase SERS sensor for explosives detection*, Nanotechnology (IEEE-NANO), 2011 11th IEEE Conference on, 15-18 Aug. 2011; **2011**; pp 301-306.

100. Luck, J. R. Carbon monoxide sensor. Google Patents: **1975**.

101. Alkire, R. C.; Kolb, D. M.; Lipkowski, J. *Advances in Electrochemical Science and Engineering*. Wiley: **2006**.

102. Lee, W.-Y.; Lee, K. S.; Kim, T.-H.; Shin, M.-C.; Park, J.-K. Microfabricated Conductometric Urea Biosensor Based on Sol-Gel Immobilized Urease. *Electroanalysis* **2000**, 12, 78-82.

103. Ellington, A. D.; Szostak, J. W. In vitro selection of RNA molecules that bind specific ligands. *Nature* **1990**, 346, 818-822.

104. Mascini, M.; Palchetti, I.; Tombelli, S. Nucleic Acid and Peptide Aptamers: Fundamentals and Bioanalytical Aspects. *Angewandte Chemie International Edition* **2012**, 51, 1316-1332.

105. Grönwall, C.; Ståhl, S. Engineered affinity proteins—Generation and applications. *Journal of Biotechnology* **2009**, 140, 254-269.

106. Klussmann, S. *The Aptamer Handbook: Functional Oligonucleotides and Their Applications*. Wiley: **2006**.

107. Kuriyan, J.; Konforti, B.; Wemmer, D. *The Molecules of Life: Physical and Chemical Principles*. Taylor & Francis Group: **2012**.

108. Chavez, J. L.; Leny, J. K.; Witt, S.; Slusher, G. M.; Hagen, J. A.; Kelley-Loughnane, N. Plasmonic aptamer-gold nanoparticle sensors for small molecule fingerprint identification. *Analyst* **2014**, 139, 6214-6222.

109. Jenison, R.; Gill, S.; Pardi, A.; Polisky, B. High-resolution molecular discrimination by RNA. *Science* **1994**, 263, 1425-1429.

110. Geiger, A.; Burgstaller, P.; von der Eltz, H.; Roeder, A.; Famulok, M. RNA aptamers that bind L-arginine with sub-micromolar dissociation constants and high enantioselectivity. *Nucleic Acids Research* **1996**, 24, 1029-1036.

111. Ehrentreich-Förster, E.; Orgel, D.; Krause-Griep, A.; Cech, B.; Erdmann, V.; Bier, F.; Scheller, F. W.; Rimmele, M. Biosensor-based on-site explosives detection using aptamers as recognition elements. *Anal Bioanal Chem* **2008**, 391, 1793-1800.

112. Zhang, C.; Wang, L.; Tu, Z.; Sun, X.; He, Q.; Lei, Z.; Xu, C.; Liu, Y.; Zhang, X.; Yang, J.; Liu, X.; Xu, Y. Organophosphorus pesticides detection using broad-specific single-stranded DNA based fluorescence polarization aptamer assay. *Biosensors and Bioelectronics* **2014**, 55, 216-219.

113. Mann, D.; Reinemann, C.; Stoltenburg, R.; Strehlitz, B. In vitro selection of DNA aptamers binding ethanolamine. *Biochemical and Biophysical Research Communications* **2005**, 338, 1928-1934.

114. Ferapontova, E. E.; Olsen, E. M.; Gothelf, K. V. An RNA Aptamer-Based Electrochemical Biosensor for Detection of Theophylline in Serum. *Journal of the American Chemical Society* **2008**, 130, 4256-4258.

115. Willner, I.; Zayats, M. Electronic Aptamer-Based Sensors. *Angewandte Chemie International Edition* **2007**, 46, 6408-6418.

116. Song, S.; Wang, L.; Li, J.; Fan, C.; Zhao, J. Aptamer-based biosensors. *TrAC Trends in Analytical Chemistry* **2008**, 27, 108-117.

Chapter 2

EXPERIMENTAL METHODS

2.1 Materials

2.1.1 Chemicals and reagents

Citrate-stabilized gold nanoparticles (10 nm diameter, OD1), tris-(2-carboxyethyl) phosphine hydrochloride (TCEP), glacial acetic acid, sodium acetate, sodium chloride (NaCl), 1-octanethiol, and 8-mercapto-1-octanol were purchased from Sigma-Aldrich (St. Louis, MO). Tris base was purchased from Fisher Scientific (Suwanee, GA). All aqueous solutions used with DNA were made with double-distilled water (dd-H_2O).

Gold (III) chlorate hydrate ($HAuCl_4 \cdot 3H_2O$), 1-octanethiol, 3-mercaptopropionic acid, phenylmethanethiol, 4-aminothiophenol, and tetradecylamine, were purchased from Sigma Aldrich (St. Louis, MO). Sylgard® 184 silicon elastomer kit (polydimethylsiloxane, PDMS) was purchased from Dow Corning (Midland, MI). Polyisobutylene (PIB, M_n = 200,000) and polyethylene glycol (PEG, M_n = 100,000), used as reference materials, were purchased from Sigma-Aldrich (St. Louis, MO).

Vapor sources of VOCs were made with analytical grade solvents purchased from Sigma-Aldrich (St. Louis, MO). Solvents used for vapor generation were toluene, acetonitrile, n-hexane,

n-heptane, chloroform, ethanol, methanol, cyclohexane, 2-propanol, dichloromethane, diethyl ether, tetrahydrofuran, cyclohexanone, triethylamine, anisole, 1-propanol, 1-butanol, 1-pentanol, butyraldehyde, and styrene.

2.1.2 Oligonucleotides

Single-stranded oligonucleotide sequences were purchased from Integrated DNA Technologies Inc. (Coralville, IA). Non-functionalized DNA sequences for vapor sorption studies are shown in Table 2.1, while DNA functionalized with fluorescent tags or thiols are shown in Table 2.2. A, T, C, and G stand for deoxyadenosine monophosphate (dAMP), deoxythymidine monophosphate (dTMP), and deoxycytidine monophosphate (dCMP), and deoxyguanosine monophosphate (dGMP).

Table 2.1 Non-thiolated DNA sequences for QCM measurements

Name	Sequence (5' to 3')
$(dA)_{25}$	AAA AAA AAA AAA AAA AAA AAA AAA A
$(dT)_{25}$	TTT TTT TTT TTT TTT TTT TTT TTT T
$(dC)_{25}$	CCC CCC CCC CCC CCC CCC CCC CCC C
$(dA)_{10}$	AAA AAA AAA A
$(dA)_{50}$	AAA AAA AAA AAA AAA AAA AAA AAA AAA AAA AAA AAA AAA AAA AAA AAA AA
27A	ACC TGG GGG AGT ATT GCG GAG GAA GGT
27L	AAG GAG AGG GAT GAT GGT TGT GCG CGC
24A	AAA AGG GGA AAA AAA ACC CCT TTT
24L	GAA TTA ACA AAC CAG ATA ACG ATG

Table 2.2 Thiolated DNA Oligomers for gold nanoparticle functionalization and fluorescently tagged sequence (S1) for coverage quantification

Name	Sequence (5' to 3')
S1	/Cy-5[a]/AAA AAA AAA GAG GAG GAA AAG GAG T
S2	/HS-C_6H_{12}[b]/TTT TTA CTC CTT TTC CTC CTC TTT T
$(dA)_{25}$	/HS-C_6H_{12}[b]/AAA AAA AAA AAA AAA AAA AAA AAA A
$(dT)_{25}$	/HS-C_6H_{12}[b]/TTT TTT TTT TTT TTT TTT TTT TTT T
$(dC)_{25}$	/HS-C_6H_{12}[b]/CCC CCC CCC CCC CCC CCC CCC CCC C
$(dA)_{10}$	/HS-C_6H_{12}[b]/AAA AAA AAA A
$(dA)_{50}$	/HS-C_6H_{12}[b]/AAA AAA AAA AAA AAA AAA AAA AAA AAA AAA AAA AAA AAA AAA AAA AAA AAA AA
24A	/HS-C_6H_{12}[b]/AAA AGG GGA AAA AAA ACC CCT TTT
24L	/HS-C_6H_{12}[b]/GAA TTA ACA AAC CAG ATA ACG ATG
27A	/HS-C_6H_{12}[b]/ACC TGG GGG AGT ATT GCG GAG GAA GGT
27L	/HS-C_6H_{12}[b]/AAG GAG AGG GAT GAT GGT TGT GCG CGC

[a] Cyanine fluorescence group

[b] Thiol functionalization group

2.2 Quartz crystal microbalance experiments

2.2.1 Principles

Quartz crystals exhibit piezoelectric effect. Applying an AC field to a quartz crystal carefully cut in the suitable crystal orientation induces highly stable resonance oscillations in the thickness shear mode, which can be maintained in the 1 – 30 MHz range depending on crystal configuration.[1] The Sauerbrey's equation describes the change in oscillating frequency with respect to the mass deposited on the surface of the crystal,[2]

$$\Delta f = \frac{-2\Delta m f_0^2}{\sqrt{A(\rho_q \mu_q)}} \tag{2.1}$$

where Δf is the chance in frequency (Hz), Δm is the mass change (g), f_0 is the resonance frequency (Hz), A is the piezoelectrically active crystal area (area between electrodes, cm^2), ρ_q is the density of the quartz, and μ_q is the shear modulus of the quartz. The oscillation of quartz crystals is in the thickness shear mode (TSM). Figure 2.1 illustrates the cross-sectional geometry of a quartz crystal. A standing wave is formed in the crystal from two transversal waves travelling in opposite directions, spanning half a wavelength across the thickness of the crystal. The acoustic wavelength is twice the crystal plate thickness. The 5 MHz AT-cut crystals used in this study have a thickness d_q = 333 μm, and the acoustic wavelength is 666 μm. The displacement is along the lateral direction to the surface, with maximum displacement at the center of the crystal and zero displacement at the edge of the electrode region.[3] Therefore, the crystal is most sensitive to masses deposited in the center of the crystal.[1]

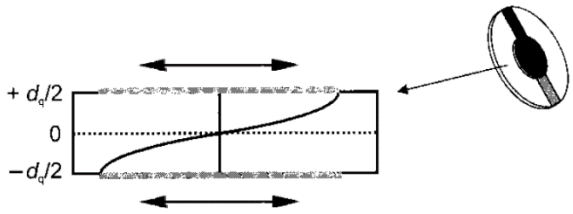

Figure 2.1 Cross-section of a quartz crystal and the thickness shear mode (TSM) oscillation in quartz crystals[3]

Because of the linear relationship between frequency change and mass change, quartz crystal osciallators can be used as a microbalance for mass measurement with nanogram sensitivity,

therefore this equipment is termed quartz crystal microbalance (QCM). As early as 1964, polymer coatings applied to quartz crystals were used for detecting organic vapor absorption.[4] In this application, the absorption of vapor into polymer films were translated in changes in quartz crystal oscillation frequency. For accurate gravimetric measurements, it is necessary that acoustically thin films are deposited on the QCM surface. For a deposited film to be acoustically thin, its thickness needs to be much smaller than the acoustic wavelength, and the modulus of the coating cannot be too low.[5] Increasing the modulus has the effect of decreasing the acoustic thickness.[6] In practice, acoustically thickness is displayed as excessive frequency change and high motional resistance. If the coating film is not acoustically thin, the film material would have viscoelastic effects, causing the film material to not move synchronously with the QCM surface across the entire thickness of the film. In the case of soft, rubbery, or thick films coated on QCM crystals, motional resistance of more than 100 Ω, as well as excessive frequency change, was observed.[7, 8]

When acoustically thin coatings are deposited on a quartz crystal, the frequency change Δf_s is directly proportional to mass change due to coating application on the crystal $\Delta m_{coating}$. When a further mass of vapor Δm_{vapor} is absorbed by the coating material, the frequency change is denoted by Δf_v. Equation 2.2, as follows, describes the simple frequency-mass relationship that is used to study sorption properties of any materials using the QCM.

$$\frac{\Delta f_v}{\Delta f_s} = \frac{\Delta f_{vapor\ sorption}}{\Delta f_{coating\ application}} = \frac{\Delta m_{vapor}}{\Delta m_{coating}} \tag{2.2}$$

2.2.2 Instrumentation

Inficon Maxtek Research QCM (East Syracuse, NY) and Stanford Research Systems QCM-100 (Sunnyvale, CA) were used as two independent data acquisition systems, serving as replicates. AT-cut quartz crystals (5 MHz, 1-inch diameter) with gold electrodes were obtained from Stanford Research Systems (Sunnyvale, CA) and used on both systems. The selection of AT-cut crystals was based on their relative insensitivity to temperature changes at room temperature ranges.[9] The circular active regions of the crystal electrodes were a standard 6.35 mm in diameter. Oscillating frequency and motional resistance of the crystals were recorded concurrently using the company supplied software packages. These two streams of data were also used to verify the acoustic thickness of coatings on the QCM crystals. The Maxtek RQCM collects data at a sampling rate of 20 Hz, while the QCM-100 collects data at a sampling rate of 1 Hz. However, both systems were verified to give identical steady state responses for the same vapor samples.

2.3 Synthesis of gold nanoparticles

2.3.1 DNA-functionalized gold nanoparticles

A number of methods for attaching organic species to gold nanoparticles have been found, including the use of citrate, phosphine, amine, carboxylate, and thiol groups.[10] Of all these methods, thiol-gold chemistry has long been established as the standard method for most gold nanoparticle applications primarily due to the stability of the products. For vapor sensors in particular, the majority of organic layer attachment has been based on thiol-gold chemistry.[11] When the ligand in question is DNA, thiol-based attachment is even more attractive. Compared

with random adsorption by the nucleobases, this end-on covalent attachment method is more stable. Practically, thiol-linked DNA would not fall off during the centrifugation process. This technique also allows for hybridization with complementary DNA segments[12] and aptamer-based solution-phase specific ligand-receptor interaction.[13, 14] Therefore, this behavior is very useful in fluorescence-based characterization of DNA surface coverage.[15] Nevertheless, although DNA-functionalized gold nanoparticles through thiol attachment can be very effective tools for molecular recognition in solution, it remains to be answered whether the conformation of DNA is retained when the nanoparticles are dried. Furthermore, DNA nucleobases are known to nonspecifically adsorb onto gold surface through weak van der Waals nucleobase-gold interactions.[16] This non-specific interaction would possibly alter the DNA conformation from its native state, thereby complicating dry-state DNA-vapor interactions. Thus, the aim of this entire study is realistically not to emphasize vapor phase molecular recognition, but to more of exploring the vapor sensing capability using the chemiresistive transduction mechanism and sequence-dependent vapor distinguishability. It needs to be emphasized that any resulting response differences could be due to conformational differences, chemical differences, or a combination of both. Therefore, it is not the scope of this study to quantify the contribution of chemical and conformational properties towards sensor responses.

Thiol-functionalized DNAs were used to functionalize citrate-stabilized gold nanoparticles following a standard protocol with minor modifications.[17] The DNA in the shipped form is in the form of two identical sequences with a disulfide bridge at the 3'-end. To convert the disulfide bond into two sulfhydryl groups, thus release 2 thiol-functionalized DNA, the disulfide bridge must be first reduced. To activate the thiol-modified DNA sequences, 3 μl of DNA solution in dd-H_2O (1 mM), 1 μl of acetate buffer (500 mM, pH 5.2) and 1.5 μl of TCEP (10 mM) were mixed

with H_2O to obtain a final volume of 10 µl and incubated for 1 hour at room temperature. The mixture was added to 1 ml of as-received citrate-stabilized gold nanoparticle solution and reacted for 16 hours in the dark at room temperature. Subsequently, 10 µl of Tris acetate (500 mM, pH 8.2) buffer was added into the gold nanoparticle solution, followed by the addition of 110 µl NaCl (1.0 M) dropwise with gentle shaking. The whole mixture was incubated in the dark for another 24 hours before use. In control experiments, H_2O was added to 1 ml of gold nanoparticle solution in place of DNA, prior to the 16-hour incubation step.

2.3.2 Small-molecule functionalized gold nanoparticles

10 nm gold nanoparticles were chosen based on previous success with chemiresistors made using this particle size.[18, 19] They were synthesized following a method developed by Chen et al.[20] with modifications. In this process, tetradecylamine acts as solvent, ligand, and Au(III) to Au(0) reducing agent. Tetradecylamine (30 mmol, 5.335 g) and gold (III) chloride trihydrate (0.1 mmol, 39.4 mg) were loaded into a 25 ml three-neck flask equipped with a magnetic stir bar. The mixture was purged with nitrogen for 10 minutes at room temperature, and then heated to 120 ^oC at a heating rate of 15 ^oC/min. Au(III) precursor disperses in tetradecylamine to form a yellow solution at 40 ^oC. Solution color changed from yellow (30-60 ^oC) to clear (60-80 ^oC) and pink (85 ^oC), indicating that the Au (III) was reduced to Au (I) and then Au (0). The formed Au(0) remains dispersed in liquid tetradecylamine. The reaction was allowed to proceed for 30 min at 120 ^oC. The nanoparticle product was separated by centrifugation for 2 minutes (5000 rpm), washed with copious ethanol, and followed by centrifugation again. This purification process was repeated three times and the final products were dispersed in nonpolar solvents such as toluene and hexane, and used for further characterization and modification.

Four types of gold nanoparticles were prepared by ligand exchange with the as-synthesized amine-capped gold nanoparticles. The four ligands are 1-octanethiol, 3-mercaptopropionic acid, 4-aminothiophenol, and 6-mercapto-1-hexanol. As an example, 4-aminothiophenol (3.0 ml) was dissolved in 5.0 ml of ethanol in a 25 ml round-bottom flask equipped with a magnetic stirring bar. After stirring for 10 min, Au nanoparticles (6.0 mg) in 2.0 ml toluene were added drop-wise to the solution within 3 minutes. The reaction solution was degassed with nitrogen for 15 minutes and allowed to stir 3 hours at room temperature. After that, the reaction solution was centrifuged at 5000 rpm for 2 minutes. After removing the supernatant, Au nanoparticles were re-dispersed in 3.0 mL of ethanol followed by centrifugation at 5000 rpm for 2 minutes. These centrifuging and re-dispersing steps remove the unbound ligands from the nanoparticles. The 4-aminothiophenol capped Au nanoparticles were dispersed in ethanol for fabrication of sensor devices. The synthesis of nanoparticles with the other three ligands follows similar procedures.

2.4 Chemiresistor fabrication

Multiple device configurations, sizes, and materials deposition techniques were employed in this dissertation. The choice of methods and devices were based on availability of equipment during the experiments and sensor manufacturing requirements.

2.4.1 Micron-scale electrode fabrication

The choice of 20 μm gap size is consistent with 5 – 20 μm spacing commonly used in nanoparticle chemiresistors (Figure 2.2).[21-24] 4-inch silicon wafer with 300 nm of thermally grown oxide was used as the substrate. Patterns were defined using standard photolithography on silicon dioxide wafers with 500 nm thermally grown silicon oxide, followed by electron-beam evaporation of metal films and lift-off processes. The electrodes deposited were made of 10 nm thick of

titanium and 200 nm thick of gold. The circular electrode has a diameter of 2.7 mm with electrode width of 20 μm and pitch width of also 20 μm. The device chip is 0.4 cm^2 in size with an active electrode area of 5.7 mm^2. The total electrode perimeter is 290 mm.

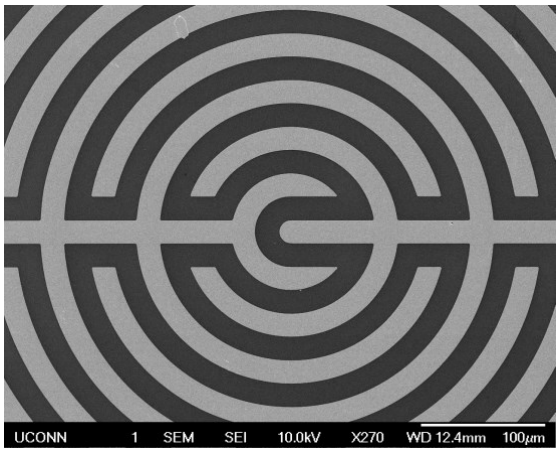

Figure 2.2 Interdigitated circular electrodes with a spacing of 20 μm.

2.4.2 Nanoscale electrode fabrication

The 50 nm nanogap devices were fabricated by a two-step lithography process on silicon wafers with 100 nm thermal oxide. Oxidized silicon wafers with 100 nm thermally grown oxide were acquired from Virginia Semiconductor (Fredericksburg, VA). Electron-beam lithography was used to define patterns of paired parallel lines 150 nm apart with triangular tips emerging from one line towards the other creating electrode gaps of 50 nm. A layer of 40 nm Pd with 10 nm Ti adhesion promoter was deposited by electron beam evaporation and the electrodes were obtained by liftoff. Ten pairs of electrodes were made per 5 × 5 mm^2 chip; each electrode pair had 10, 100, or 1000 tips (Figure 2.3). Contacts to the nanoelectrodes were made by optical lithography and

electron beam deposition / liftoff of 10 nm Ti and 200 nm Au. Each electrode pair has a substrate footprint of 600 nm × 3.4 μm for 10-tip devices, 600 nm × 34 μm for 100-tip devices, and 600 nm × 340 μm for 1000-tip devices. At the tip regions, separation between electrodes is 50 nm, while away from tips electrode separation is 250 nm. The distance between neighboring tips is 340 nm.

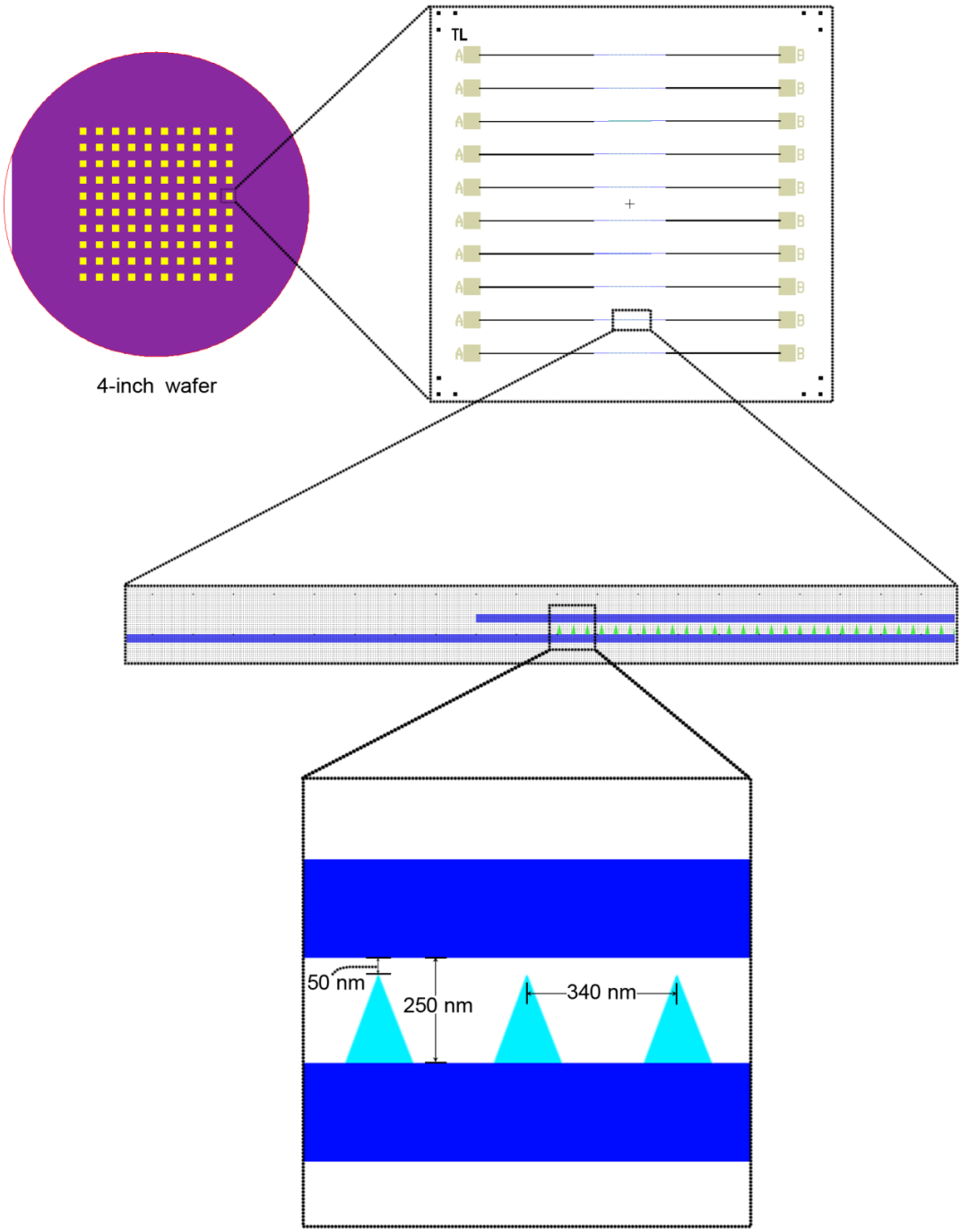

Figure 2.3 Schematic of nanoscale devices. Left: multiple dies on a wafer; right: single chip with 10 pairs of linear electrodes. Middle: close-up view of a single pair of electrodes, showing tips (cyan). The overlapped area of the electrodes is only as long as the tip regions. Bottom: tip region plan view and dimensions.

2.4.3 Drop-casting

Drop-casting is the simplest way of preparing gold nanoparticle films on solid substrates. Solutions of the sensing material is deposited onto the electrodes and evaporated to leave behind the solids (Figure 2.4). Drop-casting produces nanoparticle films with dense regions as a result of the capillary forces associated with the solvent evaporation forces, but the film is usually non-uniform.

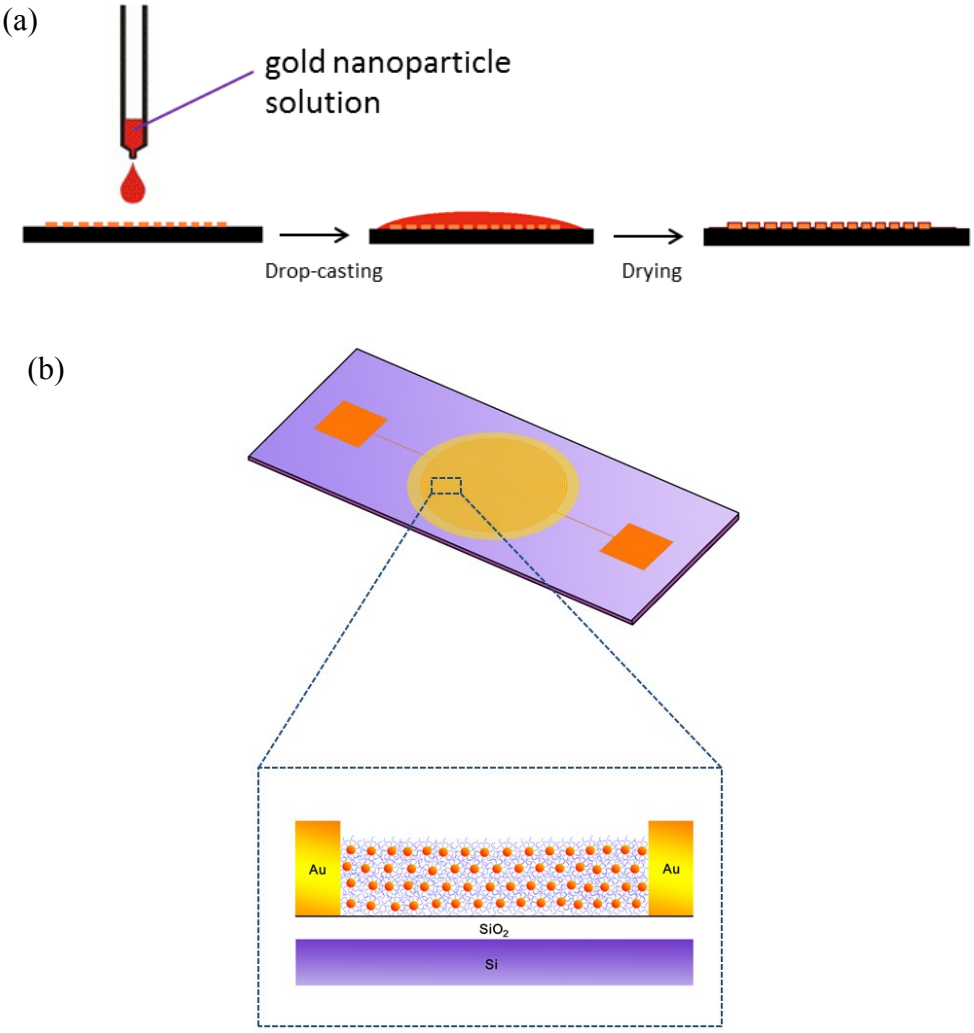

Figure 2.4 Depositing gold nanoparticles by drop casting. (a) Illustration of drop-casting procedure; (b) Structure of drop-cast chemiresistor nanocomposite film. AuNPs bridge the gaps between gold electrodes (not drawn to scale).

2.4.4 Electrospray

Electrospray, also called electrohydrodynamic atomization (EHDA), is a common technique to generate very fine liquid droplets under the influence of electrical forces. The application of electrical potential charges the liquid, causing Coulombic repulsion, and overcoming the intrinsic surface tension of the solvent. Therefore, tiny droplets are produced as a mist, which is attracted to the oppositely charged substrate to be deposited. Electrospray is a versatile technique that work with both water and organic solvent, however a combination of parameters determines the behavior and droplet size of electrospray. These parameters include applied voltage, dielectric constant, conductivity, flowrate, liquid viscosity, nozzle diameter, and jet-substrate distance.[25] The ease of experimentation resulted in a series of empirical scaling laws that help predict the dependence of droplet diameter on these parameters. Aided by these experiential findings, classical electrodynamic theories, and experimental trial and error, a suitable condition for a specific manufacturing process is usually attainable. The electrospray of gold nanoparticles has been reported.[26] For manufacturing processes that aim to produce uniform films, the stable cone-jet mode is the most suitable electrospray condition to be sought.[27]

Electrospray procedures was performed in Materials Science and Engineering Undergraduate Laboratory in Engineering II, Room 101, University of Connecticut. Figure 2.5 shows the setup of electrospray system for depositing gold nanoparticles onto microfabricated sensor electrodes. The electrospray setup was housed in a transparent plastic casing for electrical safety and humidity control. A custom made height-adjustable needle holder was connected to a horizontal stage controlled by a leadscrew to produce back-and-forth movement of the needle. A 27G blunt needle was used to discharge gold nanoparticle solutions from a 30 ml syringe that was placed on a Cole-Parmer 74905-02 syringe pump outside the casing. The connection between the

needle and syringe was through a 50 cm BD Intramedic™ 0.034" ID tubing (Franklin Lakes, NJ) which went through a small opening on the casing. High voltage was provided by a Glassman FR Series high voltage power supply (High Bridge, NJ), with the positive output connected through a metal clip on the electrospray needle, and the negative (ground) output connected to a horizontal plate that holds the sensor substrate. The distance between the electrospray needle and the sensor substrate was 10 cm.

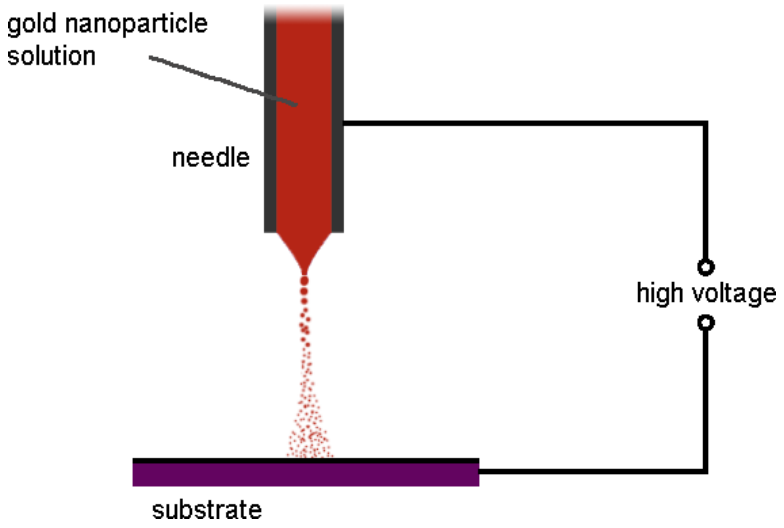

Figure 2.5 Schematics of electrospray setup for gold nanoparticle deposition on sensor electrode.

Electrospray produces fast drying, tiny droplets of liquid that evaporate within 10 seconds of landing on the substrate. The small droplets and fast drying process eliminate the coffee ring effect and produces more uniform gold nanoparticle films on the substrate. In this study, a typical

applied electrical potential of 6.5 kV and flowrate of 0.03 ml/hr, would produce a stable cone-jet, and focus the droplets within a diameter of 2 mm.

2.4.5 Dielectrophoresis

Dielectrophoresis is a method to manipulate solid particles in solution using electric fields. To a polarizable particle, the electric field can induce a dipole within the particle through accumulation of charge on its surface. If the electric field is non-uniform, the Coulomb forces acting on the particle by the electric field will not be equal, and there would be a net force on the particle. The dielectric force is expressed as

$$< \vec{F}_{DEP} >= 2\pi\epsilon_m a^3 \mathrm{Re}[K(\omega)]\nabla|\vec{E}_{rms}|^2 \tag{2.3}$$

where ϵ_m is the permittivity of the medium, a is the radius of the nanoparticle, $\vec{E}_{rms}$ is the electric field strength, and $K(\omega)$ is the frequency dependent Clausius-Mosotti factor, given by

$$K(\omega) = \frac{\epsilon_p - \epsilon_m - \frac{j}{\omega}(\sigma \quad - \sigma_m)}{\epsilon_p + 2\epsilon_m - \frac{j}{\omega}(\sigma_p + 2\sigma_m)} \tag{2.4}$$

where ϵ_p and ϵ_m are permittivities of the particles and medium, and σ_p and $\sigma_m$are conductivities of the particles and medium. From Equation 2.4, it follows that the particle and medium properties and frequency determines the sign of $K(\omega)$. If $K(\omega)$ is positive, then particles move to regions of

highest field strength (positive dielectrophoresis). If $K(\omega)$ is negative, which occurs at very high frequencies above 10 MHz, particles are repelled from these regions (negative dielectrophoresis). Electro-osmotic flow of the solvent also has an effect on the dielectrophoresis behavior of nanoparticles. The applied electric field exerts a force on the interfacial charge between the solution and the electrodes, causing the solution to flow away from the inter-electrode gap. This force opposes the dielectrophoretic force, and is strong in low frequency regimes from 100 Hz to 10, 000 Hz.[28] Therefore, careful selection of frequency is necessary for effective dielectrophoresis.

Agilent 33220A function generator was used to generate high frequency AC fields for dielectrophoretic assembly of nanoparticles. The two terminals of the function generator were connected to set-screw connectors which were fixed upright by insulating lab clamps. Nanoscale electrodes on chips were pasted and wire bonded to the contact pads on TO-3 headers, which were inserted into the set-screw connectors, facing upright. The function generator was turned on first to supply AC voltage with sinusoidal waveform, and a droplet of gold nanoparticles with the respective ligands were placed onto to the connected electrodes. After 30 s of applied voltage, the nanoparticle solution was blown off the sample using a stream of dry nitrogen gas. The AC voltage was turned off after removing the nanoparticle solution. The sensor devices were stored in dry N_2 for at least 4 hours before sensor testing.

2.5 Vapor sensor testing system

2.5.1 Vapor generation

250 ml Pyrex glass filtering flasks (Corning, NY) were used as solvent containers and bubblers. 1/4" OD glass tubes were used as gas inlet to the bubblers. The glass tubes were inserted through No. 4 single-hole stoppers, which were used to seal the mouth of the flasks. Each glass tube was kept at a fixed position so that when the stoppers were pushed tight against the mouth of flask mouth, the end of the glass tube reaches to about 3 mm from the bottom of the flask. The liquid level in the bubblers were periodically monitored and refilled to maintain the liquid level of at least 150 ml, therefore the vertical distance of rising gas bubbles would be at least 4 cm. Multiple cotton balls (> 10) were inserted into the flask to assist the dispersion of gas bubbles and also to provide additional evaporation surfaces above the solvent liquid level. This design is meant to provide additional source of vapors in excess of the vapors collected from the rising gas bubbles if the gas has not been saturated with the organic vapors. A water bubbler with the same configuration as the organic vapor bubblers was assembled.

Ultrahigh purity nitrogen (Air Gas, UHP 300, purity of 99.999%, Radnor, PA) was used as vapor carrier gas. For studies of low vapor concentration in the mixed gas stream (p/p_0 up to 0.1), an Omega 04-15 flowmeter (Stamford, CT) controls the flowrate of nitrogen into bubblers. And flow rate can vary in the range 1.8 cm^3/min to 20.0 cm^3/min. 1/4" polypropylene tubing is used for the majority of the gas line. Near the inlet of the bubbler, a short 5 cm 3/32" ID Tygon E3603 clear rubber tubing (Saint-Gobain North America, Malvern, PA) was used to connect the polypropylene tubing to the glass tubing. The connection of rubber tubing was connected to the polypropylene tubing using a Swagelok 1/4" to 1/4" compression tube fitting to hose connector

(Solon, OH). The outlet of the filtering flask was connected to a short 3 cm 5/32" ID Tygon E3603 rubber tubing, which is connected to a Swagelok 1/8" to 1/4" compression tube fitting to hose connector. For generation of higher vapor partial pressures in the mixed gas stream ($p/p_0 > 0.1$), an Omega N092-04flow meter flowmeter (range: 185 cm^3/min to 2300 cm^3/min) was used. The generation of higher vapor concentrations were primarily for studies of humidity effects on sensors and sensing materials.

The vapor generators were kept in a 30 cm × 30 cm × 20 cm (width × length × height) Styrofoam box with 2.5 cm wall thickness which maintains its temperature. The temperature control is similar to the QCM system (Section 2.2.2), with an external circulating bath that pumps circulating water through the circulating loops through the Styrofoam box. The temperature of the internal temperature of the Styrofoam box was monitored using a glass thermometer with its bulb inserted through the Styrofoam box cover to the same level as the bubblers.

2.5.2 Vapor delivery

Testing vapor concentrations are quantified as a ratio of the vapor partial pressure to its saturation vapor pressure p/p_0 at the experimental temperature. Figure 2.6 shows a schematic diagram of the vapor delivery system. Ultrahigh purity nitrogen (Air Gas, purity of 99.999%) was used as a diluent and carrier gas. Four gas lines were constructed. For vapor generation as described in the previous section (2.5.1), one line of carrier nitrogen gas was bubbled through a testing solvent bubbler and a second was bubbled through water to generate saturated vapors. The main carrier gas line or diluent line was controlled by an Omega 04-39-N flowmeter (range: 300 cm^3/min to 8700 cm^3/min), and a flowrate adjustment line was merged onto the main line before the merging of the gas streams. The flowrate adjustment line was controlled by an 04-15

flowmeter (1.8 cm^3/min to 20.0 cm^3/min). The main carrier gas line, the testing vapor line, and the humidity adjustment line merge through a 4-way joint into a single line, which enters the flow cell. All tubings downstream of the 4-way joint, as well as the connecting tubings from the vapor generator, were 1/8" stainless steel tubings to minimize vapor condensation on the inner tubing walls. A system of ball-valves was inserted along the gas lines to switch gas flows on and off. Four bypass lines were added to the flow system to isolate gas streams, allowing these gas streams to reach steady state without being introduced into the main gas stream. This design helps to improve the efficiency of the testing system while maintaining a constant flow rate through the flow cells. By adjusting the 4 flowmeters, a wide range of testing vapor concentrations from p/p_0 = 0.01 to 1 can be generated.

Vapor generators, flow cells, and exhaust tubing were kept in the fume hood at all times, while upstream flowmeters were kept outside the fume hood. The flowmeters were kept vertical by attachment to a vertical aluminum plate to ensure accuracy in readings.

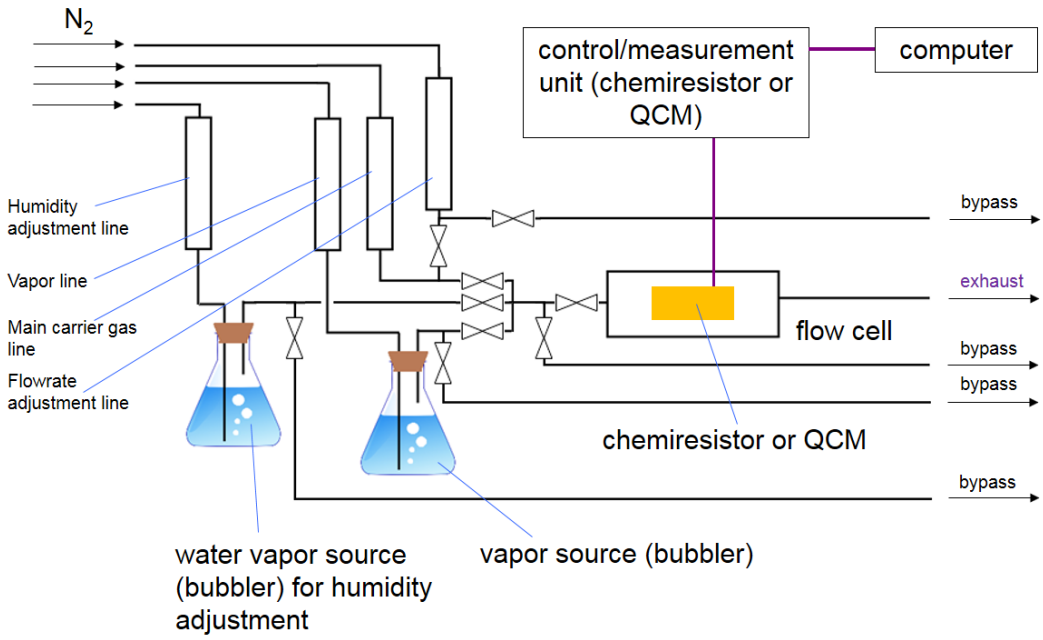

Figure 2.6 Schematics of vapor delivery and testing system, universal for both chemiresistor and QCM testing in the gas phase.

Before and after each experiment, a continuous flow of pure nitrogen was passed through the flow cell for at least 20 min to restore a constant baseline reading for both the QCM and chemiresistors. During each experiment, the total flow rate was kept constant. The flowrate adjustment line was used to compensate for changes in the total flowrate entering the flow cell due to on/off switching of the testing vapor stream into the main gas stream. As the exhaust of the flow cell was open to hood air, it is assumed that the flow cell was maintained at approximate atmospheric pressure. In all vapor sensing experiments, a steady baseline was achieved before adding testing vapors. Between experiments, the sensing chamber was purged with 620 cm^3/s N_2 for at least 20 mins to remove residual analytes.

2.5.2.1 Testing vapors alone

For studies on sensor response to dry organic vapor analytes, only the main carrier gas line, vapor line, and flowrate adjustment lines were used. Total flowrates were kept at 620 cm^3/min.

2.5.2.2 Testing vapors with relative humidity control

For studies of the effect of humidity on sensor response, all four input gas lines were used. Seven relative humidity (RH) levels were investigated to cover the entire range of possible atmospheric humidity conditions: 0 %, 17 %, 34 %, 50 %, 67 %, 84 % and 100%, with a total flow rate of 600 cm^3/min. The effect of RH on sensor response to organic vapors was measured at 0 %, 17 %, 34 %, 50 %, 67 %, 84 %, and 99%. Due to the inclusion of additional gas streams, the total flow rate was 620 cm^3/min. Humidity control is achieved by using a flowrate adjustment gas flow line with same flowrate range as the vapor flow line. At the beginning of experiment with no vapor, flowrate adjustment line is open, and vapor line is closed. The flow rate of the adjustment line is equal to the planned total gas flow rate in the vapor line during the experiments, i.e. N_2 flow rate plus gas-phase vapor flow rate. The vapor flow rate is calculated using the saturation vapor pressure and the flow rate through the bubblers, following the following equations.

$$F_{vapor,out} = F_{carrier,in} \frac{P_{vapor}}{P_{headspace} - P_{vapor}} \tag{2.5}$$

$$F_{out} = F_{carrier,in} \frac{P_{headspace}}{P_{headspace} - P_{vapor}} \tag{2.6}$$

where $F_{vapor,out}$ is the volumetric concentration of vapor from the bubbler, $F_{carrier,in}$ is the carrier gas (N_2) flowrate into the bubbler, P_{vapor} is the saturation vapor pressure, also expressed as p_0, $P_{headspace}$ is the headspace pressure in the bubbler, approximately equal to the atmospheric

pressure in the current setup, and F_{out} is the total output gas flowrate. Using these relations, the vapor flowrate and total gas flowrate from the bubblers can both be calculated. P_{vapor} can be readily obtained from NIST Chemistry Webbook.[29]

The absolute concentrations of selected vapors were also verified by GC/MS. Organic vapor levels are quantified as the ratio of the vapor partial pressure to its saturation vapor pressure (p/p_0) at 22 °C. For measuring the device response to organic vapors, special care was taken to maintain a constant water mole fraction in the gas phase. This was necessary to avoid sensor responses from changes in the humidity of the input flow streams. After each experiment, the sensors were purged by humidified nitrogen of the specified RH for 5 minutes followed by dry nitrogen for 5 minutes.

2.5.3 Flow cells

2.5.3.1 QCM flow cell

QCM crystals with or without coatings were loaded into factory-supplied Teflon flow cells. Each flow cell has two Viton® O-rings (ID: 21 mm, OD: 24.5 mm) that hold the crystal within the flow cell, and forming a sealing between the top surface of the crystal and the flow cell, creating an internal flow volume 0.1 cm^3. The inlets were connected to Cole-Parmer C-Flex® opaque rubber tubing with 1/16" ID and 1/8" OD (Vernon Hills, IL), which further connect to the combined output stream of the vapor delivery system (Section 2.5.2). The outlet of the flow cell was connected to the same kind of opaque rubber tubing that goes to the exhaust. Ring stands and clamps were used to hold the QCM flow cell in position.

Temperature control of the QCM system was achieved through a custom-made temperature controlled foam box. An Anova A-25 refrigerated and heating circulator (Stafford, TX) was used

to provide external water circulation to a temperature control loop. Thick, 1/4" ID, 1/2" OD insulated rubber tubing was used for connection from the water circulator to the temperature control loop. The temperature control loop was made with 1/4" copper tubing, and was inserted into a 15 cm × 15 cm × 15 cm (width × length × height) Styrofoam box with 2.5 cm wall thickness. The total length of the tubing inside the Styrofoam box was approximately 1 m, configured into a coil which surrounds the QCM crystal holders. Water was added into the temperature control box to increase the temperature buffering capability of the box. The water level was approximately 3 cm, with the temperature control loop partially submerged in it. While the QCM crystal holders were inserted into the temperature controlled box, the box was closed, and a glass thermometer was inserted from an opening on the cap to place the thermometer bulb next to the crystal holders.

2.5.3.2 Chemiresistor flow cell

Vapor sensing experiments were performed in a custom-made aluminum chamber that held up to 8 different sensor chips in a linear channel configuration and was sealed with Viton O-rings. The overall size of the flow channel is 1.5 cm, 0.5 cm, and 20.0 cm for width, height, and length, respectively; where the flow direction is along the length. The chamber includes holes for cartridge heaters and thermocouples for measurements above room temperature. Wire bonded chips held on TO-style packages are inserted along the channel direction. Each chip occupies a channel region 2.5 cm in length.

2.5.4 Vapor concentration verification

Vapor concentrations were verified by injecting 20 µl samples of gas upstream of the sensing chamber into a gas chromatograph (HP 6890, Hewlett Packard, Santa Clara, CA) equipped with a mass-selective detector (GC/MS). For measuring diluted gas streams, the flexible rubber

tube was punctured with a typical 22G syringe needle at a location within 10 cm upstream of the flow cell to make a small sampling hole for insertion of the gas sampling syringe. The hole is self-sealing by the rubber tubing. Similarly, reference samples of saturated vapors were obtained by sampling within 2 cm downstream of the gas output using the same tube piercing method. Using a Hamilton 20 µl gas-tight glass syringe (Reno, NV), 20 µl of gas samples were withdrawn from the gas stream, and the syringe was immediately sealed with a nitrile glove. Manual sample injection was performed within 3 minutes of gas sampling into the GC system.

A Restek dimethylsiloxane GC column (Bellefonte, PA) was used for chromatographic separation. Four representative compounds, varying in molecular size and polarity, were chosen to evaluate the efficiency of the vapor delivery system. The vapors with their respective retention times (mins) are water (0.28), ethanol (0.3), toluene (0.91), and cyclohexanone (1.97), The vapor compounds were eluted as single peaks. Integrated peaks of the vapor compounds were ratioed with those of N_2 peaks which serve as an internal standard.

To verify the efficiency of vapor dilution, three samples collected of toluene vapor of three concentrations in the typical range where sensors were tested. The presumed concentrations are $p/p_0 = 0.01$, 0.03, and 0.05 based on read value from the flowmeters. Figure 2.7 plots the GC peak ratio vs. vapor concentration for toluene. The dilution through the vapor delivery line achieves a toluene/N_2 peak area ratios which are highly linear, with regression coefficient $R^2 > 0.995$. The linearity of the concentration control through adjustment of vapor lines is verified.

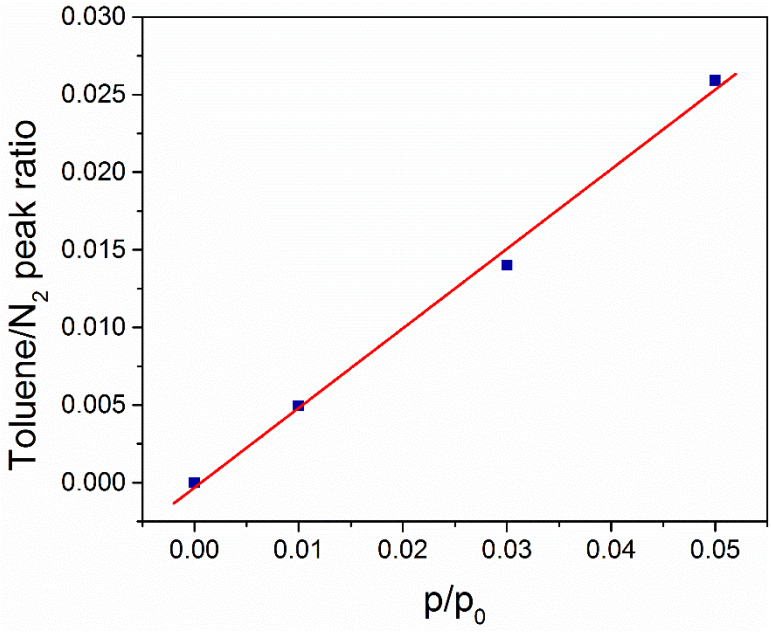

Figure 2.7 Sample linearity plot of GC peak ratio vs. vapor concentration for toluene

Vapor/N_2 ratios of diluted gas streams were referenced with that obtained from gas streams of saturated vapors exiting bubblers. For toluene, vapor/N_2 ratio at presumed $p/p_0 = 0.05$ is 0.0259, while vapor/N_2 ratio at presumed $p/p_0 = 1$ is 0.477. The error in dilution is 8.6 %. Similar comparisons were made for the other 3 vapors, and the results are presented in Table 2.3. Overall, the GC/MS measured vapor concentrations were consistent with the predicted dilution ratios achieved using the vapor delivery system, with an error of less than 10%. This shows that the vapor delivery system is a reliable vapor dilution system, though errors could have been amplified from sorption of vapors in the internal walls of tubings, vapor residuals on the sampling syringes, and loss of vapor molecules to the environment.

Table 2.3 GC vapor/N_2 peak area ratios

Vapor	Saturated vapor ($p/p_0 = 1$)	Diluted vapor ($p/p_0 = 0.05$)	GC-measured dilution factor	Error (%)
Water	0.323	0.0156	0.048	-3.4
Ethanol	0.192	0.0100	0.052	4.2
Toluene	0.477	0.0259	0.054	8.6
Cyclohexanone	0.264	0.0144	0.055	9.1

2.5.5 Sample storage

Both coated QCM samples and chemiresistor sensors were stored in dark containers filled with N_2 to minimize light-induced and oxidative damage when they were not being used.

2.6 Liquid-based sensor testing

Liquid-based analysis has been in many circumstances aided by microfluidics. As exhibited by commercial microanalytical methods such as high-performance liquid chromatography (HPLC) and capillary electrophoresis (CE), microfluidic detection helps to achieve high sensitivity and high resolution analysis using small amounts of sample, and a more compact instrument.[30] Specifically, there is successful combination of microelectronic detection devices with microfluidic flow systems to realize continuous, real-time measurement of analytes.[31] This effective combination is employed in the liquid-based sensor testing to investigate gold nanoparticle chemiresistors working in aqueous environment.

2.6.1 3D printing assisted microfluidic flow cell

Flow cells used in microfluidic studies are conventionally fabricated by soft lithography. A template is first fabricated using photolithography on SU-8 photoresist, and liquid PDMS is poured onto the SU-8 and cured to form the flow cell. This method produces accurate patterns for very small feature sizes, however for feature sizes > 10 μm, soft lithography is unnecessary and a more convenient method using 3D printing has been developed.

The interface of devices with liquid systems involves a PDMS flow channel created using a 3D-printed master. A Form 1+ 3D printer (Formlabs, Somerville, MA) was used which employed a stereolithography process in printing high resolution, defect-free features. The printer features a liquid photopolymer resin that was scanned by focused laser beams which cause local cross-linking into solid form. A model of the flow cell master was created in COMSOL Multiphysics (Burlington, MA), and passed to the 3D printer. Printing proceeds through a layer-by-layer fashion. As soon as the printing was finished, the printed model was taken out from the remaining liquid resin and washed thoroughly with isopropanol. After washing, the flow cell master was blotted to remove residual solvent, and the supporting structure was removed. Finally, the flow cell master was placed in an UV chamber to crosslink any components that were not completely crosslinked by the 3D printer. The design of the 3D-printed flow cell master is presented in Figure 2.8(a), with the printed product in Figure 2.8(b).

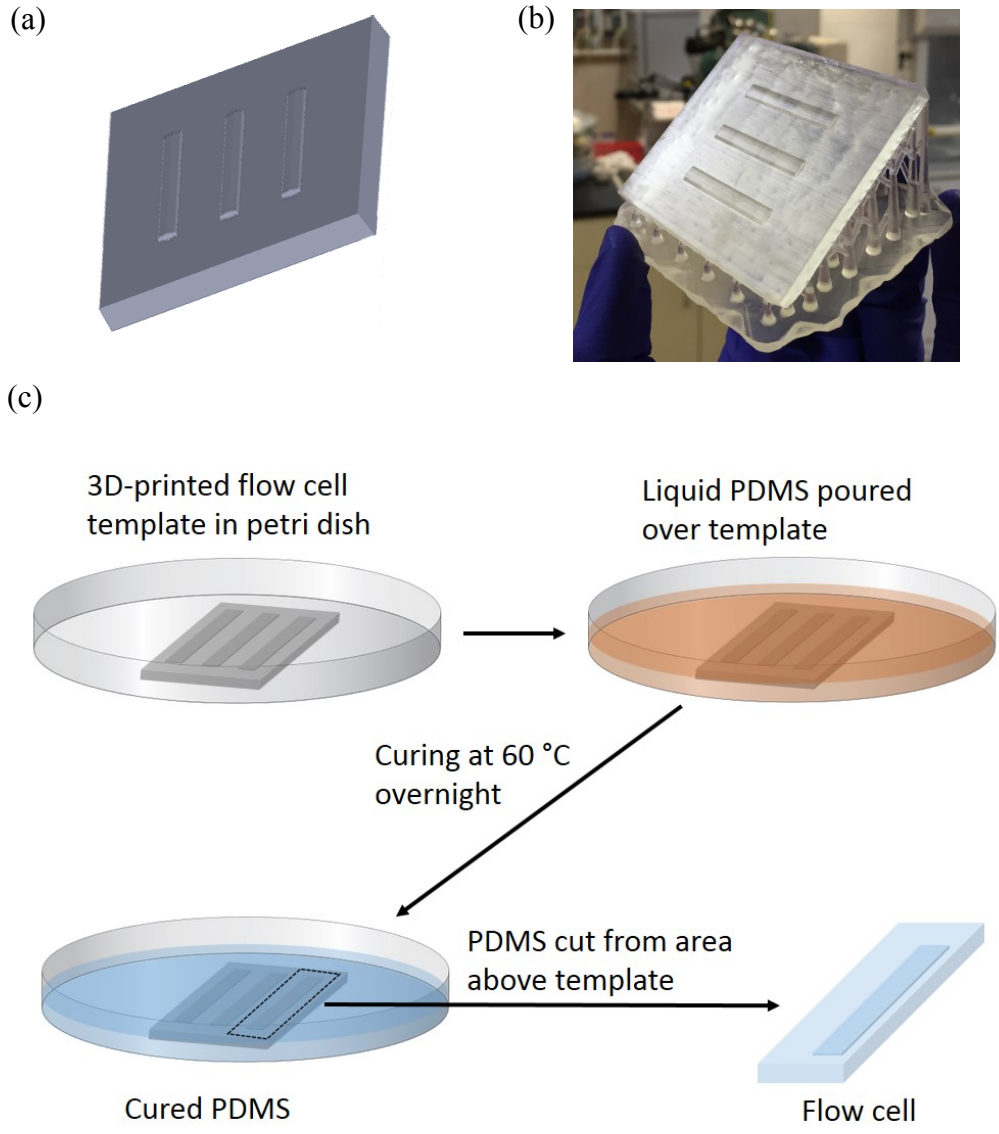

Figure 2.8 (a) Schematic of 3D-printed flow cell master in COMSOL; (b) 3D-printed flow cell master (template) product; (c) PDMS flow cell cast procedures using the 3D-printed template.

The printed flow channel template has a footprint of 3.5 cm × 0.5 cm, and an arched ceiling which prevents collapse of the flow cell. The height of the flow cell is 0.4 mm at the center and

0.1 mm at the two sides. Flow cells were cast from the 3D-printed masters in PDMS using standard soft lithography techniques.[32] First, the 3D-printed flow cell master was placed in a BD Falcon® 10 cm × 10 cm square polystyrene Integrid Petri dish (Corning Life Sciences, Tewksbury, MA), with printed features facing up. 20.0 g of liquid PDMS elastomer base and 2.0 g of curing agent were thoroughly mixed and degassed in a vacuum desiccator under constant pumping for 30 mins. The liquid mixture was slowly poured over the flow cell master attaining a height of approximately 0.5 cm above the 3D-printed piece. The petri-dish is then covered, and the liquid PDMS was cured in a temperature-controlled oven for at least 8 hours at 60 °C. After curing, solid PDMS were cut and peeled away from the master using a scalpel, with the piece centered on the flow cell region. The cut-out single flow cell measures 1.5 cm (W) × 5 cm (L) × 0.5 cm (H).

2.6.2 Microfluidic testing setup and liquid delivery

The liquid flow system consists of syringe pumps, syringes, tubings, valves, and the sensor complex. 60 ml syringes are used as reservoirs for blank solvents, blank buffer solutions, and testing solutions. In a typical experiment, 2 syringes, one with the testing solution and the other with the blank solvent that the testing solution was made in, were used. The outlets of the 2 syringes are connected through two individual 10 cm tubings into the two inlet end of a Teflon Y-junction, merging into a single stream at the tail of the Y-junction. Paper clips that pinches on the tubings were used as valves (Figure 2.9(d)). The valves ensure no backflow or undesirable mixing of the 2 liquid stream when one stream is being pumped into the flow cell. The outlet of the Y-junction was connected to the inlet of the flow cell through a 20 cm tubing. The liquid flows through the flow cell, and enters another tubing connected to the outlet of the flow cell through a Teflon fitting, and goes to waste liquid collector.

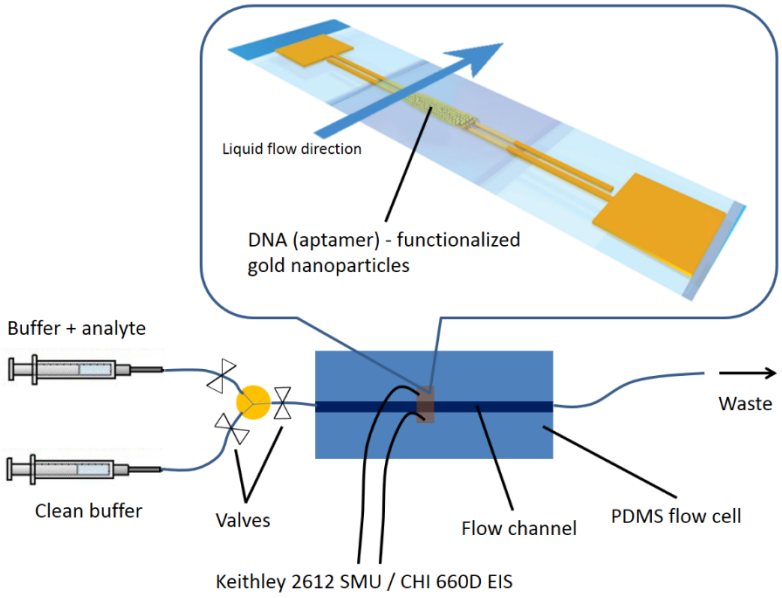

Figure 2.9 Schematic of flow system

2.7 Electrical measurements

Electrical measurements were performed using Keithley electrical measurement systems (Cleveland, OH). All the measurement instruments were connected with a desktop computer through the GPIB (IEEE-488) interface. The instruments control and measurements were performed using National Instruments LabVIEW programs (Austin, TX).

2.7.1 Electrical connections

2.7.1.1 Sensor electrical connections

TO-3 headers were used as chip carriers due to their robustness and compatibility with O-rings and sealed flow cells. 2-pin TO-3 headers (Sintermetalgalss S.r.l., Opera, Italy) were used to carry single-device chips, while 8-pin headers (Sinclair, Norton, MA) were used for parallel testing

of multiple nanoscale chemiresistors on a single chip. Individual sensor chips were pasted using double-side carbon tapes to the blank center area of the TO-3 headers.

Microfabricated chemiresistor devices were connected to the TO-3 header bonding pads for electrical measurements. A West Bond 747630E wire bonder (Anaheim, CA) was used for all wire-bonding tasks. 25 μm diameter Al (with 1% Si) wires were used for making connections from contact pads on chemiresistor chips to contact pads on TO-3 headers. The wire bonder induces ultrasonic heating that melts the metal wire and solders it to the Au or Pd bonding pads (Figure 2.10).

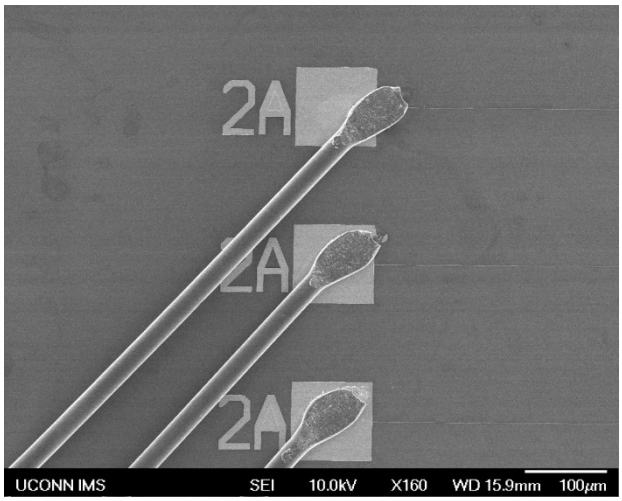

Figure 2.10 Wires bonded to the 100 μm × 100 μm contact pads on nanoscale devices

When putting the TO-3 headers carrying the sensor chips into the aluminum flow cell, Viton O-rings (ID: 19 mm, OD: 22.5 mm) were first placed around the sensor slots. The TO-3 headers were inverted and placed in each slot, tightened, and sealed with two screws. Kurt J.

Lesker Be/Cu set-screw connectors (Pittsburgh, PA) were used to connect shielded electrical cables to the TO-3 header pins, which were pointing upwards after the header installation.

2.7.1.2 Instrument electrical connections

Electrical cables from the TO-3 headers which carry individual sensors are connected to the terminals on the Keithley 7012-S 4 ×10 switch matrix card using the screw terminal connectors on the switch card. The switch card has a rating of maximum offset current less than 0.1 nA and switch actuation time of 3 ms. Therefore, the switch can be used for sequential testing of multiple devices within a short period of time. Figure 2.11 shows the connection of each devices to the switch matrix. Each "node" on the switch card represents a pair of switches that switch on or off simultaneously in response to program control. The switch matrix card is inserted into a Keithley 7002 switch system which interface the switch card with computer. The switching on and off of each individual switch pair cause each device (D1 to D8) to be connected or disconnected to the switch matrix output. It is possible to switch one, a few, or all switches on or off at the same time, but in testing, only one device is switched on at a time to collect signal from the individual sensor. Switching could either be controlled through manual switching on the panel buttons on the switch matrix, or through computer control using LabVIEW commands. The input terminal of Row 1 of the switch card is connected to a Keithley 2612 source measurement unit (SMU).

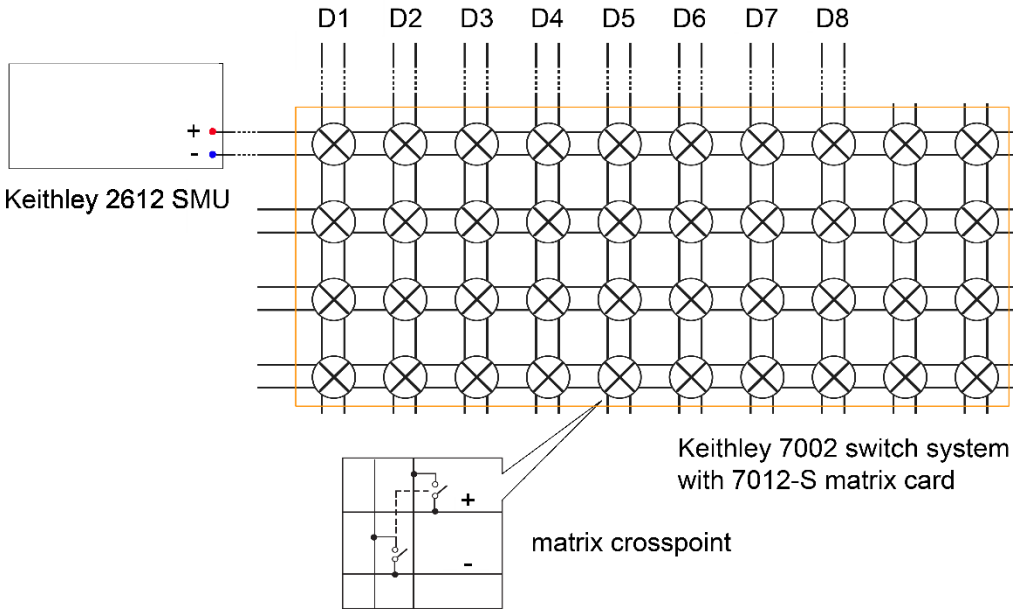

Figure 2.11 Circuit diagram of the connection of individual devices (D1 to D8) to the source measurement unit through the switch matrix. The connection allows multiple devices to be tested sequentially and cyclically at a high switching speeds.

2.7.2 Data acquisition

2.7.2.1 Current-voltage characteristics

Current-voltage (IV) responses of chemiresistor sensors were measured using triangular voltage sweep. A voltage is applied, by scanning the output voltage from 0 V to a higher voltage, down to a negative voltage, and back to 0 V. The voltage was held at each point for a current reading to be taken.

2.7.2.2 Resistance-time measurements

Resistance-time measurements are taken to evaluate real-time sensing performance of electronic sensor devices. The SMU was programmed to generate square waves at 50 – 500 Hz at

typically 1.0 V_{pp}, and DC current was recorded in the middle of each positive half-cycle. The measurement was performed by custom-designed LabVIEW programs.

2.8 Materials characterization tools

2.8.1 Scanning electron microscopy

The scanning electron microscope (SEM) is an instrument that produces images of a sample by scanning it with a focused beam of electrons. In operation, an electron source emits electrons, which are focused by electromagnetic lenses to produce a fine beam of electrons, typically with energy 0.2 keV to 40 keV. These beam of electrons are raster scanned by the scanning coils or deflector plates in the electron column. When the electron beam reaches the sample, the electrons are scattered and absorbed by the volume of specimen that it interacts with. This process produces various reflected high-energy electrons by elastic scattering, emission of secondary electrons by inelastic scattering, and emission of electromagnetic radiation. These multiple signals are collected with a number of detectors, for example, Everhart-Thornley detector typically used for secondary electrons, concentric back-scattered electron detector, in-lens secondary electron detector, and energy dispersive x-ray (EDX) detector for x-ray microanalysis.

The electron optics are essential in producing focused beams with very fine spot size. However, in the process of data acquisition, the image is pixelated, with each pixel of the computer video memory synchronized with the position of the rastering electron beam on the specimen. Therefore, unlike conventional optical systems, SEM resolution is not primarily limited by the diffraction limit. The SEM image is usually formed using secondary electrons or back-scattered electrons. The spatial resolution is determined by the interaction volume. The small interaction

volume for secondary electrons results in high spatial resolution down to < 1 nm. Comparatively, X-ray producing interaction volumes are larger, up to 1 μm^3, resulting in relatively low spatial resolution of X-ray elemental map produced from EDX spectroscopy.

Quartz crystals, micro/nano-fabricated electrodes, and sensors were characterized with a JEOL JSM-6335F (Peabody, MA) or an FEI Teneo SEM (Hillsboro, OR). Secondary electrons are usually used for obtaining topographic and morphologic information of the samples. Local elemental information was obtained with EDAX® EDX spectroscopy systems (Mahwah, NJ) attached to the above SEM instruments.

2.8.2 Transmission electron microscopy

The transmission electron microscope (TEM) operates by passing a beam of high-energy electrons through an ultra-thin specimen and forming an image from the transmitted electrons. In this imaging mode, the optical principles are similar to visible light microscopy. An electron source emits electrons by thermionic or field emission, which are extracted using a Wehnelt cylinder to form an initial electron beam. Three stages of electromagnetic and electrostatic lenses are installed in the TEM column. The condenser lenses form the primary electron beam, the objective lenses focus the beam that comes through the sample itself, and the projector lenses expand the beam onto a phosphor screen or a charge-coupled device (CCD) array for digital imaging. A significantly higher resolution image is obtained due to the small de Broglie wavelength of the electrons, which overcomes the diffraction limit of optical systems. At typical accelerating voltage of 100 keV – 300 keV used in TEM, the resolution limit can go below 0.1 nm.

In this study, an FEI Tecnai T12 TEM operating at 120 keV and a JEOL JEM-2010F TEM operating at 200 keV were used to acquire images of gold nanoparticles. To mount the samples,

gold nanoparticle solutions were diluted to a concentration with absorbance close to unity. 2 μl of as-prepared gold nanoparticle solutions were drawn using a micropipette, and the nanoparticle solution was deposited on TEM grids covered with carbon films. The samples are then allowed to stand to evaporate off solvents, and are inserted into TEM using a single-tilt holder. At this typical magnification up to 1,000,000 × used in these imaging tasks, the contrast is due to absorption of electrons by the material determined by mass and thickness.

2.8.3 Atomic force microscopy

The atomic force microscope (AFM) is a type of scanning probe microscope (SPM), which forms images of surfaces using a physical probe that scans the specimen. The probe tip can be as sharp as a single atom, and it is attached to the end of a spring-like cantilever. The cantilever is driven by a piezoelectric crystal controller, that can scan the tip with sub-nanometer precision in both the lateral and vertical directions. A diode laser is pointed towards the back of the cantilever, and the reflected laser is collected by a position-sensitive photodetector that has four quadrants. The most basic mode of AFM operation is contact mode, in which the tip is in firm contact with the solid surface. Upon interaction with the sample surface, the cantilever is displaced, causing the reflected laser to be displaced. Its position shift on the photodetector is interpreted as the angular deflection of the cantilever. The pixelated information of AFM tip deflection across the sample surface forms the deflection image. In addition to this, the cantilever defection is used as a feedback signal to the computer to adjust the immediate vertical position of the tip using the piezoelectric scanner. This feedback mechanism attempts to keep the cantilever deflection constant by adjusting the voltage applied to the scanner. In the meantime, the height information of the cantilever is recorded, and used to form the height image. Both the deflection image and the height images reflect the surface morphology of the sample, but through different aspects.

While the deflection image shows more of the roughness features and visually more three-dimensional, the height image is more reflective of the actual topography of the surface.

DNA films on quartz crystals were imaged using an Asylum Research MFP-3D AFM (Santa Barbara, CA) equipped with a diamond-coated silicon AFM tip. The imaging area was 5 μm × 5 μm at a scan speed of 5 μm/s. Both height and deflection images were collected. Deflection images were collected to accentuate the surface topographical features of DNA fibers. Nanoscale sensor devices with or without gold nanoparticles were imaged with a Nanosurf easyScan 2 AFM (Liestal, Switzerland) equipped with a standard silicon tip. The imaging area was 2.5 μm × 2.5 μm at a scan speed of 2.5 μm/s, and height images were collected. Both DNA films and sensor device samples were imaged in the contact mode, as the samples were found to be stiff enough and tip contacts did not alter the samples after repeated scanning.

2.8.4 X-ray photoelectron spectroscopy

X-ray photoelectron spectroscopy (XPS) is a technique that measures chemical information of solid surfaces. With high surface sensitivity, XPS reveals composition and bonding information of atoms typically in the range 1 – 10 nm from the surface.[33] This feature makes XPS ideal for analysis of modifications of solid surfaces using organic compounds. Ultrahigh vacuum (UHV) in the range of 10^{-10} to 5×10^{-9} Torr is necessary primarily to reduce surface contamination due to molecular adsorption. The UHV environment also helps to reduce collision of electrons with gas molecules and increase instrumental signal-to-noise ratios (SNR).

XPS spectra are obtained by illuminating a material with a beam of X-rays and detecting the kinetic energy and number of electrons that escape from the surface. Due to the relatively small inelastic mean free path of electrons, which is only a few nanometers, only those electrons

emitting from surface atoms are able to reach vacuum and be collected by the detector. Each element produces a set of characteristic peaks in the XPS spectra that has a one-to-one correspondence with its initial electron energy levels. When X-ray photons irradiate the sample, core electrons are ejected, and their kinetic energy is expressed as

$$KE = h\nu - BE - \phi \tag{2.7}$$

where KE is the kinetic energy of the photoelectrons relative to the analyzer, $h\nu$ is the X-ray photon energy, BE is the binding energy of the electrons, and ϕ is the work function of the electron analyzer. Mg or Al Kα emission is usually used for XPS electron gun, and this photon energy is sufficient to excite most core levels of interest. As core levels of atoms have distinct core level binding energies, XPS spectra reveals the composition information of samples. In addition, binding energy is also affected by the atomic oxidation state and its surround environment. These material properties are reflected as chemical shift in the XPS spectra, which helps users infer bonding information of the particular atoms.

In this study, surface functionalization of SiO_2/Si substrates and gold nanoparticles was analyzed with a Kratos Axis 165 XPS system equipped with a monochromatic Al Kα (1486.7 eV) X-ray source (Manchester, United Kingdom). Peaks generated in XPS were fitted by CasaXPS analytical software, and the atomic percentage of the different elements in materials were calculated according to the area intensity on each core-level peak. Standard relative sensitivity

factors (RSF) were located in standard database and used to normalize peak areas to atomic quantities according to[34]

$$C_A = \frac{A_A/S_A}{\sum_n A_A/S_A} \tag{2.8}$$

Gold nanoparticle samples were prepared by depositing 4 µl of as-prepared nanoparticle solutions on tantalum foils and allowing the samples to dry in air. A thin film of nanoparticle films was formed on the foil. The samples were then pasted using carbon tape on an XPS bar sample holder and loaded into the XPS sample transfer chamber. Because of residual moisture and large surface area of the gold nanoparticles, the samples were kept in the sample transfer chamber for at least 8 hours before moving into the ultra-high vacuum (UHV) sample analysis chamber. Functionalized Si SiO_2/Si samples were briefly cleaned using a stream of N_2 and loaded on to a bar sample holder. The sample was loaded into the sample transfer chamber and pumped down for 4 hours before moving into the sample analysis chamber.

2.8.5 Impedance spectroscopy

Charge carriers in a conductive material is dependent on the frequency of the external electric field. Materials being tested can usually be modeled using a combination of resistance and capacitance, i.e., RC circuits. For movement of electrons, the complex impedance is usually independent of frequency, and resistors are used to model this behavior. In an electrolyte which interfaces with conductive electrodes, faradaic impedance is usually present, showing both resistive and capacitive behavior. Because of the presence of capacitance components in the RC circuits, the complex impedance is frequency dependent. In complex systems where multiple

charge carriers are present, impedance spectroscopy helps to distinguish different types of active charge carriers and conduction mechanisms at various frequencies. Using these spectra, circuit models of the electrochemical systems can be drawn to allow determination of physical structure of the charge transport systems.

In this study, CH Instruments 660D electrochemical workstation (Austin, TX) was used to test chemiresistor devices in a two-electrode mode with a frequency range 0.1 Hz to 100 kHz.

2.9 References

1. Lu, C.; Czanderna, A. W. *Applications of Piezoelectric Quartz Crystal Microbalances*. Elsevier Science: **2012**.

2. Sauerbrey, G. Verwendung von Schwingquarzen zur Wägung dünner Schichten und zur Mikrowägung. *Zeitschrift für Physik* **1959**, 155, 206-222.

3. Janshoff, A.; Galla, H.-J.; Steinem, C. Piezoelectric Mass-Sensing Devices as Biosensors—An Alternative to Optical Biosensors? *Angewandte Chemie International Edition* **2000**, 39, 4004-4032.

4. King, W. H. Piezoelectric Sorption Detector. *Analytical Chemistry* **1964**, 36, 1735-1739.

5. Grate, J. W. Acoustic Wave Microsensor Arrays for Vapor Sensing. *Chemical Reviews* **2000**, 100, 2627-2648.

6. Martin, S. J.; Frye, G. C.; Senturia, S. D. Dynamics and Response of Polymer-Coated Surface Acoustic Wave Devices: Effect of Viscoelastic Properties and Film Resonance. *Analytical Chemistry* **1994**, 66, 2201-2219.

7. Grate, J. W.; Kaganove, S. N.; Bhethanabotla, V. R. Examination of mass and modulus contributions to thickness shear mode and surface acoustic wave vapour sensor responses using partition coefficients. *Faraday Discussions* **1997**, 107, 259-283.

8. Martin, S. J.; Frye, G. C. In *Polymer film characterization using quartz resonators*, Ultrasonics Symposium, 1991. Proceedings., IEEE 1991, 8-11 Dec 1991; **1991**; pp 393-398 vol.1.

9. Jones, R.; Meixner, H. *Sensors, Micro- and Nanosensor Technology: Trends in Sensor Markets*. Wiley: **2008**.

10. Daniel, M.-C.; Astruc, D. Gold Nanoparticles: Assembly, Supramolecular Chemistry, Quantum-Size-Related Properties, and Applications toward Biology, Catalysis, and Nanotechnology. *Chemical Reviews* **2003**, 104, 293-346.

11. Ibañez, F. J.; Zamborini, F. P. Chemiresistive Sensing with Chemically Modified Metal and Alloy Nanoparticles. *Small* **2012**, 8, 174-202.

12. Mirkin, C. A.; Letsinger, R. L.; Mucic, R. C.; Storhoff, J. J. A DNA-based method for rationally assembling nanoparticles into macroscopic materials. *Nature* **1996**, 382, 607-609.

13. Huang, C.-C.; Chiu, S.-H.; Huang, Y.-F.; Chang, H.-T. Aptamer-Functionalized Gold Nanoparticles for Turn-On Light Switch Detection of Platelet-Derived Growth Factor. *Analytical Chemistry* **2007**, 79, 4798-4804.

14. Tan, D.; He, Y.; Xing, X.; Zhao, Y.; Tang, H.; Pang, D. Aptamer functionalized gold nanoparticles based fluorescent probe for the detection of mercury (II) ion in aqueous solution. *Talanta* **2013**, 113, 26-30.

15. Demers, L. M.; Mirkin, C. A.; Mucic, R. C.; Reynolds, R. A.; Letsinger, R. L.; Elghanian, R.; Viswanadham, G. A Fluorescence-Based Method for Determining the Surface Coverage and Hybridization Efficiency of Thiol-Capped Oligonucleotides Bound to Gold Thin Films and Nanoparticles. *Analytical Chemistry* **2000**, 72, 5535-5541.

16. Opdahl, A.; Petrovykh, D. Y.; Kimura-Suda, H.; Tarlov, M. J.; Whitman, L. J. Independent control of grafting density and conformation of single-stranded DNA brushes. *Proceedings of the National Academy of Sciences* **2007**, 104, 9-14.

17. Liu, J.; Lu, Y. Preparation of aptamer-linked gold nanoparticle purple aggregates for colorimetric sensing of analytes. *Nat. Protocols* **2006**, 1, 246-252.

18. Fu, K.; Li, S.; Jiang, X.; Wang, Y.; Willis, B. G. DNA Gold Nanoparticle Nanocomposite Films for Chemiresistive Vapor Sensing. *Langmuir* **2013**, 29, 14335-14343.

19. Nagraj, N.; Slocik, J. M.; Phillips, D. M.; Kelley-Loughnane, N.; Naik, R. R.; Potyrailo, R. A. Selective sensing of vapors of similar dielectric constants using peptide-capped gold nanoparticles on individual multivariable transducers. *Analyst* **2013**, 138, 4334-4339.

20. Chen, S.; Jenkins, S. V.; Tao, J.; Zhu, Y.; Chen, J. Anisotropic Seeded Growth of Cu–M (M = Au, Pt, or Pd) Bimetallic Nanorods with Tunable Optical and Catalytic Properties. *J. Phys. Chem. C* **2013**, 117, 8924-8932.

21. Peng, G.; Tisch, U.; Adams, O.; Hakim, M.; Shehada, N.; Broza, Y. Y.; Billan, S.; Abdah-Bortnyak, R.; Kuten, A.; Haick, H. Diagnosing lung cancer in exhaled breath using gold nanoparticles. *Nature Nanotechnology* **2009**, 4, 669-673.

22. García-Berríos, E.; Gao, T.; Theriot, J. C.; Woodka, M. D.; Brunschwig, B. S.; Lewis, N. S. Response and Discrimination Performance of Arrays of Organothiol-Capped Au Nanoparticle Chemiresistive Vapor Sensors. *The Journal of Physical Chemistry C* **2011**, 115, 6208-6217.

23. Bohrer, F. I.; Covington, E.; Kurdak, Ç.; Zellers, E. T. Characterization of Dense Arrays of Chemiresistor Vapor Sensors with Submicrometer Features and Patterned Nanoparticle Interface Layers. *Analytical Chemistry* **2011**, 83, 3687-3695.

24. Ancona, M. G.; Snow, A. W.; Perkins, F. K.; Pate, B.; Park, D. Analyte kinetics in a nanocluster-based chemiresistor: A case study. *Sensors and Actuators B: Chemical* **2013**, 177, 936-946.

25. Xie, J.; Jiang, J.; Davoodi, P.; Srinivasan, M. P.; Wang, C.-H. Electrohydrodynamic atomization: A two-decade effort to produce and process micro-/nanoparticulate materials. *Chemical Engineering Science* **2015**, 125, 32-57.

26. Soliwoda, K.; Rosowski, M.; Tomaszewska, E.; Tkacz-Szczesna, B.; Celichowski, G.; Grobelny, J. Electrospray deposition of gold nanoparticles from aqueous colloids on solid substrates. *Colloids and Surfaces A: Physicochemical and Engineering Aspects* **2015**, 486, 211-217.

27. Li, X.; Huang, J.; Edirisinghe, M. Development of nano-hydroxyapatite coating by electrohydrodynamic atomization spraying. *Journal of Materials Science: Materials in Medicine* **2007**, 19, 1545-1551.

28. Hughes, M. P. *Nanoelectromechanics in Engineering and Biology*. Taylor & Francis: **2002**.

29. NIST. NIST Chemistry WebBook. **2016**.

30. Whitesides, G. M. The origins and the future of microfluidics. *Nature* **2006**, 442, 368-373.

31. Swensen, J. S.; Xiao, Y.; Ferguson, B. S.; Lubin, A. A.; Lai, R. Y.; Heeger, A. J.; Plaxco, K. W.; Soh, H. T. Continuous, Real-Time Monitoring of Cocaine in Undiluted Blood Serum via a Microfluidic, Electrochemical Aptamer-Based Sensor. *Journal of the American Chemical Society* **2009**, 131, 4262-4266.

32. Whitesides, G. M.; Ostuni, E.; Takayama, S.; Jiang, X.; Ingber, D. E. Soft Lithography in Biology and Biochemistry. *Annual Review of Biomedical Engineering* **2001**, 3, 335-373.

33. Chung, Y. *Practical Guide to Surface Science and Spectroscopy*. Academic Press: **2001**.

34. Moulder, J. F.; Chastain, J. *Handbook of X-ray Photoelectron Spectroscopy: A Reference Book of Standard Spectra for Identification and Interpretation of XPS Data*. Physical Electronics: **1995**.

Chapter 3

EQUILIBRIUM VAPOR PARTITIONING STUDIES OF DNA AS A SOLID-STATE VAPOR SENSING MATERAL

3.1 Introduction

Volatile organic compound (VOC) detection is a field of broad interest with applications in analytical chemistry, environmental regulation, industrial monitoring, and national security. Identification and quantification of compounds in vapor mixtures depends primarily on the interaction of vapor phase analytes with a stationary phase. Commonly used materials for this purpose include polymers and organically functionalized composites, including synthetic polymers (polyisobutylene, polysiloxane, polyepichlorohydrin, etc.),[1, 2] semiconductors,[3] carbon black-polymer composites,[4] cyclodextrin derivatives,[5] calixarenes,[2] graphitic materials (fullerene, graphite, carbon nanotubes, graphene, and derivatives),[6-10] ionic liquids,[11] synthetic molecular-imprinted polymers (MIPs),[12, 13] Langmuir-Blodgett films,[14] and functionalized gold nanoparticle-organic composite films.[15, 16] Depending on the transducer, sorbed vapors are detected as a change in electrical conduction, resonator frequency, fluorescence intensity, or colorimetric response,

among others.[2] Mass-sensitive transducers are advantageous because they have high sensitivity and give a directly quantifiable response.[17] Equilibrium and rate constants can be measured, which allows quantitative comparison between different sensor materials.

Due to favorable interactions with many organic vapor molecules, synthetic polymers, supramolecular materials, and composite materials are used extensively as sorptive sensing materials. However, these materials have limitations including lack of specificity, limited range of chemical properties, and polydispersity that may mask specific sorption effects. The main parameters to modify in synthetic polymers are functional groups, molecular weight, average composition,[18] and extent of crosslinking.[19] In the past decade, an emergent theme is to integrate biomolecules with conventional sensor transducers for enhanced specificity. Three classes of biomolecules have been investigated for gas-phase vapor sensing: polypeptides,[20-23] lipids,[24, 25] and DNA[26-33] and RNA.[34] In contrast to synthetic polymers, biomolecules have more precise composition, polydispersity index (PDI) of unity, and (under the right conditions) complex three-dimensional (3D) structures.

DNA has advantages due to simpler synthesis compared to proteins, a higher resistance to degradation compared to RNA,[35] and greater structural and compositional complexity than lipids. DNA oligomers are typically characterized in buffered aqueous solutions, but folded DNA nanostructures have also been observed in substrate-supported films in both air[36-38] and vacuum.[39, 40] For example, well-defined structures of DNA have been observed using scanning tunneling microscopy (STM), including base pairs, duplexes, helices, loops and turns. More complex solid-state structures of recA-DNA complexes[41] and biotin–avidin–G4-DNA complexes have also been observed.[42] Complex 3D structures may modify intermolecular interactions between solid-state

DNA and vapor molecules, making DNA a promising material for enhanced specificity in chemical sensing.

To date, transducers exploiting sorption properties of DNA include: carbon nanotube and graphene chemitransistors,[26, 28, 29, 31, 33] fluorescence enhancement and quenching phenomena[30, 32] and colloidal metal-insulator-metal ensemble chemiresistors.[27] With respect to material integration, solid-state DNA is as versatile as composite, polymer, and supramolecular materials, and can be coupled with transducers and substrates through thiol or amine modifications to DNA oligomers and/or through surface functionalization. The number of unique sequences scales as 4^N where N is the number of monomers, thus yielding an almost limitless variation of sensing materials from a few fundamental building blocks.[32] White et al. used 29 different single-stranded DNA sequences tagged with dye molecules to create sensor arrays, and measured their response to volatile compounds. The number of distinct sequences employed was roughly twice as many as other sensor arrays based on nanoparticle assemblies reported to date.[32] DNA has potential to introduce a new dimension to sensor materials by involving secondary and tertiary structures. In particular, DNA aptamers exhibit three-dimensional conformations that could confer specific binding properties to target analytes.[43-46] To date, positive evidence for specific binding behaviors of aptamers have only been established in well-controlled aqueous buffered condition.

To move towards a more general, solid-state, electronic sensing systems, the functionality of DNA is unknown. Solid-state DNA origami structures also provide an example of DNA structures that exhibit well-defined three dimensional complex conformations that may exhibit distinct sorption properties.[47] Several studies used DNA as a sensing material, but no conclusions have been made with regard to the effect of 3D molecular configurations on the sorption properties of DNA.[26, 31] Some experiments used pure water (non-salted) solutions to deposit DNA, thereby

casting uncertainty on the formation of secondary structures. Other studies did not study the effect of secondary structures on sensing behavior. Because of the lack of basic understanding of solid-state DNA on sensing, it is very important to evaluate fundamental thermodynamic interaction parameters of DNA under the broader perspective of sorptive polymer materials.

In this chapter, we use quartz crystal microbalance (QCM) as a quantitative tool to study DNA oligomers as vapor sensing materials. Sensitivity and selectivity are related to the chemical properties of DNA prepared as thin films. Sorption data of several custom-designed DNA sequences of different lengths, compositions, and sequences, prepared under both water and salted conditions, have been investigated. A linear solvation energy relationship (LSER) is used to analyze the sensing data to quantify the properties of different DNA oligomers as sensing materials. LSER coefficients are compared with conventional synthetic polymers to show similarities and differences of DNA as a sorptive material, and to show variances between different DNA sequences. The data show sequence dependent selectivity as well as the effects of salt on DNA preparation.

3.2 Materials and methods

3.2.1 Materials

DNA molecules used for film preparations are $(dA)_{25}$, $(dT)_{25}$, $(dC)_{25}$, $(dA)_{10}$, $(dA)_{50}$, 27A, 27L, 24A, and 24L. The $(dA)_{25}$, $(dT)_{25}$, $(dC)_{25}$, $(dA)_{10}$, and $(dA)_{50}$ are linear oligonucleotides with homogeneous base composition. These 5 sequences are not expected to have base-pairing or secondary structures. 27A is an adenosine triphosphate (ATP) aptamer, having a reported G-quadruplex in buffered conditions (Figure 3.1).[48] 27L is a control sequence identical to 27A in

overall base composition, but with a rearranged sequence to preclude G-quadruplex formation. Similarly, 24A is a designed loop sequence and 24L is a control sequence of identical base composition but scrambled sequence to preclude loop formation.

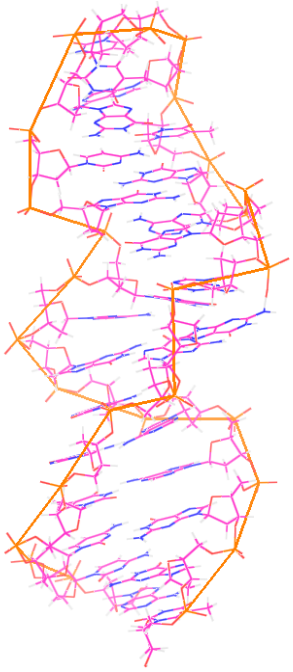

Figure 3.1 Solution phase structure of 27A[48]

3.2.2 **Fabrication of sensors**

Prior to coating with DNA, quartz crystals were cleaned by ultra-sonication in a series of soap water, deionized water, ethanol, and isopropanol, followed by treatment in a Novascan UV-ozone cleaner (Ames, IA). For fabrication of sensors without salt, a solution of 200 μM was made from the as-received lyophilized DNA sample using double-distilled water (ddH_2O). Using a micropipette, 5 μl of each DNA solution was placed at the center of quartz crystal gold electrodes. The droplets spread out to a diameter of 1 ± 0.05 cm. The solution was dried overnight in enclosed ambient air at room temperature. For DNA prepared in salt conditions, the procedure follows an

established method to preserve the secondary structures of DNA.[37] Lyophilized DNA was dissolved at a concentration 200 μM in 10 mM KCl solution. 5 μl of the DNA in salt solution was deposited at the center of a quartz crystal and dried at 4 °C overnight. The $(dA)_{25}$, $(dT)_{25}$, $(dC)_{25}$, $(dA)_{10}$, and $(dA)_{50}$ samples were made only with water solutions because of the absence of secondary structures, while 27A, 27L, 24A, and 24L samples were made with both water and salted conditions to study the possible effects of salt-induced secondary structures.

PIB-coated quartz crystals were prepared with 0.1% (w/v) solutions of PIB in chloroform. The crystals were placed on hot plates heated to 40 °C and PIB solution was drop-cast to cover the center of a quartz crystal gold electrode. Similarly, PEG-coated quartz crystals were prepared with 0.1% (w/v) solutions of PEG in distilled water. The crystals were placed on hot plates heated to 80 °C and PEG solution was drop-cast to cover the center of the quartz crystal gold electrode. The droplets spread out achieving a diameter of 1 ± 0.1 cm. After the solution droplets had evaporated, the crystal was removed from the hotplate and left in air overnight to allow residual solvent to evaporate.

3.2.3 Characterization of coating thickness and morphology

Thicknesses of DNA films on quartz crystals were estimated by cleaving quartz crystals and observing the cross sections with a JEOL-6335F scanning electron microscope (SEM). To obtain the average thickness as well as thickness profile of an entire film, multiple measurements were taken along the cross-section. Surface morphology was obtained with SEM oblique view images and an Asylum Research MFP-3D atomic force microscope (AFM). To accentuate surface morphological features, deflection mode imaging was used.

3.2.4 Characterization of sensor response to vapors

The 20 vapors used in this study were toluene, acetonitrile, n-hexane, n-heptane, chloroform, ethanol, methanol, cyclohexane, 2-propanol, dichloromethane, diethyl ether, tetrahydrofuran, cyclohexanone, triethylamine, anisole, 1-propanol, 1-butanol, 1-pentanol, butyraldehyde, and styrene. The studies were separated into two parts. First, a subset of vapors was used in real-time studies of response speed and sensitivity. Second, equilibrium constants were obtained for all vapors and used for LSER modeling.

During crystal testing, the gas streams carrying vapors were passed through QCM flow cells and discharged through an exhaust tube. Total volumetric flow rate was maintained at 320 cm^3/min. The crystal responses to vapors Δf_v (Hz), crystal frequency shifts due to coating application Δf_s (Hz), and motional resistances R were recorded concurrently before, during, and after exposures to vapors. These measurements reflect the acoustic thickness of the DNA film throughout the vapor sorption and desorption process. Only frequency responses that were obtained in the acoustically thin regimes were used to calculate the partition coefficients, or equilibrium constants, K.

3.2.5 LSER modeling

To calculate LSER parameters, the equilibrium partition coefficients, K, need to be found for each vapor-DNA pair. As we have already discussed in Chapter 2,

$$\frac{\Delta f_v}{\Delta f_s} = \frac{\Delta f_{vapor\ sorption}}{\Delta f_{coating\ application}} = \frac{\Delta m_{vapor}}{\Delta m_{coating}} \tag{2.2}$$

As absolute mass of both the coating and vapor can measured using the QCM, the fundamental thermodynamic property, *K* which is the partition coefficient, can be calculated by[49-51]

$$K = \frac{C_S}{C_V} = \frac{\Delta f_v \rho}{\Delta f_s C_V} \tag{3.1}$$

where C_S is the concentration of vapor in the sorbent phase, C_V is the concentration of vapor in the vapor phase, ρ is the density of the sorbent phase, $\Delta f_s$is the frequency shift due to the mass of the DNA applied to the sensor surface, and Δf_v is the sensor frequency shift due to vapor absorption by the DNA films. *K* values are used to regress materials properties via the LSER equation:

$$\log K = c + rR_2 + s\pi_2^H + a\sum \alpha_2^H + b\sum \beta_2^H + l \log L^{16} \tag{3.2}$$

In the LSER equation, vapor properties are characterized by parameters R_2, π_2^H, α_2^H, β_2^H, and $\log L^{16}$, representing polarizability, dopolarity, hydrogen bonding acidity, hydrogen bonding basicity, and dispersion. The multiplying terms *r, s, a, b,* and *l* are the corresponding values for the properties of sorbent materials. *r* stands for the ability of sorbent materials to interact with analyte n and π electrons, *s* is the ability of the solid phase to take part in dipolar interactions, *a* is the hydrogen bond basicity, *b* is the hydrogen bond acidity, and *l* represents phase cavity formation and dispersion interactions. Vapor analyte parameters are obtained from the literature,[34] and sorbent parameters for DNA sequences are calculated by multiple linear regression using measured K values for a set of 20 diverse vapors. The use of 20 vapors provides statistically significant fittings of LSER coefficients, as was the case in similar studies of polymers.[52-54] LSER parameters R_2, π_2^H, α_2^H, β_2^H, and $\log L^{16}$of the 20 vapors are included in Table 3.1. DNA is known to adsorb

water with increasing humidity,[55, 56] but water behaves non-ideally and can contribute to errors in the LSER analysis.[1] Therefore, water was not included in the LSER data set.

Table 3.1 LSER parameters of vapors[57]

	R_2	π_2^H	α_2^H	β_2^H	$\log L^{16}$
cyclohexanone	0.403	0.86	0	0.56	3.792
triethylamine	0.101	0.15	0	0.79	3.04
anisole	0.708	0.75	0	0.29	3.89
1-butanol	0.224	0.42	0.37	0.48	2.601
1-pentanol	0.219	0.42	0.37	0.48	3.106
1-propanol	0.236	0.42	0.37	0.48	2.031
styrene	0.849	0.65	0	0.16	3.856
butyraldehyde	0.187	0.65	0	0.45	2.27
toluene	0.601	0.52	0	0.14	3.325
acetonitrile	0.237	0.9	0.07	0.32	1.739
n-hexane	0	0	0	0	2.668
chloroform	0.425	0.49	0.15	0.02	2.48
ethanol	0.246	0.42	0.37	0.48	1.485
methanol	0.278	0.44	0.43	0.47	0.97
2-propanol	0.212	0.36	0.33	0.56	1.764
dichloromethane	0.387	0.58	0.1	0.05	2.019
cyclohexane	0.212	0.36	0.33	0.56	1.764
tetrahydrofuran	0.289	0.52	0	0.48	2.636
heptane	0	0	0	0	3.173
diethylether	0.041	0.25	0	0.45	2.015

3.3 Results and discussions

3.3.1 Characterization of DNA coatings

Figure 3.2(a) shows a typical DNA-coated QCM sensor visible to the naked eye as a translucent film occupying the center of a quartz crystal. Film morphology is shown in the Figure 3.2(b) inset as well as the AFM image in Figure 3.2(c). SEM and AFM images reveal the

morphology of the DNA film to be a mesoporous microstructure. The majority of the film consists of layers of bundled and entangled DNA strands. The bundles are 100 – 200 nm wide with length on the order of 1 μm. Typical film thickness ranges from 50 to 80 nm. For the DNA film shown in Figure 3.2(a), the average thickness is 75 nm. Using the density of solid DNA as 1.407 g/cm^3,[58] film area of 0.8 cm^2, and instrumental mass sensitivity of 0.056 Hz/ng/cm^2, the film thickness calculated from the frequency change is approximately 70 nm, which is consistent with the film thickness measured by SEM. According to Grate et al.,[15] this thickness is well within the acoustically thin regime where frequency change corresponds to mass change.

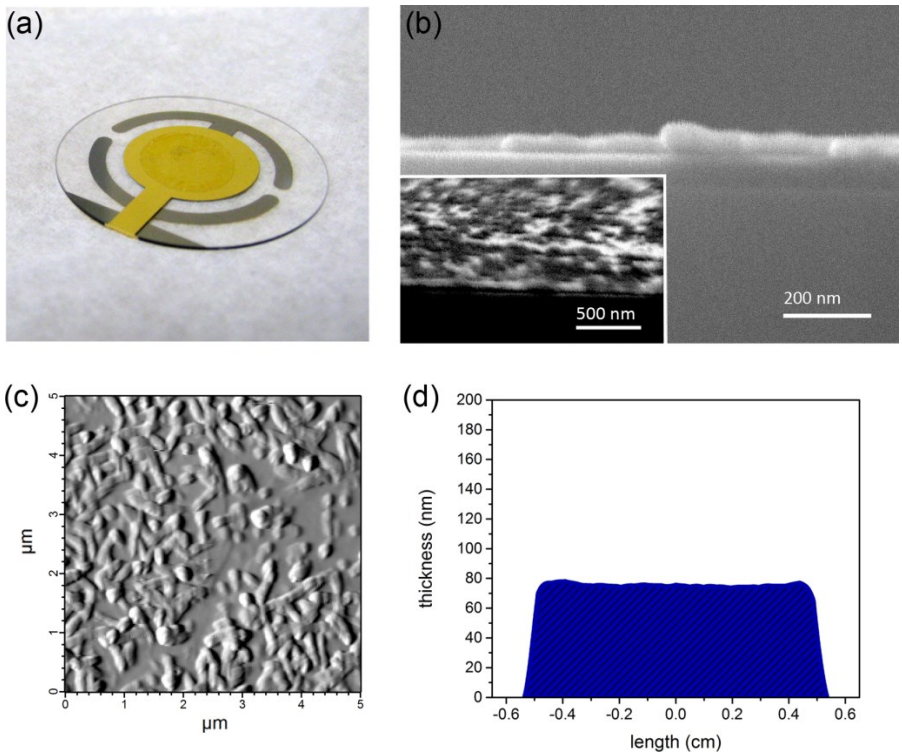

Figure 3.2 (a) Photo of a 1-inch diameter quartz crystal with DNA-coating in the middle forming a film. (b) Cross-sectional SEM image of the edge of a DNA film on a cleaved quartz crystal and (inset) surface morphology under SEM oblique view. (c) Contact mode AFM image of a DNA film. (d) Thickness profile of a DNA film from multi-point cross-section measurements by SEM.

Figure 3.3(a) shows frequency changes from casting 1, 2, and 5 nano-moles of DNA on quartz crystals. A representative selection of DNA of different molecular weights, compositions, and preparation conditions are plotted together. As shown in the figure, frequency change $-\Delta f_s$ shifts linearly with the mass of DNA deposited, covering the range of 200 – 4000 Hz. The range of frequency shifts is similar to those used for polymer-coated QCM sensors.[51, 59] The linear scaling of frequency with concentration (mass deposited) is consistent with QCM operation in the acoustically thin regime. The frequency changes of $(dA)_{25}$ and 24A prepared in 10 mM KCl and exposed to ethanol vapor are plotted in Figure 3.3(b). The mass of vapor sorbed scales linearly with coating mass with or without salt solutions for DNA film preparation. Similar trends are observed for tests on all other sorbents and vapors in this low vapor concentration range. It is also noticeable that the additional mass arising from salt ions are accurately accounted for by the QCM, which registers an additional frequency change due to the mass of salt ions. For QCM sensor studies in the remaining parts of this paper, crystals were coated with 1 nano-mole of DNA. A third parameter, motional resistance, describes the presence of viscoelastic effects in crystal oscillations. Typically a low motional resistance less than 15 Ω is indicative of an acoustically thin film.[15] Motional resistances of crystals with DNA coatings in this study were approximately 11 ± 1 Ω for all crystals studied. During vapor exposures, motional resistance shifts are in the range of 0.5 to 2 Ω. These values are consistent with previously established motional resistance changes for acoustically thin films with minimal viscoelastic contributions.[60, 61] As a reference, response characteristics for QCM crystals coated with synthetic polymers are included in Figure 3.4.

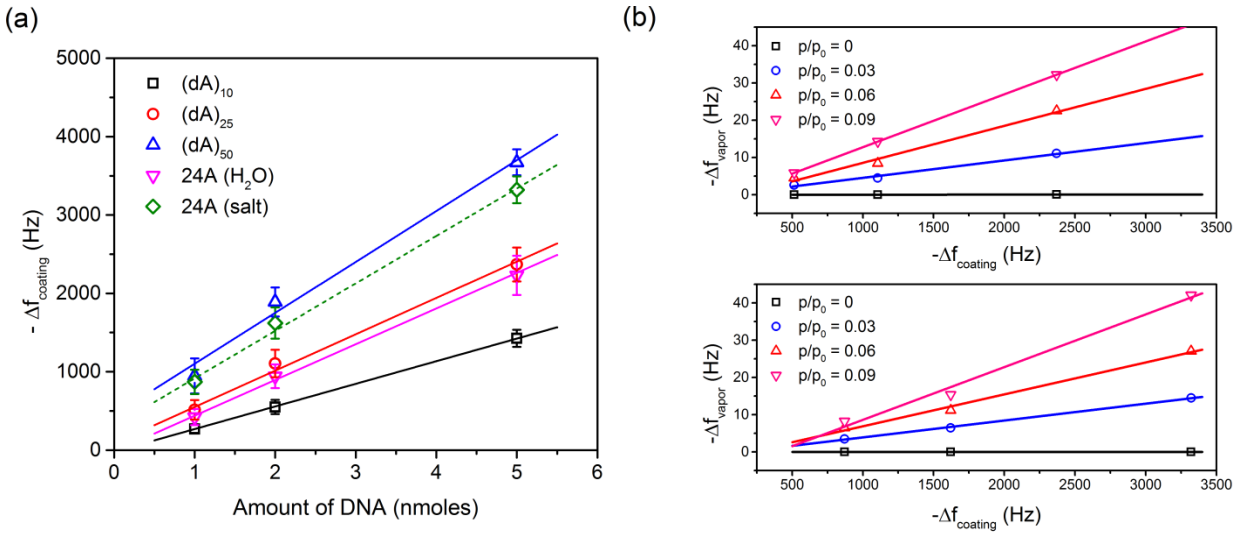

Figure 3.3 (a) Change of QCM crystal resonance frequency with added DNA mass. Solid line: DNA prepared in water; dashed line: DNA prepared with 10 mM KCl. (b) Effect of coating mass on the vapor resonance frequency change for a $(dA)_{25}$ coated quartz crystal (top); and 24A prepared with 10 mM KCl (bottom) under exposure to ethanol vapor at different vapor concentrations.

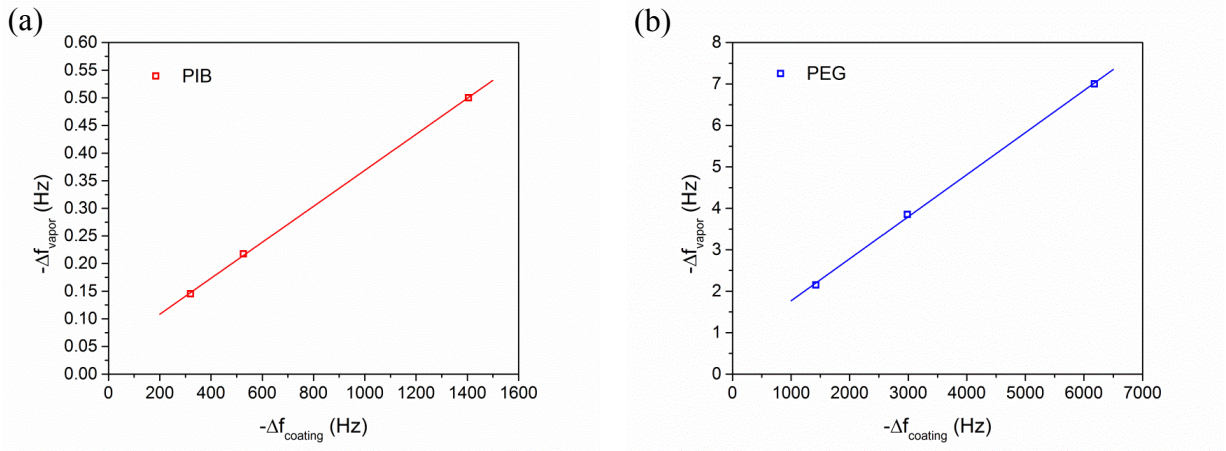

Figure 3.4 Effect of coating mass on the vapor resonance frequency change for (a) PIB- and (b) PEG- coated quartz crystal under exposure to ethanol vapor atp/p_0 = 0.06.

3.3.2 Response and recovery

Figure 3.5(a) shows example frequency changes upon exposure to and removal of organic vapors. Response rates are dependent on vapor concentration. At $p/p_0 = 0.01$, the time to reach half of the maximum response is about 30 seconds. This number decreases to less than 10 seconds for $p/p_0 = 0.03$ and less than 5 seconds for $p/p_0 = 0.06$. Slight differences in response speeds to different vapors are observed, which may be related to analyte-specific adsorption and diffusion rates.

Response rates were compared with well-known synthetic polymers polyisobutylene (PIB) and polyethylene glycol (PEG), which were coated on identical quartz crystals using identical drop casting methods. The normalized transient response profiles to toluene vapor of 5 types of DNA-coated crystals, a PIB-coated crystal, and a PEG-coated crystal are plotted in Figure 3.5(b). In general, DNA sensor responses are rapid and reversible with similar rates as PIB and PEG tested with the same experimental set-up. The use of KCl salt solutions to prepare DNA-coated crystals slightly depresses the response speed, which may be due to salt particles in the DNA layer that lower the permeability of the DNA films. However, due to limited volumetric proportions of salt, this effect is not significant. Overall, DNA-coatings have a response rate comparable to synthetic polymer-coated sensors of similar thicknesses.

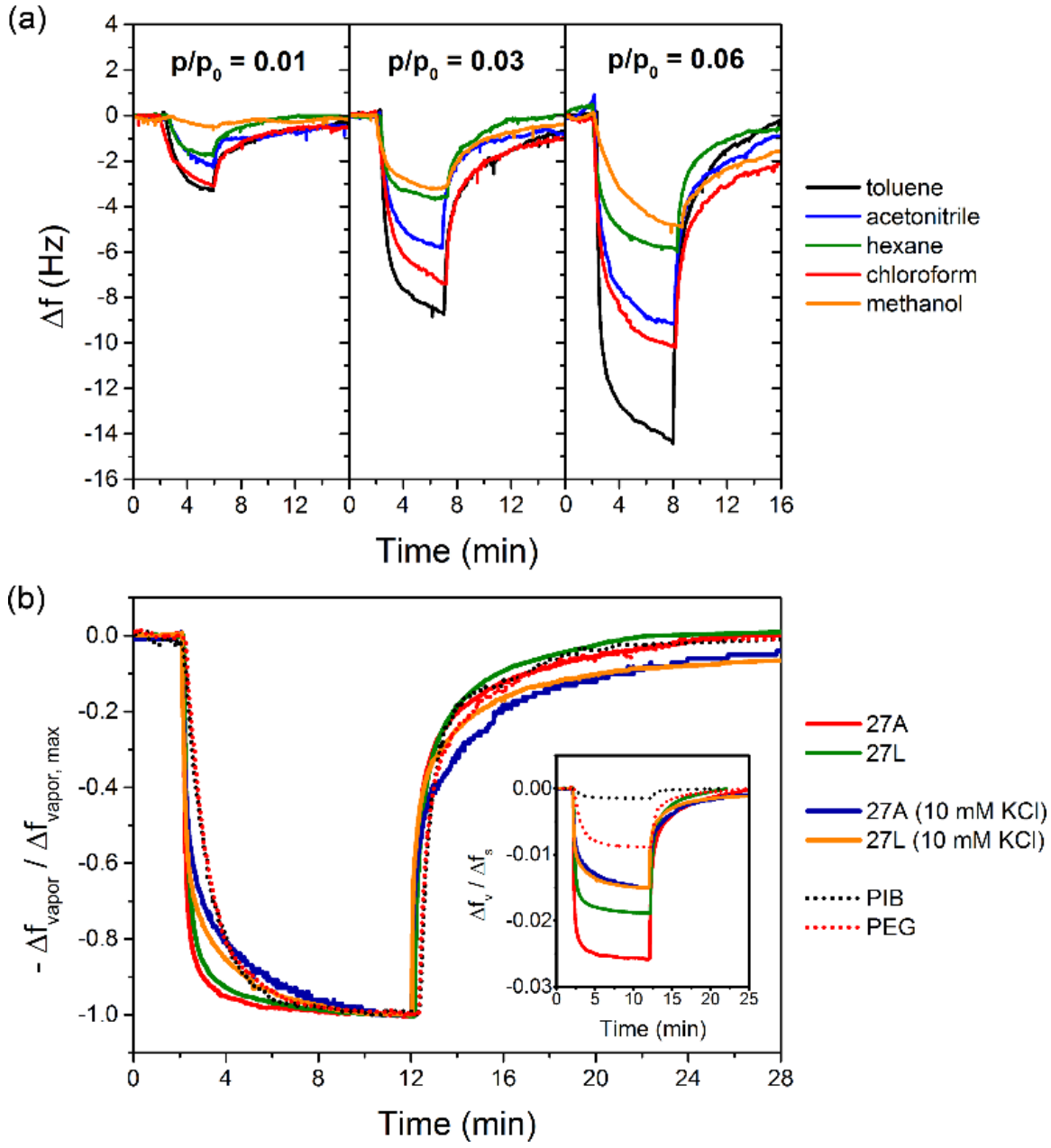

Figure 3.5 (a) Real-time QCM frequency response of a $(dA)_{25}$ sensor toward 5 common organic vapors at three concentrations. (b) Normalized real-time QCM frequency plots show reversible responses compared with PIB- and PEG-coated QCM sensors toward toluene vapor at concentration $\boldsymbol{p/p_0}$ = 0.05. Inset: Sensor response of DNA-QCM sensors, as compared to PIB- and PEG-coated quartz crystals, normalized against coating frequency change ($\Delta \boldsymbol{f_v}/\Delta \boldsymbol{f_s}$).

3.3.3 Vapor sensitivity

DNA-coated QCM sensors have been evaluated for their sensitivity and compared to other polymer-based acoustic sensors. Figure 3.6(a) shows the responses of DNA-coated sensors toward 3 organic vapors. Plots on p/p_0 and ppmv scales offer two distinct perspectives. The p/p_0 scale presents an equilibrium two-phase partition perspective, while ppmv presents performance in terms of absolute vapor concentrations that allow comparison with published results for different materials. When vapors are evaluated on a ppmv scale the response slope depends on absolute vapor pressure, which is commonly observed with sorption-based sensors regardless of transduction mechanisms.[32, 51, 62] A higher sensitivity to low vapor pressure compounds like toluene is not surprising, considering the inherently lower thermodynamic activity of these vapors.

At low concentrations, sensor responses are linear, yielding linear regression fits with $R^2 > 0.99$. The linear range is similar to QCM sensor arrays coated with synthetic polymers. For toluene, n-hexane, and triethylamine vapors, reported linear ranges for synthetic polymers are 3,000 – 11,000,[59, 61] and 14,000 ppm,[61] 250 – 4300 ppm[63, 64] respectively, depending on coating materials used. For DNA-coated QCM sensors, the corresponding values are 2,000, 8,000, and 3,000 ppm. The similarity of magnitude in the linear ranges observed for both synthetic polymers and DNA indicates similar vapor sorption properties in the low concentration range.

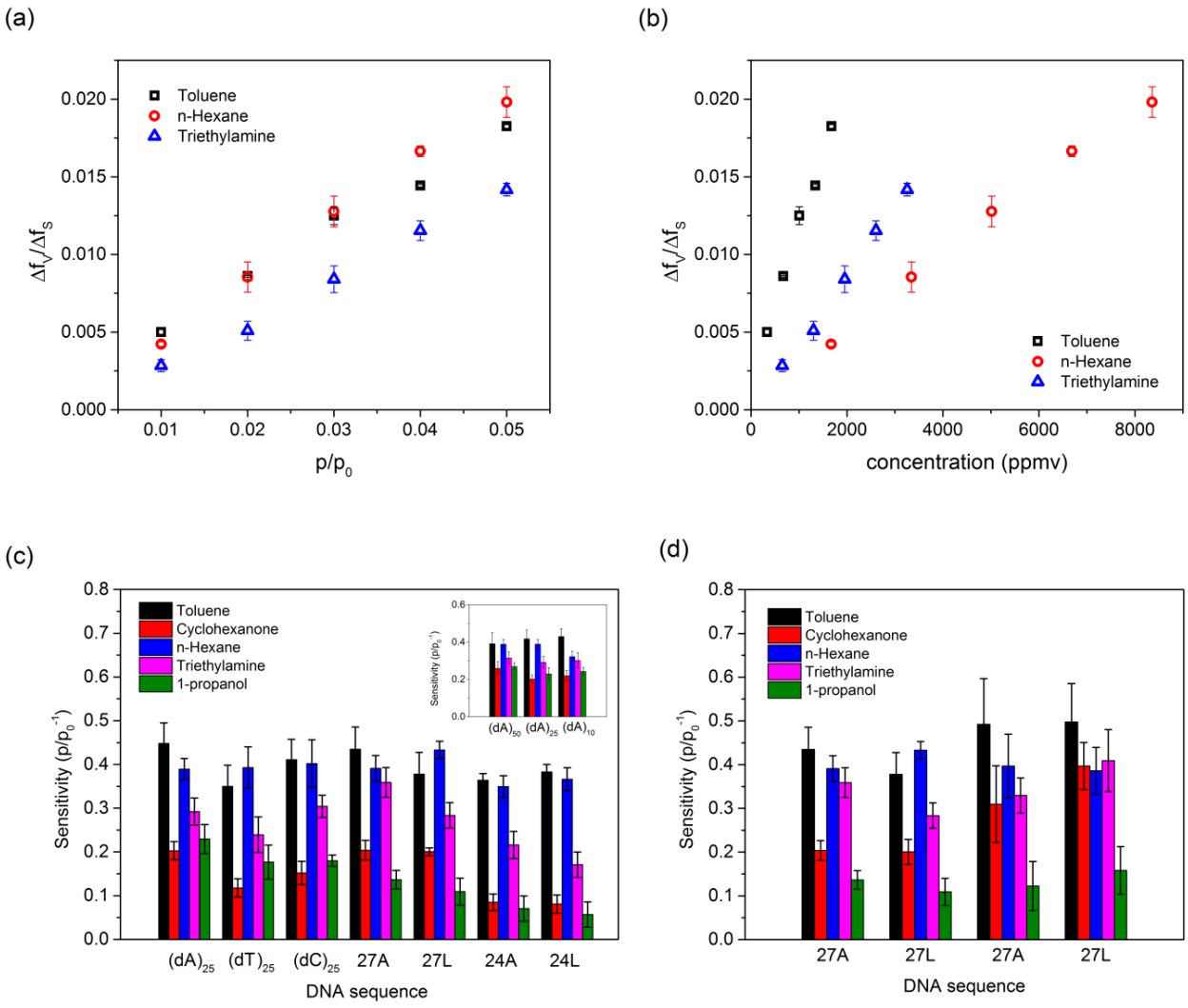

Figure 3.6 (a) Normalized vapor response frequency change (Δfv/Δfs) at several vapor concentrations for 27L sensors in units of p/p_0. (b) Same, in units of ppmv. (c) Average sensitivity on a p/p_0 scale of 7 DNA-coated QCM sensors to a group of 5 organic vapors. Inset: Average sensitivity on a p/p_0 scale of 3 homologous DNA-coated QCM sensors to the same 5 organic vapors. (d) Sensitivities of 27A and 27L prepared in water (left 2 sets) compared with 27A and 27L prepared in a 10 mM KCl solution (right 2 sets). Error bars are based on three separately prepared samples for each measurement.

Figure 3.6(c) presents average sensitivity values of 7 types of pure DNA sensor materials exposed to 5 vapors using data from three separately prepared samples. Sensitivity is defined as the slope of normalized frequency change against the ratio of the vapor's partial pressure to saturated partial pressure

$$S = \frac{d(\Delta f_v/\Delta f_s)}{d(p/p_{0)}} \tag{3.3}$$

Response differences reflect intrinsic sorption preferences of each coating material. $(dA)_{25}$, $(dT)_{25}$ and $(dC)_{25}$ have distinctive response patterns for the 5 vapors, which is a result of the nucleobase compositional differences. The response patterns of the 27A/27L and 24A/24L pairs are different from the homo-nucleotide sequences. In addition, the 27A/27L pair is also distinct from the 24A/24L pair. 27A and 27L are both more sensitive to cyclohexanone, triethylamine, and 1-propanol, while 24A and 24L show lower sensitivity toward the 5 vapors. Within each 24A/24L and 27A/27L pair, only slight differences of sensitivity profiles are observed. The latter suggests that nucleobase composition is the primary cause of sensitivity variation. Some minor differences are observed for DNA sequences with the same composition. In 27A and 27L the toluene/hexane sensitivity ratio for 27A is 1.1 while that for 27L is 0.9. However, these differences are close to the reproducibility limits of the measurements. Among all DNA sequences studied, the ratios of sensitivity for the most favorable to the least favorable analytes are about 10, for example, a 10x higher sensitivity toward toluene than 1-propanol. Compared with synthetic polymers, the relative sensitivity values are similar to those of weakly selective materials such as PIB[65] and PDMS.[51]

The inset of Figure 3.6(c) shows another comparison group with $(dA)_{10}$, $(dA)_{25}$, and $(dA)_{50}$. As the three oligonucleotides differ only in length, the sensitivity patterns are expected to show less variation, which is consistent with the data. Other than the outlier response for $(dA)_{10}$ to hexane, the response patterns are very similar. This behavior is similar to synthetic polymers such as poly(vinylpyrrolidone),[66] and simple biopolymers such as cellulose[67] where molecular weight variation results in less than 10% difference in vapor sorption isotherms. The close reproducibility of different length $(dA)_n$ sequences supports the interpretation that larger variations seen between $(dA)_n$, $(dT)_n$, and $(dC)_n$ sequences are due to composition and not film structure or other unrelated factors.

Figure 3.6(d) compares DNA prepared in 10 mM KCl to DNA prepared in water for both 27A/27L and 24A/24L pairs. When non-absorbing salt mass is added to the total mass of the DNA films, the absolute sensitivity of the DNA coated quartz crystals is reduced on a mass basis since the salt is non-sorptive. Therefore, data were normalized by DNA content, which is approximately 70% for salted samples. The effects of salt addition are most noticeable for the 27L structure where the cyclohexanone and TEA sensitivity ratios to n-hexane are significantly increased. The 27A structure also shows relative enhancement to cyclohexanone. The residual salt crystals in the dried DNA films are not expected to have significant sorption due to their non-porous nature, but they may cause polarizability and acidity/basicity changes in the DNA chains and functional groups. The salt preparation effects could also include promotion of secondary and tertiary structures. However, comparison of 27A and the control 27L, both prepared in salt conditions, show little difference, which suggests no significant secondary structure effects on vapor sorption; at least for the vapors considered in this study, and for the ATP aptamer sequence (27A).

Water vapor is treated as a separate case due to its known high affinity with DNA. DNA retains its tightly bound hydration shell of at least 15% by mass at zero humidity.[55] As expected, the sensitivity to water is almost twice that of most of the organic vapors in the same p/p_0 range (Figure 3.7(a)). The strong attraction to additional water vapor in the gas stream is consistent with the hydrogen bonding character of DNA. In addition, as DNA is capable of maintaining multiple layers of hydration shells, the sorbed water molecules on DNA can start to form a liquid-like disordered structure as humidity increases.[68] For less polar organic vapors with larger molecular sizes studied in this work, these effects are not known and less likely to occur. The sensitivity of DNA to water ($S = (\Delta f_v/\Delta f_s)/(p/p_0)$) is 0.90 (± 0.06), which is higher than common polymers poly(lactic acid) (PLA, S = 0.011)[69] and PEG (S = 0.010),[70] but much more similar compared to cellulose (S ≈ 0.4 at 25 °C)[71] and collagen (S = 0.46 at 28 °C).[72]

On the effect of water vapor on responses to organic vapors, toluene, hexane, and ethanol were tested in humid atmospheres with water vapor concentration p/p_0 = 0 to 0.12. The responses to organic vapors, expressed as $\Delta f_v/\Delta f_s$, decreased rapidly as the strongly-sorbed water vapor is introduced (Figure 3.7(b)). The competitive nature of sorption is similar to activated carbon[73] and metal-organic frameworks.[74] Water acts as an interference and decreases the sensitivity to vapors. Importantly, the motional resistance of DNA-coated QCM crystals during exposure to water vapors up to p/p_0 = 0.12 has not increased, indicating that viscoelastic effects have not set in at the humidity levels investigated.

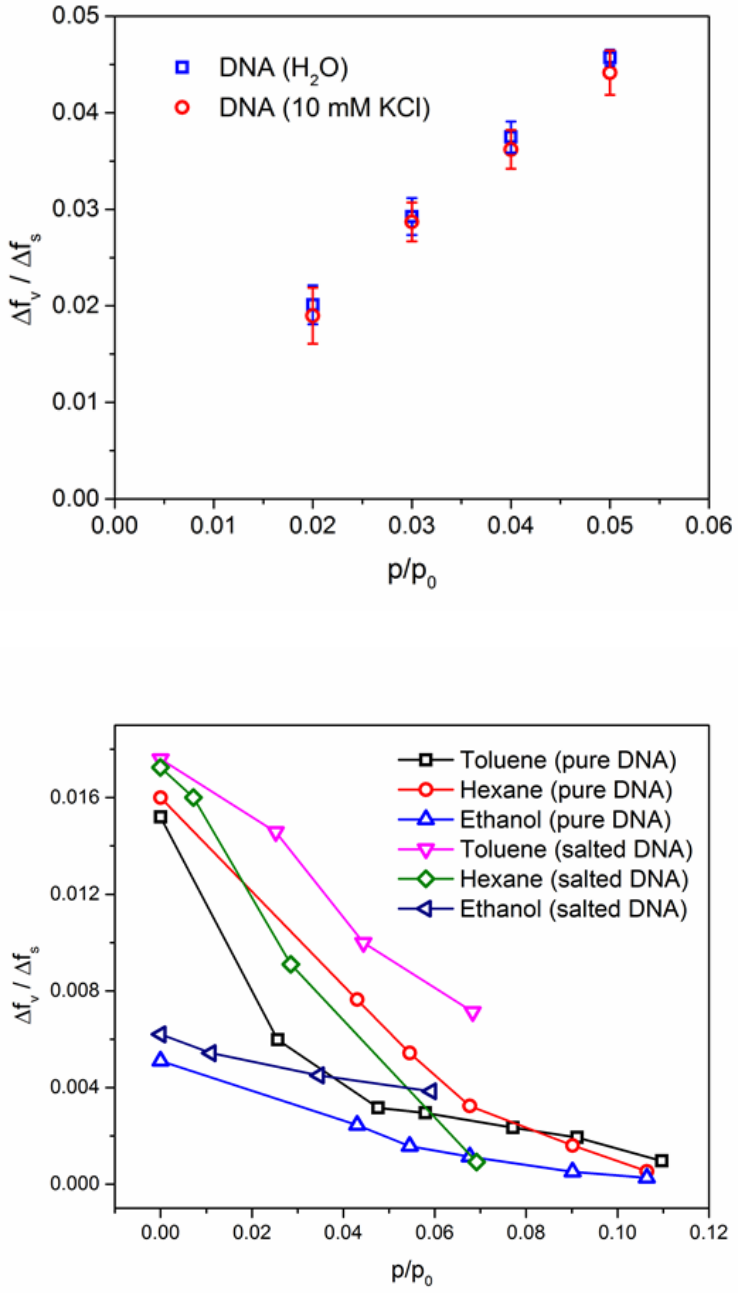

Figure 3.7 (a) Response of DNA-coated QCM crystals to water vapors in the range $p/p_0 = 0$ to 0.06; (b)Response of DNA-coated QCM crystals to selected organic vapors of concentration $p/p_0 = 0.05$ under increasing concentration of water vapor $p/p_0 = 0$ to 0.12

Table 3.2 summarizes sensitivity and limits of detection (LODs) for DNA-coated QCM sensors and QCM sensors with synthetic polymer coatings. Overall, DNA-QCM sensors have sensitivities intermediate to reported polymer-coated sensors, in the range of 10^{-6} $ppmv^{-1}$ to 10^{-5} $ppmv^{-1}$. For polymer-based sensors, the corresponding range is 10^{-6} $ppmv^{-1}$ to 10^{-3} $ppmv^{-1}$, covering three orders of magnitude. The highest sensitivity is found for polysiloxane materials while the lower end is characteristic of carbon-based polymers. DNA oligomer sensitivity values are comparable to polymers with carbon backbones. Of special interest is molecularly imprinted PIB, which has a sensitivity of 59.0×10^{-6} $ppmv^{-1}$ for toluene, an order of magnitude higher than other carbon-based polymers. This polymer is engineered to have site-selective sorption properties that attempt to mimic host-guest interactions.[13] For the other vapors, DNA oligomers exhibit higher sensitivity to n-hexane and 1-propanol but similar sensitivity to toluene and chloroform relative to the other carbon based polymers. The sensitivity to polar vapors reflects the amphiphilic nature of solid-state DNA.

Table 3.2 Sensitivity and Limits of Detection of DNA-coated QCM sensors compared to polymer-coated QCM sensors for selected VOCs

	Sensitivity[a] ($\times 10^{-6}$ ppmv^{-1})				LOD[b] (ppmv)			
	Toluene	n-Hexane	2-Propanol	Chloroform	Toluene	n-Hexane	2-Propanol	Chloroform
$(dA)_{25}$	9.9	2.3	3.2	1.7	24.7	166.2	120.4	143.7
$(dT)_{25}$	11.2	2.3	3.0	1.7	34.2	89.6	69.4	228.0
$(dC)_{25}$	14.0	2.4	3.2	2.0	31.6	99.8	76.1	226.2
$(dA)_{10}$	13.0	2.3	2.6	2.2	22.0	191.8	168.9	128.1
$(dA)_{50}$	11.3	2.4	2.9	2.2	8.7	104.2	84.5	44.0
24A (H_2O)	10.9	2.1	2.6	1.7	27.7	143.5	115.4	179.5
24L (H_2O)	11.4	2.2	2.0	1.7	24.9	129.4	140.9	168.7
27A (H_2O)	14.5	2.8	3.2	1.1	14.1	73.2	89.5	180.2
27L (H_2O)	12.4	3.1	3.3	1.2	19.4	77.4	29.8	202.5
24A (10 mM KCl)	13.7	2.2	3.0	1.8	7.1	44.4	101.5	55.5
24L (10 mM KCl)	13.0	2.1	3.4	1.8	8.5	52.7	99.7	63.4
27A (10 mM KCl)	14.7	2.8	2.9	2.0	9.8	51.7	49.0	72.6
27L (10 mM KCl)	14.8	2.9	3.3	2.0	10.1	52.0	27.4	75.7
PIB [c]	3.5	1.1	0.9	1.2	97.7	109.1	129.0	285.0
PEG [c]	1.4	0.2	0.4	2.0	60.9	631.6	285.7	42.6
PTh [59]	0.6	-	-	-	684.9	-	-	-
P3DTh [59]	1.0	-	-	-	60.6	-	-	-
PIB [13, 70]	8.6	0.7	0.1	-	174.4	101.8	89.5	-
PIB (MIP) [13]	59.0	-	-	-	10.2	-	-	-
PBD [75]	9.9	-	-	-	43.5	-	-	-
PS [75]	8.6	-	-	-	50.0	-	-	-
PDCPZ [76]	2.0	14.9	-	-	750	100.7	-	-
PS-264 [14]	-	-	654.9	131.0	-	-	2.3	11.5
PDDS [51]	-	-	428.6	43.5	-	-	3.5	34.5
PHMS [51]	-	-	711.1	184.5	-	-	2.1	8.1
PDMS [77]	300.0	-	-	243.5	2.1	-	-	6.2

[a] Defined as slope of $\Delta f_v/\Delta f_s$ against concentration in ppmv

[b] Defined as 3×noise divided by sensitivity in units of ppmv, $LOD = \frac{3\times(\Delta f_{noise}/\Delta f_s)}{sensitivity}$

[c] Used in current study as control samples

PIB: poly(isobutylene), PEG: poly(ethyleneglycol), PTh: polythiophene, P3DTh: poly(3-dodecylthiophene)
PIB (MIP): molecularly-imprinted poly(isobutylene), PDMS: polydimethylsiloxane, PBD: polybutadiene
PS: polystyrene, PDCPZ: poly(dich1orophosphazene)
PS-264: Copolymer of 92–96% polydimethylsiloxane, 3–7% diphenylsiloxane and 0.5–1% methylvinylsiloxan,
PDDS: poly(dimethyldiphenyl)siloxane, PMHS: poly(methylhydrosiloxane)

3.3.4 Chemical properties of solid-state DNA

LSER analysis is useful to characterize the chemical properties of sensor materials. The LSER coefficients of DNA with their corresponding standard errors (SEs) are plotted as a column chart in Figure 3.8. Table 3.3 shows LSER coefficients for 7 DNA oligomers determined using a set of 20 organic vapors, with multiple linear regression coefficients for each fitting $R^2 > 0.95$. Because water vapor is known to have gas-phase aggregation that leads to biased equilibrium constants, water vapor was excluded from the LSER fitting in this study, as has been the case in many previous works.[1, 7, 53, 78, 79] LSER coefficients for a number of conventional polymers are included for comparison and displayed on the same scale in Figure 3.9. Equilibrium constants (*K*) used for LSER fitting are included in Table 3.4.

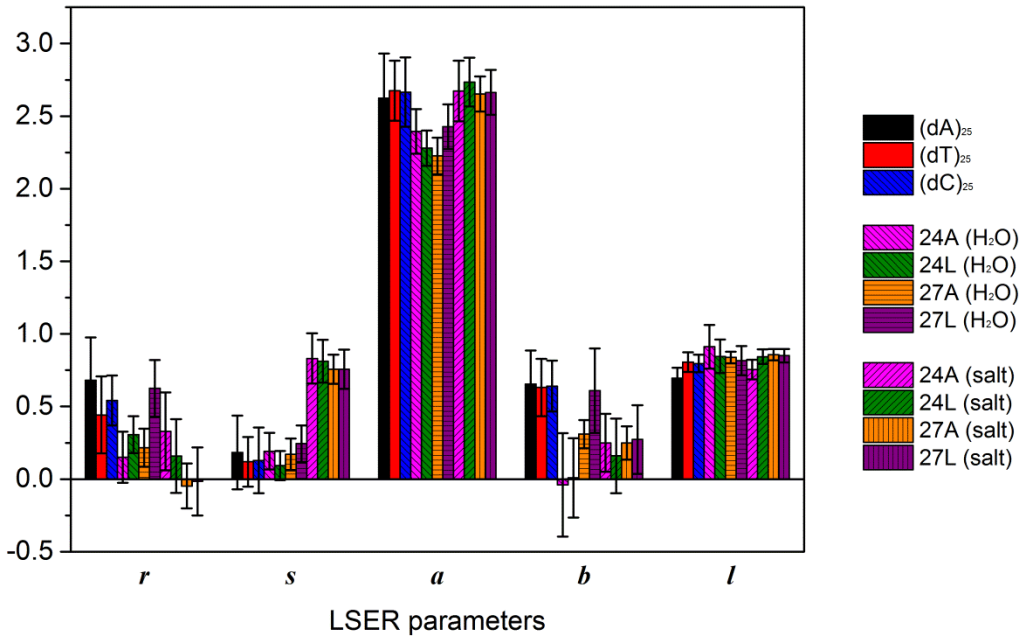

Figure 3.8 LSER parameters of 7 DNA oligomers: $(dA)_{25}$, $(dT)_{25}$, $(dC)_{25}$, 24A, 24L, 27A, 27L prepared in water; and 24A, 24L, 27A, 27L prepared in 10 mM KCl solution.

Table 3.3 LSER coefficients for 7 DNAs and synthetic polymers

	r	***s***	***a***	***b***	***l***
$(dA)_{25}$	0.68	0.18	2.62	0.66	0.70
$(dT)_{25}$	0.44	0.12	2.68	0.63	0.81
$(dC)_{25}$	0.54	0.13	2.67	0.64	0.80
24A (H_2O)	0.40	0.07	2.39	0.13	0.82
24L (H_2O)	0.31	0.09	2.28	0.01	0.85
27A (H_2O)	0.22	0.17	2.23	0.31	0.84
27L (H_2O)	0.63	0.24	2.43	0.61	0.82
24A (10 mM KCl)	0.33	0.83	2.67	0.25	0.76
24L (10 mM KCl)	0.16	0.81	2.73	0.16	0.84
27A (10 mM KCl)	-0.05	0.76	2.65	0.25	0.86
27L (10 mM KCl)	-0.02	0.76	2.66	0.27	0.85
PDMS	-0.05	0.21	0.99	0.10	0.84
PMCPS	0.02	1.65	2.71	0.38	0.72
PMPS	-0.03	0.97	1.11	0.10	0.86
PMAPS	-0.23	0.97	1.99	0.24	0.83
PMiPCAS	-0.16	0.79	2.36	0.28	0.77
CSVAL	0.05	0.23	2.22	0.46	0.85
PIB	-0.08	0.28	1.47	0.42	0.96
PEI	-0.96	1.33	2.78	0.50	0.79
PEM	0.12	1.79	2.59	1.58	0.68
PECH	0.44	1.14	1.49	1.30	0.55
PVTD	-0.01	0.60	2.42	0.60	0.94
FPOL	-0.67	1.46	1.87	2.76	0.79
SIL	0.19	1.68	2.90	1.40	0.57
OV-275	-0.12	1.77	2.48	1.23	0.50
OV-25	0.30	0.79	0.75	0.67	0.66
fullerene	-0.24	0.72	1.04	0.00	0.48
graphite	-0.27	0.86	0.94	0.00	0.46

Table 3.4 *K* values of DNA measured on QCM

	$(dA)_{25}$	$(dT)_{25}$	$(dC)_{25}$
cyclohexanone	1.30E+04	7.56E+03	1.02E+04
triethylamine	1.27E+03	1.04E+03	2.00E+03
anisole	3.22E+04	1.69E+04	1.16E+04
1-butanol	8.71E+03	6.20E+03	6.94E+03
1-pentanol	2.33E+04	1.54E+04	1.74E+04
1-propanol	5.55E+03	4.27E+03	2.48E+03
styrene	1.48E+04	1.12E+04	1.04E+04
butyraldehyde	9.89E+02	5.03E+02	3.82E+02
toluene	6.38E+03	3.46E+03	2.70E+03
acetonitrile	1.36E+03	5.67E+02	2.10E+02
n-hexane	7.75E+02	6.36E+02	2.66E+02
chloroform	3.83E+03	2.01E+03	9.58E+02
ethanol	3.60E+03	1.51E+03	9.21E+02
methanol	1.69E+03	1.08E+03	5.34E+02
2-propanol	1.78E+03	1.66E+03	1.27E+03
dichloromethane	1.69E+03	7.99E+02	3.10E+02
cyclohexane	1.06E+03	4.92E+02	6.90E+02
diethylether	1.41E+03	8.18E+02	8.53E+02
heptane	8.24E+02	7.13E+02	6.72E+02
tetrahydrofuran	3.51E+02	2.19E+02	1.77E+02

	24A	24L	27A	27L
cyclohexanone	5.46E+03	5.19E+03	1.31E+04	1.29E+04
triethylamine	9.41E+02	7.45E+02	1.56E+03	1.24E+03
anisole	2.61E+04	2.16E+04	2.35E+04	2.65E+04
1-butanol	6.07E+03	4.30E+03	7.96E+03	7.00E+03
1-pentanol	2.03E+04	1.54E+04	2.31E+04	2.08E+04
1-propanol	1.70E+03	1.38E+03	3.30E+03	2.64E+03
styrene	1.57E+04	1.31E+04	1.78E+04	1.93E+04
butyraldehyde	7.95E+02	6.47E+02	9.20E+02	9.60E+02
toluene	3.98E+03	4.18E+03	6.64E+03	3.41E+03
acetonitrile	2.29E+02	1.98E+02	3.62E+02	2.91E+02
n-hexane	8.19E+02	8.58E+02	1.10E+03	3.09E+02
chloroform	4.87E+02	4.77E+02	7.26E+02	7.48E+02
ethanol	7.26E+02	5.30E+02	9.63E+02	9.34E+02
methanol	3.91E+02	2.74E+02	4.93E+02	5.18E+02
2-propanol	1.47E+03	1.13E+03	1.79E+03	1.84E+03
dichloromethane	4.02E+02	3.18E+02	3.83E+02	2.19E+02
cyclohexane	1.49E+03	1.32E+03	1.62E+03	1.56E+03
diethylether	4.74E+02	7.52E+02	1.41E+03	1.16E+03
heptane	1.01E+03	1.54E+03	2.00E+03	7.97E+02
tetrahydrofuran	4.37E+02	3.94E+02	6.01E+02	3.98E+02

	24A (10 mM KCl)	24L (10 mM KCl)	27A (10 mM KCl)	27L (10 mM KCl)
cyclohexanone	1.59E+04	1.21E+04	1.19E+04	1.53E+04
triethylamine	1.25E+03	9.49E+02	8.62E+02	1.07E+03
anisole	3.02E+04	2.32E+04	2.03E+04	2.47E+04
1-butanol	4.49E+03	3.46E+03	6.86E+03	9.14E+03
1-pentanol	1.99E+04	1.49E+04	1.52E+04	1.83E+04
1-propanol	1.65E+03	1.12E+03	1.78E+03	2.29E+03
styrene	1.31E+04	9.56E+03	9.96E+03	1.29E+04
butyraldehyde	9.14E+02	6.80E+02	7.46E+02	9.43E+02
toluene	3.37E+03	2.56E+03	2.64E+03	3.31E+03
acetonitrile	7.67E+02	5.12E+02	3.95E+02	5.01E+02
n-hexane	2.52E+02	2.13E+02	2.87E+02	3.45E+02
chloroform	1.57E+03	1.11E+03	1.12E+03	1.41E+03
ethanol	1.06E+03	6.17E+02	7.09E+02	9.19E+02
methanol	6.72E+02	3.53E+02	3.80E+02	4.98E+02
2-propanol	1.93E+03	1.44E+03	9.12E+02	1.18E+03
dichloromethane	6.88E+02	4.60E+02	3.98E+02	5.01E+02
cyclohexane	6.94E+02	5.38E+02	5.93E+02	7.26E+02
diethylether	1.32E+03	9.26E+02	8.51E+02	1.07E+03
heptane	5.65E+02	5.20E+02	7.77E+02	9.28E+02
tetrahydrofuran	7.85E+02	7.47E+02	1.02E+03	1.23E+03

The LSER method allows classification of chemical interactions in reversible sorption processes. As acoustic and gas-liquid chromatography (GLC) methods yield somewhat different LSER coefficients,[52] literature reports of material properties from QCM or SAW sensors are used for more direct comparison. In general, hydrogen bonding basicity (*a*) and dispersion interactions (*l*) are found to be the dominant types of interaction across the different DNA oligomers.

LSER parameters for DNA are within the range of synthetic polymers. The dispersion parameter (*l*) is approximately equal to most of the siloxane-type polymers listed, in the range of 0.7 to 0.85, and stronger than carbon-based polymers. The comparison shows that DNA has relatively large free volume for vapor sorption. This property likely arises from the short strands and relatively loose chain entanglement of DNA. The sizeable dispersion interaction explains the readiness of DNA to absorb non-polar vapors. The hydrogen bonding basicity ranges from 2.2 to

2.7 and is larger than the non-polar polymers, including PDMS, PIB, OV-25, fullerene, and graphite, but weaker than the more polar polymers exemplified by PEI, PEM, and SIL. The later have H-bonding amine and carbonyl groups, which are also present on the nucleobases of DNA materials. The relatively weak hydrogen bonding acidity (*b*), ranging from 0 to 0.7, is similar to most of the siloxane and carbon-based polymers. Only highly polar PEM, FPOL, SIL, and OV-275 have stronger hydrogen bonding donating ability than DNA.

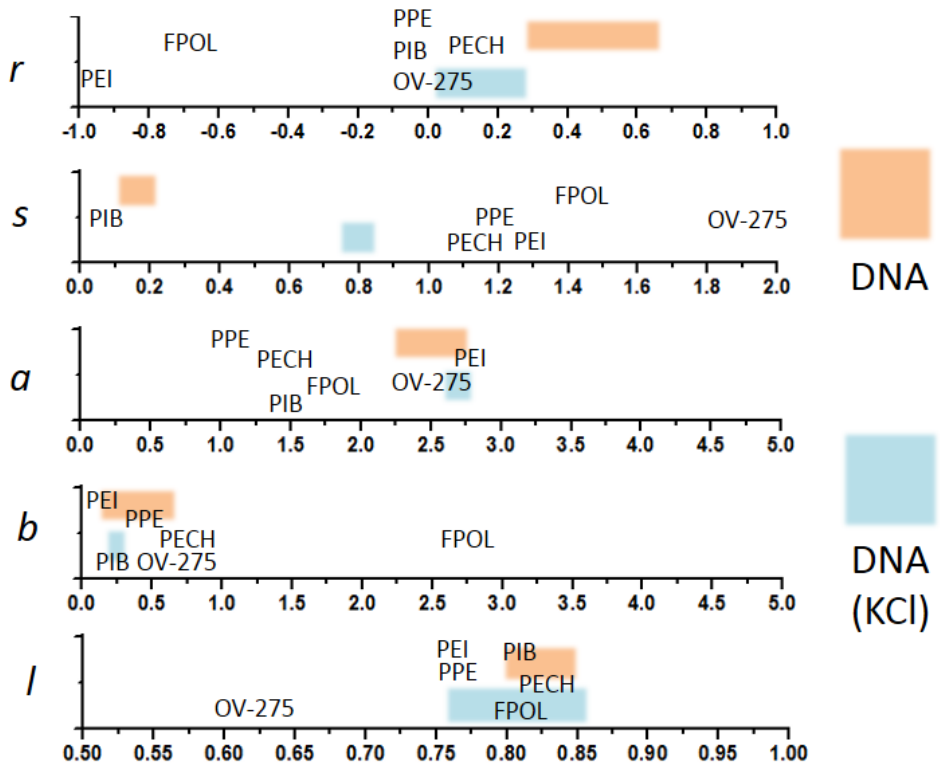

Figure 3.9 Comparison of DNA LSER with other common polymers

The positive polarization term (*r*) could be a result of heavy phosphorous atoms in the DNA backbone structure. For DNA, the r term is in the range of 0.2 to 0.7, while conventional polymers range from negative values to 0.44. In terms of dipolarity/ polarizability coefficient (*s*), DNA is relatively weak. In fact, DNA is on the order of the least dipolar polymers (PDMS, PIB, and CSVAL). This trend is surprising because DNA has plenty of polar bonds. The (*s*) coefficient is also the most obvious difference between DNA prepared in water and salt solution. The dipolar/ polarizability term is significantly larger for DNA prepared in salt solutions. In general, smaller polarizability (*R*), higher dipolarity (*s*), slightly higher hydrogen bonding basicity (*a*), and slightly weaker acidity (*b*) are observed for DNA prepared with 10 mM KCl as compared to DNA prepared in water. These LSER parameters can be used to understand the chemical origins of the trends reflected in Figure 3.6(c) and Figure 3.6(d).

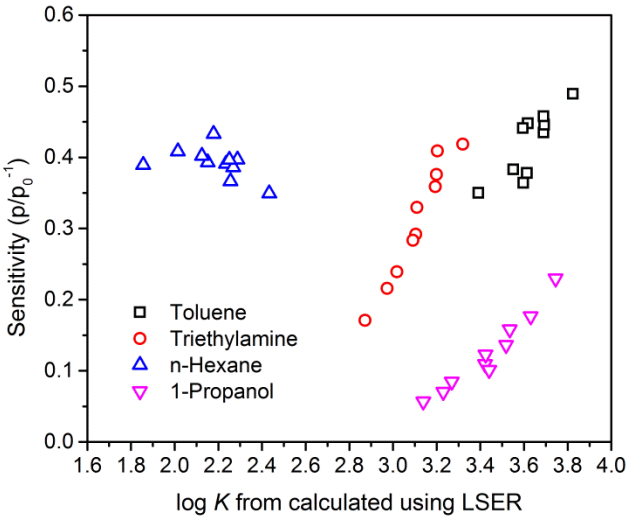

Figure 3.10 Plot of experimentally measured sensitivity values (p/p_0^{-1}) against LSER-calculated log *K* values on 4 selected vapors for a set of DNA sequences.

Figure 3.10 presents LSER-calculated K values using LSER coefficients plotted against experimentally measured sensitivity values (Figure 3.6(c), (d)). The trend for triethylamine, 1-propanol, and toluene are linear, exhibiting visual correlation between LSER-calculated log *K* values and the QCM-measured vapor sensitivity. The clustering of points for n-hexane reflects the similarity of the dispersion interaction for all of the DNA sequences since dispersion is the major term for n-hexane sorption. Hexane has zero R_2, π_2^H, $\sum \alpha_2^H$, and $\sum \beta_2^H$ values and the only non-zero term is the $\log L^{16}$term, therefore, as the dispersion (*l*) terms are very similar, the hexane sensitivity is expected to be similar. Other vapors, due to multiple non-zero LSER parameters, give more complex sensitivity patterns on these DNAs. For trimethylamine, $\sum \alpha_2^H = 0$, and since the dispersion terms (*l*) are similar for all sequences (Table 3.1), *r*, *s* and *b*, play equally important roles in determining the overall *K*. Salted 27A, 27L, 24A, and 24L have higher *s* (~ 0.8), moderate *r* (0 to 0.3), and small *b* (~ 0.2), whereas homo-polymers $(dA)_{25}$, $(dT)_{25}$, and $(dC)_{25}$ have low *s* (~ 0.2), higher *r* (0.5 to 0.7), and larger *b* (~ 0.7). No single parameter explains the variation. For 1-propanol all terms are non-zero ($R_2 = 0.236$, $\pi_2^H = 0.42$, $\sum \alpha_2^H = 0.37$, $\sum \beta_2^H = 0.48$, $\log L^{16} = 2.031$), but the *a* parameter dominates due to its larger magnitude (Table 3.3). Therefore, a generally decreasing trend is seen for vapor sensitivity from $(dA)_{25}$, $(dT)_{25}$, $(dC)_{25}$ to 27A, 27L, 24A, 24L. For toluene ($R_2 = 0.601$, $\pi_2^H = 0.52$, $\sum \alpha_2^H = 0$, $\sum \beta_2^H = 0.14$, $\log L^{16} = 3.325$), the π_2^H term is important, and increased sensitivity for salted DNA oligomers can be related to the larger *s* parameters. For many vapors, variations of sensitivity are not attributed to a single LSER parameter, but rather a combination of *r*, *s*, *a*, and *b*.

3.4 Conclusions

In this study, we demonstrate the use of mass-based sorption measurements with solid-state DNA oligomers for vapor sensing. DNA is promising as a sensing material due to the potential for complex three-dimensional secondary structures that enhance specificity for chemical sensing. We find that DNA has similar sensing properties to synthetic polymers including rate of response, reversibility, selectivity, and limits of detection. DNA has amphiphilic character with significant sorption of both polar and non-polar vapors. Sequences of the same nucleobase composition show similar selectivity, whereas sequences of different compositions show reproducible differences. LSER analysis of the sorption for 20 diverse vapors provides a quantitative basis for classifying the selectivity of different sequences as well as the effects of salt solutions on preparation. For the limited set of DNA sequences investigated, differences appear to be related to composition rather than secondary structures such as loops and/or base stacking motifs. Identification of secondary structure and their influence on selectivity may require experiments with more specifically designed aptamers for vapor analytes.

3.5 References

1. Hierlemann, A.; Zellers, E. T.; Ricco, A. J. Use of Linear Solvation Energy Relationships for Modeling Responses from Polymer-Coated Acoustic-Wave Vapor Sensors. *Anal. Chem.* **2001**, 73, 3458-3466.

2. Harsanyi, G. *Polymer Films in Sensor Applications*. Taylor & Francis: **1995**.

3. Ho, C. K.; Itamura, M. T.; Kelley, M.; Hughes, R. C. *Review of chemical sensors for in-situ monitoring of volatile contaminants*; Sandia National Laboratories: Albuquerque, 2001; pp 1-34.

4. Doleman, B. J.; Lonergan, M. C.; Severin, E. J.; Vaid, T. P.; Lewis, N. S. Quantitative Study of the Resolving Power of Arrays of Carbon Black−Polymer Composites in Various Vapor-Sensing Tasks. *Anal. Chem.* **1998**, 70, 4177-4190.

5. Wang, C.; Chen, F.; He, X.-w.; Kang, S.-z.; You, C.-c.; Liu, Y. Cyclodextrin derivative-coated quartz crystal microbalances for alcohol sensing and application as methanol sensors. *Analyst* **2001**, 126, 1716-1720.

6. Bachar, N.; Liberman, L.; Muallem, F.; Feng, X.; Müllen, K.; Haick, H. Sensor Arrays Based on Polycyclic Aromatic Hydrocarbons: Chemiresistors versus Quartz-Crystal Microbalance. *ACS Appl. Mater. Interfaces* **2013**, 5, 11641-11653.

7. Grate, J. W.; Abraham, M. H.; Du, C. M.; McGill, R. A.; Shuely, W. J. Examination of Vapor Sorption by Fullerene, Fullerene-Coated Surface Acoustic Wave Sensors, Graphite, and Low-Polarity Polymers Using Linear Solvation Energy Relationships. *Langmuir* **1995**, 11, 2125-2130.

8. Penza, M.; Cassano, G.; Aversa, P.; Cusano, A.; Cutolo, A.; Giordano, M.; Nicolais, L. Carbon nanotube acoustic and optical sensors for volatile organic compound detection. *Nanotechnology* **2005**, 16, 2536.

9. Yao, Y.; Chen, X.; Guo, H.; Wu, Z. Graphene oxide thin film coated quartz crystal microbalance for humidity detection. *Appl. Surf. Sci.* **2011**, 257, 7778-7782.

10. Schnorr, J. M.; van der Zwaag, D.; Walish, J. J.; Weizmann, Y.; Swager, T. M. Sensory Arrays of Covalently Functionalized Single-Walled Carbon Nanotubes for Explosive Detection. *Adv. Funct. Mater.* **2013**, 23, 5285-5291.

11. Tseng, M.-C.; Chu, Y.-H. Chemoselective gas sensing ionic liquids. *Chem. Commun.* **2010**, 46, 2983-2985.

12. Hirsch, T.; Kettenberger, H.; Wolfbeis, O. S.; Mirsky, V. M. A simple strategy for preparation of sensor arrays: molecularly structured monolayers as recognition elements. *Chem. Commun.* **2003**, 432-433.

13. Fu, Y.; Finklea, H. O. Quartz Crystal Microbalance Sensor for Organic Vapor Detection Based on Molecularly Imprinted Polymers. *Anal. Chem.* **2003**, 75, 5387-5393.

14. Zhang, S.; Chen, Z. K.; Bao, G. W.; Li, S. F. Y. Organic vapor detection by quartz crystal microbalance modified with mixed multilayer Langmuir–Blodgett Films. *Talanta* **1998**, 45, 727-733.

15. Grate, J. W. A Sorptive Behavior of Monolayer-Protected Gold Nanoparticle Films Containing Alkanethiols and Alkanedithiols. *Anal. Chem.* **2003**, 75, 6759-6759.

16. Steinecker, W. H.; Rowe, M. P.; Zellers, E. T. Model of Vapor-Induced Resistivity Changes in Gold−Thiolate Monolayer-Protected Nanoparticle Sensor Films. *Analytical Chemistry* **2007**, 79, 4977-4986.

17. Lu, C.; Czanderna, A. W. *Applications of Piezoelectric Quartz Crystal Microbalances*. Elsevier Science: **1984**.

18. Abraham, M. H.; Whiting, G. S.; Doherty, R. M.; Shuely, W. J. Hydrogen bonding : XV. A new characterisation of the McReynolds 77-stationary phase set. *J. Chromatogr. A* **1990**, 518, 329-348.

19. Janák, K.; Horká, M.; Tesařík, K. Effect of repeated cross-linking of SE-54 stationary phase film on the chromatographic properties of capillary columns. *J. Chromatogr. A* **1989**, 471, 237-244.

20. Nagraj, N.; Slocik, J. M.; Phillips, D. M.; Kelley-Loughnane, N.; Naik, R. R.; Potyrailo, R. A. Selective sensing of vapors of similar dielectric constants using peptide-capped gold nanoparticles on individual multivariable transducers. *Analyst* **2013**, 138, 4334-4339.

21. McAlpine, M. C.; Agnew, H. D.; Rohde, R. D.; Blanco, M.; Ahmad, H.; Stuparu, A. D.; Goddard, W. A.; Heath, J. R. Peptide−Nanowire Hybrid Materials for Selective Sensing of Small Molecules. *J. Am. Chem. Soc.* **2008**, 130, 9583-9589.

22. Panigrahi, S.; Sankaran, S.; Mallik, S.; Gaddam, B.; Hanson, A. A. Olfactory receptor-based polypeptide sensor for acetic acid VOC detection. *Mater. Sci. Eng., C* **2012**, 32, 1307-1313.

23. Goldsmith, B. R.; Mitala, J. J.; Josue, J.; Castro, A.; Lerner, M. B.; Bayburt, T. H.; Khamis, S. M.; Jones, R. A.; Brand, J. G.; Sligar, S. G.; Luetje, C. W.; Gelperin, A.; Rhodes, P. A.; Discher, B. M.; Johnson, A. T. C. Biomimetic Chemical Sensors Using Nanoelectronic Readout of Olfactory Receptor Proteins. *ACS Nano* **2011**, 5, 5408-5416.

24. Yano, K.; Yoshitake, H.; Bornscheuer, U. T.; Schmid, R. D.; Ikebukuro, K.; Yokoyama, K.; Masuda, Y.; Karube, I. Development of a chemical vapor sensor using piezoelectric quartz crystals with coated unusual lipids. *Anal. Chim. Acta* **1997**, 340, 41-48.

25. Wyszynski, B.; Somboon, P.; Nakamoto, T. In *PEG Lipopolymers as Coatings for QCM Odor Sensors. Effect of Tether's Chain-length*, Sensors, 2006. 5th IEEE Conference on, 22-25 Oct. 2006; **2006**; pp 456-459.

26. Kybert, N. J.; Lerner, M. B.; Yodh, J. S.; Preti, G.; Johnson, A. T. C. Differentiation of Complex Vapor Mixtures Using Versatile DNA–Carbon Nanotube Chemical Sensor Arrays. *ACS Nano* **2013**, 7, 2800-2807.

27. Fu, K.; Li, S.; Jiang, X.; Wang, Y.; Willis, B. G. DNA Gold Nanoparticle Nanocomposite Films for Chemiresistive Vapor Sensing. *Langmuir* **2013**, 29, 14335-14343.

28. Staii, C.; Johnson, A. T.; Chen, M.; Gelperin, A. DNA-Decorated Carbon Nanotubes for Chemical Sensing. *Nano Letters* **2005**, 5, 1774-1778.

29. Lu, Y.; Goldsmith, B. R.; Kybert, N. J.; Johnson, A. T. C. DNA-decorated graphene chemical sensors. *Applied Physics Letters* **2010**, 97, 083107.

30. Samain, F.; Ghosh, S.; Teo, Y. N.; Kool, E. T. Polyfluorophores on a DNA Backbone: Sensors of Small Molecules in the Vapor Phase. *Angewandte Chemie International Edition* **2010**, 49, 7025-7029.

31. Kybert, N.; Han, G.; Lerner, M.; Dattoli, E.; Esfandiar, A.; Charlie Johnson, A. T. Scalable arrays of chemical vapor sensors based on DNA-decorated graphene. *Nano Res.* **2014**, 7, 95-103.

32. White, J.; Truesdell, K.; Williams, L. B.; AtKisson, M. S.; Kauer, J. S. Solid-State, Dye-Labeled DNA Detects Volatile Compounds in the Vapor Phase. *PLoS Biol* **2008**, 6, e9.

33. Kwak, J.; Gallagher, M.; Ozdener, M. H.; Wysocki, C. J.; Goldsmith, B. R.; Isamah, A.; Faranda, A.; Fakharzadeh, S. S.; Herlyn, M.; Johnson, A. T. C.; Preti, G. Volatile biomarkers from human melanoma cells. *J. Chromatogr. B* **2013**, 931, 90-96.

34. Liu, Y.; Chen, M.; Wang, M. L.; Dokmeci, M. R. RNA functionalized singled-walled carbon nanotube devices for chemical sensing. *Appl. Phys. Lett.* **2013**, 103, -.

35. Alberts, B. *Molecular Biology of the Cell: Reference edition*. Garland Science: **2008**.

36. Cricenti, A.; Selci, S.; Felici, A.; Generosi, R.; Gori, E.; Djaczenko, W.; Chiarotti, G. Molecular structure of DNA by scanning tunneling microscopy. *Science* **1989**, 245, 1226-1227.

37. Beebe, T.; Wilson, T.; Ogletree, D.; Katz, J.; Balhorn, R.; Salmeron, M.; Siekhaus, W. Direct observation of native DNA structures with the scanning tunneling microscope. *Science* **1989**, 243, 370-372.

38. Arscott, P. G.; Lee, G.; Bloomfield, V. A.; Evans, D. F. Scanning tunnelling microscopy of Z-DNA. *Nature* **1989**, 339, 484-486.

39. Driscoll, R. J.; Youngquist, M. G.; Baldeschwieler, J. D. Atomic-scale imaging of DNA using scanning tunnelling microscopy. *Nature* **1990**, 346, 294-296.

40. Tanaka, H.; Kawai, T. Partial sequencing of a single DNA molecule with a scanning tunnelling microscope. *Nat. Nanotechnol.* **2009**, 4, 518-522.

41. Amrein, M.; Durr, R.; Stasiak, A.; Gross, H.; Travaglini, G. Scanning tunneling microscopy of uncoated recA-DNA complexes. *Science* **1989**, 243, 1708-1711.

42. Roger-Eitan, I.; Liu, K.; Livshits, G. I.; Borovok, N.; Rotem, D.; Kotlyar, A. B.; Porath, D. High-Resolution Scanning Tunneling Microscopy Imaging of Biotin–Avidin–G4-DNA Molecules. *J. Phys. Chem. C* **2013**, 117, 22462-22465.

43. Cho, E. J.; Lee, J.-W.; Ellington, A. D. Applications of Aptamers as Sensors. *Annual Review of Analytical Chemistry* **2009**, 2, 241-264.

44. Lee, J.-O.; So, H.-M.; Jeon, E.-K.; Chang, H.; Won, K.; Kim, Y. Aptamers as molecular recognition elements for electrical nanobiosensors. *Anal Bioanal Chem* **2008**, 390, 1023-1032.

45. Yu, Y.; Cao, Q.; Zhou, M.; Cui, H. A novel homogeneous label-free aptasensor for 2,4,6-trinitrotoluene detection based on an assembly strategy of electrochemiluminescent graphene oxide with gold nanoparticles and aptamer. *Biosens. Bioelectron.* **2013**, 43, 137-142.

46. Hagen, J. A.; Kim, S. N.; Kelley-Loughnane, N.; Naik, R. R.; Stone, M. O. Selective vapor phase sensing of small molecules using biofunctionalized field effect transistors. **2011**, 80180B-80180B.

47. Han, D.; Pal, S.; Nangreave, J.; Deng, Z.; Liu, Y.; Yan, H. DNA Origami with Complex Curvatures in Three-Dimensional Space. *Science* **2011**, 332, 342-346.

48. Lin, C. H.; Patei, D. J. Structural basis of DNA folding and recognition in an AMP-DNA aptamer complex: distinct architectures but common recognition motifs for DNA and RNA aptamers complexed to AMP. *Chem. Biol.* **1997**, 4, 817-832.

49. Grate, J. W. Acoustic Wave Microsensor Arrays for Vapor Sensing. *Chemical Reviews* **2000**, 100, 2627-2648.

50. King, W. H. Piezoelectric Sorption Detector. *Analytical Chemistry* **1964**, 36, 1735-1739.

51. Zhang, S.; Li, S. F. Y. Detection of organic solvent vapours and studies of thermodynamic parameters using quartz crystal microbalance sensors modified with siloxane polymers. *Analyst* **1996**, 121, 1721-1726.

52. Grate, J. W.; Patrash, S. J.; Kaganove, S. N.; Abraham, M. H.; Wise, B. M.; Gallagher, N. B. Inverse Least-Squares Modeling of Vapor Descriptors Using Polymer-Coated Surface Acoustic Wave Sensor Array Responses. *Anal. Chem.* **2001**, 73, 5247-5259.

53. Prikryl, P.; Sevcik, J. G. K. Characterization of sorption mechanisms of solid-phase microextraction with volatile organic compounds in air samples using a linear solvation energy relationship approach. *J. Chromatogr. A* **2008**, 1179, 24-32.

54. Tian, S.; Zhu, L.; Shi, Y. Characterization of Sorption Mechanisms of VOCs with Organobentonites Using a LSER Approach. *Environmental Science & Technology* **2003**, 38, 489-495.

55. Tao, N. J.; Lindsay, S. M.; Rupprecht, A. Structure of DNA hydration shells studied by Raman spectroscopy. *Biopolymers* **1989**, 28, 1019-1030.

56. Falk, M.; Hartman, K. A.; Lord, R. C. Hydration of Deoxyribonucleic Acid. I. a Gravimetric Study. *J. Am. Chem. Soc.* **1962**, 84, 3843-3846.

57. Abraham, M. H. Scales of solute hydrogen-bonding: their construction and application to physicochemical and biochemical processes. *Chem. Soc. Rev.* **1993**, 22, 73-83.

58. Śmiałek, M. A.; Jones, N. C.; Hoffmann, S. V.; Mason, N. J. Measuring the density of DNA films using ultraviolet-visible interferometry. *Phys. Rev. E* **2013**, 87, 060701.

59. Si, P.; Mortensen, J.; Komolov, A.; Denborg, J.; Møller, P. J. Polymer coated quartz crystal microbalance sensors for detection of volatile organic compounds in gas mixtures. *Anal. Chim. Acta* **2007**, 597, 223-230.

60. Grate, J. W.; Kaganove, S. N.; Bhethanabotla, V. R. Examination of mass and modulus contributions to thickness shear mode and surface acoustic wave vapour sensor responses using partition coefficients. *Faraday Discussions* **1997**, 107, 259-283.

61. Grate, J. W.; Nelson, D. A.; Skaggs, R. Sorptive behavior of monolayer-protected gold nanoparticle films: implications for chemical vapor sensing. *Anal. Chem.* **2003**, 75, 1868-79.

62. Grate, J. W.; Patrash, S. J.; Abraham, M. H.; Du, C. M. Selective Vapor Sorption by Polymers and Cavitands on Acoustic Wave Sensors: Is This Molecular Recognition? *Analytical Chemistry* **1996**, 68, 913-917.

63. Das, R.; Pradhan, S.; Biswas, S.; Sharma, P.; Ghosh, A.; Bandyopadhyay, R.; Pramanik, P. Aliphatic amines vapours detection by quartz crystal microbalance sensor. *Sensors and Actuators B: Chemical* **2014**, 198, 94-101.

64. Ayad, M. M.; Torad, N. L. Quartz crystal microbalance sensor for detection of aliphatic amines vapours. *Sensors and Actuators B: Chemical* **2010**, 147, 481-487.

65. Patrash, S. J.; Zellers, E. T. Characterization of polymeric surface acoustic wave sensor coatings and semiempirical models of sensor responses to organic vapors. *Anal. Chem.* **1993**, 65, 2055-2066.

66. Teng, J.; Bates, S.; Engers, D. A.; Leach, K.; Schields, P.; Yang, Y. Effect of water vapor sorption on local structure of poly(vinylpyrrolidone). *J. Pharm. Sci.* **2010**, 99, 3815-3825.

67. Prodduturi, S.; Manek, R. V.; Kolling, W. M.; Stodghill, S. P.; Repka, M. A. Water vapor sorption of hot-melt extruded hydroxypropyl cellulose films: Effect on physico-mechanical properties, release characteristics, and stability. *J. Pharm. Sci.* **2004**, 93, 3047-3056.

68. Falk, M.; Poole, A. G.; Goymour, C. G. Infrared study of the state of water in the hydration shell of DNA. *Canadian Journal of Chemistry* **1970**, 48, 1536-1542.

69. Oliveira, N. S.; Gonçalves, C. M.; Coutinho, J. A. P.; Ferreira, A.; Dorgan, J.; Marrucho, I. M. Carbon dioxide, ethylene and water vapor sorption in poly(lactic acid). *Fluid Phase Equilib.* **2006**, 250, 116-124.

70. Ying, Z.; Jiang, Y.; Du, X.; Xie, G.; Yu, J.; Tai, H. Polymer coated sensor array based on quartz crystal microbalance for chemical agent analysis. *Eur. Polym. J.* **2008**, 44, 1157-1164.

71. Smith, S. E. The Sorption of Water Vapor by High Polymers. *J. Am. Chem. Soc.* **1947**, 69, 646-651.

72. Kanagy, J. R. Influence of temperature on the absorption of water vapor by collagen and leather.

73. Rodríguez-Mirasol, J.; Bedia, J.; Cordero, T.; Rodríguez, J. J. Influence of Water Vapor on the Adsorption of VOCs on Lignin‐Based Activated Carbons. *Sep. Sci. Technol.* **2005**, 40, 3113-3135.

74. Xian, S.; Yu, Y.; Xiao, J.; Zhang, Z.; Xia, Q.; Wang, H.; Li, Z. Competitive adsorption of water vapor with VOCs dichloroethane, ethyl acetate and benzene on MIL-101(Cr) in humid atmosphere. *RSC Advances* **2015**, 5, 1827-1834.

75. Kimura, M.; Liu, Y.; Sakai, R.; Sato, S.; Hirai, T.; Fukawa, T.; Mihara, T. Detection of Volatile Organic Compounds by Analyses of Polymer-Coated Quartz Crystal Microbalance Sensor Arrays. *Sensor. Mater.* **2011**, 23, 359-368.

76. Menon, A.; Haimbodi, M.; Zhou, R.; Josse, F. Polymer-coated quartz crystal resonators for multi-information sensing. *Electron. Lett* **1997**, 33, 287-289.

77. Mirmohseni, A.; Hassanzadeh, V. Application of polymer-coated quartz crystal microbalance (QCM) as a sensor for BTEX compounds vapors. *J. Appl. Polym. Sci.* **2001**, 79, 1062-1066.

78. Grate, J. W.; Patrash, S. J.; Abraham, M. H. Method for Estimating Polymer-Coated Acoustic Wave Vapor Sensor Responses. *Anal. Chem.* **1995**, 67, 2162-2169.

79. Abraham, M. H.; Whiting, G. S.; Doherty, R. M.; Shuely, W. J. Hydrogen bonding. Part 13. A new method for the characterisation of GLC stationary phases-the laffort data set. *Journal of the Chemical Society, Perkin Transactions 2* **1990**, 1451-1460.

Appendix

Procedure for preparation of 200 μM DNA solution

Lyophilized DNA supplied from IDT: 27A

DNA molar amount in shipped vial: 70 nmol

dd-H_2O added to vial make 1 mM solution = 70 μl

To make 50 μl of 200 μM DNA solution in water, take 10 μl of 1 mM solution in vial and add 40 μl dd-H_2O.

To make 50 μl of 200 μM DNA solution in 10 mM KCl, take 10 μl of 1 mM solution add 40 μl of 12.5 mM KCl stock solution in dd-H_2O.

Chapter 4

DNA GOLD NANOPARTICLE NANOCOMPOSITE FILMS FOR CHEMIRESISTIVE VAPOR SENSING

4.1 Introduction

Using biomolecules can both either enhance the library of moderately selective receptors just like the mammalian olfactory system and may also lead to highly specific detectors. The use of DNA to functionalize glass slides as fluorescence modulation sensors,[1] chemitransistors made from carbon nanotubes (CNT)[2, 3] and graphene[4], as well as nanofunctionalized organic field-effect transistors[5] are some examples for using DNA as sensing elements, though the results suggest that DNA was used in a non-specific way. As already discussed in Chapter 1, gold nanoparticle chemiresistors offer a versatile, robust, and simple electronic sensing platform. While the intrinsic sorption properties of DNA were studied by LSER model using the QCM, the properties of DNA as a component of electronic sensing devices is unknown. In this chapter, the integration of DNA with nanoparticle chemiresistors is studied.

To make effective chemiresistor devices, the first question that needs to be answered is the effect of water. For QCM studies, the sensitivity to water is evidenced by massive absorption of

water. Likewise, for electrical devices, it is anticipated that humidity may have a significant effect on DNA-based absorptive sensors. It is therefore imperative to measure the effects of humidity on such materials. Many prior studies of chemiresistor devices have used relatively hydrophobic sensing materials that are not particularly sensitive to humidity,[6, 7] but there are at least a few examples where sensitivity to water vapor has been studied.[8] Control of humidity effects in solid state DNA-based sensing has been considered in some studies,[1, 3] but the effect of water on chemiresistive vapor sensing has not been systematically studied. Therefore, our first study is to evaluate the electrical performance under the effects of water vapor.

The second study is to evaluate the effectiveness of chemiresistors to match QCM sensitivities to organic vapors. For a chemical sensor, which is inherently a system that consists of both sensor material and transducer, this is an important aspect to consider, as statistical uncertainties with these two components are expected to multiply. The last aim of this study is to investigate sensor performance under humid conditions. This study will shed light on how a hydrophilic material will perform under field conditions. However, before the sensing experiments, it is first necessary to characterize the DNA coverage on gold nanoparticles, as nanoparticles with similar ligand coverage will be more comparable in sensing experiments.

4.2 Experimental methods

4.2.1 Oligonucleotide used in this study

To maximize the differences between DNA strands used in this study, S2, $(dA)_{25}$, $(dT)_{25}$, $(dC)_{25}$, $(dA)_{10}$, and $(dA)_{50}$ have been selected for gold nanoparticle functionalization. S2, $(dA)_{25}$,

$(dT)_{25}$, and $(dC)_{25}$ were selected for their compositional differences, while $(dA)_{10}$, $(dA)_{25}$, and $(dA)_{50}$ were selected for their length differences.

Table 4.1 Thiolated DNA Oligomers for gold nanoparticle functionalization and fluorescently tagged sequence (S1) for coverage quantification

Name	Sequence (5' to 3')
S1	/Cy-5[a]/AAA AAA AAA GAG GAG GAA AAG GAG T
S2	/HS-C_6H_{12}[b]/TTT TTA CTC CTT TTC CTC CTC TTT T
$(dA)_{25}$	/HS-C_6H_{12}[b]/AAA AAA AAA AAA AAA AAA AAA AAA A
$(dT)_{25}$	/HS-C_6H_{12}[b]/TTT TTT TTT TTT TTT TTT TTT TTT T
$(dC)_{25}$	/HS-C_6H_{12}[b]/CCC CCC CCC CCC CCC CCC CCC CCC C
$(dA)_{10}$	/HS-C_6H_{12}[b]/AAA AAA AAA A
$(dA)_{50}$	/HS-C_6H_{12}[b]/AAA AAA AAA AAA AAA AAA AAA AAA AAA AAA AAA AAA AAA AAA AAA AAA AAA AA

[a] Cyanine fluorescence group

[b] Thiol functionalization group

4.2.2 Fluorescence quantification of DNA coverage on gold nanoparticles

In solution, S2 modified gold nanoparticles were studied with the aid of a fluorescence-based method [9]. After preparation of S2 modified gold nanoparticles, 100 µl of gold nanoparticle solution was washed with dd-H_2O twice by centrifugation at 15,000 *g* for 40 minutes to remove free S2 DNA. The pellet of gold nanoparticles was subsequently dispersed into 100 µl NaCl solution (100 mM). The concentration of gold nanoparticle solution was determined by measuring the absorbance at 520 nm using a UV-Vis spectrophotometer (Thermo Scientific NanoDrop ND-

1000). Afterwards, 1.5 µl of Cy5-labeled S1 (100 µM) was added to the gold nanoparticle solution to hybridize with the S2 immobilized on the gold nanoparticles. The mixture was kept in the dark with gentle shaking at room temperature for 2 hours. Two additional rounds of washing with 100mM NaCl solution were carried out, and the unhybridized S1 in the supernatant was measured after each washing step. The concentration of free S1 was determined using a fluorospectrometer (Thermo Scientific NanoDrop 3300). The quantity of S2 chemisorbed on gold nanoparticles approximately equals the amount of S1 consumed through complimentary base paring. The amount of S1 consumed due to hybridization was determined as the difference between the initial amount of S1 added and free, unhybridized S1 measured in the supernatant, summed from each of the three washings.

$$\text{DNA per AuNP} = \frac{\text{Moles}_{\text{Initial amount of S1}} - \text{Moles}_{\text{unhybridized S1}}}{\text{Moles}_{\text{AuNP}}} \qquad (4.1)$$

4.2.3 Deposition of DNA-functionalized nanoparticles on 20 µm circular electrodes

DNA-functionalized gold nanoparticle stock solutions were first removed of excess buffer salts (e.g., NaCl) through centrifugation processes. 1 ml of nanoparticle solution was subjected to centrifugation at relative centrifugation force (RCF) = 15,000 *g* for 40 minutes, the supernatant was removed, and the concentrate was re-dispersed in 1.5 ml dd-H_2O. This washing procedure was repeated twice. The final product obtained from centrifugation was suspended in 20 µl of dd-H_2O to form a DNA-functionalized gold nanoparticle concentrate. The concentrated solution for drop-casting was standardized using a UV-Vis spectrophotometer (Thermo Scientific NanoDrop ND-1000, Waltham, MA) to have absorbance = 2.5.

For drop casting, 4 µl of gold nanoparticle concentrated solution was deposited on each sensor area. The droplet readily wets the electrode areas, and was evaporated under a dry air atmosphere at room temperature. DC resistances measured in air have a resistivity in the range of 300 kΩ to 800 kΩ. Figure 4.1 gives an overview of the detailed fabrication process.

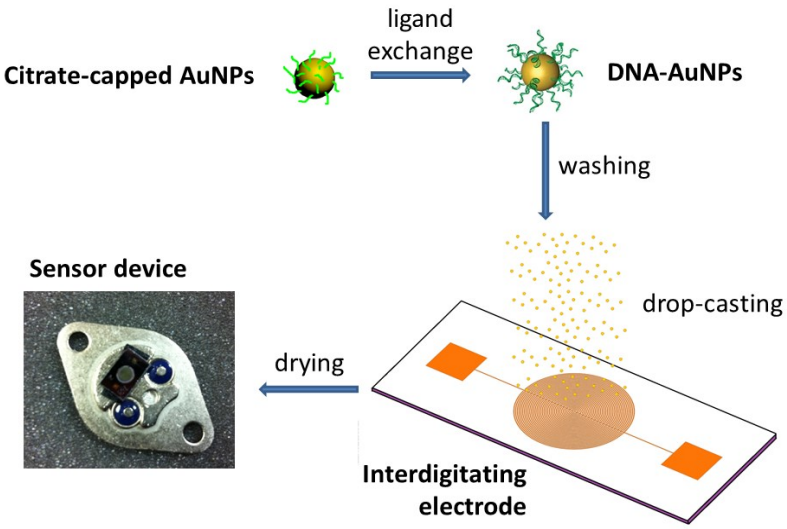

Figure 4.1 Procedure for farbicating chemiresistor sensors with DNA-functionalized gold nanoparticles

4.2.4 Characterization of sensor materials

DNA-functionalized gold nanoparticles were characterized both in solution and in dried drop-cast forms. Functionalized nanoparticles were first examined with TEM to verify the nanoparticle size and morphology. To prepare the TEM samples, 1 µl of as prepared DNA-functionalized gold nanoparticles were dropped and dried on a 300 mesh copper grid. For XPS measurement, gold nanoparticle concentrates after centrifugation and washing were drop-cast on oxygen-plasma treated indium foils before insertion in to the XPS vacuum chamber. The use of

indium foils was to reduce sample charging by the ejection photoelectrons. Surface analysis was performed on both DNA-functionalized gold nanoparticles and control nanoparticles without DNA to measure elemental composition. The DNA coverage obtained from S2 characterization was used as a reference for estimating $(dA)_{25}$, $(dT)_{25}$, and $(dC)_{25}$ coverage with XPS. IV curves were measured between 1 V and -1 V with a ramp rate of 0.1 V/s. The SMU was programmed to generate a 1.0 V_{pp} square wave at 500 Hz.

4.3 Results and discussion

4.3.1 Characterization of DNA-AuNP surface functionalization

The attachment of thiol-functionalized DNA to gold nanoparticles was apparent from visual inspection. For all sequences studied, DNA-functionalized gold nanoparticles were observed to maintain good dispersion in solution. By contrast, direct addition of Tris acetate (500 mM, pH 8.2) buffer solution to citrate-stabilized gold nanoparticles without DNA resulted in nanoparticle aggregation within a few hours. A change in solution color from light red to light purple was an indication of aggregation. These observations are consistent with superior stabilization of nanoparticles in electrolyte solutions through synergistic electrostatic and steric mechanisms.[10] Gold nanoparticles with citrate capping alone are known to be less resistant to aggregation as they are predominantly electrostatically stabilized.[11] For S2, the fluorescence-based technique shows that surface coverage is 40 (±6) DNA oligonucleotides per nanoparticle. For 10 nm diameter particles, the surface density is 1.3 x 10^{13}/cm^2, which can be compared with literature data: 5 x 10^{12}/cm^2 [12] and 3.7 x 10^{13}/cm^2 [13, 14] for 25-mers, and 1.4 x 10^{13}/cm^2 for a 15

mer.[15] Previous studies have shown that ss-DNA oligomers of 25-mer size are generally coiled structures that extend 0.7 to 1.0 nm from the particle surface.[16-18]

TEM analysis shows isolated 10 nm diameter gold nanoparticles (Figure 4.2(a)) Surface analysis was performed with XPS to verify that DNA is present on gold nanoparticle films after drop-casting and drying. Figure 4.2(b) shows measurements of nitrogen and phosphorous content for DNA-functionalized gold nanoparticles compared with control samples. Nitrogen contents of all DNA-functionalized samples were within the range of 3 ~ 4 % and phosphorous was approximately 1 %. Due to the minute amount of sulfur per molecule, no Sulfur 2p signals were observed on any sample.[13] The phosphorous signal from the DNA-functionalized gold nanoparticle films serves as direct evidence of successful DNA adsorption onto nanoparticles. No phosphorous is measured on control samples. There is a small N 1s signal from control samples that may originate from residual buffer salts, as Tris buffer also contains nitrogen. However, the DNA samples have a 3x higher N 1s signal that is consistent with DNA coverage of the gold nanoparticles. Estimates of surface coverage for $(dA)_{25}$, $(dT)_{25}$, and $(dC)_{25}$- functionalized gold nanoparticles are obtained by comparing XPS surface phosphorous percentages to S2 as a reference. Results are 42, 36, and 36 molecules/particle for $(dA)_{25}$, $(dT)_{25}$, and $(dC)_{25}$, respectively. Other elemental signatures such as C and O were not useful for distinguishing DNA and control samples.

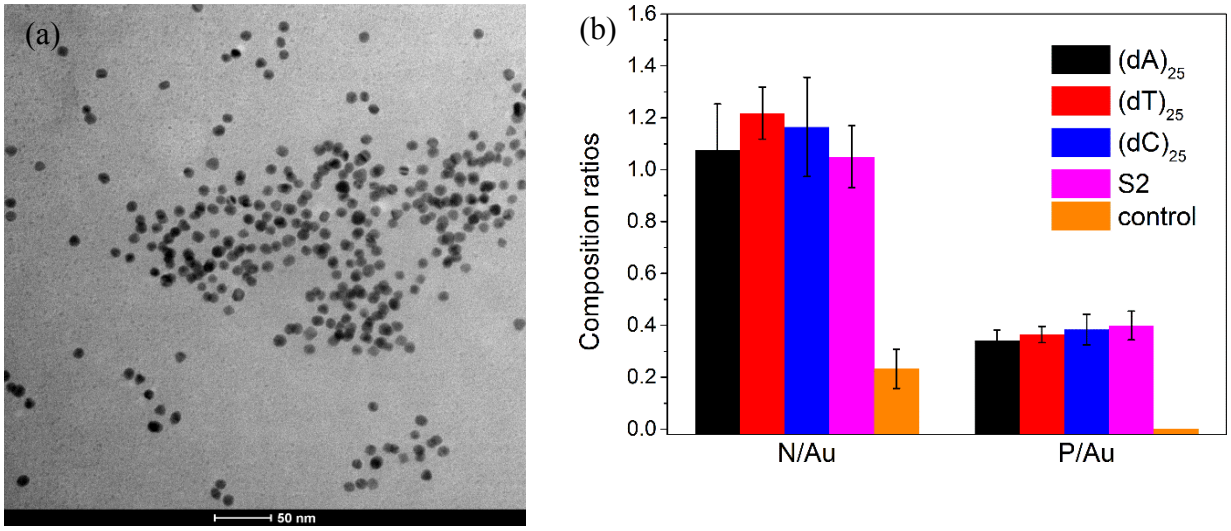

Figure 4.2 (a) TEM image of 10 nm DNA-functionalized gold nanoparticles. (b) Surface composition of nitrogen and phosphorous on DNA-functionalized gold nanoparticles compared to controls with citrate capped gold nanoparticles; control samples have no P signal.

4.3.2 Electrical properties and sensitivity to relative humidity

DNA-functionalized gold nanoparticle sensors display a distinctive dichotomous behavior in response to RH. In this study, R/R_0 is used to characterize the ratio of resistance at a specific RH to the resistance at RH = 0%, and $\Delta R/R$ is used to characterize sensor response to analytes at fixed RH. Water vapor is not treated as an analyte, but as an environmental factor that modifies the baseline resistance of the sensor at a specific RH. R_0 is the sensor baseline resistance at zero RH or in a dry atmosphere. For all sensors, R/R_0 increases from 1 at RH = 0% to around 2 at 34%, and then decreases rapidly, reaching 0.01 above RH = 50% (Figure 4.3(a)). This dichotomous behavior is atypical for nanoparticle-based chemiresistive sensors. This can be seen by comparing water vapor sensing behavior between DNA-functionalized gold nanoparticles and alkanethiol-

functionalized gold nanoparticles. To that end, 1-octanethiol and 8-mercapto-1-octanol functionalized gold nanoparticle sensors were prepared using the standard protocol by Woltjen et al.[19] and subjected to identical vapor testing conditions. The R/R_0 trends with increasing RH for these devices are shown in Figure 4.3(b). The monotonic trends are similar to previously published gold nanoparticle chemiresitive sensors with alkanethiol-type ligands.[19, 20] Similarly, studies of condensed DNA films with no nanoparticles also report monotonous resistivity trends across the RH range from 0% to 100%.[21] The distinctive behavior of DNA-gold nanoparticle films is therefore an indication that the conduction mechanism of DNA-gold nanoparticle films has contributions from both nanoparticles and the polyelectrolyte matrix.

The distinctive response of DNA gold nanoparticle devices can be understood from two separate conduction mechanisms. At low RH levels (0% to 40%), the upward trend in R/R_0 is governed predominantly by matrix-swelling effects common to gold nanoparticle chemiresistive sensors. In this RH range, the effects of ionic conduction are insignificant compared to the electronic current. At higher RH levels (40% to 100%), ionic conduction becomes significant and R/R_0 decreases. Similar effects of decreasing resistivity at higher vapor concentrations have been observed in studies of tetraoctylammonium bromide (TOAB) functionalized gold nanoparticles.[22,8] In that study, residual ionic species solvated by vapors were proposed as one possible source of increasing conductance. The difference here is that DNA intrinsically contains ionic species that may contribute to conductivity at high RH levels. Voids in the film may also contribute to ionic conduction, as water condensation on the hydrophilic SiO_2 surface under high RH levels is likely.[23]

The significant response to increasing humidity for all ss-DNA devices studied is indicative of the favorable hydration of DNA oligomers. Water is integral to DNA structure with significant interactions at both phosphate and base sites, and the hydration shell has been described as a

monolayer of water on the DNA surface area.[24] Estimates for hydrated ds-DNA are near 30 H_2O per nucleotide pair with waters strongly bound even at 0% RH.[25] Base specific interactions have been observed in crystallographic studies but these effects are complicated by structure.[26] For example, it was reported that the strength of water interaction first decreases, but then increases with increasing AT content.[24] In Figure 4.3(a) and other data, S2 has the strongest response to water even though it has significant T content and $(dT)_{25}$ has the weakest response. Further study is needed to separate base composition from sequence and structure effects.

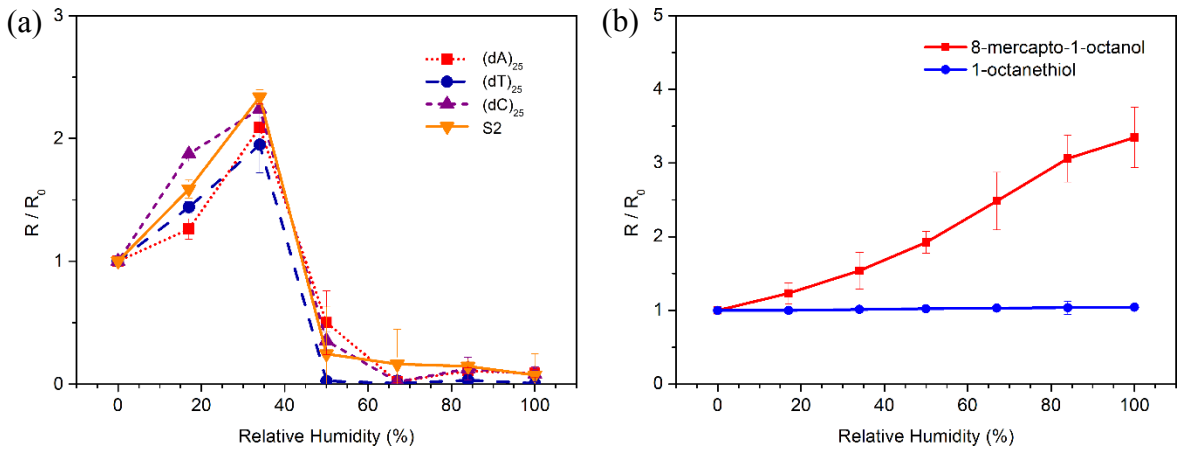

Figure 4.3 (a) Effect of RH on baseline resistance of DNA-functionalized gold nanoparticle films; (b) Effect of RH on resistance of two types of alkanethiol-functionalized gold nanoparticle films.

To further characterize the conduction mechanisms, electrochemical impedance spectroscopy (EIS) measurements were performed. The EIS results are consistent with a RH dependent conduction mechanism (Figure 4.4). At low RH levels, only a single semicircle is observed on the Nyquist plot, indicating an electron-transfer-limited process.[27] At higher RH levels of 50% for $(dA)_{25}$, a linear response appears in the low frequency region, which is

characteristic of a diffusion-limited charge transfer process. The source of this diffusion limited charge transfer is a frequency-dependent ion diffusion/transport in the polyelectrolyte (DNA).[27] As RH increases, the semicircle radius first increases and then decreases – a trend that corresponds closely with the DC resistance measured using the source measurement unit. In the range of RH from 84% to 100%, the linear portion of the curve becomes increasingly vertical, indicating increasing capacitive behavior, which confirms the dominance of ionic conduction.[28] These Nyquist plots substantially reflect the transition from electronic to ionic conduction as RH increases.

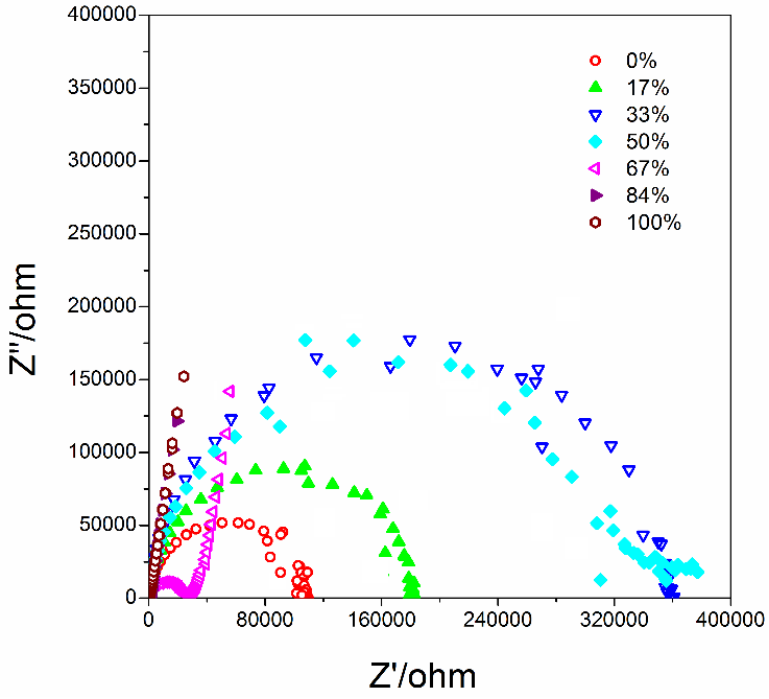

Figure 4.4 Nyquist plots recorded for $(dA)_{25}$ at RH levels 0% to 100%.

4.3.3 Vapor Sensing

4.3.3.1 Sensing under dry conditions

Responses to several organic vapors were measured at constant RH for a range of different RH conditions. For testing at RH = 0%, the relative humidity was automatically maintained as no water vapor was introduced. For testing under humid conditions, the RH is maintained by turning off the flowrate adjustment N_2 when the vapor flow is turned on, and turning the flowrate adjustment N_2 stream back on when the vapor flow is turned off. The flowrate adjustment line's flow rate is calculated to be equal to the total volumetric flowrate in the vapor flow stream equal to the sum of N_2 and the organic vapor flow rates. Figure 4.5(a) shows the response of 4 different DNA-gold nanoparticle sensors to hexane at RH = 0%. Sensor responses are expressed as the commonly used $\Delta R/R$ where R is the baseline resistance of the sensor at a given RH, and ΔR is the vapor induced change from the baseline. The plots show a rapid response, good reversibility, and near-linear dependence on hexane vapor pressure. All four sequences show a response to hexane vapor, but there are clear sequence dependent intensity differences. S2 and $(dC)_{25}$ have the largest response, while $(dT)_{25}$ has the smallest. Figure 4.6(b) shows the real-time sensor response of S2 to ethanol at different RH levels. Both positive and negative responses are observed, depending on RH, with a trend towards negative $\Delta R/R$ response at increasing RH. The S2 data show no significant response for the two highest RH values.

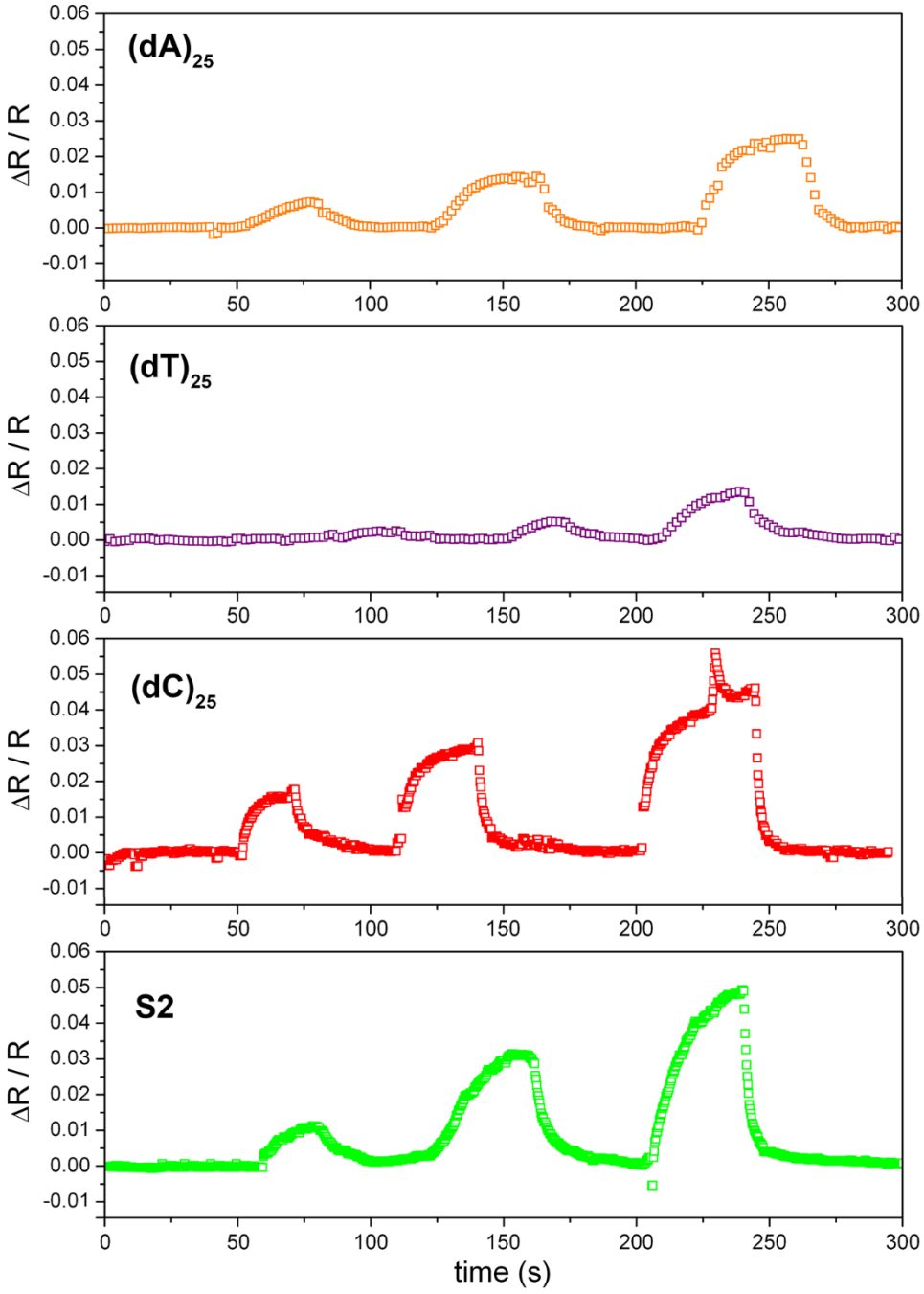

Figure 4.5 Real-time response of 4 types of DNA-functionalized gold nanoparticle sensors on hexane vapor at RH = 0% with p/p_0 = 0.012, 0.024 and 0.036.

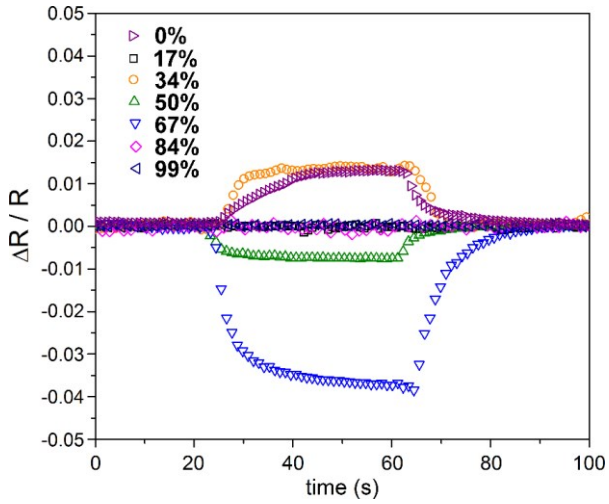

Figure 4.6 Real-time response of a S2 sensor against ethanol vapor equivalent to $\boldsymbol{p/p_0 = 0.036}$ at seven RH levels ranging from 0% to 99%.

4.3.3.2 Effect of high vapor concentrations

For sensing organic vapors, the ΔR/R values are all positive (Figure 4.7 and Figure 4.8), indicating a swelling-dominated sensor-analyte interaction. For most analytes, $(dA)_{50}$ gives a much larger response than $(dA)_{10}$. Such strong dependence of response to chain length is consistent with alkanethiol-gold nanoparticle sensors. When bulkier ligands are used, larger volume of organic phase separating individual nanoparticles provides more absorption volume and therefore enhanced gold nanoparticle-analyte interaction and sensitivity.[29]

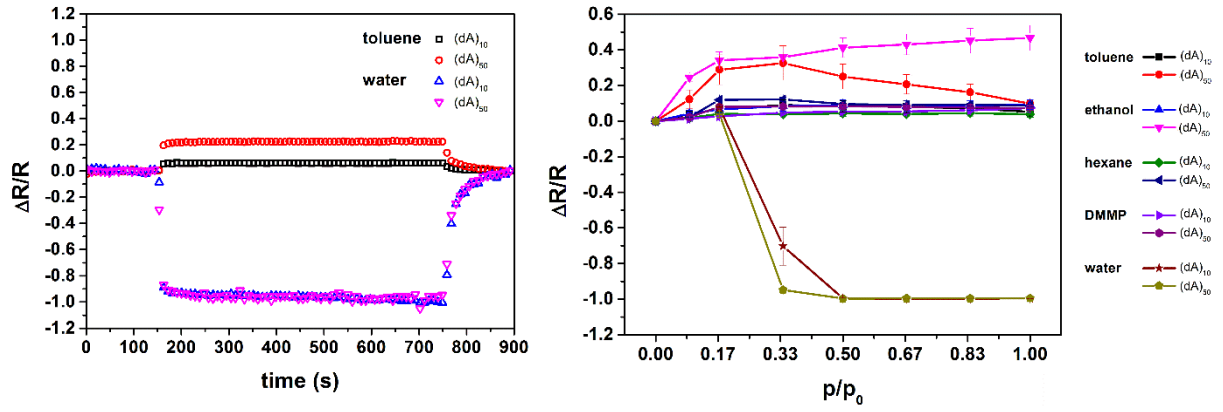

Figure 4.7 (a) Real-time sensing plot of toluene and water vapor at $p/p_0 = 0.5$; (b) Response characteristics of $(dA)_{10}$ and $(dA)_{50}$ sensors towards organic and water vapor across the full concentration range.

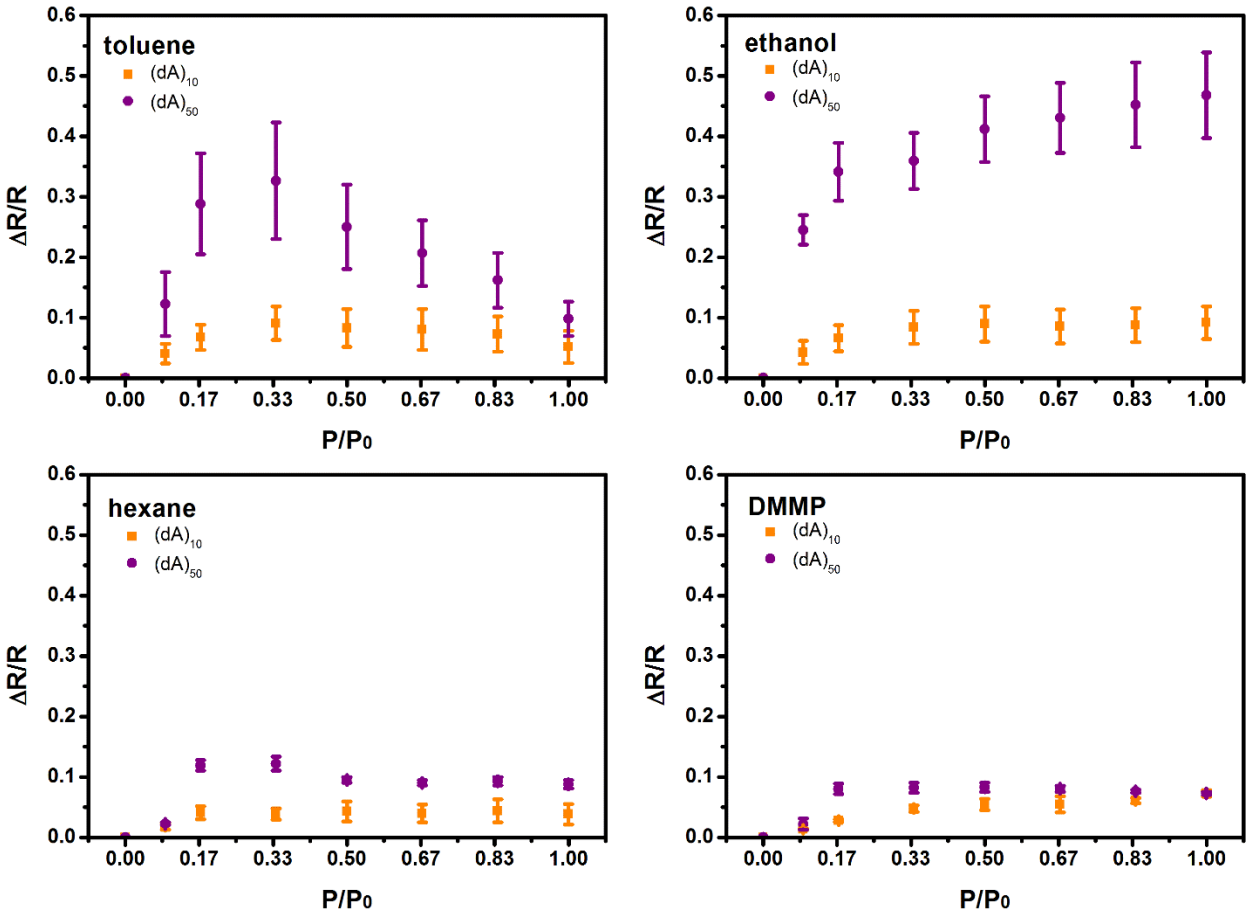

Figure 4.8 Response patterns of $(dA)_{10}$ and $(dA)_{50}$ sensors towards 4 organic vapors across the full concentration range

The detailed response patterns of $(dA)_{10}$ and $(dA)_{25}$ sensors towards organic vapors are summarized in Figure 4.8. At low concentration, the response increases with concentration before saturating. A downward trend above $p/p_0 = 0.33$ is unexpected and may suggest additional changes of the sensing layer beyond simple swelling. A continuous rising trend is only observed with ethanol. This may be related to the fact that although ethanol is a poor solvent for DNA, it is known to interact strongly with dried DNA.[30] Toluene gives a large response, possibly as a result of π-π stacking with nucleobases. In the LSER model, π-π stacking is classified as a type of polarization-polarizability interaction (rR_2). Comparatively, the sensors display less sensitivity to hexane and DMMP.

In the relatively low p/p_0 range (< 0.33), DNA-gold nanoparticle sensors respond to organic vapors linearly – a trend also observed in alkanethiol-gold nanoparticle chemiresistive sensors. The sensitivity in this range, expressed as $(\Delta R/R) / (p/p_0)$ for $(dA)_{10}$ and $(dA)_{50}$, is summarized in Table 4.2. The sensitivities of DNA-gold nanoparticle sensors are on the same order of magnitude as those of alkanethiol-gold nanoparticle sensors for toluene and ethanol,[31, 32] but that for hexane is more than one order of magnitude less than what has been reported for alkanethiols.[32] This disparity with hexane might stem from the non-polar nature of hexane and lesser interaction with polar, hydrophilic DNA molecules. Interestingly, $(dA)_{50}$ sensors have much more significant response dissimilarities towards the different vapors. For $(dA)_{10}$ sensors, the response differences are much smaller.

Table 4.2 Sensitivity of $(dA)_{10}$ and $(dA)_{50}$ sensors for 4 Vapors

Vapor	Sensitivity $(\Delta R/R)/(p/p_0)$	
	$(dA)_{10}$	$(dA)_{50}$
Toluene	0.41	1.65
Ethanol	0.35	2.06
Hexane	0.24	0.71
DMMP	0.18	0.47

4.3.3.3 Comparison with QCM studies

Responses to a series of vapors using both chemiresistors and QCM crystals were compared to evaluate the similarity or differences in response behaviors of the two different systems. Figure 4.9 shows a sample of exposure of a pair of $(dA)_{25}$-modified quartz crystal and gold nanoparticle chemiresistors to three vapors, at $p/p_0 = 0.05$. The comparative plots show increasing resistance for chemiresistors and decreasing frequency for the quartz crystals. The 3-vapor comparison shows good agreement between vapor sensitivity on the two instruments. For example, the sensitivity toward toluene and hexane are similar on the quartz crystal sensor and the chemiresistor, while the sensitivity to trimethylamine is lower. Further inspection indicates the response magnitude of chemiresistors to trimethylamine is approximately 0.8 that of toluene/hexane, while for the quartz crystal, the number is 0.6. This may indicate a dependence of sensitivity on solvent vapor polarity. Figure 4.10 shows sensitivity plots from the all of DNA sequences studied. Both types of sensors display good linearity within the range $p/p_0 = 0.01$ to 0.05. The uncertainty in electronic devices is higher due to more uncertainties in the manufacturing process.

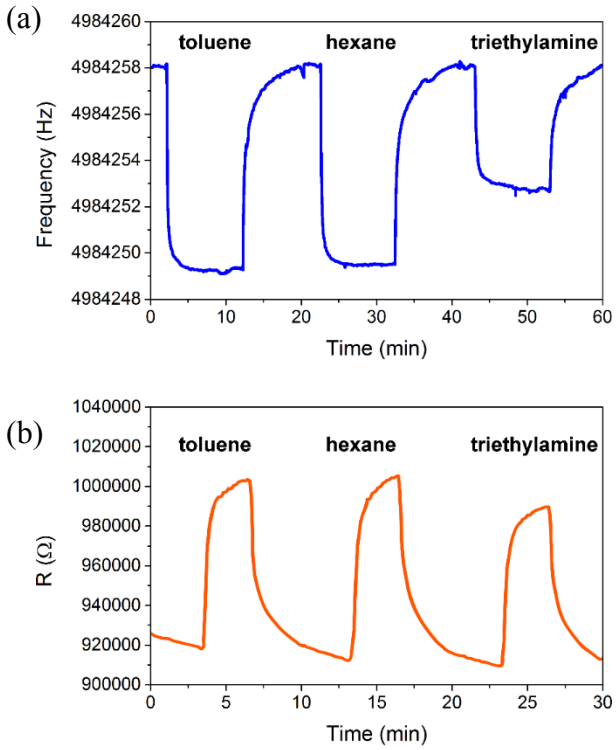

Figure 4.9 Comparison of real-time responses of (a) DNA-coated quartz crystals and (b) DNA-functionalized gold nanoparticles to three selected organic vapors at $p/p_0 = 0.05$

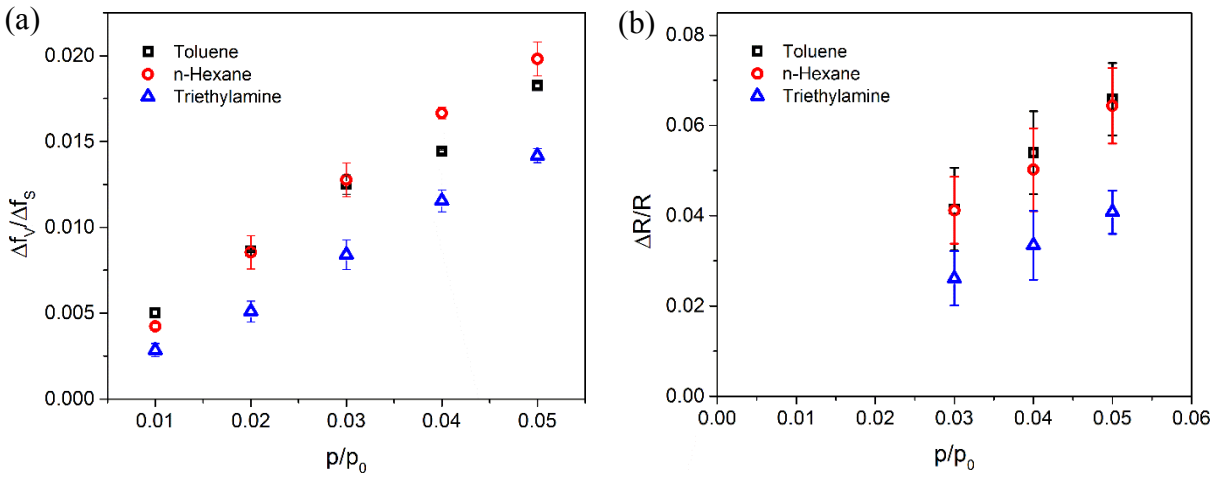

Figure 4.10 Trend of QCM (a) and chemiresistor (b) responses with change in vapor concentration. $(dA)_{25}$ was used as the DNA coating on quartz crystals and gold nanoparticle ligands on chemiresistors.

Dielectric constants and dipole moments are used to describe the macroscopic and microscopic polarity of solvents, respectively. The distribution of absorbed vapor molecules to the DNA is more isolated in nature, and is more accurately determined by the individual dipoles than by dielectric constant, which depends more on the collective orientation and interaction between the dipoles.[33] Therefore, dipole moment is used to discuss the relationship between vapor molecule polarity and the sensor response. Figure 4.11(a) plots the ratio between chemiresistor response ($\Delta R/R$) and QCM response ($\Delta f_v/\Delta f_s$) against dipole moments. The general trend shows an increase in the response ratio with increasing dipole moment. Similar studies have previously reported using C-8 gold nanoparticles deposited on both quartz crystals and chemiresistors to evaluate the sensing mechanisms of gold nanoparticle chemiresistors.[34] Figure 4.11(b) was produced for DNA-coated quartz crystals and DNA-functionalized gold nanoparticles, following the same analysis as that produced for C-8 gold nanoparticles in literature. This plot shows the normalized CR/QCM response ratio for DNA-functionalized gold nanoparticles. A trivial difference is that on the QCM crystal, DNA films instead of DNA-functionalized gold nanoparticles were deposited. Contrary to the literature-reported study, which shows volumetric sensitivity of C-8 gold nanoparticles decreases with respect to dielectric constant or dipole moment, this study using DNA-functionalized gold nanoparticles shows the CR/QCM ratio increases with dipole moment.

In the case of C-8 nanoparticles, it was reasoned that the higher dielectric constant vapors caused the electron tunneling medium to have increased dielectric constant thus offsetting the apparent resistance increase caused by increase in inter-particle spacing. If the DNA behaves like

the C-8 layer, the same CR/QCM ratio trend would be expected for DNA. However, the opposite trend was displayed. Therefore, it is speculated that additional effects in the sorption of vapor molecules were affecting electron tunneling. One possible reason could be that the sorption of vapor molecules was site-specific within the layer of DNA, and higher dipole moment vapors have higher ability to cause volume expansion of solid DNA. Volume expansion and rearrangement of DNA-chains might have been caused by the more polar nitrile and alcohols associated with specific functional groups on the DNA. This site specific effect would be much weaker for aromatics like toluene and alkanes like hexane. This explanation is speculative, and requires further experimental verification.

In general, the chemiresisitor/QCM response ratios for all vapors fall within a limited range, which indicates that the chemiresistors effectively translate the intrinsic response profiles that would be displayed by DNA-coated quartz crystals. The ratio of sensitivity falls within a range of 2.5 to 5.5, from non-polar to polar molecules, respectively.

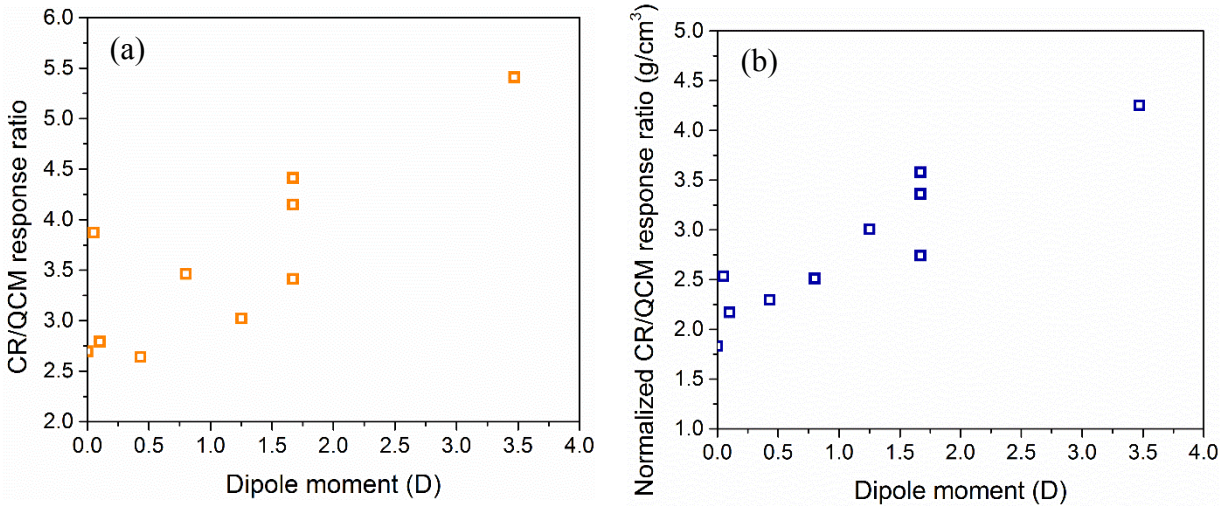

Figure 4.11 (a) Ratio of responses of chemiresistors and QCM to 10 selected vapors; (b) Ratio of responses of chemiresistors and QCM to multiple vapors, normalized using the molar mass and density to reflect volumetric response ratios. Dipole moments were obtained from experimental values measured at 20 °C.[35]

4.3.3.4 Sensing under controlled humidity levels

Combination plots of sensor responses to all organic vapors at different RH levels are shown in Figure 4.12. ΔR/R values are all positive when water vapor is not present, indicating a swelling dominated behavior. These positive responses are similar to that of water vapor (Figure 4.3(a)). However, mostly negative ΔR/R responses are observed for RH in the range of 50% to 67%, while reduced responses are observed in the ranges of RH = 17% to 34% and 84% to 100%. The response patterns are sensitive to RH with highest sensitivity in the range of 50% to 67%. Interestingly, this region is near where the sensitivity to water vapor peaks and then rapidly decreases, although the correlation is not simple. Qualitatively, the response patterns are similar for each of the different DNA sequences with sensitivities that peak in the same regions, but there are sequence dependent patterns that distinguish each different DNA oligomer at a given RH as well as different patterns

with RH. For example, $(dA)_{25}$ has the strongest peak response to all vapors, but the RH dependence is different for each vapor. Absolute values of response signals vary between different devices, but the qualitative trends are reproducible. Sensors fabricated with this method typically have a root-mean-square (rms) baseline noise on the order of 0.2% ~ 0.3% that is not strongly dependent on humidity. Table 4.3 summarizes the sensitivity for the 4 types of sensors at two working conditions with RH levels of zero and 50%.

Table 4.4 compares limits of detection (LOD) for ss-DNA with organothiol gold nanoparticle sensors that have been widely studied in the literature. For direct comparison, vapor concentrations have been converted to part-per-million. Depending on the analyte, reported LOD values range from a few to a few hundred ppm.[36] Qualitatively, LODs of ss-DNA gold nanoparticle sensors in both dry and humid atmosphere are comparable to organothiol gold nanoparticle sensors. Intermediate RH levels appear to improve the LOD values for the DNA based sensors.

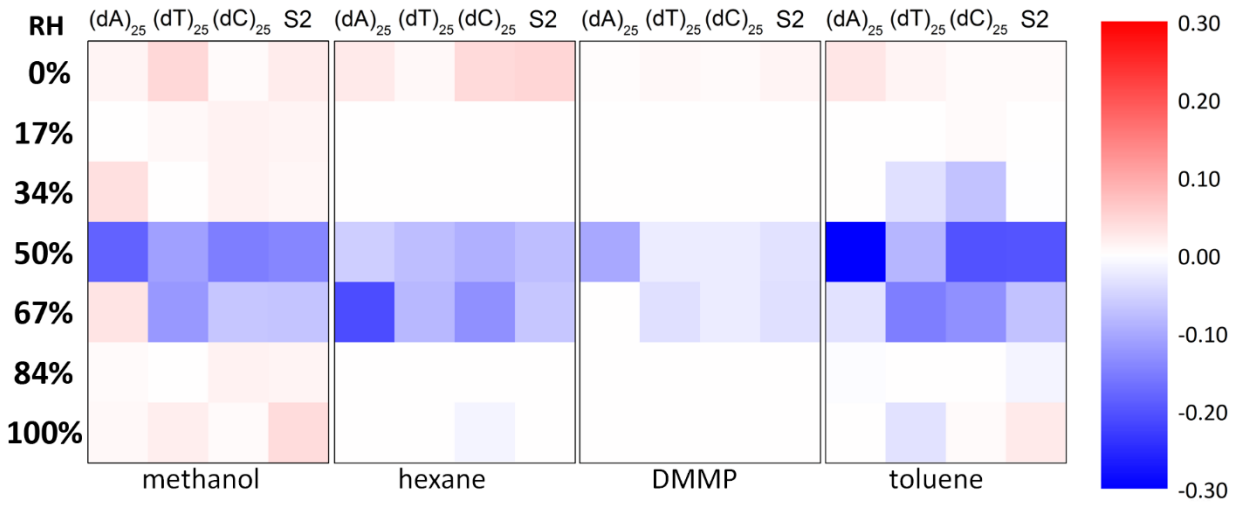

Figure 4.12 Heat plot of sensor response to 5 vapors across all RH levels (0% ~ 99%) for methanol, hexane, DMMP, and toluene. Concentrations are $p/p_o = 0.036$ for all five vapors.

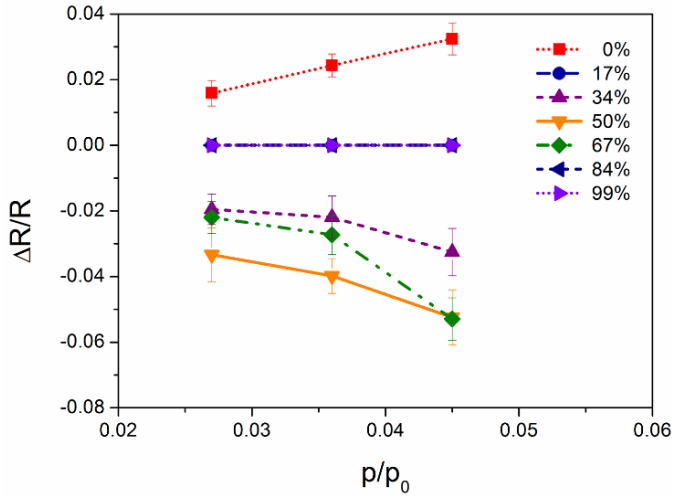

Figure 4.13 Effect of RH levels on responses towards ethanol at $p/p_o = 0.027$, 0.036 and 0.045 on a set of $(dC)_{25}$ sensors.

Table 4.3 Sensitivity of 4 types of DNA-gold nanoparticle sensors to 5 vapors at two RH levels

		Sensitivity [a]			
RH (%)	Vapor	$(dA)_{25}$	$(dT)_{25}$	$(dC)_{25}$	S2
0	Ethanol	0.35	0.11	0.92	0.31
	Methanol	0.14	0.44	0.20	0.75
	Hexane	0.69	0.23	1.22	1.37
	DMMP	0.00	0.23	0.12	0.38
	Toluene	0.82	0.19	0.35	0.23
50	Ethanol	-2.17	-0.72	-1.06	-1.91
	Methanol	-9.45	-3.09	-7.85	-7.64
	Hexane	-1.59	-2.13	-4.50	-3.50
	DMMP	-2.83	-0.64	-0.66	-0.90
	Toluene	-9.03	-2.36	-5.64	-5.58

[a] Slope from linear approximation of $\Delta R/R$ - p/p_o plots, in the form of Figure 4.10.

Table 4.4 Comparison of LODs of DNA-gold nanoparticle sensors with reported alkanethiol Au nanoparticle sensors

	LOD (ppm)			
Vapor	DNA (RH = 0%) [a]	DNA (RH = 50%) [a]	octanethiol[34, 37]	hexanethiol[22]
Ethanol	475	266	4.9 to 49	242
Methanol	171	145	150	326
Toluene	211	32	0.082 to 2.3	48

[a] Defined as three times the baseline noise divided by sensitivity as appeared in Table 4.3.

In field applications, cross-sensitivity to water is a complicating issue for sensors that function by vapor absorption into a condensed phase. Previous studies with SAW sensors have

investigated the effects RH has on baseline and sensitivity towards organic vapors.[38] Similar effects are observed here in DNA functionalized gold nanoparticle chemiresistive sensors, but the volcano shaped response is distinctive from previous studies with alkanethiol gold nanoparticles that generally report weakening sensor response with increasing RH.[8] We rationalize this behavior based on hydration and chain flexibility and their influence on the conduction mechanism. In a dry state, the sensor response is primarily from swelling of the composite organic-gold nanoparticle matrix, similar to alkanethiols, and we do not expect significant conformational changes in DNA upon adsorption of organic vapors. The weak response sensitivity for the range of RH levels from 17% to 34% is unexpected since it is weaker than both the dry state and intermediate humidity. It may be that at low RH water is held so tightly by the DNA so as to exclude organic sorption. The water may alter the DNA matrix to be more hydrophilic resulting in weaker interactions with hydrophobic molecules like hexane, as seen in Figure 4.12(c). At higher RH in the range of 50% to 67%, the DNA becomes hydrated and vapors may displace weakly held water, yielding an enhanced response. At the highest RH levels approaching 100%, sensitivity appears to decrease significantly. The decrease is most likely caused by an increasing ionic conduction contribution that is insensitive to vapor sorption. Representative effects of RH levels on sensor response for a range of analyte concentrations are shown in Figure 4.13. The data reflect similar trends as Figure 4.12. Under dry conditions sensors respond linearly with resistance proportional to concentration, and resemble swelling-dominated alkanethiol-gold nanoparticle chemiresistive sensors.[19, 22, 39] At higher RH values, resistance decreases proportional to concentration, except at 17, 84, and 99% RH where the responses is muted.

As mentioned earlier, resistance decrease upon vapor sorption have also been reported for TOAB/gold nanoparticle mixtures for both polar and non-polar vapors.[22] It was speculated that

solvation effects may increase ion mobility or cause restructuring of the gold nanoparticle film to enhance conductivity. Decreased resistance has also been observed in some alkanethiol functionalized gold nanoparticles for sensing of polar molecules like water and alcohols.[19, 39] Water vapor, in particular, could enhance ionic conductivity from impurities in films.[37] An explanation for the negative ΔR/R regions observed here is possibly more complicated since in addition to previously offered explanations there is the possibility of ligand-binding induced release of water from the hydration shell around the DNA. The increase in response over dry state sensors could partially be attributed to the increase in chain flexibility due to hydration. At even higher RH, the sensors again become less sensitive to organic vapors, because the sorption of organic vapors, if occurred, does not alter the primary ionic conduction significantly.

The response patterns of sensors with 4 different types of DNA are distinctive, therefore offering vapor identification capabilities. The sensitivity under humid conditions is similar to that under dry conditions, prompting us to believe that the sensor-analyte interaction arises from the inherent interaction parameters between DNA and analyte vapor molecules governed by thermodynamics, regardless of the environment. However, the effect of RH on the sensor response is significant. Therefore, practical vapor phase applications may require accurate control of RH in the sampling atmosphere, or a RH monitoring mechanism to actively correct for sensor response changes following RH changes.[38]

4.4 Conclusions

In summary, chemiresistive vapor sensors using DNA-functionalized gold nanoparticles were fabricated. In contrast to most alkanethiol-functionalized gold nanoparticles, DNA-

functionalized gold nanoparticle sensors are highly sensitive to water sorption. At low relative humidity (up to 40%), sensors behave similarly to organothiol-functionalized gold nanoparticle sensors that respond to vapor partitioning and film swelling. At higher humidity (40% to 100%), sensors behave increasingly like a polyelectrolyte with ionic conduction contributions to the electrical response. The high sensitivity to humidity indicates that careful control of water content is needed to distinguish analytes. The sensing of 5 vapors with 4 ss-DNA oligomer sequences was studied at different relative humidity values and sequence dependent response patterns were observed. The findings suggest that DNA-functionalized gold nanoparticle chemiresistors are comparable to alkanethiol-gold nanoparticle chemiresistive vapor sensors in terms of sensitivity and LOD.

Further, the sensing performance of DNA-functionalized gold nanoparticle sensors was compared with QCM. Sensing was non-specific, but the chemiresistors were able to translate the QCM-derived selectivity of materials. Continued study is needed to build the foundation for high specificity vapor sensing with DNA materials. While cost and complexity likely do not justify the use of random DNA as a weakly specific sensing material, understanding effects such as base sequence and sensing conditions will be necessary to design improved sensors that use aptamers for high specificity. It is however encouraging to know that the sorptive behavior of DNA is translated from the QCM-based study to chemiresistor devices, and if DNA-analyte interactions could be confirmed with QCM studies, that would be replicable on the chemiresistor sensors.

4.5 References

1. White, J.; Truesdell, K.; Williams, L. B.; AtKisson, M. S.; Kauer, J. S. Solid-State, Dye-Labeled DNA Detects Volatile Compounds in the Vapor Phase. *PLoS Biol* **2008**, 6, e9.

2. Staii, C.; Johnson, A. T.; Chen, M.; Gelperin, A. DNA-Decorated Carbon Nanotubes for Chemical Sensing. *Nano Letters* **2005**, 5, 1774-1778.

3. Kybert, N. J.; Lerner, M. B.; Yodh, J. S.; Preti, G.; Johnson, A. T. C. Differentiation of Complex Vapor Mixtures Using Versatile DNA–Carbon Nanotube Chemical Sensor Arrays. *ACS Nano* **2013**, 7, 2800-2807.

4. Lu, Y.; Goldsmith, B. R.; Kybert, N. J.; Johnson, A. T. C. DNA-decorated graphene chemical sensors. *Applied Physics Letters* **2010**, 97, 083107.

5. Hammock, M. L.; Knopfmacher, O.; Naab, B. D.; Tok, J. B.-H.; Bao, Z. Investigation of protein detection parameters using nanofunctionalized organic field-effect transistors. *ACS Nano* **2013**, 7, 3970.

6. Zilberman, Y.; Ionescu, R.; Feng, X.; Müllen, K.; Haick, H. Nanoarray of Polycyclic Aromatic Hydrocarbons and Carbon Nanotubes for Accurate and Predictive Detection in Real-World Environmental Humidity. *ACS Nano* **2011**, 5, 6743-6753.

7. Bayn, A.; Feng, X.; Müllen, K.; Haick, H. Field Effect Transistors Based on Polycyclic Aromatic Hydrocarbons for the Detection and Classification of Volatile Organic Compounds. *ACS Applied Materials & Interfaces* **2013**, 5, 3431-3440.

8. Pang, P.; Guo, Z.; Cai, Q. Humidity effect on the monolayer-protected gold nanoparticles coated chemiresistor sensor for VOCs analysis. *Talanta* **2005**, 65, 1343-1348.

9. Demers, L. M.; Mirkin, C. A.; Mucic, R. C.; Reynolds, R. A.; Letsinger, R. L.; Elghanian, R.; Viswanadham, G. A Fluorescence-Based Method for Determining the Surface Coverage and Hybridization Efficiency of Thiol-Capped Oligonucleotides Bound to Gold Thin Films and Nanoparticles. *Analytical Chemistry* **2000**, 72, 5535-5541.

10. Pomogailo, A. D.; Kestelman, V. N. Principles and Mechanisms of Nanoparticle Stabilization by Polymers. In *Metallopolymer Nanocomposites*, Springer Berlin Heidelberg: **2005**; Vol. 81, pp 65-113.

11. Storhoff, J. J.; Elghanian, R.; Mirkin, C. A.; Letsinger, R. L. Sequence-Dependent Stability of DNA-Modified Gold Nanoparticles. *Langmuir* **2002**, 18, 6666-6670.

12. Herne, T. M.; Tarlov, M. J. Characterization of DNA probes immobilized on gold surfaces. *J Am Chem Soc* **1997**, 119, 8916-8920.

13. Petrovykh, D. Y.; Kimura-Suda, H.; Whitman, L. J.; Tarlov, M. J. Quantitative analysis and characterization of DNA immobilized on gold. *J Am Chem Soc* **2003**, 125, 5219-5226.

14. Petrovykh, D. Y.; Kimura-Suda, H.; Tarlov, M. J.; Whitman, L. J. Quantitative characterization of DNA films by X-ray photoelectron spectroscopy. *Langmuir* **2004**, 20, 429-440.

15. Ray, S. G.; Cohen, H.; Naaman, R.; Rabin, Y. Where is the sodium in self-assembled monolayers of single-stranded DNA? *J Am Chem Soc* **2005**, 127, 17138-17139.

16. Mourougou-Candoni, N.; Naud, C.; Thibaudau, F. Adsorption of thiolated oligonucleotides on gold surfaces: An atomic force microscopy study. *Langmuir* **2003**, 19, 682-686.

17. Levicky, R.; Herne, T. M.; Tarlov, M. J.; Satija, S. K. Using self-assembly to control the structure of DNA monolayers on gold: A neutron reflectivity study. *J Am Chem Soc* **1998**, 120, 9787-9792.

18. Zhang, R. Y.; Pang, D. W.; Zhang, Z. L.; Yan, J. W.; Yao, J. L.; Tian, Z. Q.; Mao, B. W.; Sun, S. G. Investigation of ordered ds-DNA monolayers on gold electrodes. *J Phys Chem B* **2002**, 106, 11233-11239.

19. Wohltjen, H.; Snow, A. W. Colloidal Metal−Insulator−Metal Ensemble Chemiresistor Sensor. *Analytical Chemistry* **1998**, 70, 2856-2859.

20. Joseph, Y.; Guse, B.; Yasuda, A.; Vossmeyer, T. Chemiresistor coatings from Pt- and Au-nanoparticle/nonanedithiol films: sensitivity to gases and solvent vapors. *Sensors and Actuators B: Chemical* **2004**, 98, 188-195.

21. Han Ha, D.; Nham, H.; Yoo, K.-H.; So, H.-m.; Lee, H.-Y.; Kawai, T. Humidity effects on the conductance of the assembly of DNA molecules. *Chemical Physics Letters* **2002**, 355, 405-409.

22. Ibañez, F. J.; Zamborini, F. P. Chemiresistive Sensing of Volatile Organic Compounds with Films of Surfactant-Stabilized Gold and Gold−Silver Alloy Nanoparticles. *ACS Nano* **2008**, 2, 1543-1552.

23. Segev-Bar, M.; Shuster, G.; Haick, H. Effect of Perforation on the Sensing Properties of Monolayer-Capped Metallic Nanoparticle Films. *The Journal of Physical Chemistry C* **2012**, 116, 15361-15368.

24. Chalikian, T. V.; Sarvazyan, A. P.; Plum, G. E.; Breslauer, K. J. Influence of Base Composition, Base Sequence, and Duplex Structure on DNA Hydration - Apparent Molar Volumes and Apparent Molar Adiabatic Compressibilities of Synthetic and Natural DNA Duplexes at 25-Degrees-C. *Biochemistry-Us* **1994**, 33, 2394-2401.

25. Tao, N. J.; Lindsay, S. M. Structure of DNA Hydration Shells Studied by Raman-Spectroscopy. *Biopolymers* **1989**, 28, 1019-1030.

26. Berman, H. M.; Sowri, A.; Ginell, S.; Beveridge, D. A Systematic Study of Patterns of Hydration in Nucleic-Acids .1. Guanine and Cytosine. *J Biomol Struct Dyn* **1988**, 5, 1101-1110.

27. Zhou, Y.; Qin, Z.-Y.; Li, L.; Zhang, Y.; Wei, Y.-L.; Wang, L.-F.; Zhu, M.-F. Polyaniline/multi-walled carbon nanotube composites with core–shell structures as supercapacitor electrode materials. *Electrochimica Acta* **2010**, 55, 3904-3908.

28. Mao, L.; Zhang, K.; On Chan, H. S.; Wu, J. Surfactant-stabilized graphene/polyaniline nanofiber composites for high performance supercapacitor electrode. *Journal of Materials Chemistry* **2012**, 22, 80-85.

29. García-Berríos, E.; Gao, T.; Woodka, M. D.; Maldonado, S.; Brunschwig, B. S.; Ellsworth, M. W.; Lewis, N. S. Response versus Chain Length of Alkanethiol-Capped Au Nanoparticle Chemiresistive Chemical Vapor Sensors. *The Journal of Physical Chemistry C* **2010**, 114, 21914-21920.

30. Fang, Y.; Hoh, J. H.; Spisz, T. S. Ethanol-induced structural transitions of DNA on mica. *Nucleic Acids Research* **1999**, 27, 1943-1949.

31. Snow, A. W.; Wohltjen, H. Materials, method and apparatus for detection and monitoring of chemical species. 6221673 B1, Apr 24, 2001, Apr 24, 2001.

32. Han, L.; Daniel, D. R.; Maye, M. M.; Zhong, C.-J. Core−Shell Nanostructured Nanoparticle Films as Chemically Sensitive Interfaces. *Analytical Chemistry* **2001**, 73, 4441-4449.

33. Jatkar, S. Relationship between Dielectric Constant of Liquids and Solids and Dipole Moments. *Nature* **1944**, 153, 222.

34. Steinecker, W. H.; Rowe, M. P.; Zellers, E. T. Model of Vapor-Induced Resistivity Changes in Gold−Thiolate Monolayer-Protected Nanoparticle Sensor Films. *Analytical Chemistry* **2007**, 79, 4977-4986.

35. McClellan, A. L. *Tables of Experimental Dipole Moments*. W. H. Freeman: **1963**.

36. Ibañez, F. J.; Zamborini, F. P. Chemiresistive Sensing with Chemically Modified Metal and Alloy Nanoparticles. *Small* **2012**, 8, 174-202.

37. Guo, J. L.; Pang, P. F.; Cai, Q. Y. Effect of trace residual ionic impurities on the response of chemiresistor sensors with dithiol-linked monolayer-protected gold (nano)clusters as sensing interfaces. *Sensor Actuat B-Chem* **2007**, 120, 521-528.

38. Zellers, E. T.; Han, M. Effects of Temperature and Humidity on the Performance of Polymer-Coated Surface Acoustic Wave Vapor Sensor Arrays. *Analytical Chemistry* **1996**, 68, 2409-2418.

39. Han, L.; Daniel, D. R.; Maye, M. M.; Zhong, C. J. Core-shell nanostructured nanoparticle films as chemically sensitive interfaces. *Analytical Chemistry* **2001**, 73, 4441-4449.

Chapter 5

DIELECTROPHORETIC ASSEMBLY OF GOLD NANOPARTICLES IN NANOSCALE JUNCTIONS FOR MINIATURE CHEMIRESISTORS

5.1 Introduction

In Chapter 1, it has been discussed that miniaturization is a future trend for sensor development. To meet these technological requirements, new materials and fabrication technologies are required. In recent years, the integration of nanotechnology and analytical chemistry has created sensors with enhanced functionality and performance. Notably, the utilization of high surface area and quantum size effects associated with nanomaterials such as carbon nanotubes,[1] graphene,[2] nanometer-thick InAs films,[3] MoS_2,[4] and gold nanoparticles[5] have produced highly sensitive electronic chemical sensors. However, while nanoscale materials have been extensively studied, nanoscale device platforms and scaling have been less explored.

Chemiresistor sensors fabricated using small molecule functionalized metallic nanoparticles have been extensively investigated over the past decade. Typically, nanoparticle-based chemiresistors consist of dense self-assembled nanocomposite films of nanoparticles spanning two electrodes, forming a resistive electrical conduction paths. These films are usually

100 – 300 nm thick on microfabricated electrodes with spacing 5 to 20 μm. To fabricate at this dimensional scale, various deposition methods, mostly through top-down approaches such as air-brushing,[5] drop-casting,[6] ink-jet printing,[7] electron-beam-induced crosslinking,[8] solution phase assembly,[9] and layer-by-layer assembly,[10, 11] have been used. Numerous types of ligands, including small-molecule organothiols,[6, 12] alkylamines,[13, 14] oligopeptides,[15] and oligonucleotides,[16] have been successfully employed to functionalize metallic nanoparticles, creating chemiresistor sensors with good sensitivity and moderate selectivity for a wide range of volatile chemicals. Nanoparticle-based sensors have been investigated for selective vapor sensing,[17] as gas chromatography (GC) detectors,[18] and for pattern recognition based analyte identification.[6, 12, 19, 20]

Despite many advancements in this field, nanoparticle chemiresistor sensors can be further improved. First, devices are relatively large with electrode and film dimensions generally in the range of microns, and film thickness > 100 nm. Vapor sorption is a bulk effect that leads to film swelling and dielectric permittivity changes of the nanocomposite films, and response times are dependent on film thickness.[21, 22] Response times of conventional micron size devices are generally slow compared to input concentration changes.[21] Size reduction of chemical sensors is one approach to increase response speed and improve performance. Nanoparticle films with thickness above 100 nm are robust and give good reproducibility,[22] but response times are limited by vapor analyte mass transport and partitioning into the active sensing layers. For thinner films fabricated with layer-by-layer techniques,[10] SEM images show incomplete coverage of the substrate with voids and isolated islands of gold nanoparticles, leading to non-linear response with respect to number of nanoparticle layers.[10, 19] Figure 5.1(a) shows the typical structure of a very thin layer formed by depositing 5 layers of 1,12-dodecanedithiol-functionalized gold nanoparticles

on 10 μm gap interdigitated electrodes. The sensors based on these < 20 nm films are faster than other chemiresistors, but have a cruder film structure, with lots of voids and isolated nanoparticle islands. The presence of these relatively clustered nanoparticle gives us the hint that creating nanoscale electrodes that capture these islands is one possible solution of creating a more defect-free chemiresistor (Figure 5.1(b)). However, the random nature of these islands indicates that a more controllable fabrication technique is required.

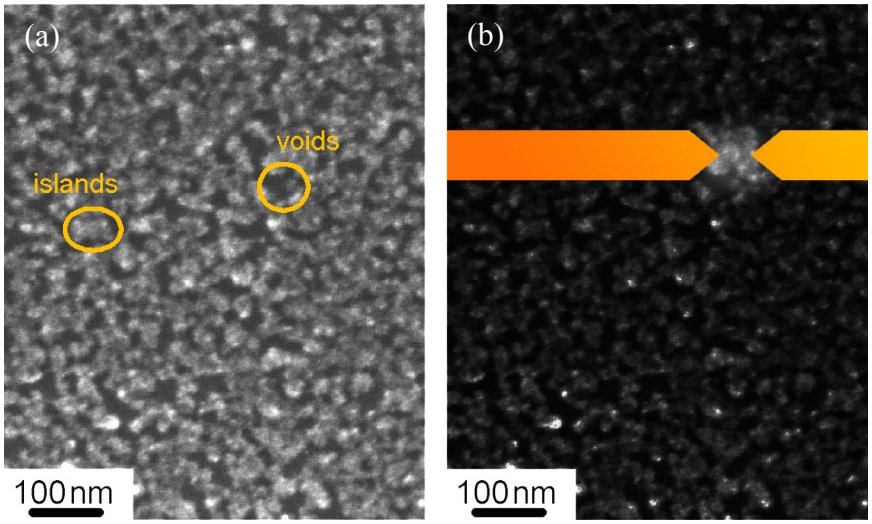

Figure 5.1 (a) Isolated islands and voids formed by attempts at depositing very thin, five layers of gold nanoparticles on micron-scale chemiresistors;[10] (b) Schematics drawn using the same SEM image as part (a), of a possible way of connecting an isolated highlighted island of nanoparticles to a pair of electrodes, creating a nanoscale chemiresistor.

Another approach to improve response times is through reduction of the active sensing volume, so long as the basic sensing mechanisms are not attenuated. Initial studies have shown that sensitivity and selectivity remains unchanged for devices scaled down to electrodes with

spacing as small as 150 – 300 nm.[23, 24] However, these purely top-down approaches do not offer control of local assembly of nanoparticles. Microstructures similar to those observed in Figure 5.1 are expected. In these studies, noise levels generally increase with decreasing sensor size, leading to deteriorated LOD by one to three orders of magnitude.[18, 23]

A second improvement possible with smaller devices is the ability to integrate a large number of independent chemiresistors on a single chip to achieve portability, low power, low cost, redundancy, and integration with other electronic devices. Small, fast devices are necessary for portable sensor arrays integrated with handheld vapor sampling systems.[25] Similar to the scaling problem above, it is a challenge to integrate many different organic capping ligands at different spatial locations on device arrays, especially when devices are nanoscale.

Dielectrophoresis (DEP) has been demonstrated as an effective technique to achieve localized assembly of nanostructures.[26] It has been demonstrated that by applying AC electric fields to nanogap junctions, particles in the range of 10 to 60 nm can be locally trapped to bridge between electrodes.[27-31] However, achieving nanoparticle based sensors this way has to overcome possible sintering of nanoparticle assemblies[31, 32] and/or irreversible chemical modification of nanoparticle surfaces.[29] In addition, most work has been limited to aqueous solvents, which limits the range of organic capping agents and sensor function.

In this chapter, we report the fabrication and testing of nanoscale chemiresistors with inter-electrode distances of 50 nm. The fabrication of sensors on this scale requires both the fabrication of nm-scale electrodes and controlled deposition of nanoparticles. To fabricate the electrodes needed for this work, a combination of photolithography and electron-beam lithography is used. While photolithography is sufficient to define patterns on the micron scale, electron-beam

lithography is used to produce electrode patterns on the order of 10 – 1000 nm.[23, 33] Dielectrophoresis is used to assemble nanoparticles into clusters localized at the nanoscale electrode regions. We introduce ethanol as a solvent to assemble nanoparticles with different ligand types. With the small inter-electrode distances, the minimum thickness to form a percolation pathway is dramatically reduced and response speed is increased by up to a factor of twenty. The results demonstrate that at even at this very small length scale the collective swelling of organic-capped gold nanoparticles still occurs. Comparison with micron-scale chemiresistors shows that capping layer dependent analyte selectivity is preserved. As proof-of-concept for single chip sensor arrays, we demonstrate an array of four types of nanoparticle capping ligands fabricated on a single chip that generates unique patterns for 6 different vapors.

5.2 Experimental methods

5.2.1 Solvents for gold nanoparticle deposition

Ligands used for the nanoparticles are 1-octanethiol, 3-mercaptopropionic acid, 4-aminothiophenol, and 6-mercapto-1-hexanol. All 4 types of as-synthesized thiol-functionalized nanoparticles were eventually re-dispersed in ethanol for dielectrophoresis. The choice of ethanol is to achieve sufficient solubility of the gold nanoparticles while keeping a relatively polar solvent ($\epsilon_r = 24.5$) to assist dielectrophoresis. Our attempts with toluene as a solvent ($\epsilon_r = 2.4$) did not produce dielectrophoretic assembly of gold nanoparticles in our system. For the larger 20 μm devices, drop-casting was used to deposit nanoparticles on the electrode devices. In this case, toluene was used to re-disperse nanoparticles functionalized with 1-octanethiol and 4-

aminothiophenol, while ethanol was used to re-disperse nanoparticles functionalized with 3-mercaptopropionic acid and 6-mercapto-1-hexanol.

5.2.2 Deposition of gold nanoparticles onto 50 nm devices

An AC voltage of 1 MHz and 4 volts peak-to-peak (V_{pp}) was supplied by a function generator to wire-bonded nanogap devices. A 2 µl droplet of each gold nanoparticle ethanol solution was placed onto a sensor chip to cover the electrode area. Because of the small chip size, the ethanol droplet spread out to cover the entire chip surface. Typical chemiresistor baseline resistances ranged from 20 to 200 kΩ in room air.

5.2.3 Deposition of gold nanoparticles onto 20 µm device substrates

Gold nanoparticle solutions in toluene or ethanol were drop-cast onto 20 µm devices. A 4 µl droplet of nanoparticle solution was placed onto each circular electrode region using a micropipette, and the solvent was evaporated with gentle heating (~ 50 °C) of the substrate. The solid films formed in this process were briefly blown with a stream of dry N_2, and were stored in dry N_2 for at least 4 hours before sensor testing.

5.2.4 Electrical characteristics

All I-V scans were triangular voltage sweeps that ramped from 0 to 0.9 V, down to -0.9 V, and back to 0 V. The ramp rate was 0.05 V/s.

5.2.5 Vapor testing

The vapor analytes are: water, ethanol, toluene, hexane, cyclohexanone, and acetonitrile at concentrations of $p/p_0 = 0.01$ to 0.05 in the sensing chamber. The test chamber and the vapor generators were maintained at 22 °C. Both 20 µm and nanoscale devices were loaded into the testing chamber for simultaneous testing.

High speed vapor switching experiments were performed with a separate configuration using an optical chopper (Stanford Research Systems SR540, Sunnyvale, CA) to rapidly switch vapor concentrations on and off.[34] A rotating optical chopper blade was positioned between a gas delivery tube outlet and a sensor chip. Testing vapor carried by nitrogen was directed at the sensor chip through the gas delivery tube, and the sensor chip was held stationary in air. A flow of 620 cm^3/min nitrogen containing $p/p_0 = 0.025$ ethanol vapor was directed at the sample and the electrical resistance was measured at a sampling rate of 25 samples per second.

5.3 Results and discussion

5.3.1 Microstructural characterization of nanoscale devices

A representative optical microscopy image of a single chip bearing multiple types of nanoparticles is shown in Figure 5.2(a). The separation between each chemiresistor device is 200 μm; four devices are shown in the image. Figure 5.2(b) shows an SEM image of a pair of electrodes with 10 triangular tips without any nanoparticles. Figure 5.2(c) shows the same region after dielectrophoresis; the new features in the image are assemblies of Au nanoparticles. The nanoparticles have an average diameter of 10 ± 2 nm (Figure 5.3). The active sensing region is estimated from the images as 0.0025 μm^2 for each tip. Some particles are also seen on the SiO_2 regions surrounding the electrodes, but close inspection shows that nanoparticle assembly is enhanced near the electrodes, including electrode edges as well as nanogap regions. For the conventional chemiresistors in this study, a multilayered film of gold nanoparticles of thickness 200 – 300 nm that covers the 20 μm space between electrodes is necessary to obtain a conduction

path above the percolation threshold,[10] which is typical for micron-scale chemiresistors made with gold nanoparticles.[18, 23, 24]

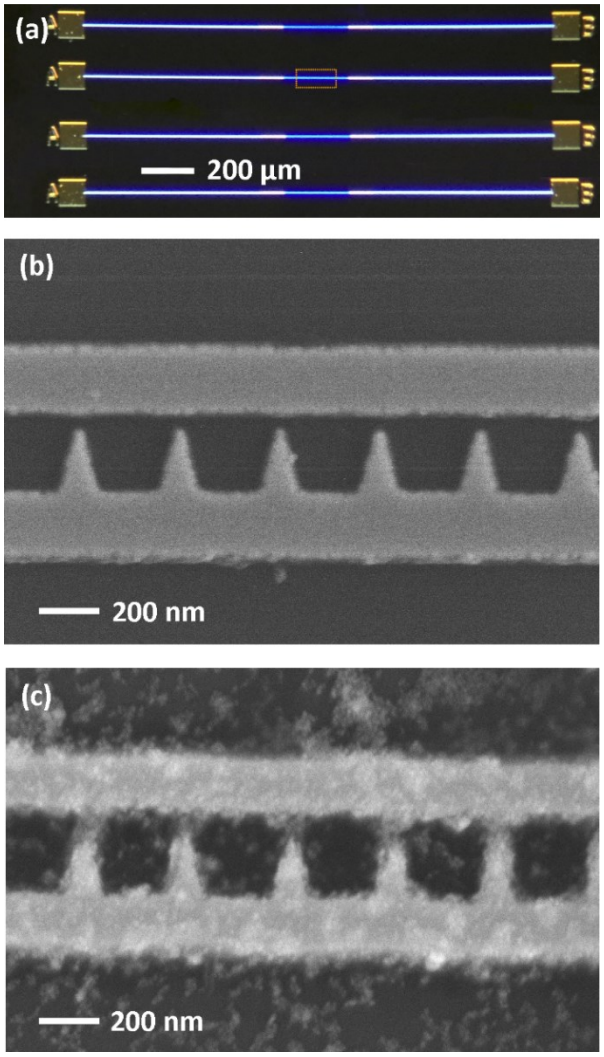

Figure 5.2 (a) Plan view image of a multi-device sensor chip. The center region of each horizontal line is a pair of electrodes separated by 250 nm with periodic tips protruding toward the counter electrode. The orange enclosed region in (a) is magnified and show in (b) and (c). (b) Tip region before deposition of nanoparticles. (c) Tip region after dielectrophoretic deposition of 1-octanethiol functionalized gold nanoparticles.

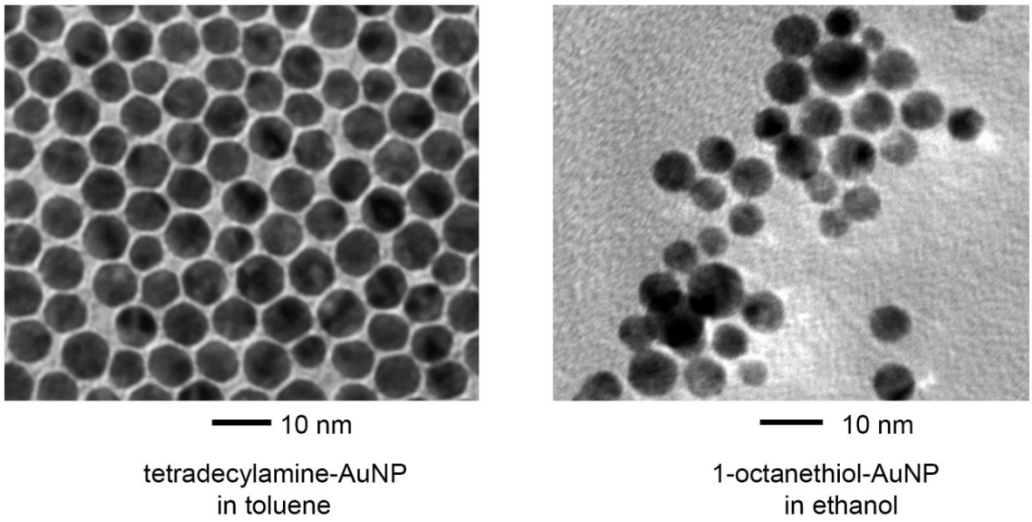

Figure 5.3 TEM images of tetradecylamine-functionalized gold nanoparticles (synthesis intermediate), and 1-octanethiol-functionalized gold nanoparticles (final product).

Figure 5.4(a) shows a high-resolution SEM image of a single tip modified by dielectrophoresis with nanoparticles. Individual nanoparticles can be observed at the tip region, which covers approximately a 50 nm × 50 nm area. At least 10 discrete nanoparticles can be resolved from the ensemble. Selected point EDX data confirm that the gap regions contain gold nanoparticles; EDX data (spectrum) show Au signal only in the tip region (orange cross) and not in the region between electrodes (purple cross). Figure 5.4(b) shows an AFM image of a dielectrophoresis-modified tip region. The morphology was stable and there were no changes after multiple scans of the same regions. In addition, SEM imaging before and after scanning confirmed no observable sample damage by AFM. A line scan across the AFM image confirms a concentration of nanoparticles in the tip region, and the height of the nanoparticle clusters is 30 – 40 nm, which is similar to the electrode thickness. Based on the SEM and AFM data, we estimate each active sensor tip region to consist of 2 to 3 layers of nanoparticles in the middle, and 1 layer

of nanoparticles at the sides. Therefore, each active sensor contains approximately 20 – 30 nanoparticles.

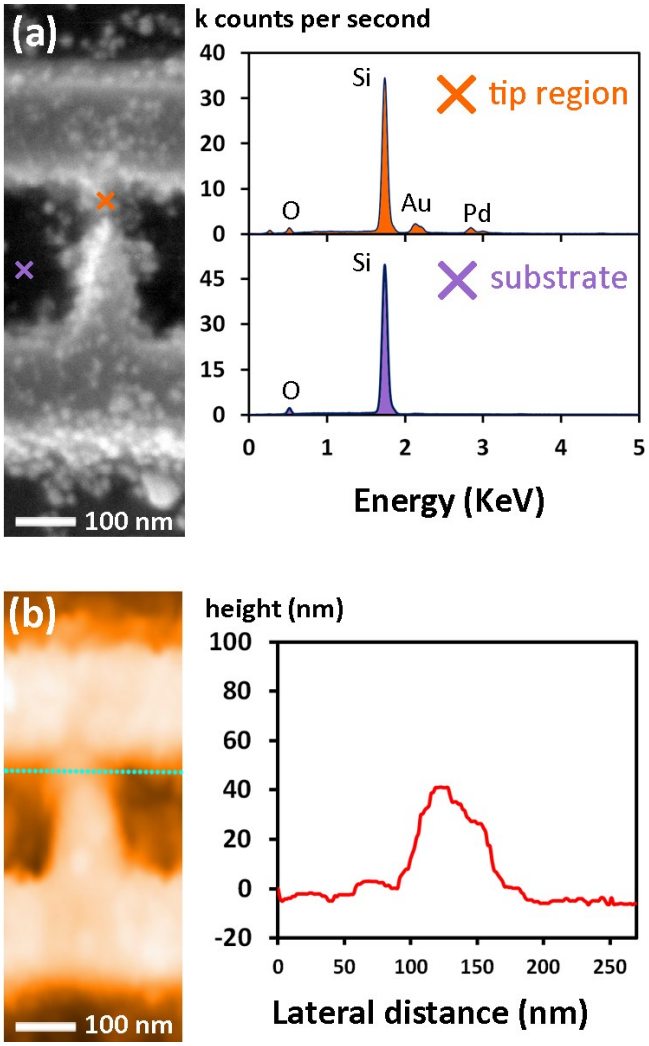

Figure 5.4 (a) Left: SEM image of a single tip with gold nanoparticles densely assembled at the tip region. Right: Selected point EDX spectra of a single tip region with assembled gold nanoparticles. Orange cross corresponds to a tip region and purple cross corresponds to a position on the substrate away from the tips. (b) Left: AFM topographic image of a single tip with gold nanoparticles assembled at the tip region. Right: Cross-sectional profile along the dashed line showing nanoparticle cluster with height 40 nm relative to the substrate surface.

5.3.2 Dielectrophoresis parameters

Figure 5.5 shows the result of dielectrophoresis for nanoelectrodes with different numbers of tips. Parts (a), (b), and (c) are all performed with 30 s dielectrophoresis at 4 V_{pp} and 1 MHz using aminothiophenol functionalized gold nanoparticles. Nanoparticles are concentrated in the gap regions and around the outer edges of the electrodes. For the 10-tip array, at least 9 out of 10 tips are bridged by nanoparticles. As the number of tips increases to 100 and 1000, the number of nanoparticles is less at the tip regions, between electrodes, and on the outer edges of the electrodes. This is consistent with nanoparticle deposition as a mass transfer limited process spread over the region of overlap between electrodes.[31] The region of influence (ROI) of a pair of nanogap electrodes at the current conditions is on the order of a few hundred nanometers. As the gap size is 50 nm and tip-tip separation is 340 nm, the ROI of dielectrophoretic forces from neighboring tips overlap, and there is competition for nanoparticles. The density of nanoparticles is less for devices with longer overlapping electrode regions because of nanoparticle depletion in solution and the finite time for assembly. However, if an extended period of dielectrophoresis is carried out, the number of captured nanoparticles increases, as shown in Figure 5.5(e) and (f) for a 1000 tip sample. When no electric field is applied, no concentrated assembly of nanoparticles is seen anywhere around the electrodes; only a randomly dispersed residue of leftover nanoparticles is observed after solution removal (Figure 5.5(d)).

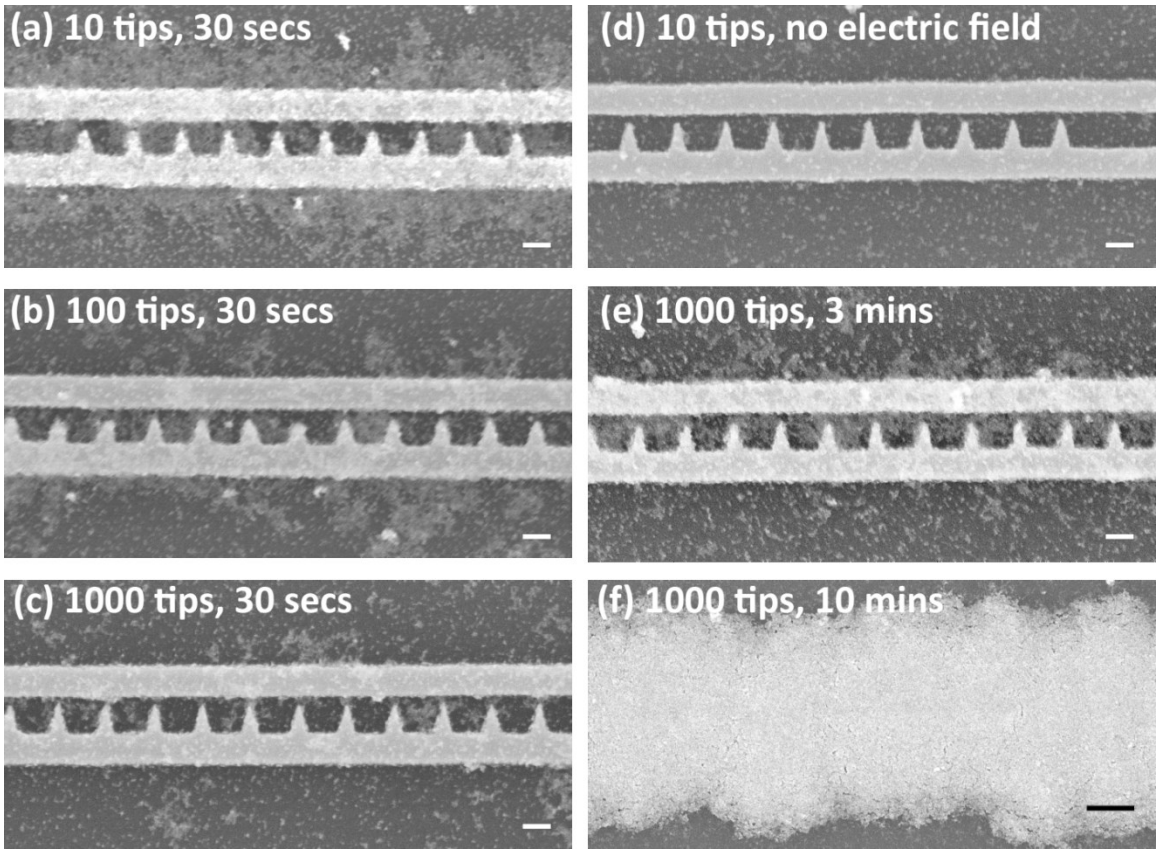

Figure 5.5 SEM images after nanoparticle assembly for aminothiophenol-functionalized gold nanoparticles after different dielectrophoresis durations (30 s, 3 min, 10 min) on 10, 100, and 1000 tip devices. Scale bars for (a) to (e) are 100 nm, and scale bar for (f) is 1 μm.

5.3.3 Electrical characteristics

Current-voltage (IV) measurements of 1000-tip nanoscale and micron-scale devices recorded in a nitrogen flow are shown in Figure 5.6. The devices with 20 μm electrode spacing and multilayered nanoparticle films show linear IV characteristics, which has been justified by Joseph et al. using percolation theory.[10] Nanoscale devices also show linear IV behavior, but the resistance is higher. For 20 μm devices, a multilayer nanoparticle network is required for a good conduction pathway. Nanoscale electrodes form conduction paths with films that are thinner by

about a factor of 10. Resistances of the devices fabricated with 4-aminothiophenol functionalized gold nanoparticles shown in Figure 5.5 (a), (b), and (c), corresponding to 10, 100, and 1000 tips were 35, 30, and 25 kΩ respectively. The resistance of a 1000 tip device after a longer time of 3 min dielectrophoresis had a lower resistance of 10 kΩ. The heavily covered electrodes after 10 min dielectrophoresis had resistance reduced to 3 kΩ. Resistances measured on sensors using other ligands (1-octanethiol, 3-mercaptopropionic acid, and 6-mercapto-1-hexanol) show similar trends, but have different baseline values; a comparison of baseline resistances is show in Figure 5.7(a). A set of reference devices with gold nanoparticles functionalized with a series of linear-chain alkanethiols were also measured (Figure 5.7 (b)), and their resistances increase with chain length, consistent with literature reports.[9, 35] The resistance scaling confirms that capping ligands effectively separate the metallic cores, and particles are not sintered.

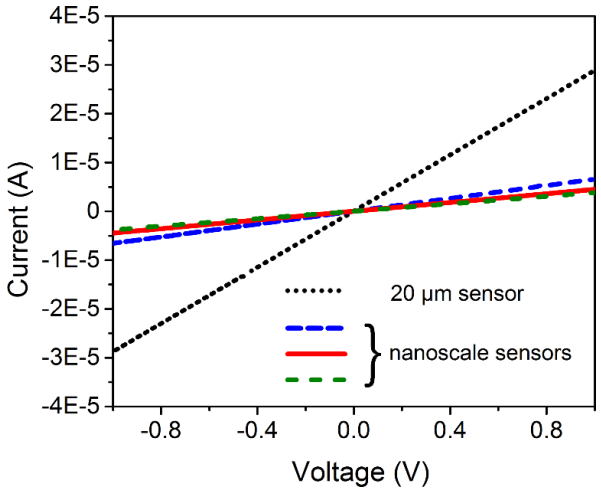

Figure 5.6 I-V characteristics of 3 nanoscale sensors compared to a micron-scale sensor using 1-octanethiol-functionalized gold nanoparticles.

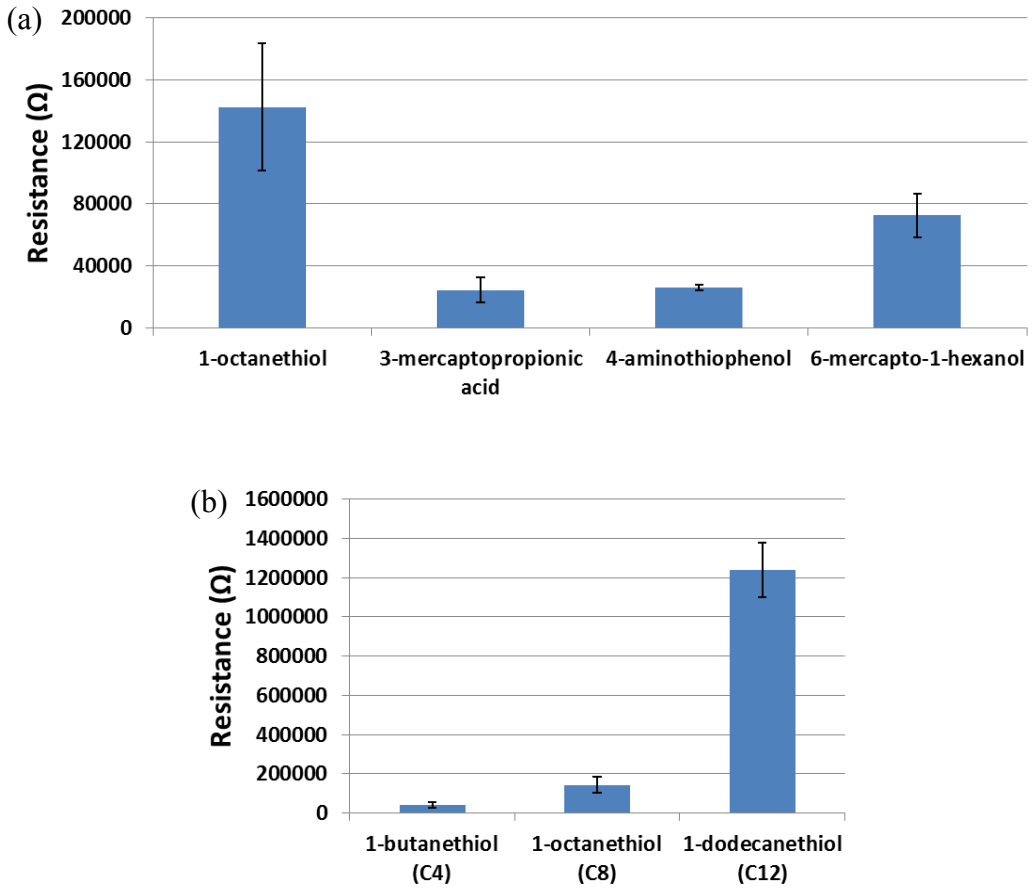

Figure 5.7 (a) Average baseline resistances of 50 nm nanoscale sensor devices fabricated with gold nanoparticles functionalized with 4 types of capping ligands; (b) a comparison of resistance values of 50 nm nanoscale devices using series of linear chain alkanethiol-functionalized gold nanoparticles. In each study, at least 3 devices were measured; all measurements used devices with 1000 tips.

For fixed assembly time, the conductance does not scale with the number of tips, as might have been expected. The lack of scaling is attributed to incomplete filling of nanogaps in the larger arrays. Increasing dielectrophoresis time from 30 s to 10 min decreases resistance, but the lack of scaling indicates that the conduction paths across some tip regions are incomplete even after

extended assembly time. This may be due to changes of the electric field spatial distribution during assembly. Extended assembly times lead to undesirable thicker films and slower vapor response rates. Improving the efficiency of the dielectrophoresis may be useful to improve device performance for large tip arrays.

As the measured resistance of each device is dependent on film nanostructure, dimensions, and electrical contacts, a more useful indication of the electrical properties is resistivity, which normalizes film dimensions. Resistivity is calculated using $\rho = R \times A / L$, where R is the film resistance, A is the estimated cross-sectional area of the actively conducting part of the nanoparticle films, and L is distance between the two electrodes (50 nm for the nanoscale sensors, 20 μm for the control sensors). To evaluate the resistivity of our nanoscale chemiresistors, sensors made with 1-octanethiol-functionalized gold nanoparticles are compared with literature values for the same ligand. Previous work has addressed the calculation of resistivity for nanoparticle films deposited between electrodes.[36] For both 50 nm and 20 μm electrode designs, the thickness of nanoparticle films is less than 3× the electrode thickness. Therefore, the electric field penetrates through the entire nanoparticle film, and film resistivity calculations based on the nanoparticle film thickness are valid. Resistivity data are summarized in Table 5.1. The resistivity of 1-octanethiol nanoparticle sensors from the literature cover a range of 10 to 8,000 Ω·m,[18, 24, 37, 38] while the present 50 nm nanogap devices are 0.9 ± 0.3 Ω·m. The relatively low resistivity of the nanoscale devices is similar to sensors made with propanethiol-functionalized gold nanoparticles (0.2 Ω·m).[9] Sensors made using the other 3 ligands are also < 10 Ω·m. On the other hand, the 20 μm sensors have a resistivity of 300 Ω·m, which is within the range of micron-sized devices studied by others. Steinecker et al.[24] point out that discrepancies among resistivity values in different reports may be due to differences in core diameters, ligand overlap, or synthesis methods of the nanoparticles.

There is no obvious dependence on particle size from Table 5.1, and there is a large range of reported resistivity. It is possible that a more direct, void-free conduction path or partial sintering resulting from dielectrophoresis may contribute to the relatively low resistivity values for the nanogap devices. The number of nanoparticles along the direction between electrodes is only 5 or 6. During dielectrophoresis at 4 V_{pp}, the root-mean-squared (rms) electric field across each 50 nm junction is 5.7×10^7 V/m. The large electric field could promote structural reorganization to create more direct conduction paths or smaller particle-particle separations that yield lower resistivity. Lastly, for larger sensors with μm to mm length scales, the films are subject to defects, and there could be bottlenecks in electrical conduction that contribute to higher resistivity. Scanning electron microscopy (SEM) images often show incomplete coverage of the substrate with voids and isolated islands of gold nanoparticles.[10, 19] Because of the non-uniformity in cross sectional area, resistivity values based on ideal geometric dimensions may be overestimated.

Table 5.1 Resistivity data for chemiresistors with alkanethiol-functionalized gold nanoparticles

Ligand	NP diameter (nm)	Resistivity (Ω·m)	Reference
Octanethiol	4.3	3400	[24]
Octanethiol	8	1360	[18]
Octanethiol	3.7	8060	[37]
Octanethiol	3.9 – 4.5	550	[38]
Octanedithiol	2	11	[9]
Propanedithiol	2	0.2	
Hexanethiol	1.7	400	[23]
Dodecanedithiol	4	11.1	[10]
Octanethiol	10	0.9 ± 0.3	This work, 50 nm device
Octanethiol	10	300 ± 20	This work, 20 μm device

5.3.4 Sensor response characteristics

5.3.4.1 Size scaling of chemiresistors

In vapor sensing experiments, response is expressed as ΔR/R, where R is the baseline resistance in pure nitrogen and ΔR is the change in sensor resistance due to vapor analytes. Neglecting contact resistance, the nanoparticles can be visualized as a network of tunnel junctions, each individually modulated by vapor sorption. Assuming each tunnel junction has resistance R and every tunnel junction changes by ΔR upon vapor sorption, for a linear chain of N gold nanoparticles the change in resistance would be $N\times\Delta$R. Expressing the signal as the ratio of change in resistance versus baseline resistance, we have $(N\times\Delta\mathrm{R})/(N\times R) = \Delta R/R$, which is identical to the response of a single tunnel junction. This scaling argument is consistent with early studies using gap distances from 15 μm down to 100 nm.[23] In the present studies, our 1000-tip devices were used for vapor exposure sensing experiments due to smaller device-to-device variation.

5.3.4.2 Sensor response in air

Figure 5.8 presents response profiles for our two different sized sensors fabricated using 4 different capping ligands tested in air by exposure to a 0.7 s pulse of diluted ethanol vapor. The times to reach saturation for nanoscale devices are < 0.3 s for all 4 devices, while times for the 20 μm devices are at least 0.6 s. Similarly, recovery times after each vapor pulse are significantly shorter for the nanoscale devices. The time constants for sensor response (time to reach 63.2% of steady state response) are about 0.03 s for nanoscale devices and 0.08 s for 20 μm devices, while time constants for sensor recovery (time to go below 36.8% of steady state response) are in the range of 0.1 – 0.18 s for nanoscale devices, and 0.36 – 0.48 s for 20 μm devices. The enhanced

response and recovery rates originate from the thinner layers and smaller sensing volumes of the nanoscale sensors. Figure 5.9 shows consecutive vapor exposures of the two types of sensors towards ethanol vapor. The response speeds and resistivity changes show good reversibility and stability under repeated testing for both sensors.

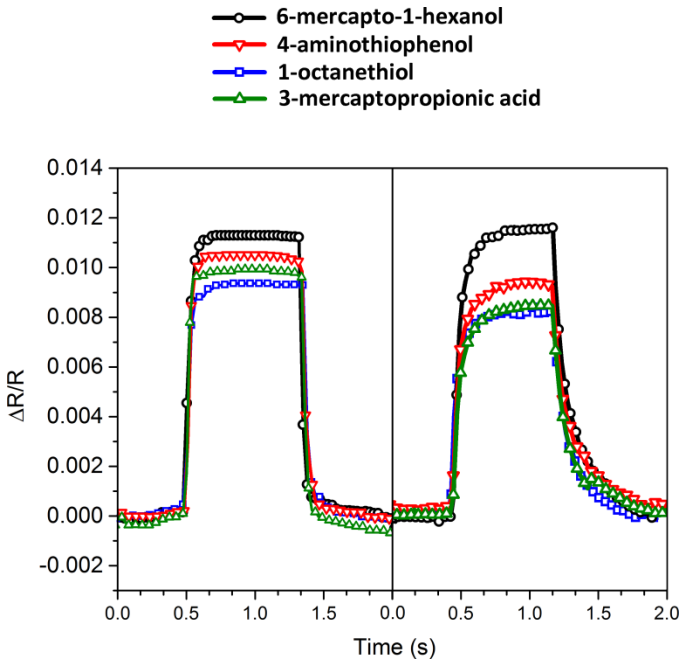

Figure 5.8 Real-time sensor response to a pulse of ethanol vapor ($p/p_0 = 0.025$) switched on and off by an optical chopper in air. Left: 50 nm nanoscale sensor; right: 20 μm sensor.

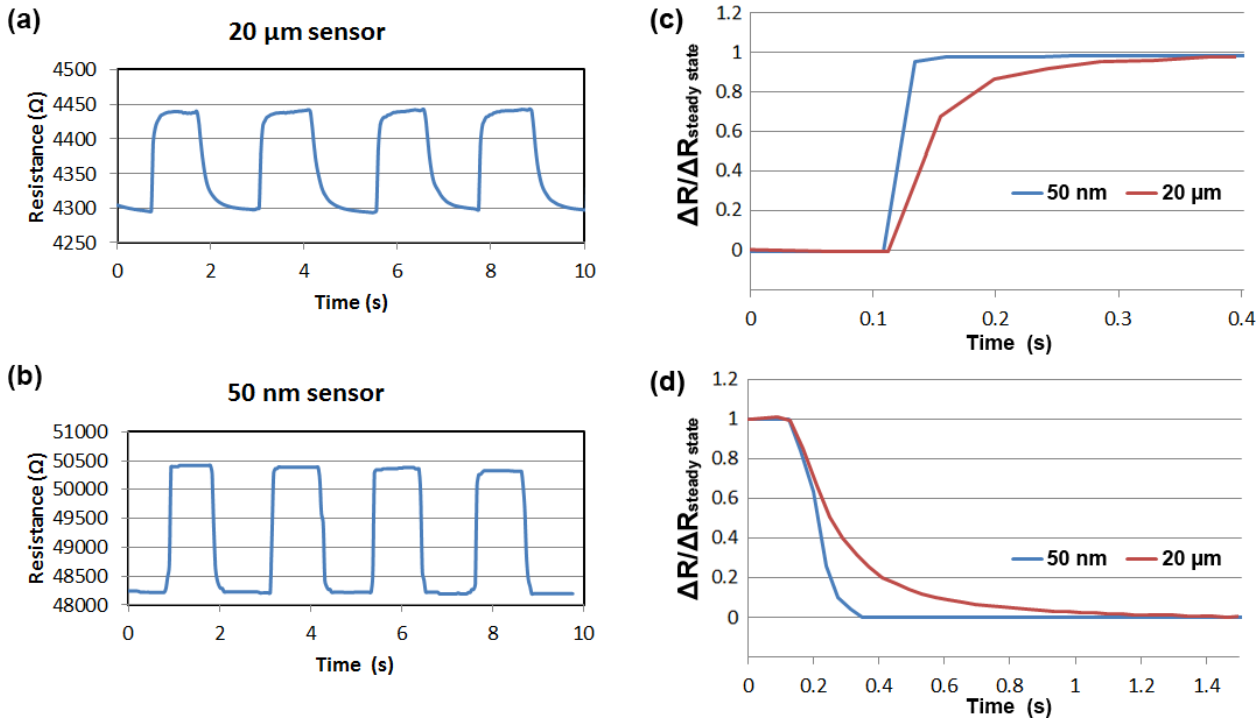

Figure 5.9 Transient responses of (a) 20 µm and (b) 50 nm sensors toward multiple pulses of ethanol vapor in air; note the scale difference. (c) and (d) are zoom-in plots of response and recovery profiles.

5.3.4.3 Sensor response in flow cell

Testing of sensors in a controlled flow chamber provides more accurate control of partial pressures and allows for cross comparison with benchmarks. Figure 5.10 shows response profiles of a pair of devices tested side-by-side in the same testing chamber. The residence time per device of the flow cell is $\tau = V/q$ = 2.5 cm^3 / 10.3 cm^3/s = 0.24 s. For the optical chopper measurements described above, the equivalent residence time is much shorter, approximately 0.03 s. Therefore, response times for the flow chamber measurements are longer for both 50 nm and 20 µm devices. Times to reach saturation for 20 µm devices are approximately 50 s, whereas the times for nanogap

devices are only 8 s. Similarly, times to recover to baseline are about 80 s for 20 µm devices, and only 4 s for nanoscale devices. This is a 20× increase in response rates for the same experimental setup. Based on a number of experimental and theoretical studies,[21, 39, 40] a 10× thinner film should produce a response rate increase by a factor of 100. The results here are qualitatively consistent with expectations. Figure 5.10 also compares the sensitivity of the two devices (inset). In the range of vapor concentrations studied (p/p_0 = 0.01 to 0.05), responses are linear and the average sensitivities are similar. The selectivity properties of the two sensors are also similar, as would be expected for the same ligand capping chemistries.

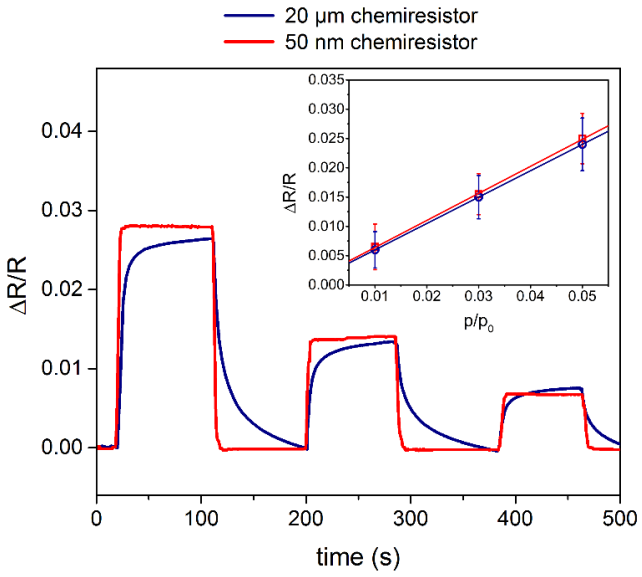

Figure 5.10 Real-time response profiles of a pair of differently-sized chemiresistor sensors fabricated using 1-octanethiol-functionalized gold nanoparticles, tested concurrently inside the same chamber. Sequential exposures to an atmosphere of hexane at p/p_0 = 0.05, 0.03, and 0.01 was carried out. Inset: response vs. vapor concentration for 3 replicates of the experiment.

5.3.4.4 Sensor array response

Figure 5.11(a) compares response patterns of 50 nm and 20 μm devices for a set of six representative vapors covering a wide range of chemical properties. The $\Delta R/R$ responses for the same ligand capping chemistry are similar for the two sensors, within a margin of 15%, and the response patterns are distinctive for each vapor. For example, the 20 μm sensor response to toluene follows $\Delta R/R$ = 0.010, 0.008, 0.006 and 0.013, while the 50 nm sensor response is 0.011, 0.009, 0.009, and 0.015 for the same ordering of the capping ligands. Detailed response values are summarized in Table 5.2. Sensors functionalized with 6-mercaptohexanol show enhanced sensitivity for ethanol and acetonitrile, while 1-octanethiol functionalized nanoparticles show selectivity for hexane and toluene. Figure 5.11(b) compares the response patterns in the form of sensitivity, $S = d(\Delta R/R)/d(p/p_0)$), in radar plots where each axis represents a different capping ligand. The similarity of the response envelopes for both size devices demonstrates that chemical properties of capping ligands are not changed by scaling. The combined sensitivity and selectivity data suggest that the sensing mechanisms are similar for the two types of sensors. We might expect that at some very small length-scale the mechanism for sensing would change or become muted, but that was not observed for these nanoscale devices. Thus, even 0.0025 μm^2 is sufficient to transduce analyte-induced swelling of the nanoparticle networks.

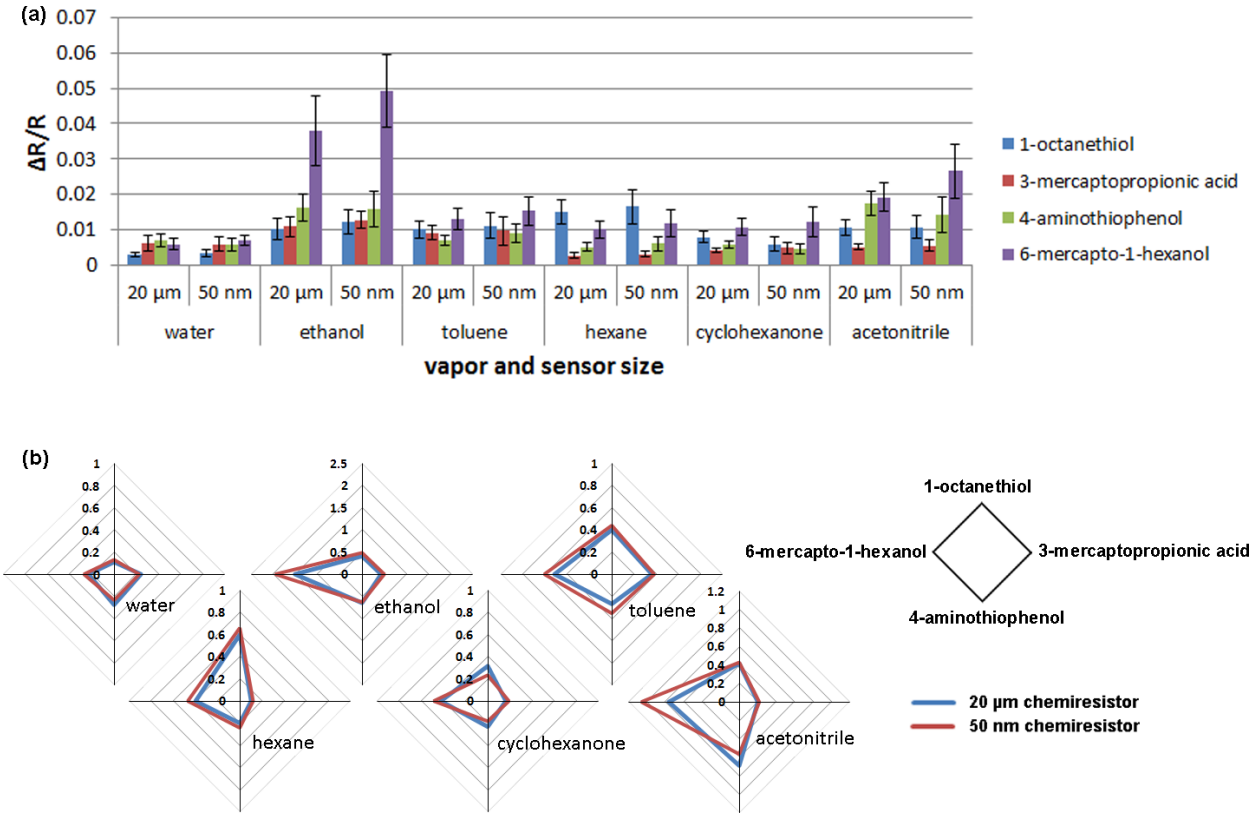

Figure 5.11 (a) Response selectivity of 20 µm and 50 nm chemiresistors both fabricated using gold nanoparticles functionalized with 4 types of ligands and tested against 6 vapors at p/p_0 = 0.03; (b) Radar plots show envelope patterns for sensor sensitivity calculated using the same data from part (a), providing a visual comparison between the two different devices. Axis labels for the radar plots are shown on the right.

Table 5.2 Responses (ΔR/R) of 20 μm and 50 nm chemiresistors both fabricated using gold nanoparticles functionalized with 4 types of ligands and tested for sensing 6 vapors at p/p_0 = 0.03.

		ΔR/R	
vapor	ligand	50 nm chemiresistors	20 μm chemiresistors
water	1-octanethiol	0.003	0.003
	3-mercaptopropionic acid	0.006	0.006
	4-aminothiophenol	0.006	0.007
	6-mercapto-1-hexanol	0.007	0.006
ethanol	1-octanethiol	0.012	0.010
	3-mercaptopropionic acid	0.013	0.011
	4-aminothiophenol	0.016	0.016
	6-mercapto-1-hexanol	0.049	0.038
toluene	1-octanethiol	0.011	0.010
	3-mercaptopropionic acid	0.010	0.008
	4-aminothiophenol	0.009	0.006
	6-mercapto-1-hexanol	0.015	0.013
hexane	1-octanethiol	0.017	0.015
	3-mercaptopropionic acid	0.003	0.003
	4-aminothiophenol	0.006	0.005
	6-mercapto-1-hexanol	0.012	0.010
cyclohexanone	1-octanethiol	0.006	0.008
	3-mercaptopropionic acid	0.005	0.004
	4-aminothiophenol	0.005	0.006
	6-mercapto-1-hexanol	0.012	0.011
acetonitrile	1-octanethiol	0.011	0.010
	3-mercaptopropionic acid	0.005	0.005
	4-aminothiophenol	0.014	0.017
	6-mercapto-1-hexanol	0.027	0.019

The ratios of baseline noise levels to baseline resistance ($R_{noise}/R_{baseline}$) are typically in the range of 4×10^{-4} to 8×10^{-4} for 50 nm devices and 1×10^{-4} to 2×10^{-4} for the 20 μm devices. Given that the response magnitudes (ΔR/R) are similar, the signal-to-noise (S/N) ratios for 50 nm devices are about 4-times degraded compared to the 20 μm sensors. The sensor volume of a 1000-tip nanoscale sensor is about 10^{-10} mm^3, compared to approximately 10^{-3} mm^3 for a 20 μm

sensor. As a result of the relatively low noise levels, the real-time signals of 20 μm devices did not have to be filtered, while percentile filtering was used for the 50 nm device data. While size reduction from the 20 μm devices to 50 nm devices is significant, the deterioration of S/N ratio is comparatively less significant. This non-proportional scaling is probably related to fewer metal-insulator-metal tunnel junctions and fewer defects in the conduction paths. Table 5.3 lists the sensitivity and limits of detection (LODs) for the 2 types of sensors with 4 different capping ligands. The LODs observed for the 20 μm chemiresistors for toluene/octanethiol and ethanol/octanethiol analyte/capping ligand pairs are within an order of magnitude of literature data.[24, 41] The LODs for 50 nm chemiresistors are a few times higher than the 20 μm devices due to the lower S/N ratio.[14]

Table 5.3 Sensitivity and limits of detection (LOD) of 50 nm and 20 μm chemiresistors

vapor	ligand	device type			
		50 nm chemiresistors		20 μm chemiresistors	
		Sensitivity[a]	LOD[b] (ppm)	Sensitivity[a]	LOD[b] (ppm)
water	1-octanethiol	0.13	349.1	0.11	80.5
	3-mercaptopropionic acid	0.23	124.1	0.24	46.5
	4-aminothiophenol	0.23	100.4	0.28	56.6
	6-mercapto-1-hexanol	0.27	198.7	0.23	41.6
ethanol	1-octanethiol	0.48	234.4	0.41	54.1
	3-mercaptopropionic acid	0.50	140.2	0.43	65.2
	4-aminothiophenol	0.63	92.6	0.65	60.1
	6-mercapto-1-hexanol	1.96	68.7	1.52	15.8
toluene	1-octanethiol	0.44	130.3	0.40	27.8
	3-mercaptopropionic acid	0.38	92.8	0.36	39.2
	4-aminothiophenol	0.35	83.6	0.27	73.1
	6-mercapto-1-hexanol	0.61	111.6	0.52	23.4
hexane	1-octanethiol	0.66	470.4	0.60	100.5
	3-mercaptopropionic acid	0.12	1601.0	0.10	744.8
	4-aminothiophenol	0.24	661.4	0.20	532.0
	6-mercapto-1-hexanol	0.47	784.4	0.40	164.3
cyclohexanone	1-octanethiol	0.23	30.9	0.32	4.5
	3-mercaptopropionic acid	0.19	23.5	0.16	11.0
	4-aminothiophenol	0.18	20.5	0.23	10.7
	6-mercapto-1-hexanol	0.49	17.6	0.43	3.6
acetonitrile	1-octanethiol	0.43	428.9	0.42	85.8
	3-mercaptopropionic acid	0.22	524.8	0.20	224.8
	4-aminothiophenol	0.57	167.2	0.69	91.1
	6-mercapto-1-hexanol	1.06	205.3	0.76	50.8

[a]Sensitivity is calculated from the linear approximation of $\Delta R/R - p/p_0$ plots, in the form of Figure 5.10.

[b]LOD is defined as 3× baseline noise divided by sensitivity and converted to units of ppm.

5.3.5 Multiple devices on a single chip

Sequential dielectrophoresis was investigated to achieve integrated devices with different sensing materials on adjacent sensors. Each pair of electrodes was connected to a function generator, one pair at a time. During assembly, neighboring electrode pairs remain open circuit. As demonstrated in Figure 3, nanoparticle assembly occurs only on connected electrodes. In addition, dielectrophoresis on neighboring electrodes do not cause already filled electrode pairs to change resistance. Thus, it is possible to sequentially fill electrode pairs with nanoparticles of different organic capping ligands. Figure 5.12 shows a sensor chip mounted on a TO-3 package with 4 pairs of electrodes, each modified by a different chemistry using sequential dielectrophoresis. The two radar plots compare results for this single chip sensor having 4 integrated devices vs. results from a set of 4 separate sensor chips, each with one of the four different organic capping ligands. The same 4 capping ligands are used for both the integrated and non-integrated sensors. The radar plots show that response selectivity is similar for both device arrangements, and there is no loss of fidelity by sensor integration. The occupied sensing area of the integrated chip is very small and it should be possible to integrate tens, hundreds, or more chemiresistor devices onto a single chip, each with a different capping ligand.

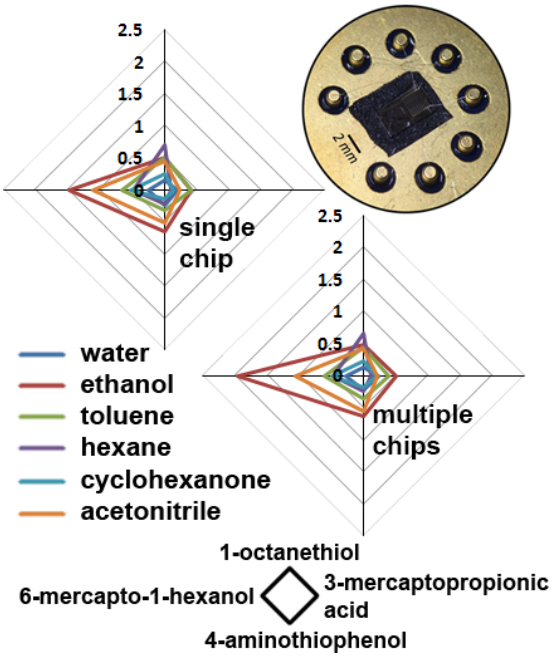

Figure 5.12 Comparison of single-chip vs. multi-chip sensor arrays. Left: sensitivity for an integrated single-chip sensor array made by sequential dielectrophoresis. Right: sensitivity for a multi-chip sensor array, each with a different type of gold nanoparticle. The axis labels for the radar plots are shown at the bottom. The photograph shows an image of an integrated, single-chip sensor.

5.4 Conclusions

In this chapter, we demonstrate scaling of chemiresistor sensors to arrays of nanoscale devices with sensing volumes down to 0.0025 um^2. Dielectrophoresis is shown to allow ligand-capped gold nanoparticles to be deposited locally in nanoscale junctions with 50 nm electrode spacing. The nanoscale sensors have similar sensitivity and selectivity characteristics as chemiresistor devices with larger, micron-scale electrode spacing. The similarity suggests that both sensors operate with the same basic vapor sorption mechanism, and that even very small volumes can transduce analyte sorption. In addition to the smaller scale, nanoscale sensors are

shown to have faster response and recovery, with time scales less than one second for pulse testing in air. We demonstrate that sequential dielectrophoresis can be used to prepare sensors with different sensing materials integrated into a single chip. The results show proof-of-concept for highly functional chemical vapor sensor arrays integrated into small, low power packages with fast response and recovery. By extension, it may be possible to assemble microfabricated sensor chips with tens to hundreds of different sensing chemistries, including built-in redundancy.

5.5 References

1. Kauffman, D. R.; Star, A. Carbon Nanotube Gas and Vapor Sensors. *Angewandte Chemie International Edition* **2008**, 47, 6550-6570.

2. Robinson, J. T.; Perkins, F. K.; Snow, E. S.; Wei, Z.; Sheehan, P. E. Reduced Graphene Oxide Molecular Sensors. *Nano Lett.* **2008**, 8, 3137-3140.

3. Nah, J.; Kumar, S. B.; Fang, H.; Chen, Y.-Z.; Plis, E.; Chueh, Y.-L.; Krishna, S.; Guo, J.; Javey, A. Quantum Size Effects on the Chemical Sensing Performance of Two-Dimensional Semiconductors. *J. Phys. Chem. C* **2012**, 116, 9750-9754.

4. Perkins, F. K.; Friedman, A. L.; Cobas, E.; Campbell, P. M.; Jernigan, G. G.; Jonker, B. T. Chemical Vapor Sensing with Monolayer MoS2. *Nano Lett.* **2013**, 13, 668-673.

5. Wohltjen, H.; Snow, A. W. Colloidal Metal−Insulator−Metal Ensemble Chemiresistor Sensor. *Analytical Chemistry* **1998**, 70, 2856-2859.

6. Peng, G.; Tisch, U.; Adams, O.; Hakim, M.; Shehada, N.; Broza, Y. Y.; Billan, S.; Abdah-Bortnyak, R.; Kuten, A.; Haick, H. Diagnosing lung cancer in exhaled breath using gold nanoparticles. *Nature Nanotechnology* **2009**, 4, 669-673.

7. Raguse, B.; Chow, E.; Barton, C. S.; Wieczorek, L. Gold Nanoparticle Chemiresistor Sensors: Direct Sensing of Organics in Aqueous Electrolyte Solution. *Anal. Chem.* **2007**, 79, 7333-7339.

8. Steinecker, W. H.; Sun Kyu, K.; Bohrer, F. I.; Farina, L.; Kurdak, C.; Zellers, E. T. Electron-Beam Patterned Monolayer-Protected Gold Nanoparticle Interface Layers on a Chemiresistor Vapor Sensor Array. *IEEE Sens. J.* **2011**, 11, 469-480.

9. Wang, L.; Shi, X.; Kariuki, N. N.; Schadt, M.; Wang, G. R.; Rendeng, Q.; Choi, J.; Luo, J.; Lu, S.; Zhong, C.-J. Array of Molecularly Mediated Thin Film Assemblies of Nanoparticles: Correlation of Vapor Sensing with Interparticle Spatial Properties. *Journal of the American Chemical Society* **2007**, 129, 2161-2170.

10. Joseph, Y.; Guse, B.; Vossmeyer, T.; Yasuda, A. Gold Nanoparticle/Organic Networks as Chemiresistor Coatings: The Effect of Film Morphology on Vapor Sensitivity. *The Journal of Physical Chemistry C* **2008**, 112, 12507-12514.

11. Vossmeyer, T.; Guse, B.; Besnard, I.; Bauer, R. E.; Müllen, K.; Yasuda, A. Gold Nanoparticle/Polyphenylene Dendrimer Composite Films: Preparation and Vapor-Sensing Properties. *Adv. Mater.* **2002**, 14, 238-242.

12. Cooper, J. S.; Raguse, B.; Chow, E.; Hubble, L.; Müller, K.-H.; Wieczorek, L. Gold Nanoparticle Chemiresistor Sensor Array that Differentiates between Hydrocarbon Fuels Dissolved in Artificial Seawater. *Anal. Chem.* **2010**, 82, 3788-3795.

13. Dirk, S. M.; Howell, S. W.; Price, B. K.; Fan, H.; Washburn, C.; Wheeler, D. R.; Tour, J. M.; Whiting, J.; Simonson, R. J. Vapor Sensing Using Conjugated Molecule-Linked Au Nanoparticles in a Silica Matrix. *J. Nanomater.* **2009**, 481270 (Article ID) 1-9.

14. Ibañez, F. J.; Zamborini, F. P. Chemiresistive Sensing of Volatile Organic Compounds with Films of Surfactant-Stabilized Gold and Gold−Silver Alloy Nanoparticles. *ACS Nano* **2008**, 2, 1543-1552.

15. Nagraj, N.; Slocik, J. M.; Phillips, D. M.; Kelley-Loughnane, N.; Naik, R. R.; Potyrailo, R. A. Selective sensing of vapors of similar dielectric constants using peptide-capped gold nanoparticles on individual multivariable transducers. *Analyst* **2013**, 138, 4334-4339.

16. Fu, K.; Li, S.; Jiang, X.; Wang, Y.; Willis, B. G. DNA Gold Nanoparticle Nanocomposite Films for Chemiresistive Vapor Sensing. *Langmuir* **2013**, 29, 14335-14343.

17. Snow, A. W.; Ancona, M. G. Sensitivity, Selectivity, and Nanodimensional Effects in Gold Nanocluster Vapor Sensors. *IEEE Sens. J.* **2014**, 14, 3330-3336.

18. Cai, Q.-Y.; Zellers, E. T. Dual-Chemiresistor GC Detector Employing Monolayer-Protected Metal Nanocluster Interfaces. *Analytical Chemistry* **2002**, 74, 3533-3539.

19. Bohrer, F. I.; Covington, E.; Kurdak, Ç.; Zellers, E. T. Characterization of Dense Arrays of Chemiresistor Vapor Sensors with Submicrometer Features and Patterned Nanoparticle Interface Layers. *Analytical Chemistry* **2011**, 83, 3687-3695.

20. Grate, J. W.; Nelson, D. A.; Skaggs, R. Sorptive Behavior of Monolayer-Protected Gold Nanoparticle Films: Implications for Chemical Vapor Sensing. *Anal. Chem.* **2003**, 75, 1868-1879.

21. Ancona, M. G.; Snow, A. W.; Perkins, F. K.; Pate, B.; Park, D. Analyte kinetics in a nanocluster-based chemiresistor: A case study. *Sensors and Actuators B: Chemical* **2013**, 177, 936-946.

22. Ibañez, F. J.; Zamborini, F. P. Chemiresistive Sensing with Chemically Modified Metal and Alloy Nanoparticles. *Small* **2012**, 8, 174-202.

23. Ancona, M. G.; Snow, A. W.; Foos, E. E.; Kruppa, W.; Bass, R. Scaling Properties of Gold Nanocluster Chemiresistor Sensors. *IEEE Sens. J.* **2006**, 6, 1403-1414.

24. Steinecker, W. H.; Rowe, M. P.; Zellers, E. T. Model of Vapor-Induced Resistivity Changes in Gold−Thiolate Monolayer-Protected Nanoparticle Sensor Films. *Analytical Chemistry* **2007**, 79, 4977-4986.

25. Wilson, D. M.; Hoyt, S.; Janata, J.; Booksh, K.; Obando, L. Chemical sensors for portable, handheld field instruments. *IEEE Sens. J.* **2001**, 1, 256-274.

26. Hughes, M. P. *Nanoelectromechanics in Engineering and Biology*. Taylor & Francis: **2002**.

27. Gierhart, B. C.; Howitt, D. G.; Chen, S. J.; Smith, R. L.; Collins, S. D. Frequency Dependence of Gold Nanoparticle Superassembly by Dielectrophoresis. *Langmuir* **2007**, 23, 12450-12456.

28. Kumar, S.; Yoon, S.-H.; Kim, G.-H. Bridging the nanogap electrodes with gold nanoparticles using dielectrophoresis technique. *Curr. Appl. Phys.* **2009**, 9, 101-103.

29. Leiterer, C.; Berg, S.; Eskelinen, A.-P.; Csaki, A.; Urban, M.; Törmä, P.; Fritzsche, W. Assembling gold nanoparticle chains using an AC electrical field: Electrical detection of organic thiols. *Sens. Actuators, B* **2013**, 176, 368-373.

30. Strobel, S.; Sperling, R. A.; Fenk, B.; Parak, W. J.; Tornow, M. Dielectrophoretic trapping of DNA-coated gold nanoparticles on silicon based vertical nanogap devices. *PCCP* **2011**, 13, 9973-9977.

31. Barsotti, R. J.; Vahey, M. D.; Wartena, R.; Chiang, Y.-M.; Voldman, J.; Stellacci, F. Assembly of Metal Nanoparticles into Nanogaps. *Small* **2007**, 3, 488-499.

32. Xiong, X.; Busnaina, A.; Selvarasah, S.; Somu, S.; Wei, M.; Mead, J.; Chen, C.-L.; Aceros, J.; Makaram, P.; Dokmeci, M. R. Directed assembly of gold nanoparticle nanowires and networks for nanodevices. *Appl. Phys. Lett.* **2007**, 91, 063101.

33. Tseng, A. A.; Kuan, C.; Chen, C. D.; Ma, K. J. Electron beam lithography in nanoscale fabrication: recent development. *Electronics Packaging Manufacturing, IEEE Transactions on* **2003**, 26, 141-149.

34. Borini, S.; White, R.; Wei, D.; Astley, M.; Haque, S.; Spigone, E.; Harris, N.; Kivioja, J.; Ryhänen, T. Ultrafast Graphene Oxide Humidity Sensors. *ACS Nano* **2013**, 7, 11166-11173.

35. Snow, A. W.; Ancona, M. G.; Park, D. Nanodimensionally Driven Analyte Response Reversal in Gold Nanocluster Chemiresistor Sensing. *Langmuir* **2012**, 28, 15438-15443.

36. Snow, A. W.; Wohltjen, H. Size-Induced Metal to Semiconductor Transition in a Stabilized Gold Cluster Ensemble. *Chem. Mater.* **1998**, 10, 947-949.

37. Yang, C.-Y.; Li, C.-L.; Lu, C.-J. A vapor selectivity study of microsensor arrays employing various functionalized ligand protected gold nanoclusters. *Anal. Chim. Acta* **2006**, 565, 17-26.

38. Terrill, R. H.; Postlethwaite, T. A.; Chen, C.-h.; Poon, C.-D.; Terzis, A.; Chen, A.; Hutchison, J. E.; Clark, M. R.; Wignall, G. Monolayers in Three Dimensions: NMR, SAXS, Thermal, and Electron Hopping Studies of Alkanethiol Stabilized Gold Clusters. *Journal of the American Chemical Society* **1995**, 117, 12537-12548.

39. Briglin, S. M.; Lewis, N. S. Characterization of the Temporal Response Profile of Carbon Black−Polymer Composite Detectors to Volatile Organic Vapors. *J. Phys. Chem. B* **2003**, 107, 11031-11042.

40. Hitchman, M. L. *Measurement of dissolved oxygen*. John Wiley & Sons Canada, Limited: **1978**.

41. Guo, J.; Pang, P.; Cai, Q. Effect of trace residual ionic impurities on the response of chemiresistor sensors with dithiol-linked monolayer-protected gold (nano)clusters as sensing interfaces. *Sens. Actuators, B* **2007**, 120, 521-528.

Chapter 6

AQUEOUS-PHASE GOLD NANOPARTICLE CHEMIRESISTOR SENSORS

6.1 Introduction

As our thermodynamic characterization in Chapter 3 has shown, solid-state DNA shows prevalent non-specific vapor sorption behavior in the gas phase, with LSER parameters within the range exhibited by synthetic polymers. To achieve specific sensing of analytes that employs biomolecular recognition, the most practical way is to perform detection in an environment that mimics the native folding environment of the aptamers, i.e., a buffered aqueous environment. This can be done either through directly putting the sensors in an aqueous environment as typically done in aptamer-based sensors,[1, 2] or more ideally, encapsulating the sensors in a micro-environment mimicking the aqueous environment.[3, 4] Both of these two ways showed the desired specific sensing, but the direct liquid is more straightforward and more abundantly used in exploratory studies.[1] Therefore, as a proof of concept for the combination of chemiresistor transduction mechanism and molecular recognition, the first step is to experiment with aptamer-incorporating chemiresistors that work directly in free-flow aqueous conditions.

To utilize aptamers in aqueous conditions, it is intuitive to learn from past experiences of aqueous phase detection of analytes on other platforms. To date, a variety of platforms have been

developed, with some examples shown in Figure 6.1. In surface plasmon resonance (SPR), biomolecular sensing elements can be directly conjugated to a physically fixed flat gold surface.[5] Similarly, quartz crystal microbalances coated with aptamer can perform biomolecular detection as a result of oscillation frequency changes associated with aptamer-target binding.[6] This is the similar case for photonic crystals functionalized with aptamers,[7] which use a fixed surface for immobilizing biomolecular recognition elements, but in this case nanostructured surfaces are needed in the transducer. Closer to the current electronic sensor design is the aptamer based liquid gated field effect transistor (FET) graphene sensor, which uses a fixed piece of graphene as the conduction channel.[8] In this scheme, the individual aptamer molecules are fixed onto the sensor by attachment to the graphene sheet. In another similar example using carbon nanotubes as the FET channel, the carbon nanotubes were grown by chemical vapor deposition (CVD) on substrates, and electrical leads were patterned on top of the nanotubes. This way, the carbon nanotubes were immobilized on the devices, and biotins can then be chemically bonded to the carbon nanotube surface.[9]

Learning from these examples, it can be generalized that the aptamer-based chemiresistors should first employ strong bonding to immobilize the biomolecular sensing elements to the solid surfaces, and secondly maintain a natural folding environment. Most of these sensing systems developed for aqueous sensing utilize optical and electrochemical transduction mechanisms, with only FET being a simpler electrical transducer. It remains to be seen whether gold nanoparticle-based chemiresistor is more sensitive or more selective than the FET, as well as the other sensing platforms. However, there are advantages inherent to the chemiresistor system. First, there is no need to presort semiconducting carbon nanotubes, and there are no stacking forces between DNA

and carbon rings that could alter the conformation of aptamers. Second, there are size reduction benefits that were discussed in Chapter 5.

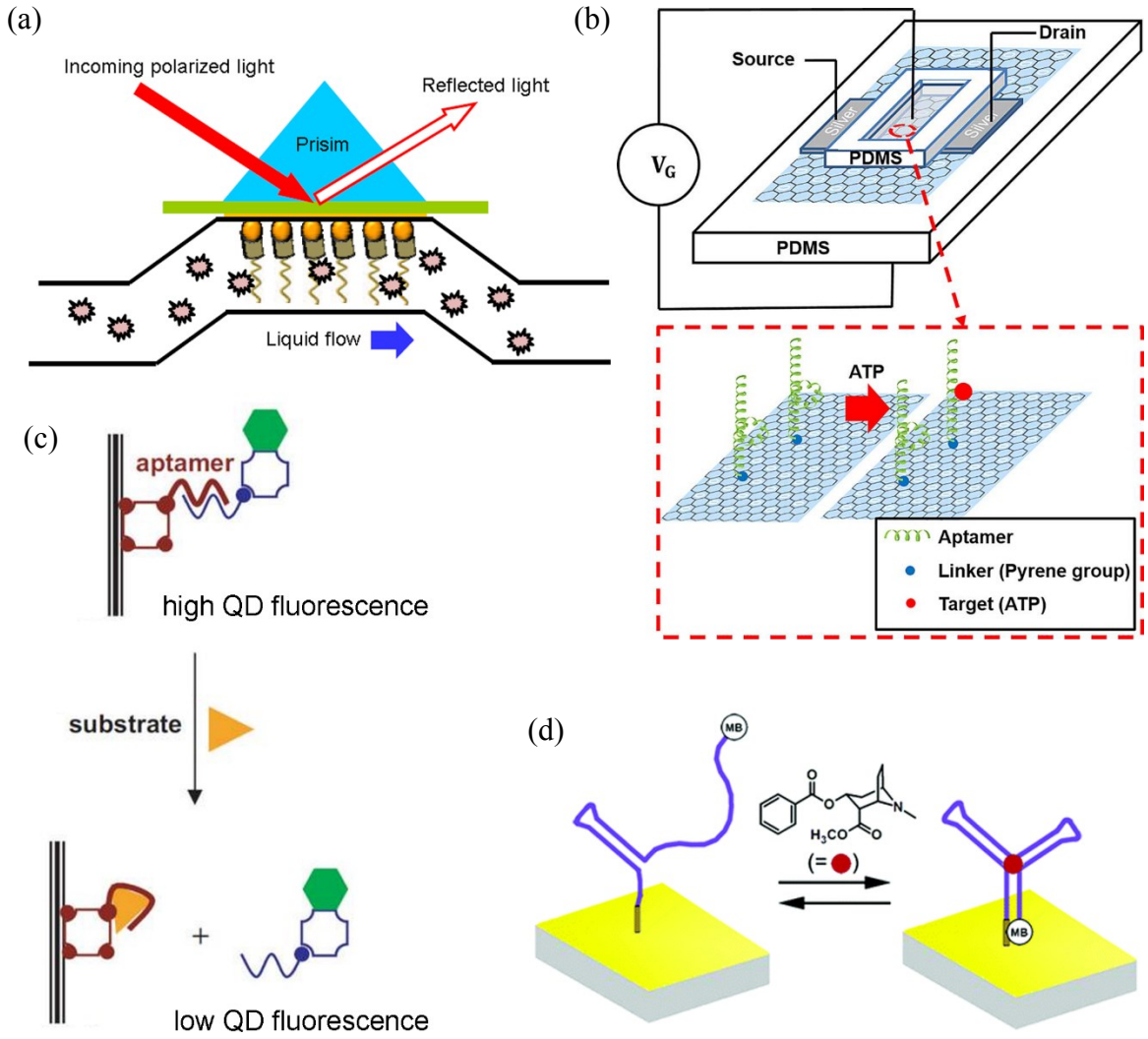

Figure 6.1 Aqueous biomolecular detection systems: state of the art. (a) SPR platform;[6] (b) FET platform;[8] (c) Fluorescence;[10] and (d) Electrochemical sensor.[11]

Specifically, the current gold nanoparticle system needs to overcome two challenges: (1) maintain nanoparticle attachment to the substrate, and (2) forming a high-quality conductive path. Ideally, aqueous based tunneling devices operate similarly to tunneling devices that operate in air or vacuum in terms of working principles, with the tunneling current dependent on various properties of the medium and the tunnel junction material.[12] A network of gold nanoparticles could work similarly in a liquid environment as they are work in a gas-phase environment, so long as the film integrity is intact.

In the seminal work by Raguse et al.,[13] it was shown that at low frequency (< 10 Hz) AC and DC conditions, electron tunneling through a densely-packed, organic-ligand functionalized nanoparticle film dominates over other forms of charge transport through an ion-rich aqueous medium. This work engendered many ensuing studies that capitalized on nanoparticle chemiresistors to perform sensing of dissolved hydrocarbons and seawater[14] and bacteria metabolites in biological fluids.[15] A simplified circuit model of nanoparticle films operating in aqueous conditions is shown in Figure 6.2(a), and which can be represented mathematically using Equation 6.1.

$$Z^{-1} = \left(\frac{2}{j\omega C_{dl}} + R_E\right)^{-1} + {R_{NPF}}^{-1} \tag{6.1}$$

Solution resistance R_E is defined as resistance from the bulk solution, not including the double layer impedance arising from the electrode-solution interface. At 5 μm interelectrode spacing and in a solution with 1M KCl, $R_E < 0.1\ \Omega$. When 1-hexanethiol was used to functionalize the gold nanoparticles producing a film thickness of ~ 600 nm, the film resistance through 5 μm

inter-electrode spacing is ~ 6 MΩ. Although the solution resistance is orders of magnitude smaller than nanoparticle film resistance, the double layer capacitance C_{dl} is sufficiently small at ~ 15.6 μF/cm^2. As a result, at low frequencies (< 10 Hz) or DC conditions, because of the double layer effects, the impedance through the liquid conduction path is at least 2 orders of magnitude higher than that through the nanoparticle film, making the signal from the nanoparticle film dominant over that through the aqueous solution (Figure 6.2(c), (d)). R_{NPF} is the resistance of organic-ligand functionalized gold nanoparticle film. When the nanoparticle film is absent or the nanoparticle film conduction path is incomplete, the equivalent circuit is represented by in Figure 6.2(b), and the impedance between two electrodes is simply

$$Z^{-1} = \left(\frac{2}{j\omega C_{dl}} + R_E\right)^{-1} \tag{6.2}$$

In this case, the majority of the impedance at low frequencies arises from the double layer capacitance, C_{dl}. When a nanoparticle film is present between the electrodes, R_{NPF} provides a bypass path for electrical conduction, and if the film resistance is sufficiently small, the low frequency electrical conduction would be dominated by electron transfer through the nanoparticle film. Key to this success is that the chemiresistors fabricated with water-insoluble gold nanoparticles functionalized with small-molecule thiols are stable in an aqueous environment, and are not degraded by liquid flow.

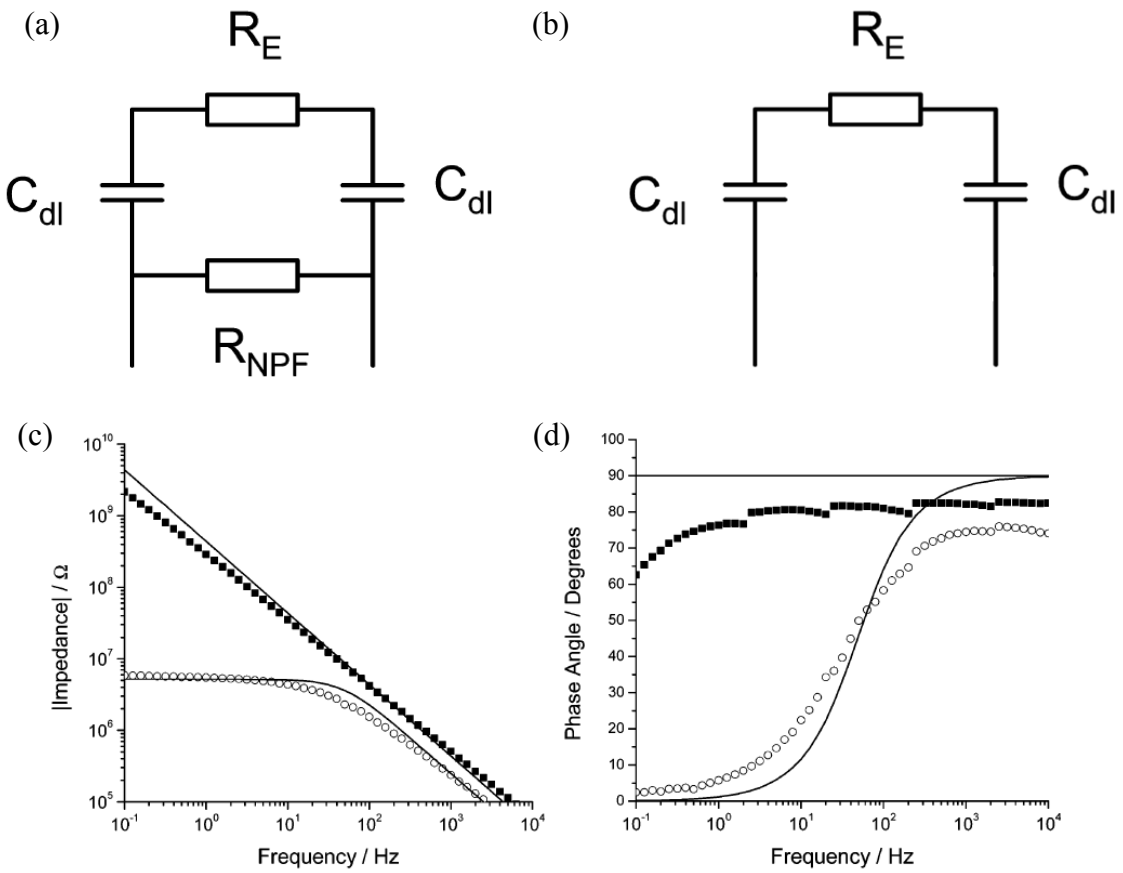

Figure 6.2 (a) Equivalent circuit model of a gold nanoparticle film in an aqueous environment; (b) Equivalent circuit model of a pair of blank electrodes immersed in an aqueous environment; (c) Bode (|Z|) and (d) Bode (phase) plots using gold band electrodes covered with hexanethiol-AuNP films (open circles) and without deposited AuNP films (solid squares) immersed in 1 M KCl solution. The primary differences are in the low frequency region (< 100 Hz).[13]

However, film integrity of aqueous-phase soluble gold nanoparticles in aqueous environment would be a challenge. As the nanoparticles are themselves water-soluble, the

maintenance of sensor integrity in aqueous environment with water-soluble gold nanoparticles is more challenging than for other types of sensing platforms mentioned above. While the recognition element is water-soluble, some mechanisms, either in terms of chemical bonding, or physical confinement of the biomolecules, become necessary in maintaining the integrity of the sensor devices. The molecular electronic devices by Liu et al.[16] uses amine functionalization of the carbon nanotube ends to enable direct bonding with thrombin aptamers. Through the covalent bridge between the thrombin aptamer and the carbon nanotubes, the thrombin aptamer was successfully immobilized on the device. The device showed reversible binding with the target thrombin. Importantly, the conduction was verified to be electronic, and ionic conduction was ruled out. The thrombin-aptamer binding event was proposed to alter the rigidity of the G4 conformation in the DNA structure and promote tight π packing, thus enhancing DNA charge transport.[17] The verification of predominantly electronic conduction occurring through DNA in nanoscale junctions immersed in Tris-HCl buffer solutions is an encouraging sign that detecting electronic conduction through biomolecules in nanoscale junctions is feasible.

As we have observed in Chapter 3, dense films of DNA-functionalized gold nanoparticles can work in a similar way as alkanethiol-functionalized gold nanoparticles in the gas phase. However, in the highly hydrated state, the DNA films on the micron-scaled devices are swollen and the device conductivity increased remarkably. This study presents a complicating issue to the reliable chemical sensor operation in aqueous conditions using DNA-functionalized gold nanoparticles. In principle, signals associated the ionic conduction regime could possibly carry information on the molecular binding events, but this electrochemical detection is less novel, requires different interpretation and instrumentation, thus it is out of the scope of this study. To maintain electronic conduction through aqueous films, which is required for the electron

tunneling-based detection, effective immobilization of the nanoparticles on devices to create a sufficiently dense film is essential.

In this chapter, the investigation is focused on fabrication conditions that produce nanoparticle films that work well with DNA functionalization and aqueous environment. In a step-by-step approach, we will start with evaluating the aqueous performance of alkanethiol-functionalized gold nanoparticle films and DNA-functionalized gold nanoparticle films on micron-scale devices, and move on to evaluating the effect of using these nanoparticles on nanoscale devices. We examine the film integrity using IV measurements and SEM across all types of devices to identify suitable fabrication conditions. While micron-sized gaps on devices show limited success with deposition of DNA-functionalized gold nanoparticles, the nanoscale devices are shown to be advantageous. Combining the film integrity benefits of nanoscale electrodes that we discovered in Chapter 5 and additional substrate surface modification techniques, it is shown that DNA-functionalized gold nanoparticles could be successfully immobilized in 50 nm junctions, while in the meantime achieving a satisfactory film electronic conductance. This success is a significant progress towards aqueous-based electron tunneling devices that use biomolecular recognition elements.

6.2 Fabrication of devices

6.2.1 Device designs

For testing in liquid environments, electrodes must be properly designed to interface with the liquid environment while allowing connection to the electronic systems in air. Photolithography-fabricated contact lines that go underneath the flow cell body are one of the

neatest designs that are compatible with liquid flow cells, which have also been used by others in similar experiments.[13, 16] As the micro-fabricated contact lines are usually very thin (< a few hundred nanometers), the presence of these lines underneath the PDMS barrier that separates liquid and air would not cause issues with liquid leakage as long as proper sealing of the microfluidic cell is in place.

6.2.1.1 5 µm devices

By using similar dimensions but longer contact lines, 5µm devices were designed to be compatible with the PDMS flow cell. Figure 6.3 illustrates the design of devices. The devices have parallel electrodes separated by 5 µm, with four devices on a single chip, arranged in a linear configuration. The devices were fabricated using standard photolithography.

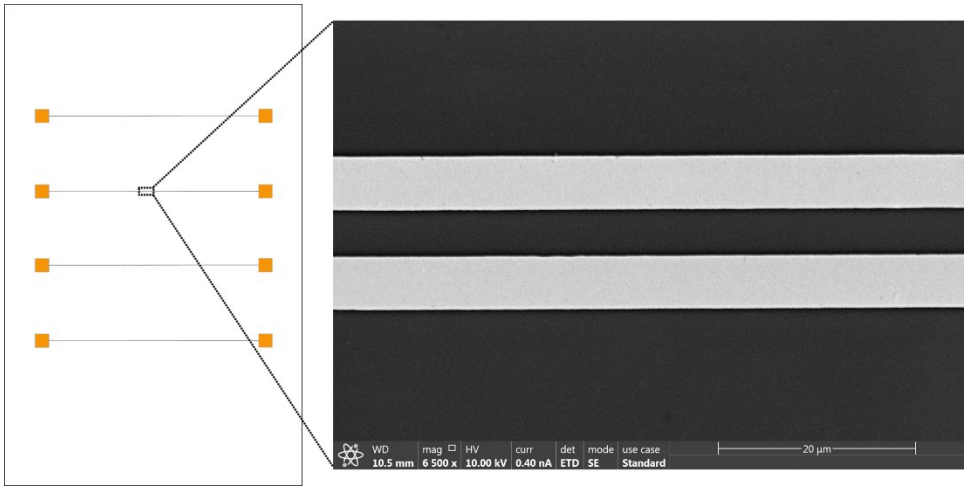

Figure 6.3 Schematic of 5 µm parallel line devices, four on a chip, that work with the custom-designed PDMS flow cell. The local area is magnified in this SEM image to show the parallel line electrodes.

6.2.1.2 50 nm devices

The 50 nm devices, in the form of 10 pairs of parallel lines on a 4 mm × 4mm chip, were similar in design to those used in gas-phase chemiresistors in Chapter 5 (Figure 2.3).

6.2.2 Surface functionalization of device substrates

Substrates were first cleaned by washing with water, acetone, and ethanol, followed by UV-ozone cleaning. Next, exposed SiO_2 surfaces on the substrates were treated with silanizing agent prior to gold nanoparticle deposition to enhance adhesion of nanoparticles to the surface.[18, 19] The patterned SiO_2 chips were immersed in a solution containing 2% v/v MPTES in toluene for 2 h at room temperature, followed by rinsing with copious amounts of toluene, removal of solvent by blowing with a stream of nitrogen. The patterned substrates were cured in an oven at 110 °C for 1 h as a necessary step to improve the coupling capability of the thiol-functionalized silane.[18]

6.2.3 Fabrication sensor devices with citrate-functionalized gold nanoparticles

Citrate-functionalized gold nanoparticles were deposited through electrospray (details in Chapter 2) on both 5 μm and 50 nm devices. A solution of citrate-stabilized gold nanoparticles (OD = 1) was sprayed at a flowrate of 0.05 ml/h and an electrode potential of 6.0 kV. For 5 μm devices, the nozzle was scanned along the chip surface, allowing 4 parallel devices to be fabricated simultaneously. For 50 nm devices, multiple chips were arranged in a line and sprayed-coated concurrently.

6.2.4 Fabrication of sensor devices with DNA-functionalized gold nanoparticles

24A (ATP/adenosine aptamer) was used for electrospray fabrication of aqueous chemiresistor sensors. DNA-functionalized gold nanoparticles were electrosprayed onto silanized patterned in a similar way as citrate-functionalized gold nanoparticles on both 5 μm and 50 nm

devices. A solution of DNA-functionalized gold nanoparticles (OD = 1) was sprayed at a flowrate of 0.05 ml/h and an electrode potential of 5.7 kV. Similar to citrate-functionalized gold nanoparticles, for 5 μm devices, the nozzle was scanned along the chip surface, allowing 4 parallel devices to be fabricated simultaneously. For 50 nm devices, multiple chips were arranged in a line and sprayed-coated concurrently.

6.3 Microfluidic experimental setup

6.3.1 Preparation of flow cells

Cured, cut PDMS flow cells were obtained from the soft lithography processes described in Chapter 2. On a single piece of PDMS flow cell, inlet and outlet ports were punched with a No. 3 biopsy punch, and 1/8" plastic tubings were connected to the flow cells using Teflon fittings. The finished, cured flow cell has a thickness of approximately 0.5 cm. Under the internal elastic force of the rubbery flow cell, the punched holes contract to form holes that are 1.5 mm in diameter, which produces a tight fit for the inserted Teflon fittings.

Two types of flow cells were prepared. For experiments with 5 μm devices, the flow cell has a channel width of 0.5 cm and channel height of 0.5 mm. For experiments with 50 nm devices, the flow cell channel has a height of 1.5 mm to accommodate the additional height of the extra chip which will be placed inside the flow channel. To prepare this flow cell, a thin sheet of cured PDMS of thickness 1 mm and was made by pouring liquid PDMS into a Petri dish and curing directly. A 3.5 cm × 0.5 cm rectangular void in was carved out in the center of the thin PDMS sheet to match the footprint of the flow channel fabricated using 3D printing and casting. The dimension of the thin PDMS sheet also matches that of the 3D-printing fabricated flow cell. The

3D-printing fabricated flow cell was then stacked on top of the 1 mm PDMS sheet to make a heightened flow cell with unchanged lateral dimensions.

6.3.2 Printed circuit board (PCB) device holder

A custom-made PCB serves as the holder of the microfluidic flow cell and the devices, and the interface between the microelectronic parts and the measurement instruments. The PCB was designed by Amadeusz Nasuta from Machine Shop of UConn Engineering Technical Services, and custom-manufactured by Where Labs, LLC (dirtypcbs.com, Muscatine, IA). Figure 6.4 shows the plan view of the PCB and a finished product. Contact stripes on the circuit board were gold-plated, and positioned 6 mm apart, in alignment with the spacing of neighboring devices on the 5 µm devices chip. The ends of the contact stripes are connected to a set of vertical contact pins (1 mm diameter), which connect to SMU or electrochemical workstations.

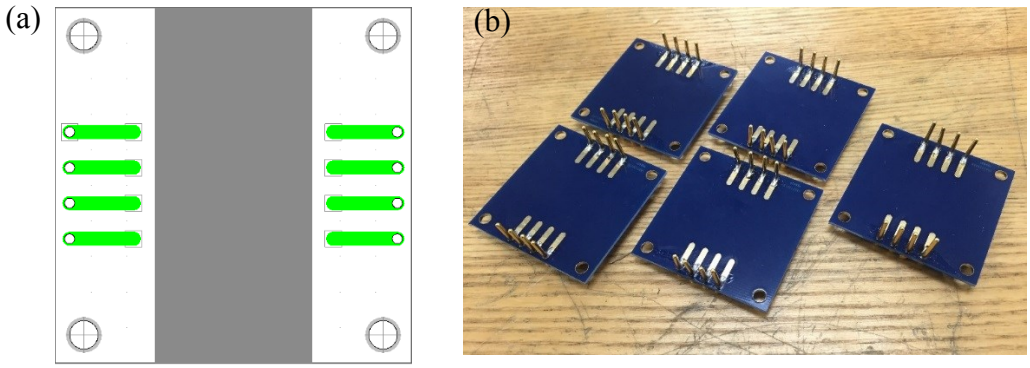

Figure 6.4 (a) circuit board design and (b) photo of a complete PCB product

6.3.3 Integration of 5 μm devices with liquid flow systems

Each Si/SiO_2 chip carrying nanoparticle devices were first pasted against a glass slide using double-sided tape. The use of glass slide provides strength to the thin Si/SiO_2 chip which may be easily broken upon removal from the PCB device holder after experiments. The back of the glass slide was then pasted on the PCB chip holder. A PDMS flow cell was then aligned with the device and pressed against the device using elastic bands wrapped around the flow cell and the PCB chip holder. Contact pads from the devices were then wire bonded to the contact stripes on the PCB device holder.

6.3.4 Integration of 50 nm devices with liquid flow systems

5 μm Si/SiO_2 chips were used as baseboards for the nanoscale devices. The devices were pasted using double side tape on the non-patterned regions in the center of the larger Si/SiO_2 chips, and a selected pair of contact pads on the nanoscale device chip were wire bonded to the gold fingers on the larger Si/SiO_2 chips, creating a "tethered" design. The 50 nm device chips were pasted on the surface of 5 μm devices using carbon tape, with one pair of parallel line electrodes wire-bonded to one parallel lines on the 5 μm devices. As the conductance through the aqueous solution is much smaller than that through the device at low frequencies, exposing the contact pads and bonding wires to the liquid environment are not expected to cause a problem with electrical measurements.

A PDMS flow cell with 1.5 mm channel height was then pressed against the Si/SiO_2 chip, completely encasing the 5 mm × 5 mm die. Elastic bands were then wrapped around the flow cell and the PCB chip holder to press the flow cell against the chip. Contact pads on the Si/SiO_2 chip were then wire bonded to the contact stripes on the PCB device holder.

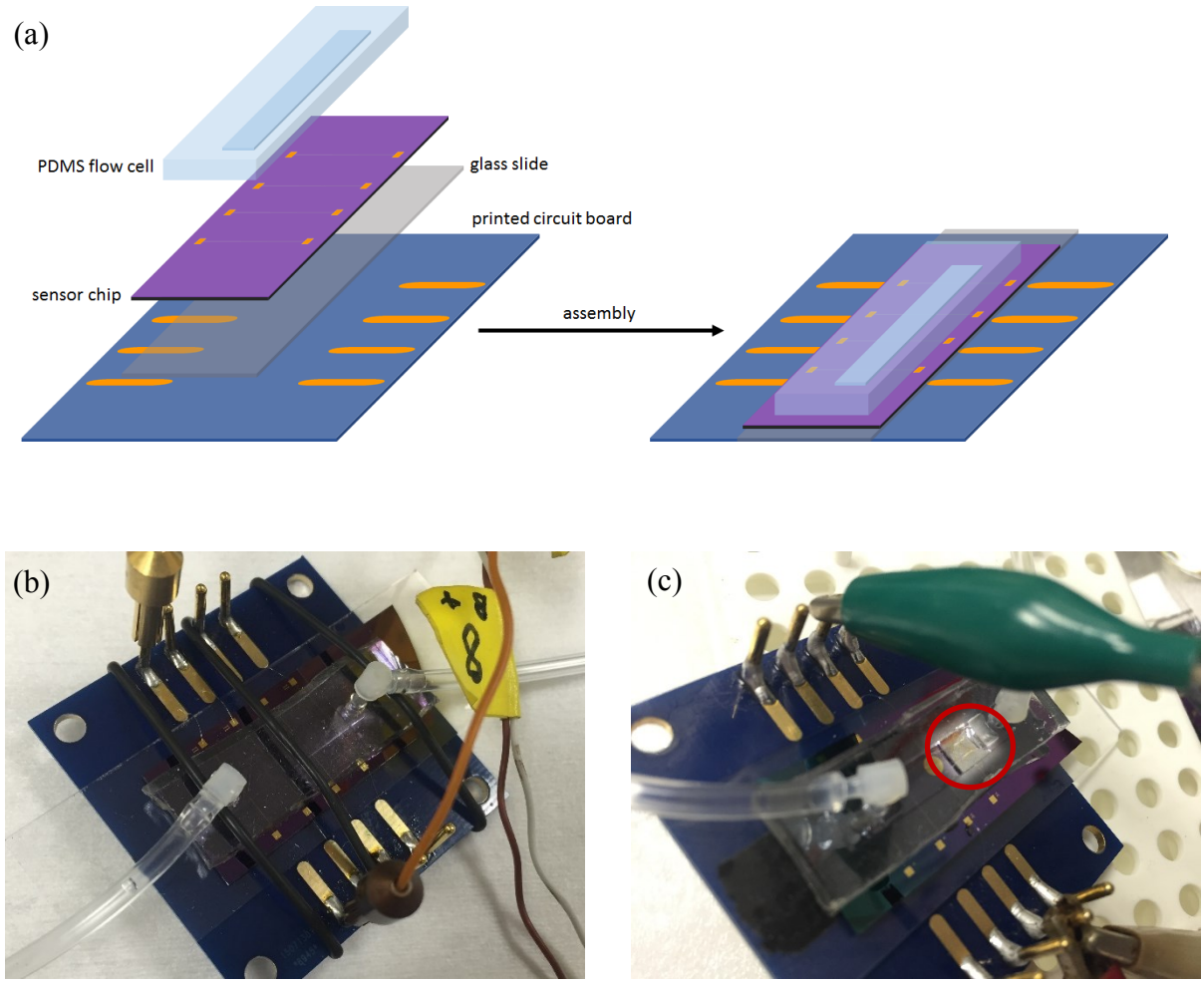

Figure 6.5 (a) Assembly of microfluidic setup, and photos of microfluidic setup for (b) 5 µm device; (c) 50 nm device. The 50 nm device is highlighted and circled in (c) as the small chip pasted and wire-bonded to electrodes on the large chip along the channel direction.

6.4 Results and discussion

6.4.1 Characterization of SiO_2 surface functionalization

Silanized SiO_2 surface compared with cleaned was found to be more hydrophobic than the surface just after oxygen plasma cleaning, as indicated by contact angle observations. XPS analysis

shows presence of sulfur species on the surface after extensive washing with toluene, indicating the successful modification of the surface with molecules containing sulfhydryl groups.

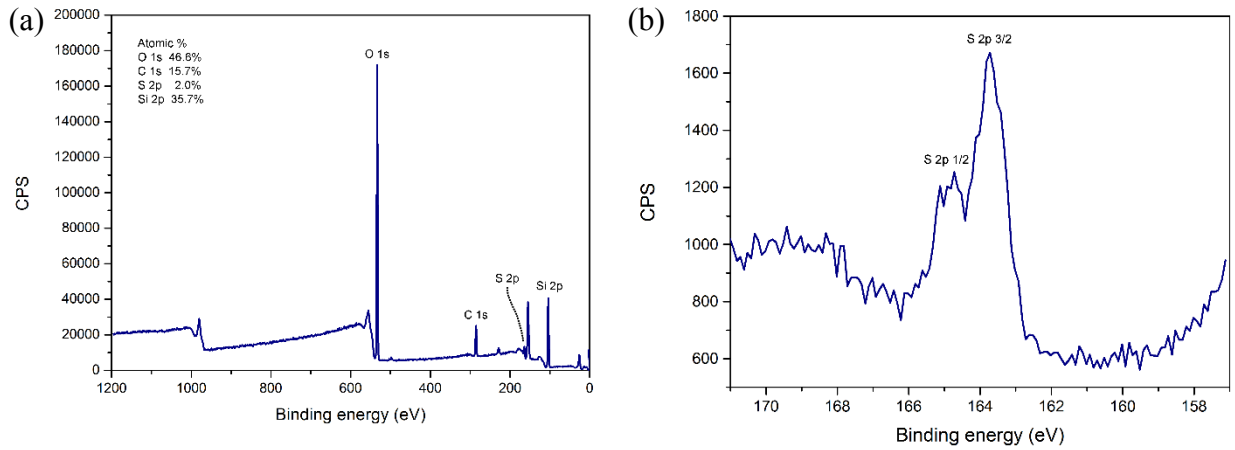

Figure 6.6 XPS of MPTES-treated SiO_2 surface: (a) survey scan; and (b) S 2p peaks scan.

6.4.2 Characterization of nanoparticle attachment

Nanoparticle attachment under liquid conditions is a key issue with the aqueous-phase sensors. To date, the only type of gold nanoparticle chemiresistors that work under aqueous environments are those developed by Raguse et al.[13-15] This type of chemiresistors were purposely rendered water-insoluble through a ligand-exchange procedure. The initial water soluble ligand 4-dimethylaminopyridine (DMAP) which protects the gold nanoparticles were replaced with water-insoluble, thiolated small molecule ligands before any contact with aqueous environments. In an effort to learn more about these water-soluble gold nanoparticle films, we have performed solubility tests with water-soluble citrate-functionalized gold nanoparticle films drop-cast on MPTES-treated SiO_2 surface in water. Not surprisingly, the film of citrate-functionalized gold

nanoparticles turned red upon contact with water, and the majority of the gold nanoparticles were redissolved. Still, after continuous washing with water, it was noticed that minute amount of gold nanoparticles remained. For microfabricated devices with interelectrode spacing in the range 5 μm to 20 μm, this dissolution process in water would be catastrophic to the device integrity, as a contiguous film would be necessary for electronic conductance through the devices. However, close inspection of these damaged nanoparticle film reveals clusters of nanoparticle clusters that were resistant to the solvent. This observation shows non-uniform quality of gold nanoparticle attachment to the silanized SiO_2 surface. The clusters range from tens to over a hundred nm in dimensions. Therefore, it can be speculated that solvent-resistant chemiresistor devices in this size range could be fabricated. In Chapter 5, it is also observed that when the device dimensions are small, in the tens of nm range, the film quality requirement for working devices would be much reduced. For example, thickness less than 50 nm is sufficient.

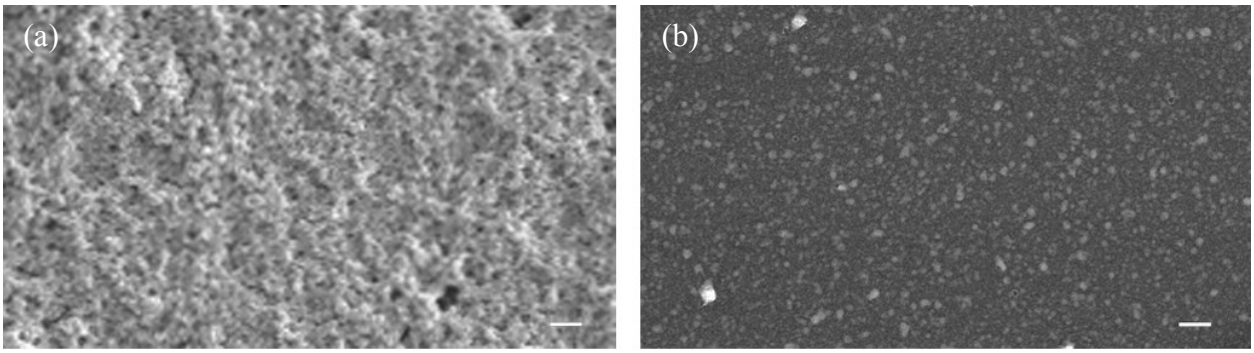

Figure 6.7 Effect of initial washing on citrate-functionalized gold nanoparticles on MPTES-treated SiO_2 surface. (a) before wash; (b) after wash. Scale bar: 1 μm.

Electrosprayed nanoparticles on devices are deposited as thick films visible to the naked eye, however it is not surprising that upon the first washing with copious amount of water, only minute amount of gold nanoparticles was left behind. Subsequent exposure of the as-made devices to water was performed by gentle dropping of water using pipette and blotting away using a piece of Kimwipe (Kimberly-Clark, Irving, TX). SEM reveals nanoparticles on the SiO_2 surfaces within and around the parallel electrode regions remain attached to the surface (Figure 6.8(a), (b)). Therefore, remaining nanoparticles were more resistant to subsequent exposure to water.

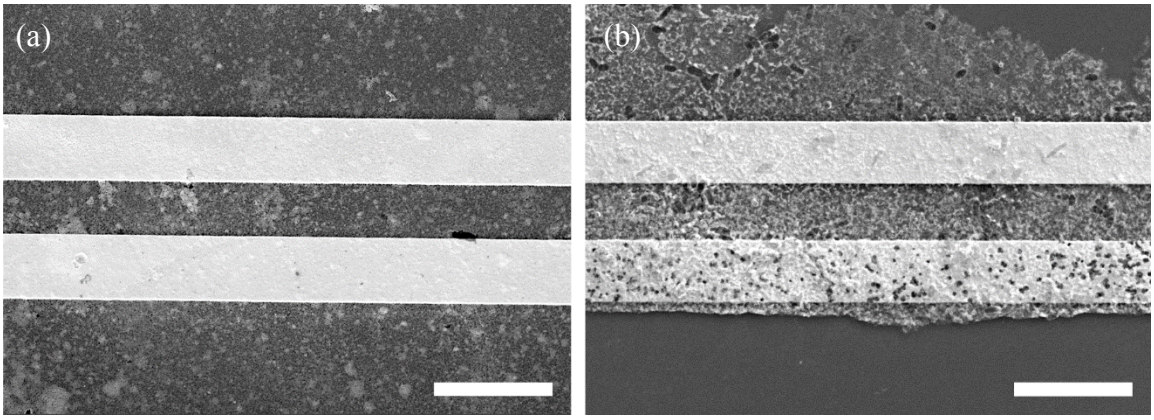

Figure 6.8 Effect of water exposure on washed aptamer-functionalized gold nanoparticle films on 5 μm devices. Scale bar: 10 μm.

For nanoparticles assembled on nanoscale devices through dielectrophoretic assembly, washing expectedly removes loosely-attached nanoparticles from the devices. However, considerable amounts of nanoparticles were found to remain at tip regions (Figure 6.9). Repeated exposure to water after the first washing does not significantly remove more nanoparticles from the device surface. The presence of remaining gold nanoparticles serves as a basis for operability

of sensors in water. All aqueous nanoparticles were electrosprayed in this study. Electrospray of nanoparticles is shown to have minimized the coffee ring effect associated with drying of large droplets of nanoparticle solutions and formed more uniform thickness nanoparticle thin films.

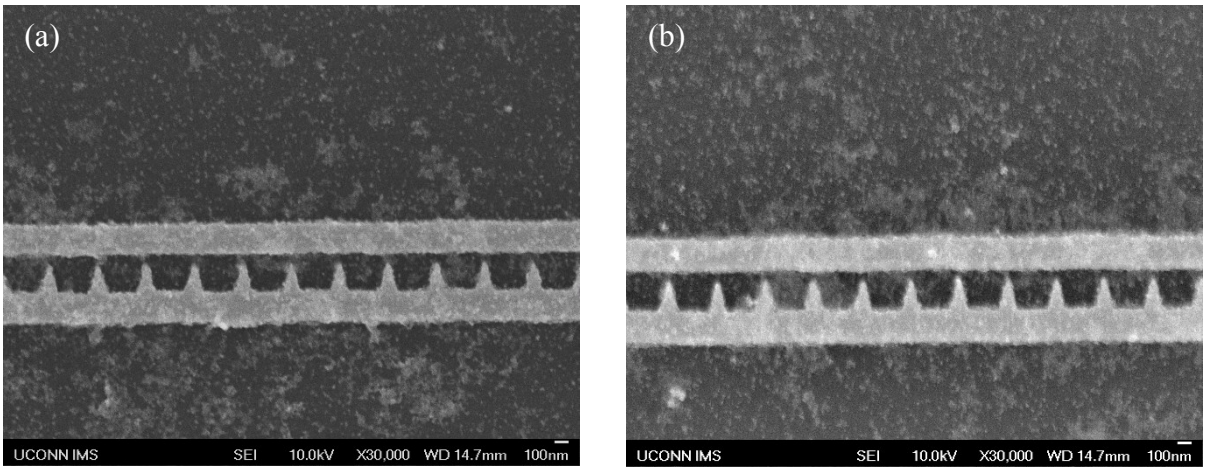

Figure 6.9 Effect of contact with water on washed aptamer-functionalized gold nanoparticle films on 50 nm devices (a) before contact with water; (b) after contact with water.

6.4.3 Current-voltage measurements

Current-voltage characteristics were obtained from multiple sets of comparative experiments to examine the performance of these devices in an aqueous environment. For IV curves performed in water, the maximum voltage applied is 50 mV to prevent electrochemical reactions from occurring. Before testing, blank 5 μm and 50 nm devices were first characterized to serve as references (Figure 6.10). The distances between electrodes were different by 2 orders of magnitude, but the electrical behaviors were similar. The 5 μm device shows a slightly looped

IV curve due to capacitance arising from the electrodes, but the absolute current for both devices are well below 10^{-9} A.

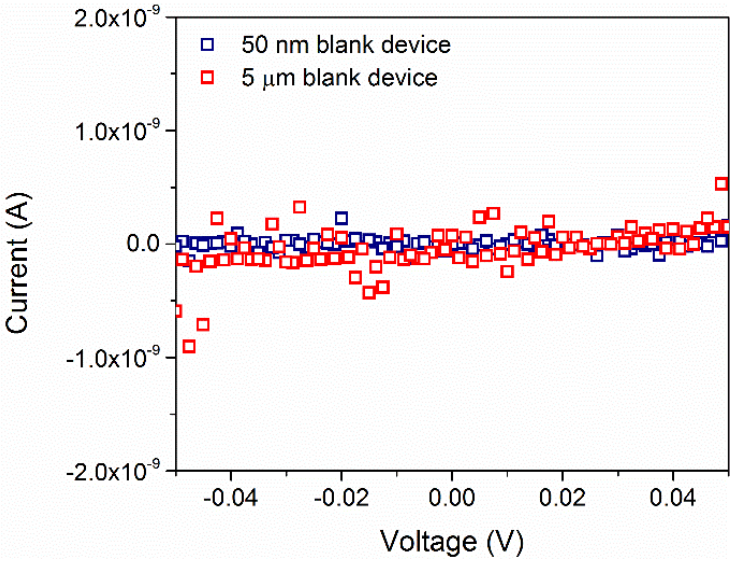

Figure 6.10 IV characteristics of 5 μm and 50 nm blank devices in 1× PBS

Figure 6.11 shows the IV curves of 4 typical devices studied for their performance in nitrogen gas and in solution. Citrate-functionalized gold nanoparticles are similar to aptamer-functionalized gold nanoparticles in both sizes. As derived from Figure 6.11(a) and (b), the as-fabricated 5 μm devices show resistances measured in nitrogen as about 40 MΩ for citrate-functionalized gold nanoparticles, and 100 MΩ for aptamer-functionalized gold nanoparticles. These values are larger than dedicated vapor sensors because the washing step removes layers of the soluble nanoparticles after they were deposited by electrospray. The nanoparticles that remain attached to the SiO_2 substrate form the limited conduction pathway.

When immersed in a buffered aqueous solution (1× phosphate buffered saline, PBS), the IV curves show noisier and more scattered points with very small slopes. Compared with a blank 5 μm device, the IV curves are similar. This behavior indicates a significantly hydrated and swollen gold nanoparticle film in which interparticle electron tunneling could not occur. Because of the very thin layers of nanoparticles, the ionic conduction behavior in high-humidity hydrated multilayered nanoparticle films that were observed in Chapter 4 was not observed here. The most likely reason for the missing high ionic conductivity behavior is the limited number of particles that results in poorly conductive, non-contiguous films that remained after the destructive washing step before testing. In fact, the non-tunneling films with limited ionic conductivity covering the 5 μm gap devices does not mean that sensing could not occur. For example, immobilized citrate or aptamers would still be capable of sorbing analyte molecules, but the chemiresistive mechanism that was the initial design goal could not be achieved. Despite this, alternative methods such as electrochemical detection could be capable of extracting meaningful signals from these devices. After the in-solution testing, the devices were taken out from the solution and dried in a nitrogen atmosphere again. The conductivity as indicated by the IV curves increased slightly, which reflects that the film structures were altered during the immersion and testing steps. The instability of the nanoparticle films could be a potential problem for repeated testing and transportation of the aqueous-based aptamer chemiresistors. The possible cause for this is again the lack of a continuous film that remained after the washing steps. The resistance values in both buffered solution and in nitrogen were only slightly higher than blank devices, but from the SEM images, the observation of remaining gold nanoparticles attached to the surface shows that the surface modification techniques were effective for these electrosprayed nanoparticles.

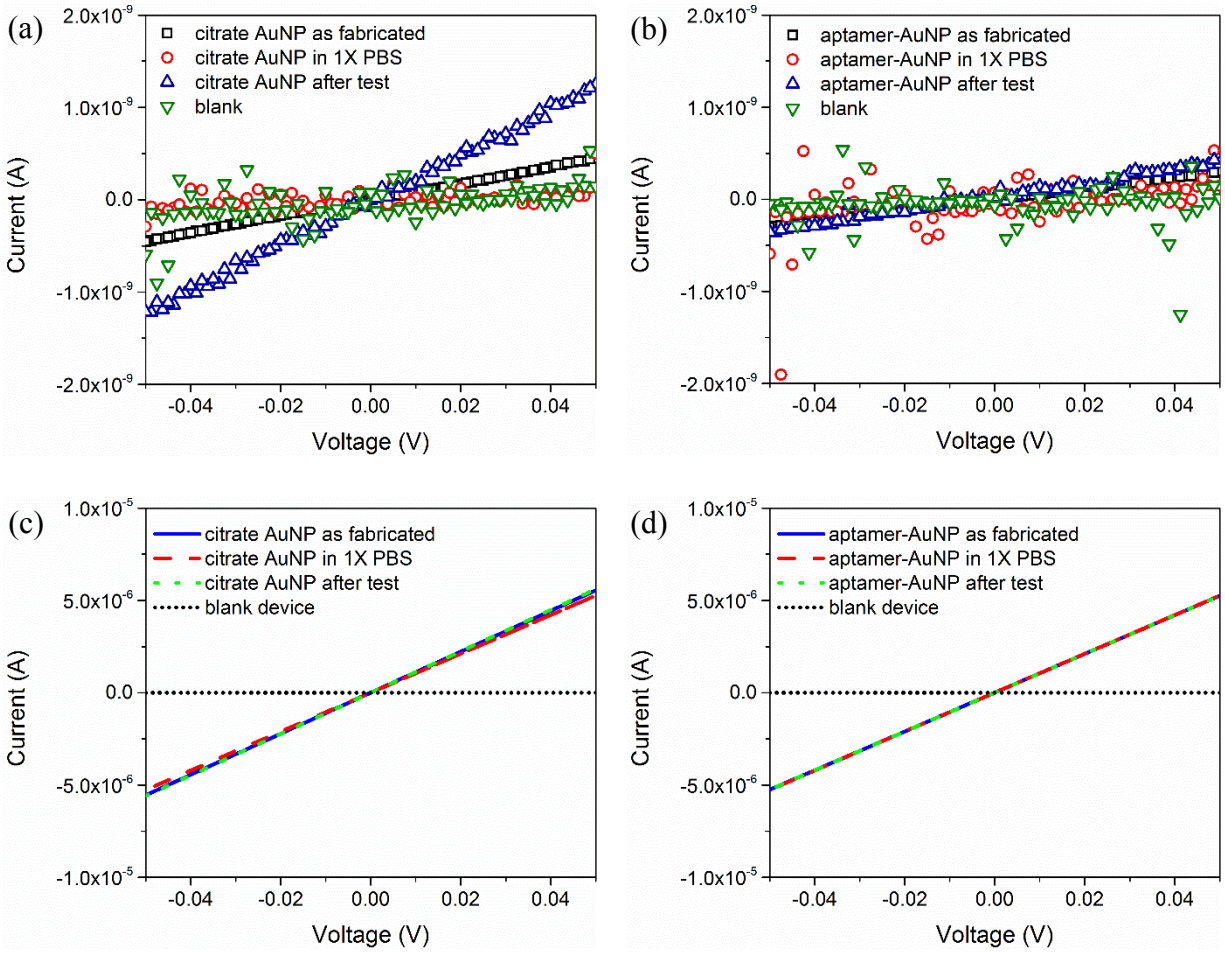

Figure 6.11 IV characteristics of gold nanoparticle devices (a) citrate-functionalized gold nanoparticles on 5 µm device; (b) ATP aptamer functionalized gold nanoparticles on 5 µm device; (c) citrate-functionalized gold nanoparticles on 50 nm device; (d) ATP aptamer functionalized gold nanoparticles on 50 nm device.

In comparison, Figure 6.11 (c) and (d) demonstrate the corresponding effect in 50 nm devices. While the blank devices show similar behavior as the 5 µm devices (Figure 6.10), the resistances of 50 nm devices before, during, and after the solution immersion was nearly equal. It is evident from the multiple IV curves in both citrate-functionalized gold nanoparticle devices and

aptamer-functionalized gold nanoparticle devices that the initial conductive paths of the 50 nm devices were not altered by the aqueous environments. The IV curves show no capacitive effects, and are shaped similar to the gas-phase nanoscale devices discussed in Chapter 5. Furthermore, the resistances of about 10 kΩ are also similar to the small molecule thiols that were reported earlier in Chapter 5. Given the relatively lower biomolecular attachment density due to larger molecular size and conformational folding of biomolecules, the interparticle distances in this nanoparticle film are likely to be similar to that consisting of small molecule thiol gold nanoparticles. Therefore, resistance is similar. Overall, exposure to aqueous environments removes loosely-attached gold nanoparticles and only relatively strongly attached gold nanoparticles remain, but the short conduction path in the 50 nm devices are less prone to solvent damage compared to the 5 μm devices.

6.4.4 Impedance measurements

Figure 6.12(a) shows the impedance spectra of three devices performed in 1× PBS buffer. In both 50 nm blank device and 5 μm device, the impedance-frequency relationships are typically of an open circuit device, which is consistent with the IV measurements in the previous section. On the log scale, the complex impedance goes up linearly with decreasing frequency, which indicates a simple RC-circuit without nanoparticle film resistance. The 50 nm devices with gold nanoparticles, on the other hand, shows flat impedance-frequency behavior at frequencies < 500 Hz. The transition frequency from resistance-dominated region to solution capacitance-dominated region is slightly more than 10 Hz, which is lower than the ink-jet printed gold nanoparticle chemiresistors with organic ligands measured in 1 M KCl solution (Figure 6.2).[13] The impedance of the 50 nm device with gold nanoparticles is about two orders of magnitude smaller than blank 50 nm device at 10 Hz. Therefore, the relative resistance of the nanoparticle film is larger

compared to nanoparticles functionalized with small-molecule water-insoluble thiols, reasonably due to some swelling of the nanoparticle films, but the overall liquid-phase behavior of the devices was similar to nanoparticles functionalized by small organic thiols.[13]

The phase angles of the three devices are considered in Figure 6.12(b). The 5 μm and blank 50 nm and devices show very similar phase angle-frequency relationships of 65° to 80°, suggesting capacitance-dominated behavior, consistent with the impedance spectra. The 50 nm device with aptamer-functionalized gold nanoparticles shows a rapid decrease of the phase angle to 0° when the frequency is below 500 Hz. Therefore, at IV testing conditions when DC current is measured, the electrical behavior is dominated by resistance contribution from the gold nanoparticle film. Overall, the existence of a transition frequency, similar slope to open circuit devices at higher frequencies (> 500 Hz) in the impedance spectra, and the rapid decrease to 0° phase angle at lower frequencies (< 500 Hz) all indicates that the electronic conduction of the 50 nm device was dominant at low frequencies.

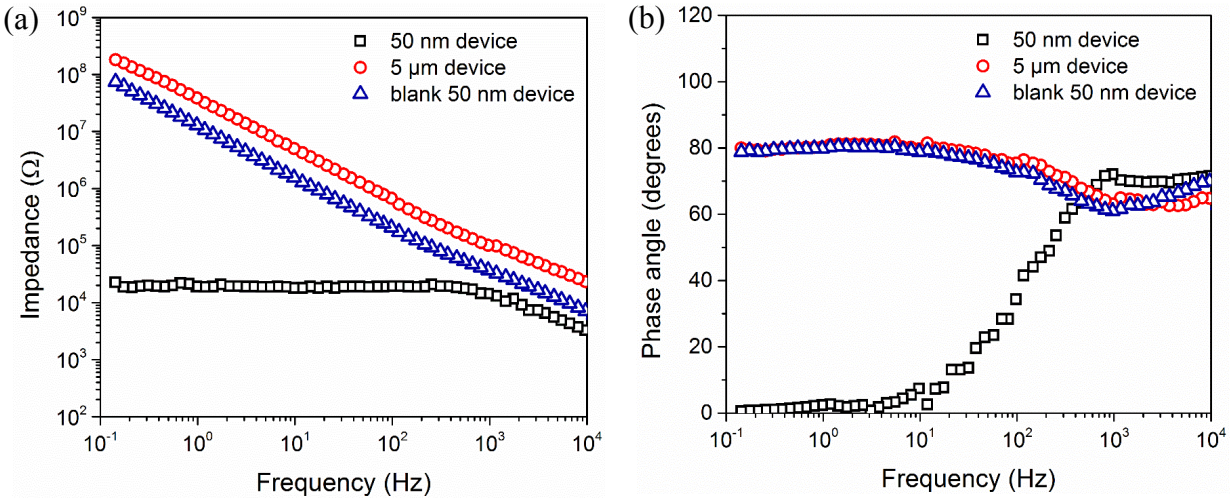

Figure 6.12 (a) Impedance spectra of typical aqueous-based chemiresistor sensors of 50 nm and 5 μm gap sizes. (b) Phase angles of the three devices. The functionalization of gold nanoparticles is ATP-aptamer. For blank devices, no nanoparticles were deposited.

6.4.5 Elemental analysis

EDX analysis of the repetitively-washed gold nanoparticle film were performed. The nanoscale devices show the presence of nitrogen and phosphorus that are compositional elements of DNA. These are elements in addition to gold and carbon that is commonly found in typical gold nanoparticles protected with small-molecule organic ligands (Chapter 5). The elemental information shown in the EDX spectra is supportive of the fact that gold and DNA remains on the surface after repeated gentle water exposure, and the Au-surface bonding and oligonucleotide-nanoparticle bonding were strong enough to these gentle solvent exposures.

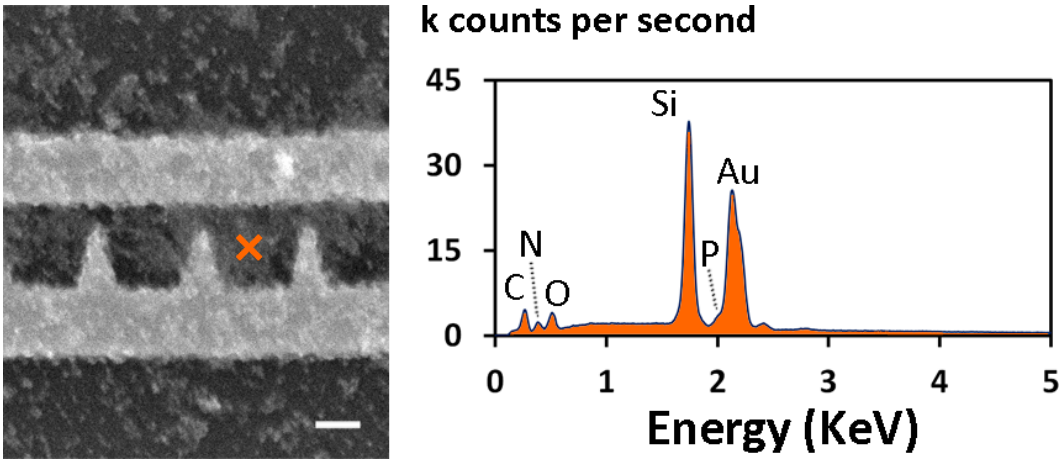

Figure 6.13 Selected point EDX analysis of ATP/adenosine aptamer-functionalized gold nanoparticles on nanoscale devices. Scale bar: 100 nm.

6.4.6 Sensing of nucleobases in static conditions

Preliminary studies of the water-based sensing of gold nanoparticles were performed in static conditions to reduce possible changes to the devices caused by flowing media. Figure 6.14(b) shows the higher end of the IV curves obtained from blank buffer, 1 mM adenosine, and 1 mM guanosine. The buffers used are all 1× PBS. Adenosine is the target for the ATP aptamer, while guanosine is the 2-ringed purine nucleoside with the most similar structure to adenosine. The addition of both analytes results in a slight decrease in the current, with the response to adenosine slightly bigger than that to guanosine. The inset shows the overall IV curve, with responses relatively weak. The low response could be due to low percentage of aptamers having the right configuration due to immobilization on gold nanoparticles, limited effectiveness of the buffer chosen, or possibly the failure of analyte insertion into the electron tunneling path. The effectiveness of PBS buffer with the ATP/adenosine aptamer system has been well-documented,[21]

but a number of other Tris-based buffer systems[22, 23] might be more effective in this detection procedure.

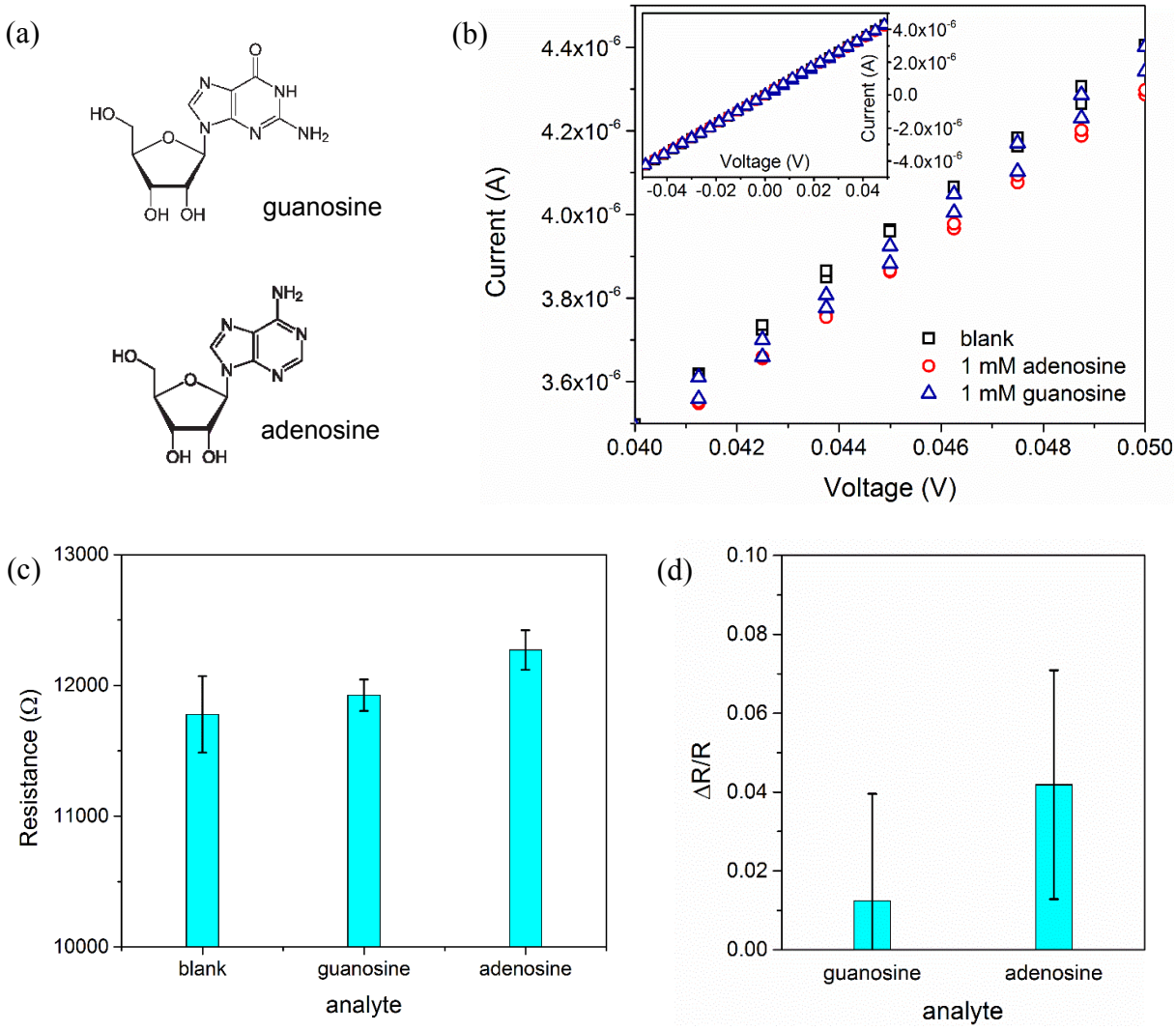

Figure 6.14 (a) Structures of two analytes tested for ATP/adenosine aptamer: guanosine, a non-target; and adenosine, a target. (b) High voltage portion (0.04 – 0.05 V) of the IV curves obtained from two analytes at concetrations of 1 mM in nanoscale chemiresistor in 1× PBS; (c) Average resistance values of the nanoscale devices in 1 mM analytes. (d) Average change in resistance in part (c) expressed as $\Delta R/R$.

Figure 6.14(b) and (c) summarize the resistance values of multiple devices in blank buffer, 1 mM adenosine, and 1 mM guanosine. Guanosine generates a slight increase in resistance, which is within the margin of error, while adenosine produces a resistance increase of about 4%. Despite relatively large margin of errors and moderate sensitivity, these preliminary results show that the ATP/adenosine-aptamer-based chemiresistors are more selective to adenosine than to guanosine. Given the structural similarity between adenosine and guanosine, the selectivity of nanoscale sensors shows promise for specific detection of analytes based on aptamer-analyte interactions.

6.4.7 Device function and performance summary

Chapters 4, 5, and 6 provided much insights into the working mechanisms of organic functionalized gold nanoparticles under various conditions across different device sizes. As an overall summary, Table 6.1 reviews the working mechanism for hydrophilic, electrolyte functionalized gold nanoparticle chemiresistors in comparison to water-insoluble, small molecule functionalized gold nanoparticle chemiresistors. The comparison highlights two important aspects. First, for chemiresistors prepared using small-molecule hydrophobic ligands, conduction and sensing mechanisms shown by extensive studies in literature[24] and relevant work in this thesis do not change with relative humidity. In contrast, gold nanoparticles functionalized with an electrolyte respond to water vapor, and activate ionic conduction. This process causes swelling behavior to be masked. In the aqueous condition, film damage occurs, causing the nanoparticle films to lose conductivity and sensing ability.

Second, because of the water-soluble nature of the gold nanoparticles, creating chemiresistors in the nanoscale dimensions prove advantageous over micron-scale dimensions. On the nanoscale electrode platform, the films are less prone to solvent damage, and the critical

thickness of the nanoparticle films for electrical conduction is much reduced. As a result, an aqueous-based sensor has a higher manufacturing success rate on the nanoscale device platform, while the micron-scale devices fabricated with the current deposition technique do not produce films that are stable enough in aqueous environments. As demonstrated in Chapter 6, nanoscale chemiresistors functionalized with DNA aptamer were still conductive based on tunneling mechanism, and were sensitive to analytes in the aqueous sensing environments.

Table 6.1 Summary of performances of chemiresistor sensors fabricated with gold nanoparticles with two classes of surface functionalization molecules and electrode gap dimensions

Nanoparticle functionalization	Device gap dimension	Experimental conditions	Conduction mechanism	Transducing mechanism
DNA and hydrophilic electrolyte molecules	μm	dry (0% RH)	electron tunneling	swelling-induced tunneling resistance change
		low RH (< 60%)	electron tunneling, some ionic contribution	swelling-induced tunneling resistance change
		high RH (> 60%)	ionic	(sensor is non-operational)
		aqueous	(low conductivity)	(sensor is non-operational)
	nm	dry (0% RH)	electron tunneling	swelling-induced tunneling resistance change
		aqueous	electron tunneling	swelling-induced tunneling resistance change
small molecule thiols, hydrophobic, and non-electrolyte molecules	μm	dry/humid	electron tunneling	swelling-induced tunneling resistance change
		aqueous	electron tunneling	swelling-induced tunneling resistance change
	nm	dry/humid	electron tunneling	swelling-induced tunneling resistance change
		aqueous	electron tunneling	swelling-induced tunneling resistance change

6.5 Summary

In this chapter, a preliminary study of the concept of aqueous-based chemiresistors fabricated using water-soluble materials was conducted. For typical micron-scale devices with 5

μm or larger electrode spacing, the stability of the nanoparticle film in an aqueous environment is a challenging issue, as the nanoparticles are themselves soluble. Functionalization of the SiO_2 surface with MPTES was shown to be effective in attaching the water-soluble citrate-functionalized and oligonucleotide-functionalized gold nanoparticles, but mild washing conditions remove part of the nanoparticle films, making them non-conductive. Although fully-hydrated, the DNA-functionalized gold nanoparticle film showed different behavior than DNA-functionalized nanoparticle films tested in high-humidity gas phase. While an intact gold nanoparticle film in the gas phase showed much reduced electrical resistance due to inter-particle ionic conduction, the partially damaged nanoparticle film in the aqueous phase was virtually non-conductive. This observation substantiates the obvious importance of maintaining nanoparticle film integrity in microelectronic devices.

When the electrode gap spacing is reduced to 50 nm, the nanoparticle films would still to be prone to damage by washing fluids. However, the possibility of a break in the electrical conduction path is much reduced. In this study, at least 40% of the nanoscale devices show resistance values in the range of 10 kΩ to 50 kΩ in aqueous conditions, compared to none of the 5 μm devices being more conductive than 1 GΩ in the same conditions. Therefore, having fewer nanoparticles bridging the electrode gaps offers a practical advantage of more robust chemiresistive film. Importantly, the use of nanoscale devices lowers the device resistance, thus the associated signals, into a measurable range. As the signal is entirely based on simple electrical measurements, the transduction mechanism is greatly simplified. Different from other extensively studied multi-step detection mechanisms, the aptamer-gold nanoparticle chemiresistor is more direct, miniaturizable, and its signals are easier to interpret. But it firstly needs to be tested to show

linear range and signal-to-noise ratios, and next to find the LODs of this system. Secondly it needs to be tested for compatibility with other aptamer-analyte pairs.

6.6 References

1. Cho, E. J.; Lee, J.-W.; Ellington, A. D. Applications of Aptamers as Sensors. *Annual Review of Analytical Chemistry* **2009**, 2, 241-264.

2. Tjong, V.; Tang, L.; Zauscher, S.; Chilkoti, A. "Smart" DNA interfaces. *Chemical Society Reviews* **2014**, 43, 1612-1626.

3. Nielsen, L. J.; Olsen, L. F.; Ozalp, V. C. Aptamers Embedded in Polyacrylamide Nanoparticles: A Tool for in Vivo Metabolite Sensing. *ACS Nano* **2010**, 4, 4361-4370.

4. Li, Z.; Muhandiramlage, T. P.; Keogh, J. P.; Hall, H. K.; Aspinwall, C. A. Aptamer-functionalized porous phospholipid nanoshells for direct measurement of Hg2+ in urine. *Analytical and Bioanalytical Chemistry* **2014**, 407, 953-960.

5. Homola, J. Surface Plasmon Resonance Sensors for Detection of Chemical and Biological Species. *Chemical Reviews* **2008**, 108, 462-493.

6. He, P.; Liu, L.; Qiao, W.; Zhang, S. Ultrasensitive detection of thrombin using surface plasmon resonance and quartz crystal microbalance sensors by aptamer-based rolling circle amplification and nanoparticle signal enhancement. *Chemical Communications* **2014**, 50, 1481-1484.

7. Jahns, S.; Bräu, M.; Meyer, B.-O.; Karrock, T.; Gutekunst, S. B.; Blohm, L.; Selhuber-Unkel, C.; Buhmann, R.; Nazirizadeh, Y.; Gerken, M. Handheld imaging photonic crystal biosensor for multiplexed, label-free protein detection. *Biomed. Opt. Express* **2015**, 6, 3724-3736.

8. Mukherjee, S.; Meshik, X.; Choi, M.; Farid, S.; Datta, D.; Lan, Y.; Poduri, S.; Sarkar, K.; Baterdene, U.; Huang, C. E.; Wang, Y. Y.; Burke, P.; Dutta, M.; Stroscio, M. A. A Graphene and Aptamer Based Liquid Gated FET-Like Electrochemical Biosensor to Detect Adenosine Triphosphate. *IEEE Transactions on NanoBioscience* **2015**, 14, 967-972.

9. Star, A.; Gabriel, J.-C. P.; Bradley, K.; Grüner, G. Electronic Detection of Specific Protein Binding Using Nanotube FET Devices. *Nano Letters* **2003**, 3, 459-463.

10. Wang, R. E.; Zhang, Y.; Cai, J.; Cai, W.; Gao, T. Aptamer-Based Fluorescent Biosensors. *Current Medicinal Chemistry* **2011**, 18, 4175-4184.

11. Tang, Y.; Ge, B.; Sen, D.; Yu, H.-Z. Functional DNA switches: rational design and electrochemical signaling. *Chemical Society Reviews* **2014**, 43, 518-529.

12. Jiang, X. Fabrication of Nanogap Electrodes by Selective-area Copper Atomic Layer Deposition. Doctoral Dissertation, University of Connecticut, Storrs, 2014.

13. Raguse, B.; Chow, E.; Barton, C. S.; Wieczorek, L. Gold Nanoparticle Chemiresistor Sensors: Direct Sensing of Organics in Aqueous Electrolyte Solution. *Analytical Chemistry* **2007**, 79, 7333-7339.

14. Cooper, J. S.; Raguse, B.; Chow, E.; Hubble, L.; Müller, K.-H.; Wieczorek, L. Gold Nanoparticle Chemiresistor Sensor Array that Differentiates between Hydrocarbon Fuels Dissolved in Artificial Seawater. *Analytical Chemistry* **2010**, 82, 3788-3795.

15. Webster, M. S.; Cooper, J. S.; Chow, E.; Hubble, L. J.; Sosa-Pintos, A.; Wieczorek, L.; Raguse, B. Detection of bacterial metabolites for the discrimination of bacteria utilizing gold nanoparticle chemiresistor sensors. *Sensors and Actuators B: Chemical* **2015**, 220, 895-902.

16. Liu, S.; Zhang, X.; Luo, W.; Wang, Z.; Guo, X.; Steigerwald, M. L.; Fang, X. Single-Molecule Detection of Proteins Using Aptamer-Functionalized Molecular Electronic Devices. *Angewandte Chemie International Edition* **2011**, 50, 2496-2502.

17. Genereux, J. C.; Barton, J. K. Mechanisms for DNA Charge Transport. *Chemical Reviews* **2010**, 110, 1642-1662.

18. Goss, C. A.; Charych, D. H.; Majda, M. Application of (3-mercaptopropyl)trimethoxysilane as a molecular adhesive in the fabrication of vapor-deposited gold electrodes on glass substrates. *Analytical Chemistry* **1991**, 63, 85-88.

19. Grabar, K. C.; Allison, K. J.; Baker, B. E.; Bright, R. M.; Brown, K. R.; Freeman, R. G.; Fox, A. P.; Keating, C. D.; Musick, M. D.; Natan, M. J. Two-Dimensional Arrays of Colloidal Gold Particles: A Flexible Approach to Macroscopic Metal Surfaces. *Langmuir* **1996**, 12, 2353-2361.

20. Whitesides, G. M.; Ostuni, E.; Takayama, S.; Jiang, X.; Ingber, D. E. Soft Lithography in Biology and Biochemistry. *Annual Review of Biomedical Engineering* **2001**, 3, 335-373.

21. Li, Z.; Wang, Y.; Liu, Y.; Zeng, Y.; Huang, A.; Peng, N.; Liu, X.; Liu, J. A novel aptasensor for the ultra-sensitive detection of adenosine triphosphate via aptamer/quantum dot based resonance energy transfer. *Analyst* **2013**, 138, 4732-4736.

22. Huizenga, D. E.; Szostak, J. W. A DNA Aptamer That Binds Adenosine and ATP. *Biochemistry* **1995**, 34, 656-665.

23. Li, N.; Ho, C.-M. Aptamer-Based Optical Probes with Separated Molecular Recognition and Signal Transduction Modules. *Journal of the American Chemical Society* **2008**, 130, 2380-2381.

24. Peng, G.; Tisch, U.; Adams, O.; Hakim, M.; Shehada, N.; Broza, Y. Y.; Billan, S.; Abdah-Bortnyak, R.; Kuten, A.; Haick, H. Diagnosing lung cancer in exhaled breath using gold nanoparticles. *Nature Nanotechnology* **2009**, 4, 669-673.

Chapter 7

CONCLUSIONS AND OUTLOOK

7.1 Summary and conclusions

In this dissertation, progressive studies on new materials and new fabrication technologies in nanogap chemiresistor sensors were performed. The aim has been to explore new materials for molecular recognition that will enhance the selectivity of sensors, and to investigate fabrication techniques to integrate these materials into working electronic devices.

First, the solid-state sorption behavior of DNA was studied using a QCM. The partition coefficients of various vapors on thin DNA coatings on quartz crystals were obtained, and modeled with LSER equations to identify the hydrogen bonding terms. It was found that the solid-state LSER parameters of DNA sequences studied were sequence-dependent, and the addition of buffer salts during deposition also changes the interaction parameters. However, the range of LSER parameters that were displayed by linear DNA and aptamers were very narrow. DNA was shown to be no more special than synthetic polymers in the solid state. Therefore, solid DNA is capable of absorbing vapor molecules, but further studies in aqueous buffered condition would be

necessary for specific aptamer-analyte interactions. However, the findings from this study serve as a reference for new materials that might show gas-phase specific interactions. In addition, the success of gas-phase LSER modeling of biomolecules suggests that liquid-phase LSER modeling of DNA is also possible, which may provide additional insights into well-established molecular recognition concepts. For example, molecular recognition events should show differences in both gas-solid and liquid-solid LSER parameters from typical polymers.

Second, the integration of DNA with gold nanoparticle chemiresistors was studied. In dry atmosphere, DNA-functionalized gold nanoparticles behaving similarly as chemiresistors using gold nanoparticles functionalized by small molecule thiol ligands. The sorption of vapor molecules causes swelling of the DNA on nanoparticles. However, as humidity level increases, ionic conduction in the DNA is activated, and the resistance decreases sharply. At the intermediate relative humidity range, the sensors very sensitive to organic vapors, partially because of high sensitivity of ionic conduction to chemical potential of water vapors. Over a relative humidity of 60%, the sensors become dominated by water vapor sorption and become unresponsive to organic vapors. The chemiresistor sensitivity profiles agree well with those obtained on the QCM, highlighting the ability of the chemiresistor sensor to translate mass change into electrical signals and preserving material selectivity. This study also points out the potential problems of an ionic, hydrophilic material as sensing material. Despite the hydration of the nanoparticle film, the material is stationary and localized, creating highly conductive charge transport pathways.

Third, an attempt to downsize the chemiresistors was performed. The primary reason, applicable to all kinds of sensing materials, is to enable small sensors for portable, interconnected technology. The more specific reason for biomolecules is to reduce the amount, thus cost, of using

these expensive materials. Microfabricated electrodes of 50 nm spacing were used, and as a testing material, small-molecule thiols were used as the ligands on gold nanoparticles. Dielectrophoretic assembly was used to confine nanoparticle deposition within a small area in between electrodes on the devices. To attain good permittivity of the solvent, ethanol was used to form a dilute solution of the nanoparticles for dielectrophoretic assembly. The nanoscale devices showed similar selectivity as 20 μm devices fabricated using drop-cast gold nanoparticles. However, as the nanoparticle film between the nanoscale electrodes were just one to two layers thick, the response speed of the nanoscale devices is much higher. This study also reflects the technological feasibility combined top-down and bottom-up approaches for device fabrication.

Lastly, the first steps toward aqueous-based chemiresistors using DNA-functionalized gold nanoparticles were developed. Using a combination of electrospray technique and MPTES-modified substrates, thin layers of DNA-functionalized gold nanoparticles were deposited onto the substrate. The electrospray technique provides the advantage of more uniform thickness and minimized coffee ring effect, while the silanized surface helps to attach the water-soluble nanoparticles, preventing them from being washed off by flowing liquid medium. A significant size-effect of the electrode gap spacing was demonstrated in this study. The 5 μm spacing devices were rendered irreversibly non-conductive by flowing solutions and immersion in buffered solutions, with the majority of the nanoparticles being washed off. Because of the relatively long distance between electrodes, the conducting paths are easily damaged by the dissolution of the aqueous buffer. On the other hand, when the inter-electrode spacing is much reduced, the probability of a damaged electron conduction path is reduced, resulting in higher number of successful working chemiresistor devices, with resistance in the range of 10 to 20 kΩ. Using nanoscale chemiresistors as a sensor platform and ATP-aptamer-functionalized gold nanoparticles

as the sensing material, preliminary studies on adenosine and guanosine were performed. The resistance increase was found to be higher for the aptamer target adenosine than for the non-target guanosine. These findings show that nanoscale chemiresistors are promising ways to enhance speed and miniaturize devices. Furthermore, this technique produces more robust sensors that help to incorporate water-soluble sensing elements into devices that work in aqueous environment, potentially applicable for other aqueous sensor-analyte pairs.

7.2 Future work

7.2.1 Arrays of nanoscale sensors

As we have learned from Chapter 5, chemiresistors can be downscaled to 50 nm electrode spacing and still exhibit similar selectivity behavior as the typical micron-scaled chemiresistors. This manufacturing proof-of-concept prompts the experimentation of multiple types of chemiresistors on a single chip, fully realizing the *lab-on-a-chip* concept. The current design utilizes 4 pairs of electrodes, with each device occupying a total chip-area of 0.4 mm^2. As the dielectrophoretic assembly process of gold nanoparticles is highly localized, albeit causing some excessive deposition of gold nanoparticles around the microfabricated electrodes, the necessary area where one device needs to occupy should be comfortably reduced to 1 μm^2, with multiple pairs of separate electrodes offering built-in redundancy. Figure 7.1 illustrates a proposed design for a highly integrated sensor array, with the core part as small as 20 μm × 20 μm. The sensor array should fit conveniently on some of the tiniest microchips and packages.

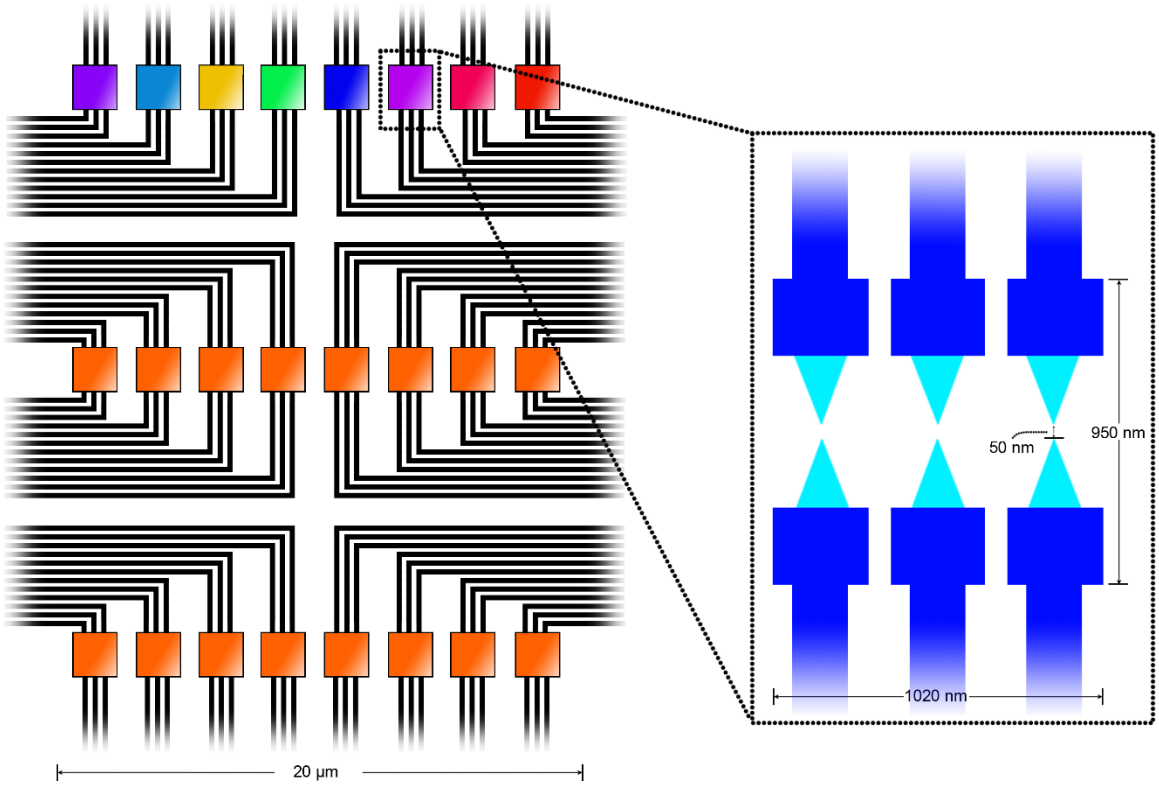

Figure 7.1 Design of an array of chemiresistor sensors using the 50 nm gap double-tip configuration, with dimensions that are capable of being packaged into a single microchip

The chemical sensor array could be in judiciously integrated with physical sensor components, for example nanoscale thermometers,[1] to enhance its information availability. Further, referencing back to the discussions in Chapter 1, the sensor arrays could be integrated with other microfabricated electrical components to produce "smart dusts" – field deployable sensor systems that combine sensing, data processing, and transmitting capabilities. Lastly, the microchips would be integrated with data processing mechanisms, e.g. artificial neural networks (ANN), to assist in producing powerful sensor systems that enable efficient identification of analytes and analyte mixtures.

7.2.2 Biomolecular chemiresistor sensors

Chemical sensors based on biomolecular recognition elements are highly relevant technologies today. This is especially true in a society that where improving healthcare and raising environmental awareness are some of the most pressing issues. As reflected by the liquid-based gold nanoparticle chemiresistor studies, integrity of the composite films in aqueous system is practically overcome by shortening the electrical conduction paths. Along this line of thought, receptor-analyte pairs of high importance for medical diagnostics can be incorporated into nanoscale chemiresistors. The simplicity of the functionalized chemiresistor sensors can potentially advance many of the current sensing mechanisms. For example, blood glucose sensors, which currently relies on amperometric signals from redox reactions that involve glucose, could be improved using the simple chemiresistor devices, by incorporating the enzymes into nanoscale chemiresistors. Receptor-analyte pairs that are not yet commercialized, including biochemiresistors that employ a 2-step indirect transduction mechanism,[2] aptamer-based fluorescence sensors,[3] aptamer-based SPR sensors,[4] are likely to be reproduced and simplified in the chemiresistors. Depending on the availability of known receptor-analyte pairs that are of value, a series of new chemiresistor products can be produced and tested for their efficiency. Similarly, detection of aqueous analytes of environmental concerns is also possible, by using aptamers for TNT[5], organophosphorus pesticides,[6] bisphenol A,[7] and heavy metals.[8] In all of these applications, the use of gold nanoparticle chemiresistors will dramatically reduce the complexity of the sensing systems, and it remains to be studied whether the electrical system can have sensitivity that meet the requirements for real-world sensing tasks.

By extension, robust nanoscale chemiresistors would potentially be adapted for an encapsulated-device design, where specific sensors for volatile small molecules can be encased in

a local environment preserves the native conformation of biomolecular recognition elements. Encapsulation has been an intuitive and popular technique to create local environment compatible with supramolecular structures. Recent studies using fluorescence detection mechanisms have shown successful aptamer-target binding events within enclosed native environments for detection of intracellular ATP[9] and mercury ions.[10] The use of nanoscale chemiresistors, which offer greater reliability in nanoparticle film integrity, would possibly create robust chemiresistors that operate in an encased native environment, but are deployed in air. These sensors will respond to gas phase analytes that dissolve and diffuse to the aptamers, and will possibly expand the range of analytes for detection by biomolecular recognition elements (Figure 7.2).

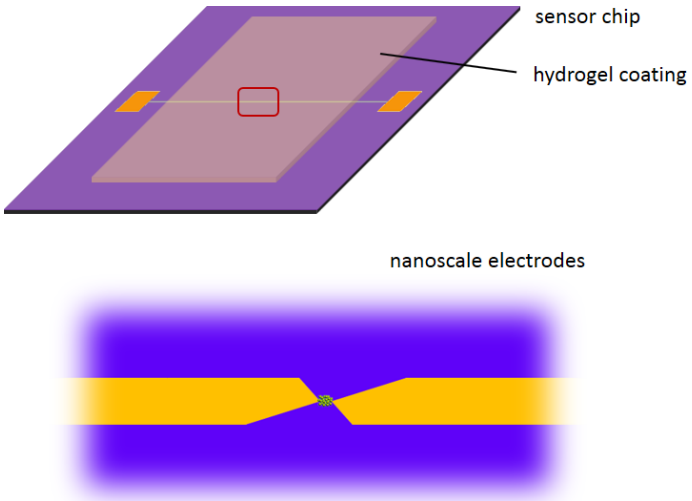

Figure 7.2 Schematics of aptamer-functionalized gold nanoparticle nanoscale chemiresistors encapsulated with a hydrogel for detection of volatile molecules

7.3 References

1. Lee, J.; Kotov, N. A. Thermometer design at the nanoscale. *Nano Today* **2007**, 2, 48-51.

2. Lai, L. M. H.; Goon, I. Y.; Chuah, K.; Lim, M.; Braet, F.; Amal, R.; Gooding, J. J. The Biochemiresistor: An Ultrasensitive Biosensor for Small Organic Molecules. *Angewandte Chemie International Edition* **2012**, 51, 6456-6459.

3. Wang, R. E.; Zhang, Y.; Cai, J.; Cai, W.; Gao, T. Aptamer-Based Fluorescent Biosensors. *Current Medicinal Chemistry* **2011**, 18, 4175-4184.

4. Bai, Y.; Feng, F.; Zhao, L.; Wang, C.; Wang, H.; Tian, M.; Qin, J.; Duan, Y.; He, X. Aptamer/thrombin/aptamer-AuNPs sandwich enhanced surface plasmon resonance sensor for the detection of subnanomolar thrombin. *Biosensors and Bioelectronics* **2013**, 47, 265-270.

5. Ho, M. Y.; D'Souza, N.; Migliorato, P. Electrochemical Aptamer-Based Sandwich Assays for the Detection of Explosives. *Analytical Chemistry* **2012**, 84, 4245-4247.

6. Zhang, C.; Wang, L.; Tu, Z.; Sun, X.; He, Q.; Lei, Z.; Xu, C.; Liu, Y.; Zhang, X.; Yang, J.; Liu, X.; Xu, Y. Organophosphorus pesticides detection using broad-specific single-stranded DNA based fluorescence polarization aptamer assay. *Biosensors and Bioelectronics* **2014**, 55, 216-219.

7. Jo, M.; Ahn, J.-Y.; Lee, J.; Lee, S.; Hong, S. W.; Yoo, J.-W.; Kang, J.; Dua, P.; Lee, D.-k.; Hong, S.; Kim, S. Development of Single-Stranded DNA Aptamers for Specific Bisphenol A Detection. *Oligonucleotides* **2011**, 21, 85-91.

8. Chen, Z.; Li, L.; Mu, X.; Zhao, H.; Guo, L. Electrochemical aptasensor for detection of copper based on a reagentless signal-on architecture and amplification by gold nanoparticles. *Talanta* **2011**, 85, 730-735.

9. Nielsen, L. J.; Olsen, L. F.; Ozalp, V. C. Aptamers Embedded in Polyacrylamide Nanoparticles: A Tool for in Vivo Metabolite Sensing. *ACS Nano* **2010**, 4, 4361-4370.

10. Li, Z.; Muhandiramlage, T. P.; Keogh, J. P.; Hall, H. K.; Aspinwall, C. A. Aptamer-functionalized porous phospholipid nanoshells for direct measurement of Hg2+ in urine. *Analytical and Bioanalytical Chemistry* **2014**, 407, 953-960.